The Dissertation Committee for Guillermo Blanc
certifies that this is the approved version of the following dissertation:

Studying Star Formation at Low and High Redshift with Integral Field Spectroscopy

Committee:

Karl Gebhardt, Supervisor

Neal J. Evans II

Gary J. Hill

Volker Bromm

Eric Gawiser

Studying Star Formation at Low and High Redshift with Integral Field Spectroscopy

by

Guillermo Blanc, Licenciado, Magister

DISSERTATION

Presented to the Faculty of the Graduate School of

The University of Texas at Austin

in Partial Fulfillment

of the Requirements

for the Degree of

DOCTOR OF PHILOSOPHY

THE UNIVERSITY OF TEXAS AT AUSTIN

May 2011

Dedicated to my wife Isidora, my mother Alicia, and my father Neville.

Acknowledgments

Above all, I would like to thank my dear wife Isidora for all the sacrifices she had to make to be by my side during my Ph.D. Thanks to her unconditional support, endless love, invaluable company, and charming humor, these years in graduate school have been the bests of my life so far. I thank my parents, Alicia and Neville, who, since I was a little kid, provided me with the human and academic education that allowed me to successfully get to this point in life. A special thanks to my Ph.D. supervisor Karl Gebhardt, who, most of the time without knowing it, has taught me valuable lessons on how to be a good scientist. These include: always putting in doubt your new and exciting result, until you cannot find a way to prove yourself wrong; not being afraid of things you do not know how to do, and just go ahead and learn how to do them; never care too much about politics; and most importantly, have a good time while doing research. Many thank to Phillip McQueen and Gary Hill for designing and constructing VIRUS-P, and for their advice on the use of the instrument. I would like to acknowledge David Doss, and the staff at McDonald Observatory for their invaluable help during the observations, and my good friends Josh Adams, Jeremy Murphy, Bill Hicks, and Bonnie Tyler with whom we spent countless hours collecting photons at the 2.7m telescope.

Studying Star Formation at Low and High Redshift with Integral Field Spectroscopy

Publication No. _____

Guillermo Blanc, Ph.D.
The University of Texas at Austin, 2011

Supervisor: Karl Gebhardt

In this thesis I focus mainly in studying the process of star formation in both high redshift, and local star forming galaxies, by using an observational technique called *integral field spectroscopy* (IFS). Although these investigations are aimed at studying the star formation properties of these objects, throughout this work I will also discuss the geometric, kinematic, and chemical structures in the inter-stellar medium of these galaxies, which are intimately connected with the process of star formation itself. The studies presented here were conducted under the umbrella of two different projects. First, the HETDEX Pilot Survey for Emission Line Galaxies, where I have studied the properties of Lyα emitting galaxies across the $2 < z < 4$ range, with an emphasis in trying to understand the process by which Lyα photons, produced in large quantities in the active star forming regions, are able to escape the

ISM of these objects, allowing us to detect them in the Lyα line. The second project from which results are presented here is the VIRUS-P Exploration of Nearby Galaxies (VENGA), an ongoing campaign to obtain spatially resolved spectroscopy over a broad wavelength range for large portions of the disks of 30 nearby spiral galaxies. In this thesis, the VENGA data is used to study the physical parameters that set the rate of star formation in the different environments present within galaxies in the local universe.

Table of Contents

Acknowledgments **v**

Abstract **vi**

List of Tables **xi**

List of Figures **xiii**

Chapter 1. Introduction **1**

Chapter 2. The HETDEX Pilot Survey: The Evolution of the Lyα Escape Fraction from the UV Slope and Luminosity Function of $1.9 < z < 3.8$ LAEs **9**

2.1 Introduction 11
2.2 The HETDEX Pilot Survey 16
2.3 LAE Sample 22
2.4 The UV slope of Lyman alpha emitters 24
2.4.1 Measurement of the UV continuum Slopes, UV Luminosities, and Lyα EWs 24
2.4.2 Dust Properties of LAEs and comparison to Previous Measurements 29
2.4.3 Evolution of the Dust Properties of LAEs 31
2.5 UV versus Lyα SFRs and the Escape Fraction of Lyα Photons 34
2.5.1 Estimation of the Star Formation Rate and the observed $SFR(Ly\alpha)$ to $SFR(UV)$ ratio. 35
2.5.2 Dust Corrected $SFRs$ and Estimation of the Lyα Escape Fraction 38
2.5.3 Evolution of the Lyα Escape Fraction in LAEs 41
2.5.4 The Relation between f_{esc}(Lyα) and Dust 42
2.6 The Lyα Luminosity Function 46

2.6.1 Measurement of the Luminosity Function 47
2.6.2 Comparison with Previous Measurements 50
2.6.3 Evolution of the Lyα Luminosity Function 51
2.7 Evolution of the Lyα Luminosity Density and the Global Escape Fraction of Lyα Photons. 53
2.8 Conclusions 61

Chapter 3. The Spatially Resolved Star Formation Law from Integral Field Spectroscopy: VIRUS-P Observations of NGC 5194 84

3.1 Introduction 86
3.2 Observations 92
3.3 Data Reduction 94
3.3.1 Flux Calibration 96
3.4 Other Data 99
3.4.1 THINGS HI Data 99
3.4.2 BIMA SONG CO Data 100
3.4.3 HST NICMOS Paschen-α Data 100
3.5 Measurement of Emission Line Fluxes 101
3.5.1 Photospheric Absorption Lines and Continuum Subtraction 101
3.5.2 Emission Line Fluxes 103
3.5.3 Extinction Correction from the Balmer Decrement . . . 103
3.6 Measurement of Gas Mass Surface Densities 105
3.7 Photoionization and shock-heating by the central AGN 107
3.8 Contribution from the Diffuse Ionized Gas and Calculation of SFR Surface Densities 109
3.9 The Spatially Resolved Star Formation Law 116
3.9.1 The Fitting Method 120
3.9.2 Fits to the Molecular and Total Gas Star Formation Laws 123
3.10 Balmer Absorption and the N[II]/Hα Ratio, Implications for Narrow-Band Imaging 124
3.11 Comparison with Previous Measurements and Theoretical Predictions 130
3.12 Summary and Conclusions 136

Chapter 4. The VIRUS-P Exploration of Nearby Galaxies (VENGA): Survey Design, Data Processing, and First Results on NGC0628 **177**

4.1 Introduction . . . 178
4.2 Survey Design . . . 184
4.2.1 The VENGA Sample . . . 185
4.2.2 Observing Strategy . . . 188
4.3 Observations . . . 189
4.3.1 NGC0628 Data . . . 191
4.4 Data Reduction and Calibration . . . 192
4.4.1 Basic CCD Processing, Cosmic Ray Rejection, and Fiber Tracing . . . 192
4.4.2 Wavelength Calibration and Characterization of the Instrumental Spectral Resolution . . . 194
4.4.3 Flat Fielding . . . 195
4.4.4 Sky Subtraction . . . 197
4.4.5 Spectrophotometric Flux Calibration . . . 200
4.4.6 Astrometry and Absolute Flux Calibration . . . 201
4.4.7 Spectral Extraction, Combination of Frames, and Formatting of RSS Files . . . 204
4.5 Spectral Analysis Pipeline . . . 207
4.5.1 Stellar Kinematics . . . 208
4.5.2 Emission Line Fluxes and Ionized Gas Kinematics . . . 209
4.6 Results . . . 212
4.6.1 A previously undetected low-luminosity AGN in NGC0628 212
4.6.2 Diffuse Ionized Gas . . . 214
4.6.3 The Nebular Oxygen Abundance Gradient in NGC0628 218
4.6.4 The impact of Metallicity in the Star Formation Efficiency 221
4.7 Summary and Conclusions . . . 224

Chapter 5. Summary **255**

Bibliography **259**

Vita **278**

List of Tables

2.1 Properties of HETDEX Pilot Survey LAEs 81
2.1 Properties of HETDEX Pilot Survey LAEs 82
2.1 Properties of HETDEX Pilot Survey LAEs 83
2.2 Lyα luminosity function Best Fit Schechter Parameters, Luminosity and SFR Density 83
2.3 Lyα Escape Fraction History Best Fit Paramenters 83

3.1 Nebular Emission Line Fluxes, Gas Surface Densities, and SFR Surface Densities 162
3.1 Nebular Emission Line Fluxes, Gas Surface Densities, and SFR Surface Densities 163
3.1 Nebular Emission Line Fluxes, Gas Surface Densities, and SFR Surface Densities 164
3.1 Nebular Emission Line Fluxes, Gas Surface Densities, and SFR Surface Densities 165
3.1 Nebular Emission Line Fluxes, Gas Surface Densities, and SFR Surface Densities 166
3.1 Nebular Emission Line Fluxes, Gas Surface Densities, and SFR Surface Densities 167
3.1 Nebular Emission Line Fluxes, Gas Surface Densities, and SFR Surface Densities 168
3.1 Nebular Emission Line Fluxes, Gas Surface Densities, and SFR Surface Densities 169
3.1 Nebular Emission Line Fluxes, Gas Surface Densities, and SFR Surface Densities 170
3.1 Nebular Emission Line Fluxes, Gas Surface Densities, and SFR Surface Densities 171
3.1 Nebular Emission Line Fluxes, Gas Surface Densities, and SFR Surface Densities 172
3.1 Nebular Emission Line Fluxes, Gas Surface Densities, and SFR Surface Densities 173

3.1 Nebular Emission Line Fluxes, Gas Surface Densities, and SFR Surface Densities 174
3.1 Nebular Emission Line Fluxes, Gas Surface Densities, and SFR Surface Densities 175
3.1 Nebular Emission Line Fluxes, Gas Surface Densities, and SFR Surface Densities 176

4.1 The VENGA Sample 249
4.2 Bulge Structural Parameters 250
4.3 Stellar Masses and Star Formation Rates 251
4.4 VENGA Observing Runs 252
4.4 VENGA Observing Runs 253
4.5 Summary of Red-setup Observations of NGC0628 254
4.6 Fitted Emission Lines 254

List of Figures

2.1 Limiting Lyα luminosity (5σ) as a function of redshift for the survey. The survey depth varies across the observed area due to changes in atmospheric transparency, Galactic extinction, and instrumental configuration. Hence, the background color indicates the fraction of the total survey area over which a given limit is reached. White points mark the redshift and Lyα luminosities (with error-bars) of the 99 objects classified as LAEs. The dotted black and white lines show the mean and best limits over the whole survey respectively. Even below this last limit, the completeness of the survey is not zero, explaining why we see 2 points below this curve. 67

2.2 Redshift distribution of the 99 LAEs in the Pilot Survey (solid histogram). Error-bars represent Poisson uncertainties only. Also shown is the incompleteness-corrected predicted redshift distribution (dotted line) given by our flux limit and assuming the Gronwall et al. (2007) Lyα luminosity function with no evolution over $2 < z < 4$. 68

2.3 UV continuum slope as a function of redshift for the 89 LAEs with broad-band optical counterparts. Objects are color coded by field. The right axis shows the equivalent E(B-V) assuming a Calzetti et al. (2000) attenuation law. The horizontal lines mark the assumed intrinsic UV slope corresponding to a dust-free stellar population ($\beta_0 = -2.23$, solid line), and the mean for the whole sample (dotted line). Also shown are the mean UV slopes for two redshift bins at $1.9 < z < 2.8$ and $2.8 < z < 3.8$ (black squares), with two sets of error-bars corresponding to the standard deviation in β within each bin (large error-bars) and the formal error in the mean (small error-bars). 69

2.4 $E(B-V)$ distribution of LAEs in our sample (Poisson error-bars), together with that of BX/LBGs taken from Erb et al. (2006) and Reddy et al. (2008) (solid histograms). The median of each distribution is marked by the vertical dashed lines. . . 70

2.5 Rest-frame Lyα EW distribution of LAEs in our sample (dashed black histogram). The distributions for low ($E(B-V) < 0.45$) and high ($E(B-V) > 0.45$) reddening objects are shown (blue and red histograms respectively). Also shown are the best-fit exponential distribution ($N \propto \exp[-EW/w_0]$) to the whole sample ($w_0 = 77 \pm 7$Å, solid black line) and the low reddening sample ($w_0 = 74 \pm 7$Å, dotted blue line). 71

2.6 UV versus Lyα derived $SFRs$ for the 83 LAEs in the final sample. Values are not corrected for dust extinction. The solid line shows the median SFR(Lyα) to $SFR(UV)$ ratio of 0.83. The expected range for dust-free normal stellar populations is marked by the dashed lines. Dotted lines mark ratios of 0.01, 0.1, 1, 10, and 100. 72

2.7 Rest-frame Lyα EW, and $SFR(Ly\alpha)$ to $SFR(UV)$ ratio (not corrected for dust) as a function of redshift. The median EW of 71Å and ratio of 0.83 are marked by solid horizontal lines. The dotted lines on the top panel indicate the maximum EW range for young normal stellar populations with metallicities between solar and one 1/50 solar from Schaerer (2003). Dotted lines in the bottom panel display the allowed range in the $SFR(Ly\alpha)$ to $SFR(UV)$ ratio for dust-free normal stellar populations. The open boxes show the median EW and ratio for the two redshift bins at $1.9 < z < 2.8$ and $2.8 < z < 3.8$. 73

2.8 Rest-frame Lyα EW and $SFR(Ly\alpha)$ to $SFR(UV)$ ratio (not corrected for dust) as a function of E(B-V). Symbols are the same as in Figure 2.7. 74

2.9 Same as Figure 2.6, but with $SFR(UV)$ corrected for dust. Error-bars include the uncertainty in the correction. The solid line marks the median escape fraction of 29%. 75

2.10 Escape fraction of Lyα photons as a function of redshift for the 83 LAEs in the final sample. The solid horizontal line denotes the median escape fraction of 29%. Also shown is the median escape fraction for the two redshift bins at $1.9 < z < 2.8$ and $2.8 < z < 3.8$ (open red stars), with error-bars corresponding to the standard deviation of $\log(f_{esc})$ within each bin. The escape fractions of LAEs at $z = 0.3$ with their median from Atek et al. (2009) (green triangles, red open square) are also displayed. . 76

2.11 Lyα escape fraction as a function of E(B-V). Dashed lines show the expected correlation for different values of the parameter $q = \tau_{Ly\alpha}/\tau_{\lambda=1216}$. The red line displays the relation for LBGs showing Lyα in emmission from Kornei et al. (2010). Green triangles show the values for $z \simeq 0.3$ LAEs from Atek et al. (2009). 77

2.12 Lyα luminosity function of the HETDEX Pilot Survey sample of 80 LAEs in COSMOS and HDF-N, shown before and after applying the completeness correction (open black and filled red circles respectively). Poisson error-bars are included. Also displayed are the completeness corrected luminosity function for the two redshift bins at $1.9 < z < 2.8$ and $2.8 < z < 3.8$ (blue and green stars respectively), and the luminosity functions of van Breukelen et al. (2005); Gronwall et al. (2007); Ouchi et al. (2008); Hayes et al. (2010),and Cassata et al. (2011). Schechter fits to the full sample, as well as the low-z and high-z samples, are also presented (solid red, blue, and green curves respectively). The red dashed line denotes the best Schechter fit to the $L(Ly\alpha) \leq 10^{43}$erg s^{-1} bins. 78

2.13 Contours show 1, 2, and 3σ confidence limits for the luminosity function parameters L^* and ϕ^*. Stars show our results for the full sample and the two redshift bins at $1.9 < z < 2.8$ and $2.8 < z < 3.8$. The parameters estimated by van Breukelen et al. (2005); Gronwall et al. (2007); Ouchi et al. (2008); Hayes et al. (2010), and Cassata et al. (2011) are also presented (filled circles). 79

2.14 *Top panel:* SFR density (ρ_{SFR}) as a function of redshift. The solid and dotted lines show the total ρ_{SFR} from Bouwens et al. (2010a) and its typical uncertainty of 0.17 dex. Blue, green, and red filled circles show $\rho_{SFR,Ly\alpha}$ derived from the Lyα luminosity function in the two redshift bins at $1.9 < z < 2.8$ and $2.8 < z < 3.8$, as well as for the full sample. Black filled circles show the derived densities at different redshifts from the luminosity functions of van Breukelen et al. (2005); Shimasaku et al. (2006); Kashikawa et al. (2006); Gronwall et al. (2007); Dawson et al. (2007); Ouchi et al. (2008); Deharveng et al. (2008); Ouchi et al. (2010); Cowie et al. (2010); Hayes et al. (2010); Hibon et al. (2010), and Cassata et al. (2011). Raw values computed without applying an IGM correction are shown by the open circles below each measurement. Values computed integrating the Lyα luminosity functions all the way down to $L(Ly\alpha) = 0$ are shown by the open circles above each measurement. *Bottom panel:* Escape fraction of Lyα photons for the overall galaxy population, derived from the ratio between the Lyα derived $\rho_{SFR,Ly\alpha}$ and the total value at each redshift. The dashed line marks an escape fraction of 100%. Solid lines shows our best fit to the data given by Equation 2.8, while dotted lines show the best fit powerlaw functions. Purple, orange, and cyan colors indicate fits to the escape fraction measurements including an IGM correction and an integration limit for the luminosity function, ignoring the IGM correction, and ignoring the luminosity function integration limit respectively. The black dashed line shows the result of Hayes et al. (2011). 80

3.1 *Left:* HST+ACS V-band image of NGC5194 and its companion NGC 5195 (Mutchler et al., 2005). The central 4.1×4.1 kpc^2 region sampled by the $1.7' \times 1.7'$ VIRUS-P field of view is marked in red. *Right:* Map of the 738 regions sampled by VIRUS-P in the 3 dither positions. Each region has a diameter of $4.3''$ corresponding to $\sim$170 pc at the distance of NGC5194. 143

3.2 *Left:* DSS image of Feige 34. Superimpossed is the 6 dither position pattern used to observe spectro-photometric standard stars. *Right:* Flux measured by each fiber as a function of its distance to the PSF centroid (filled circles). Also shown are the best-fitted Moffat PSF (solid line), and its fiber-sampled light distribution (dashed line). 144

3.3 Continuum normalized spectra around the Hβ, MgII, and Hα features for 3 regions having the highest, median and lowest (top, middle, bottom) S/N per resolution element in the continuum. Crosses show the data with error bars. Red crosses mark the data points used to fit the best linear combination of stellar templates (green solid line). Black crosses were masked in the fit due to the presence of nebular emission. 145

3.4 Nebular emission spectrum of the same regions shown in Figure 3.3, obtained by subtracting the best-fitted linear combination of stellar templates from the observed spectrum. Masked parts of the spectra correspond to the regions around strong night sky emission lines showing background subtraction residuals. . 146

3.5 Hα versus Paα fluxes of all regions showing 5σ detections of Paα emission in the NICMOS narrow-band image. Fluxes are corrected for dust extinction using the Balmer decrement derived values. The solid line shows the Hα/Paα=8.15 ratio predicted by recombination theory. Median error bars for the corrected fluxes are shown. 147

3.6 [NII]λ6584/Hα versus [OIII]λ5007/Hβ line ratio for the 735 regions. The solid line marks the theoretical threshold of Kewley et al. (2001) separating AGNs from star-forming galaxies. Dotted lines mark the $\pm$0.1 dex uncertainty in the threshold modeling. The 17 regions above the threshold and having angular distances to the galaxy nucleus of $< 15''$ are flagged as "AGN affected" and are shown as filled triangles. Open diamonds show the 718 regions unaffected by AGN contamination used to construct the SFL. 148

3.7 Map of the [NII]λ6584/Hα emission line ratio in the central region of NGC 5194. Regions flagged as "AGN affected" are marked by black crosses. 149

3.8 Histogram of the [SII]/Hα of H II regions (solid) and pointings towards DIG (dotted) in the Milky Way as measured by WHAM (Madsen et al., 2006). Vertical lines mark the mean values for the two distributions. 150

3.9 Observed [SII]/Hα emission line ratio for the 718 regions unaffected by AGN contamination. The thin dashed and dotted lines show the mean ratio observed in H II regions and pointings towards the DIG in the Milky Way respectively. The thick dashed and dotted lines show the former ratios scaled down by a factor $Z' = 1.0/1.5$. The left axis shows the fraction of the flux coming from H II regions in the disk given by Equation 3.8. The solid red curve shows the DIG correction applied to the data given by Equation 3.9, and the continuation of the function to fluxes lower than f_0 is marked by the dashed red line. 151

3.10 *Left:* Map of the extinction corrected Hα nebular emission flux in the central 4.1×4.1 kpc^2 of NGC 5194. *Right:* Same map after removing the DIG contribution to the Hα emission line flux, that is, showing only the flux coming from H II regions in the disk of NGC 5194. 152

3.11 Atomic gas suface density versus SFR surface density for the 718 regions unaffected by AGN contamination. Upper limits in Σ_{SFR} correspond to regions with $C_{HII} = 0$. The vertical dashed line marks the HI to H_2 transition threshold at 10 $M_\odot pc^{-2}$. The diagonal dotted lines correspond to constant depletion timescales $\tau = SFE^{-1}$ of 0.1, 1, 10 and 100 Gyr. 153

3.12 Molecular gas suface density versus SFR surface density for the 718 regions unaffected by AGN contamination. Upper limits in Σ_{SFR} correspond to regions with $C_{HII} = 0$. Upper limits in Σ_{H_2} correspond to regions with non-detection in CO at the 1σ level. The diagonal dotted lines correspond to constant depletion timescales $\tau = SFE^{-1}$ of 0.1, 1, 10 and 100 Gyr. Also shown is the best-fitted power law from the Monte Carlo method (black solid line), and the best-fitted parameters. 154

3.13 Total gas suface density versus SFR surface density for the 718 regions unaffected by AGN contamination. Upper limits in Σ_{SFR} correspond to regions with $C_{HII} = 0$. Upper limits in Σ_{HI+H_2} correspond to regions with non-detection in CO at the 1σ level. The diagonal dotted lines correspond to constant depletion timescales $\tau = SFE^{-1}$ of 0.1, 1, 10 and 100 Gyr. Also shown is the best-fitted power law from the Monte Carlo method (black solid line), and the best-fitted parameters. 155

3.14 *Left:* The observed molecular SFL in linear space (top), together with the 200 Monte Carlo realizations of the data for the best-fitted parameters (bottom). The grid used to compare the model to the data is shown in red, and each box in the grid shows a cross, color-coded according to the number of points in the grid (with red corresponding to the highest value and black corresponding to zero). *Center-Top:* Number of data-points per grid elements in the model versus the data. *Center-Bottom and Right:* Reduced χ^2 for each of the three free parameter in the fit (A, N, and ϵ), marginalized over the other two parameters. Red crosses show the χ^2 obtained for each sampled combination of parameters. The best-fitted quadratic function to the minimum χ^2 is shown in green. The best-fitted χ^2, together with the 1σ, 2σ, and 3σ levels are shown as horizontal dotted lines. The blue and black vertical dashed lines marks the best-fitted parameter and its 1σ uncertainty respectively. 156

3.15 ([NII]λ6548+[NII]λ6584+Hα)/Hα ratio as a function of extinction corrected Hα flux for the 718 regions under study. The solid line marks the observed mean value of 1.65. The dashed line marks the 1.67 value expected by assuming line ratio of [NII]λ6584/Hα=0.5 and [NII]λ6548/[NII]λ6584=0.335. 157

3.16 Bias introduced by the missestimation of the strength of the Hα absorption feature or equivalently of the continuum level. Black dots show show the fraction of the observed flux that we would observe if the stellar absorption was not considered at all. Red dots show the same fluxes corrected using a constant absorption EW=-2.4Å. Dark blue and green dots correspond to understimations and overestimations of the continuum by a 10%. Light blue and orange dots correspond to understimations and overestimations of the continuum by a 50%. 158

3.17 VIRUS-P observed Hα fluxes (before dust exticntion correction) versus Hα fluxes measured in the continuum subtracted image from Calzetti et al. (2005) (balck crosses). Data-points to the right of the vertical dotted line were used to scale the narrow-band fluxes in order to account for flux calibration and apperture discrepancies. The green crosses show the Hα fluxes that would have been measured by VIRUS-P if the continuum would have been overestimated by a 30% (see Figure 3.16). . . 159

3.18 Molecular gas SFL as measured by VIRUS-P. Symbols are the same as in Figure 3.12. The black solid line shows our best fitted power-law obtained using the Monte Carlo method described in §9.1. Previous measurements by Kennicutt et al. (2007) and Bigiel et al. (2008) are shown as the green and orange dahsed lines respectively. Also shown are fits to our data (rejecting upper limits) using the FITEXY (solid green line) and OLS bisector (solid orange line) methods. 160

3.19 Comparison of the observed SFL for atomic gas (top), molecular gas (center), and total gas (bottom) and the theoretical model proposed by Krumholz et al. (2009b). Symbols are the same as in Figures 3.11, 3.12, and 3.12. The solid orange line show the Krumholz et al model for $Z' = 1.0/1.5$ and $c = 4$. 161

4.1 Digital Sky Survey cutouts of the 30 galaxies in the VENGA sample. The targets are oredered by Hubble type from earlier to later. White boxes show the VIRUS-P $1.7' \times 1.7'$ pointings obtained on each galaxy. 227

4.2 Stellar mass versus star formation rate for the VENGA galaxies with SFR measurements in Table 4.3 (red circles), and star forming galaxies in the SDSS MPA/JHU catalog (black dots). The red and black histograms show the distributions for the VENGA and SDSS galaxies respectively. The stellar mass histogram includes the VENGA targets without SFR measurements. 228

4.3 Histogram of the logarithm of the VIRUS-P 4.235″ fiber size in physical units (parsecs) for each galaxy in the VENGA sample, given the distances adopted in Table 4.1. The vertical dashed line marks the median spatial resolution of 300 pc. 229

4.4 Sky spectrum in raw units (before flux calibration) at different UT times (color coded) during the night of November 7th 2008. 230

4.5 Relative sky brightness as a function of UT time for the same night shown in Figure 4.4, at three different wavelength (blue, green, and red). Filled circles correspond to measurements of the sky brightness from the off-source background frames. The beginning and end of observations of the same target are shown as vertical dashed lines. Solid color curves show cubic spline fits to the sky brightness. The black open diamonds and black solid curve show the relative sky brightness averaged over the full spectrum. 231

4.6 Attempted and actual relative positions of the three sets of dithered exposures for the three pointings obtained on NGC0628. Stars and solid circles mark the attempted fiducial positions for dithers 1, 2, and 3 (red, green, and blue respectively). Crosses mark the actual position at which each exposure was obtained. The open squares and dashed color circles show the average fiber position of the actual observations. 232

4.7 Map of the r-band flux reconstructed from the VENGA spectral data-cube of NGC0628. Black contours mark steps in surface brightness of 1 magnitude. Black dots mark the position of each fiber. This and all maps presented in this work where constructed using the PLOT_VELFIELD IDL routine written by Michele Cappellari (http://www-astro.physics.ox.ac.uk/ mxc/idl/), and correspond to linearly interpolated maps based on the discrete values at the position of each fiber. 233

4.8 Map of the r-band flux after doing aperture photometry matching the VIRUS-P fiber size in the SDSS mosaic image of NGC0628. Black contours mark steps in surface brightness of 1 magnitude. 233

4.9 Map of the signal-to-noise ratio per spectral resolution element in continuum of the VENGA NGC0628 data-cube. Contours are the same as in Figure 4.7. 234

4.10 *Top panel:* Spectrum of fiber 1805 (S/N=128) in the VENGA data-cube of NGC0628. The observed spectrum is shown in blue with 1σ uncertainties marked by the cyan envelope. The solid red line shows the best-fit stellar plus emission line spectrum, while the dotted red line shows the stellar component of the fit without the emission lines. The four vertical cyan bands represent regions masked around sky line residuals. *Bottom Panels:* Zoomed in regions around Hβ, Mgb, and Hα (left to right). 235

4.11 Same as Figure 4.10 for fiber 1800 (S/N=77). 236

4.12 Same as Figure 4.10 for fiber 1001 (S/N=25). 237

4.13 Same as Figure 4.10 for fiber 758 (S/N=15). 238

4.14 Stellar velocity field in NGC0628. Contours are the same as in Figure 4.7. 239

4.15 Ionized gas velocity field in NGC0628. Contours are the same as in Figure 4.7. 239

4.16 Map of the Hα emission line flux in NGC0628. Contours are the same as in Figure 4.7. 240

4.17 Signal-to-noise ratio as a function line flux for all transitions in Table 4.6. Each dot corresponds to an individual fiber in the NGC0628 data-cube. The horizontal solid, dashed, and dotted lines mark the median S/N, and the 5σ and 3σ detection limits respectively. 241

4.18 Diagnostic [NII]/Hα vs [OIII]/Hα BPT diagram. The dust-corrected line ratios for each fiber are shown as blakc dots. Median errorbars for these line ratios are shown on the upper left corner of the diagram. The filled red circle shows the integrated flux ratio across the whole data-cube. Dashed and dotted curves show the AGN/star-formatioon selection criteria of Kewley et al. (2001) and Kauffmann et al. (2003) respectively. Open red diamonds with The horizontal and vertical lines show divide the right part of the diagram in regions typically populated by Seyfert galaxies (top) and LINERS (bottom). Regions above both AGN selection criteria and laying at less than 500 pc from the center of the galaxy are shown as open red diamonds with error-bars. 242

4.19 Map of the [NII]/Hα ratio across NGC0628. Black contours show Hα flux. Fibers classified as AGN dominated are marked in the central part of teh galaxy. The thick oval contour marks a galactocentric radius of 500 pc. 243

4.20 NGC0628 map of the Hα emission line flux, overlaid with contours surrounding pure DIG regions (red) and pure HII regions (blue). 243
4.21 Histogram of the [SII]/Hα emission line ratio for all fibers (black), HII region dominated fibers (blue), and DIG dominated fibers (red). 244
4.22 [SII]/Hα emission line ratio as a function of Hα flux. Horizontal dashed lines show the fiducial values adopted for HII regions and the DIG. The best fit given by Equation 4.4 is shown as the solid red line. 245
4.23 Map of the nebular oxygen abundance computed using the NS method, for HII region dominated fibers. White contours mark constant galactocentric radii in steps of 0.1 R_{25}. 246
4.24 Oxygen nebular abundance as a function of isophotal radius for HII region dominated fibers in NGC0628. Best single and broken power-law fits are shown in blue and red respectively. The measurement of Rosales-Ortega et al. (2011) is shown as the black dashed line. 247
4.25 Star formation efficiency as a function of oxygen nebular abundance for HII region dominated fibers having significant measurements of Σ_{H_2}. 248

Chapter 1

Introduction

When trying to answer the fundamental question "How did we get here?", a critical bottleneck in the chain of physical processes that ultimately lead to our origin, is the assembly of galaxies by the process of star formation, and their subsequent evolution throughout the history of the universe. Under the currently accepted paradigm of ΛCDM cosmology, the formation and subsequent evolution of galaxies takes place at the bottom of potential wells in the gravitational field of the universe, which trace overdensities in the large-scale dark matter distribution (a.k.a. dark matter halos, Blumenthal et al., 1984). Accretion of baryonic material into these halos, combined with merging processes, ultimately trigger star formation giving raise to galaxies.

Although consensus has been reached concerning this big picture, the details of the baryonic physics behind galaxy formation in the centers of dark matter halos are still aggressively debated. The triggering of star formation and the variables that set the star formation rate (Leroy et al., 2008), the role that different types of feedback processes like radiation pressure from young stars, active galactic nuclei, mechanical energy injection and enrichment due to supernova explosions (Kauffmann et al., 1999; Croton et al., 2006; Thompson,

2008), as well as accretion of gas from the inter-galactic medium (IGM, Dekel et al., 2009), have at regulating the gaseous budget, structure, kinematics, and chemical composition of the inter-stellar medium (ISM), and the impact that major and minor mergers, as well as secular evolution processes, play at configuring the diverse morphologies observed in galaxies (Toomre & Toomre, 1972; Kormendy & Kennicutt, 2004), are the main current areas of research in the field of galaxy formation and evolution. All these processes play a major role in determining how galaxies evolve throughout cosmic time, building up their stellar mass and shaping their present day structure.

To fully understand these processes, the problem of galaxy formation and evolution must be approached from different directions. One approach is the characterization of high redshift galaxy populations in terms of their physical properties (mass, star formation rate, metallicity, gas and dust content, morphology, clustering, etc.), and the study of the evolutionary paths these systems follow across cosmic time. Another essential approach is the detailed study of the present day descendants of these high redshift systems. Because of their proximity to us, nearby galaxies offer an ideal laboratory to study, in detail, the physical processes that shape galaxies during their lives, allowing us to properly interpret the observational results obtained at high redshift.

In this thesis I focus mainly in studying the process of star formation in both high redshift and local star forming galaxies, by using an observational technique called *integral field spectroscopy* (IFS). Although these investigations are aimed at studying the star formation properties of these objects,

throughout this work I will also discuss the geometric, kinematic, and chemical structures in the ISM of these galaxies, which are intimately connected with the process of star formation itself.

As mentioned above, the main tool I have used to conduct the studies presented in this thesis is optical integral field spectroscopy. Traditionally, spectroscopic observations of astronomical objects at optical and near-infrared (near-IR) wavelengths have been typically carried out by placing a narrow slit (or multiple slits) in the focal plane of the optical system, and dispersing the passing light orthogonally to the slit's spatial direction. This poses a series of disadvantages, including the necessity to apply uncertain corrections for the wavelength dependent loss of light through the slit, caused by either atmospheric differential refraction (ADR), or a wavelength dependent point-spread-function (PSF). In particular, slit spectroscopic observations of extended sources are also limited by the fact that only the small fraction of the object's area sampled by the slit can be observed at once. Furthermore, when performing non-targeted spectroscopy with the goal of discovering new sources by surveying blank parts of the sky, the small areas typically subtended by these narrow slits seriously limit the efficiency of these surveys.

Integral field spectroscopy is a powerful observational technique which does not suffer from the above problems. Integral field spectrographs are design to provide spectroscopic information for all spatial resolution elements over the field of view of the instrument. Once reduced and extracted, the product is a three-dimensional data-cube with information across a wavelength axis

for every resolution element in the two-dimensional spatial plane. The amount of information obtained is given by the size of the field of view, the wavelength range covered, and the spatial and spectral resolution of the instrument.

The work presented in this thesis is based on observations carried out using the Visual Integral-field Replicable Unit Spectrograph Prototype (VIRUS-P, Hill et al., 2008a). This instrument, since it was commissioned in 2006 on the 2.7m Harlan J. Smith telescope at McDonald Observatory, has allowed the execution of a large number of extra-galactic and galactic studies (Hill et al., 2008b; Adams et al., 2009, 2010, 2011b,a; Blanc et al., 2009, 2010, 2011; Yoachim et al., 2010; Shetrone et al., 2010; Murphy et al., 2011; Finkelstein et al., 2011).

VIRUS-P was designed as a prototype instrument for VIRUS, a massively replicated integral field spectrograph currently being built for the 9.2m Hobby Eberly Telescope. VIRUS will be used to conduct the Hobby Eberly Telescope Dark Energy Experiment (HETDEX, Hill et al., 2008b, 2010). This project will measure the power spectrum of the spatial distribution of galaxies at $2.0 < z < 3.5$ using a sample of $\sim 7 \times 10^5$ spectroscopically detected Lyα emitters (LAEs). The goal of HETDEX is to use the galaxy power spectrum to constrain the density and equation of state of dark energy, as well as the curvature of the universe at high redshift (Jeong & Komatsu, 2006, 2009; Koehler et al., 2007). HETDEX will construct a unique and exciting astronomical dataset due to the fact that it is a blind spectroscopic survey, which will fully map 60 deg^2 of sky by obtaining spectra for $\sim 400 \times 10^6$ small regions

subtending a solid angle of 1.8 arcsec^2 each. The exploratory power of such dataset is enormous, and HETDEX will not only allow the study of cosmology, but of many other important subjects in astrophysics such as the properties and evolution of galaxies in the high and low redshift universe, the physics of super-massive black holes and active galactic nuclei (AGN), the structure and kinematics of the Milky Way, and the late phases of stellar evolution (Castanheira et al., 2010). HETDEX observations are expected to start during the first semester of 2012, and survey data will be acquired during a period of 4 years.

In preparation for such an endeavor, from 2007 to 2010 we conducted the HETDEX Pilot Survey for emission line galaxies (Adams et al., 2011b; Blanc et al., 2011; Finkelstein et al., 2011). The Pilot Survey not only provided a proof of concept for HETDEX, showing the ability of blank field IFS to recover the proper number of LAEs necessary to conduct the Dark Energy Experiment, but also helped to guide the design and construction of the VIRUS spectrograph. The Pilot Survey design and observations, as well as the data reduction and emission line detection pipelines are presented in Adams et al. (2011b). In Chapter 2 of this thesis, I present the first scientific results obtained from this project. I have studied the properties of LAEs across the $2 < z < 4$ range, with an emphasis in trying to understand the process by which Lyα photons, produced in large quantities in the active star forming regions within these galaxies, are able to escape the ISM of these objects, allowing us to detect them in the Lyα line. As discussed in Chapter 2, the

escape of Lyα photons is a complex radiative process which depends on the geometry, kinematics, and chemical composition (mainly the presence of dust) of the ISM. Therefore, while these dependences make it difficult to study this problem, they also imply that we can learn about the properties of the gas in these young star-forming systems in the early universe by studying the escape of Lyα photons.

While the study of high redshift galaxies is of great importance in order to understand the early stages of galaxy formation and evolution, the interpretation of the observational results obtained at high redshift is limited by our understanding of the physical processes giving rise to the distribution of galaxy properties we can measure. In particular, the formation and consequent evolution of stars plays a key role at driving the evolution of galaxies, building up their stellar mass, shaping their morphologies, and consuming, recycling, and ejecting gas from these systems, while also enriching the ISM with heavy chemical elements. We currently posses a broad general picture of the physics behind the formation of stars (Shu et al., 1987; McKee & Ostriker, 2007), but many issues within our current theory of star formation remain unresolved. These issues include the formation and disruption of giant molecular clouds (GMCs), the variables setting the star formation rate (SFR) both in GMC and galactic scales, and the relative importance that chemistry, turbulence, gravity, and magnetic fields have at regulating the efficiency of the star formation process (McKee & Ostriker, 2007, and references within).

Observations of star forming regions in the local universe (both in the

Milky Way and in nearby galaxies), are necessary to obtain a detailed understanding of star formation in galactic and sub-GMC scales. Chapter 3 of this thesis presents such a study, in which I have used the VIRUS-P spectrograph to spectroscopically map the central region (4×4 kpc^2) of the nearby SA(s)bc galaxy NGC5194 (a.k.a. M51a, The Whirlpool Galaxy), in order to measure very accurately the SFR surface density across the disk of this system on sub-kpc scales. In particular I created a map of the Hα emission line flux over the central region of NGC5194, which in conjunction with the fluxes of other emission lines like Hβ, [OIII]λ5007, [NII]λ6583, and [SII]λ6717, can be used to measure the SFR, correcting for the effects of interstellar dust attenuation, emission from the diffuse ionized component of the ISM, and the presence of AGN activity in the center of the galaxy.

In Chapter 3, I use the SFR measurements with VIRUS-P, together with publicly available maps of 21 cm. HI, and CO (J=1-0) emission, to investigate the relation between the surface density of atomic and molecular gas (Σ_{HI}, Σ_{H_2}) and the surface density of the SFR (Σ_{SFR}) across the disk of NGC5194 (a.k.a. the spatially resolved Star Formation Law, or Schmidt-Kennicutt Law, Schmidt, 1959; Kennicutt, 1998b; Kennicutt et al., 2007; Bigiel et al., 2008). I perform a detailed study of the systematics affecting the measurements of Hα SFRs, the challenges involved in extracting the parameters of the star formation law (SFL) from the observational data, and compare my results to the theoretical model of galactic scale star formation of Krumholz et al. (2009b).

The observations of NGC5194 described in Chapter 3 were taken as part of a larger project called the VIRUS-P Exploration of Nearby Galaxies (VENGA, Blanc et al., 2010). This project is an ongoing campaign to obtain spatially resolved spectroscopy over a large wavelength range (3600Å-6800Å) for large portions of the disks of 30 nearby spiral galaxies. We are constructing an unprecedented spectroscopic dataset for these type of objects. The sample spans a wide range in Hubble types, SFR, and morphologies, including galaxies with classical and pseudo-bulges, as well as barred and unbarred objects. Ancillary multi-wavelength data including HST optical and NIR, Spitzer IRAC and MIPS, and far-UV GALEX imaging, as well as Spitzer mid-IR IRS spectroscopy, CO maps, and HI 21cm maps, are available for many galaxies in the sample. VENGA will allow a large number of studies on star-formation, structure assembly, stellar populations, gas and stellar dynamics, chemical evolution, ISM structure, and galactic feedback, and will also provide the best local universe control sample for IFU studies of high-z galaxies.

A description of the VENGA sample and survey strategy is provided in Chapter 4. The data reduction and spectral analysis pipelines for the survey are also presented, together with early results regarding the gas phase oxygen abundance gradient in the face-on SA(s)c galaxy NGC0628. Finally, a summary of the most important results and conclusions from all the above studies is given in Chapter 5. These results exemplify the power of integral integral field spectroscopy as a tool to study the evolution of galaxies across cosmic time.

Chapter 2

The HETDEX Pilot Survey: The Evolution of the Lyα Escape Fraction from the UV Slope and Luminosity Function of $1.9 < z < 3.8$ LAEs

We study the escape of Lyα photons from Lyα emitting galaxies (LAEs) and the overall galaxy population using a sample of 99 LAEs at $1.9 < z < 3.8$ detected through integral-field spectroscopy of blank fields by the HETDEX Pilot Survey. For 89 LAEs with broad-band counterparts we measure UV luminosities and UV slopes, and estimate $E(B-V)$ under the assumption of a constant intrinsic UV slope for LAEs. These quantities are used to estimate dust-corrected star formation rates (SFR). Comparison between the observed Lyα luminosity and that predicted by the dust-corrected SFR yields the Lyα escape fraction. We also measure the Lyα luminosity function and luminosity density ($\rho_{Ly\alpha}$) at $2 < z < 4$. Using this and other measurements from the literature at $0.3 < z < 7.7$ we trace the redshift evolution of $\rho_{Ly\alpha}$. We compare it to the expectations from the star-formation history of the universe and characterize the evolution of the Lyα escape fraction of galaxies. LAEs at $2 < z < 4$ selected down to a luminosity limit of $L(Ly\alpha) > 3-6 \times 10^{42}$ erg s^{-1} (0.25 to 0.5 L^*), have a mean $\langle E(B-V) \rangle = 0.13 \pm 0.01$, implying an attenuation of $\sim 70\%$ in the UV. They show a median UV uncorrected $SFR =$

11 $M_{\odot}yr^{-1}$, dust-corrected $SFR = 34$ $M_{\odot}yr^{-1}$, and Lyα equivalent widths (EWs) which are consistent with normal stellar populations. We measure a median Lyα escape fraction of 29%, with a large scatter and values ranging from a few percent to 100%. The Lyα escape fraction in LAEs correlates with $E(B-V)$ in a way that is expected if Lyα photons suffer from similar amounts of dust extinction as UV continuum photons. This result implies that a strong enhancement of the Lyα EW with dust, due to a clumpy multi-phase ISM, is not a common process in LAEs at these redshifts. It also suggests that while in other galaxies Lyα can be preferentially quenched by dust due to its scattering nature, this is not the case in LAEs. We find no evolution in the average dust content and Lyα escape fraction of LAEs from $z \sim 4$ to 2. We see hints of a drop in the number density of LAEs from $z \sim 4$ to 2 in the redshift distribution and the Lyα luminosity function, although larger samples are required to confirm this. The mean Lyα escape fraction of the overall galaxy population decreases significantly from $z \sim 6$ to $z \sim 2$. Our results point towards a scenario in which star-forming galaxies build up significant amounts of dust in their ISM between $z \sim 6$ and 2, reducing their Lyα escape fraction, with LAE selection preferentially detecting galaxies which have the highest escape fractions given their dust content. The fact that a large escape of Lyα photons is reached by $z \sim 6$ implies that better constraints on this quantity at higher redshifts might detect re-ionization in a way that is uncoupled from the effects of dust.

2.1 Introduction

Lyα photons are produced in large amounts in star forming regions, therefore it was predicted nearly half a century ago that the Lyα emission line at 1216Å should be a signpost for star-forming galaxies at high redshift (Partridge & Peebles, 1967). Actual observations of Lyα emitting (LAE) galaxies at high redshift had to wait for the advent of 8-10m class telescopes (Hu et al., 1998). A little more than a decade has passed since their discovery, and thanks to a series of systematic surveys at optical and near-infrared wavelengths, large samples of LAEs, usually containing from tens to a few hundred objects, have been compiled over a wide range of redshifts from $z \sim 2$ to $z \sim 7$ (eg. Cowie & Hu, 1998; Rhoads et al., 2000; Kudritzki et al., 2000; Malhotra & Rhoads, 2002; Ouchi et al., 2003; Gawiser et al., 2006a; Ajiki et al., 2006; Gronwall et al., 2007; Ouchi et al., 2008; Nilsson et al., 2009; Finkelstein et al., 2009; Guaita et al., 2010; Hayes et al., 2010; Ono et al., 2010; Adams et al., 2011b). Space based ultra-violet (UV) observations have also been used to study Lyα emitting galaxies at lower redshifts, all the way down to the local universe (Kunth et al., 1998, 2003; Hayes et al., 2005, 2007; Atek et al., 2008; Deharveng et al., 2008; Cowie et al., 2010).

The intrinsic production of both Lyα and UV continuum photons in a galaxy is directly proportional to the number of ionizing photons produced by young stars, which is proportional to the star formation rate (SFR) (Kennicutt, 1998a; Schaerer, 2003). In practice, we do not expect the observed Lyα luminosity of galaxies to correlate well with their SFR because the resonant

nature of the n=1-0 transition in hydrogen makes the escape of Lyα photons a non-trivial radiative process.

In principle, the large number of scatterings suffered by a Lyα photon before escaping the neutral medium of a galaxy increase its probability, with respect to that of continuum photons outside the resonance wavelength, of being absorbed by a dust grain. Hence, we would expect even small amounts of dust in a galaxy's inter-stellar medium (ISM) to severely decrease the equivalent width (EW) of the Lyα line (Hummer & Kunasz, 1980; Charlot & Fall, 1993). In reality the situation is far more complicated, and it is not clear how the extinction suffered by Lyα, and that suffered by continuum photons, relate. One scenario which has been proposed by several authors (Neufeld, 1991; Haiman & Spaans, 1999; Hansen & Oh, 2006) is the possible enhancement of the Lyα EW due to the presence of a very clumpy dust distribution in a multi-phase ISM. For this type of ISM geometry most of the dust lives in cold neutral clouds embedded in an ionized medium. In this scenario, Lyα photons have a high probability of being scattered in the surfaces of these clouds, spending most of their time prior to escape in the inter-cloud medium and actually suffering less dust extinction than non-resonant radiation, which can penetrate into the clouds where it has a higher chance of being absorbed or scattered by dust grains. Recently, Finkelstein et al. (2009) claimed that this process can simultaneously explain the Lyα fluxes and continuum spectral energy distributions of many objects in their sample of LAEs at $z \sim 4.5$.

At high redshift the Lyα line can also be affected by scattering in

the inter-galactic medium (IGM), as escaping Lyα photons bluewards of the line center can be redshifted into the resonance wavelength. This effect is particularly important at $z > 5$ as the density of neutral gas in the universe increases, but even at lower redshifts, when the universe is almost completely ionized, intervening Lyα forest absorption can occur. To first order, the IGM transmission blue-wards of Lyα is $\sim$ 90%, 70%, and 50% at $z \sim$ 1.9, 3.0, and 3.8 respectively (Madau, 1995). In the naive case where the line profile escaping a galaxy is symmetric and centered at the Lyα resonance, since only photons bluewards of the line are affected, we can expect attenuations of $\sim$ 5%, 15%, and 25% on the emerging flux at these redshifts. In reality the process can be significantly different. While inflow of IGM gas onto galaxies can introduce further attenuation red-wards of the line resonance (Dijkstra et al., 2007), outflows in a galaxy's ISM can redshift the emerging spectrum so as to be completely unaffected by the IGM (Verhamme et al., 2008). For example, in a sample of 11 LBGs and LAEs at $z \sim 3-5$, Verhamme et al. (2008) find no need to introduce IGM absorption to successfully fit the observed line profiles. This, combined with the inherent stochasticity of intervening absorption systems towards different lines of sight, makes Lyα IGM attenuation corrections very difficult and uncertain.

The kinematics of the neutral gas inside a galaxy and in its immediate surroundings also play an important role regarding the escape of Lyα photons (Verhamme et al., 2006; Dijkstra et al., 2006; Hansen & Oh, 2006; Dijkstra et al., 2007; Verhamme et al., 2008; Adams et al., 2009; Laursen et al.,

2011; Zheng et al., 2010). Simply put, the velocity field of the neutral gas has a strong influence on the emission line profile of the Lyα line. Different combinations of geometry and velocity fields can "move" photons out of the resonance frequency either by blueshifting (typically due to in-falling gas) or redshifting (due to outflows) them, changing the number of scatterings photons experience before exiting the galaxy as well as their escape frequency. This process can affect the amount of dust extinction as well as the amount of potential IGM scattering those photons will suffer.

No clear agreement is found in the literature regarding the amount of dust present in the ISM of Lyα emitting galaxies. While most studies of narrow-band selected LAEs at $z \sim 3$ seem to indicate they are consistent with very low dust or dust-free stellar populations (Gawiser et al., 2006a, 2007; Nilsson et al., 2007; Gronwall et al., 2007; Ouchi et al., 2008), there have been recent results suggesting that the LAE population is more heterogeneous and includes more dusty and evolved galaxies, especially at lower redshifts (Lai et al., 2008; Nilsson et al., 2009; Finkelstein et al., 2009).

We use a new sample of spectroscopically detected LAEs at $1.9 < z < 3.8$ from the The Hobby Eberly Telescope Dark Energy Experiment (HETDEX) Pilot Survey (Adams et al., 2011b) to investigate the shape of the UV continuum of LAEs, as well as the Lyα luminosity function of these objects, and to address:

- The dust content of LAEs, parameterized by the dust reddening $E(B -$

V), and its evolution with redshift.

- The star-formation properties (SFR), the Lyα escape fraction in LAEs, and its evolution with redshift.
- The relation between the dust content and the escape fraction of Lyα photons.
- The relation between the dust extinction seen by continuum and resonant Lyα photons.
- The contribution of LAEs to the integrated star formation rate density at different redshifts.
- The Lyα escape fraction of the overall galaxy population and its evolution with redshift.

These galaxies have been detected through wide integral-field spectroscopic mapping of blank fields, using the Visible Integral-field Replicable Unit Spectrograph Prototype (VIRUS-P, Hill et al., 2008a). The Pilot Survey catalog of emission line galaxies is presented in Adams et al. (2011b), hereafter Paper I. The large redshift range spanned by our sample allows us to check for any potential evolution in the above properties of LAEs.

In §2 we describe the HETDEX Pilot Survey from which the sample of Lyα emitting galaxies is drawn. In §3 we present our sample of LAEs along with their luminosities and redshift distribution. §4 presents our measurement

of the UV continuum slope and derivation of the amount of dust extinction present in these objects. Discussion of any potential evolution in the dust properties of LAEs is also in this section. We compare both uncorrected as well as dust-corrected SFRs derived from both UV and Lyα in §5, where we also compute the escape fraction of Lyα photons and show how it depends on the amount of dust reddening. In §6 we present the Lyα luminosity function and check for its possible evolution with redshift. We compare the integrated SFR density derived from the Lyα luminosity function to that for the global galaxy population in §7. In this way we can assess the contribution of LAEs to the star-formation budget of the universe at these redshifts and estimate the Lyα photon escape fraction for the overall galaxy population. Finally, we summarize our results and present our conclusions in §8.

Throughout the paper we adopt a standard set of ΛCDM cosmological parameters, $H_o = 70$ km s^{-1}Mpc^{-1}, $\Omega_M = 0.3$, and $\Omega_\Lambda = 0.7$ (Dunkley et al., 2009).

2.2 The HETDEX Pilot Survey

Ever since their discovery, the standard method for detecting and selecting LAEs has been through narrow-band imaging in a passband sampling the Lyα line at a given redshift. The redshift range of these type of surveys is given by the width of the narrow-band filter used, and is typically of the order of $\Delta z = 0.1$. Hence, these studies are limited to very narrow and specific redshift ranges. In terms of surveyed volumes this limitation is compensated

by the large fields of view of currently available optical imagers which allow for large areas of the sky ($\sim 1\mathrm{deg}^2$) to be surveyed using this technique.

An alternative technique, which has been attempted for detecting LAEs over the last few years, is to do so through blind spectroscopy. This can be done either by performing very low resolution slit-less spectroscopy (Kurk et al., 2004; Deharveng et al., 2008), blind slit spectroscopy (Martin & Sawicki, 2004; Tran et al., 2004; Rauch et al., 2008; Sawicki et al., 2008; Cassata et al., 2011), or integral-field spectroscopy (van Breukelen et al., 2005).

The success of this type of surveys has been variable. While early attempts to detect LAEs at $z \sim 6$ using slit spectroscopy failed to do so, and could only set upper limits to their number density (Martin & Sawicki, 2004; Tran et al., 2004), more recent attempts at lower redshifts ($2 < z < 6$) like the ones by Rauch et al. (2008) and Cassata et al. (2011), have produced large samples of objects. Similarly, an early attempt by Kurk et al. (2004) to find LAEs at $z = 6.5$ using slit-less spectroscopy only yielded one detection, while more recently space-based UV slit-less spectroscopy with the GALEX telescope has allowed for the construction of a large sample of LAEs at $z \sim 0.3$ (Deharveng et al., 2008). The only attempt to detect LAEs using integral-field spectroscopy previous to this work was done by van Breukelen et al. (2005), who used the Visible Multi-Object Spectrograph (VIMOS) integral field unit (IFU) on the Very Large Telescope (VLT) to build a sample of 18 LAEs at $2.3 < z < 4.6$ over an area of 1.44 arcmin^2 corresponding to the VIMOS IFU field-of-view.

Although when doing spectroscopic searches for LAEs the wavelength range, and hence the redshift over which Lyα can be detected, is tens of times larger than for narrow-band imaging, surveyed volumes have been typically small due to the small areas sampled by the slits on the sky, or the small fields-of-view of most integral field units. For example, the IFU survey by van Breukelen et al. (2005) only covered $\sim 10^4$Mpc^3 because of the small area surveyed, while the $z \simeq 3.1$ narrow-band survey by Gronwall et al. (2007) covered $\sim 10^5$Mpc^3 over a very narrow range of $\Delta z = 0.04$ because of the large $36' \times 36'$ area which can be imaged with the MOSAIC-II camera. It is clear that the most efficient way of building large samples of LAEs would be to conduct spectroscopic searches over large areas of the sky.

HETDEX (Hill et al., 2008b) will survey ~ 60 deg^2 of sky[1] using the Visible Integral-field Replicable Unit Spectrograph (VIRUS, Hill et al., 2010), a wide field of view ($16' \times 16'$) integral field spectrograph currently being built for the 9.2m Hobby Eberly Telescope (HET). HETDEX will produce a sample of $\sim 8 \times 10^5$ LAEs at $1.9 < z < 3.5$ over a volume of 8.7 Gpc^3. The power-spectrum of the spatial distribution of these objects will be used to set a percent level constrain on the dark energy equation of state parameter w at these high redshifts (Hill et al., 2008b). A prototype of the instrument, VIRUS-P, is currently the largest field-of-view IFU in existence, and has been used over the last 3 years to conduct a Pilot Survey for LAEs from which the

[1]The actual HETDEX footprint corresponds to a 420 deg^2 area, but only 1/7 of the field will be covered by fibers

sample used in this work is taken from (Paper I). The Pilot Survey, described below, samples the $1.9 < z < 3.8$ range, and covers a volume of $\sim 10^6$ Mpc^3 over an area of 169 arcmin^2. This volume is ten times larger than the one covered in Gronwall et al. (2007) and Guaita et al. (2010), three times larger than the one covered by Nilsson et al. (2009), and of comparable size to the one sampled at $z = 3.1$ by Ouchi et al. (2008) but over an area 20 times smaller, exemplifying the power of integral field spectroscopy to search for emission line galaxies over large volumes.

The HETDEX Pilot Survey obtained integral field spectroscopy over $\sim$169.23 arcmin^2 of blank sky in four extra-galactic fields (COSMOS: 71.6 arcmin^2, GOODS-N: 35.5 arcmin^2, MUNICS-S2: 49.9 arcmin^2, and XMM-LSS: 12.3 arcmin^2; Scoville et al., 2007; Dickinson et al., 2003; Drory et al., 2001; Pierre et al., 2004) using VIRUS-P on the 2.7m Harlan J. Smith telescope at McDonald Observatory. The goal of the survey is to conduct an unbiased search for spectroscopically-detected emission line galaxies over a wide range of redshifts. Although a powerful dataset itself, the Pilot Survey also provides a proof of concept and a crucial test-bench for the planned HETDEX survey.

The observations and data reduction, as well as the detection and classification of emission line galaxies, are presented in Paper I, and we refer the reader to it for a more detailed description of the survey design. Briefly, each field is mapped by a mosaic of $1.7' \times 1.7'$ VIRUS-P pointings (27, 13, 16, and 4 pointings in COSMOS, GOODS-N, MUNICS-S2, and XMM-LSS respectively). The VIRUS-P IFU consists of an square array of 246 fibers,

each 4.235″ in diameter, sampling the field with a 1/3 filling factor. While a set of three dithered exposures covers the field-of-view almost completely, we observed each pointing at six dithered positions, ensuring complete coverage and improving the spatial sampling of the field and the astrometric accuracy of our detections. For each pointing, we obtained spectra at 1,476 (6×246) positions, with any point on the sky being typically sampled by 2 overlapping fibers. Overall, the Pilot Survey consists of ∼88,000 individual spectra over 169 arcmin^2 of blank sky. Each spectrum covers the 3600Å-5800Å wavelength range with $\sim$ 5Å FWHM resolution ($\sigma_{inst} \sim 130$ km s^{-1} at 5000Å).

After the data are reduced and a 1D flux-calibrated spectrum is extracted for each fiber position, we search the "blank" spectra for emission lines using an automated procedure (Paper I). Line detections are associated, when possible, with counterparts in broad-band images available for all four fields. The VIRUS-P wavelength range allows the detection of common strong emission lines present in star-forming galaxies such as Lyα at $1.9 < z < 3.8$, [OII]λ3727 at $z < 0.56$, Hβ at $z < 0.19$, [OIII]λ4959 at $z < 0.17$, [OIII]λ5007 at $z < 0.16$, as well as typical AGN lines like CIVλ1549 at $1.3 < z < 2.7$, CIII]λ1909 at $0.9 < z < 2.0$, and MgIIλ2798 at $0.3 < z < 1.1$.

Source classification is based on the presence of multiple spectral lines when available. In the case of single line detections, the spectral classification is considerably more challenging. For LAEs, only the Lyα line appears in our wavelength range, so we expect single line detections for our objects of interest. Nevertheless, [OII] emitters at $0.19 < z < 0.56$ will also appear as single line

detections in the VIRUS-P spectra. Even [OII] emitters at $z < 0.19$ that have unfavorable emission line ratios can appear as single line detections if Hβ and the [OIII] doublet are below the noise level. Our 5Å FWHM spectral resolution is not high enough to resolve the [OII]λ3727 doublet, so we cannot rely on the line profile to classify these objects. While galaxies detected in redder lines such as Hβ and [OIII]λ5007 can also appear as single line detections depending on their redshifts and line ratios, the volume over which we sample these galaxies is $\sim$ 400 times smaller than the volume over which we sample LAEs, and $\sim$ 20 times smaller than the volume over which we sample [OII] emitters. Hence, contamination from Hβ and [OIII] emitters is negligible.

The classification of single line detections is thoroughly discussed in Paper I, and is based on an EW criterion, where objects showing rest-frame $EW(Ly\alpha) > 20$Å are classified as LAEs (for 4 objects the $EW > 20$Å criterion was bypassed due to the existence of further evidence pointing towards their LAE nature; see Paper I). This EW constraint effectively reduces the contamination from low-z interlopers to a negligible level. A total of 105 Lyα detections are present in the Pilot Survey catalog presented in Paper I. Of these, 6 show X-ray counterparts indicating an AGN nature, leaving a final sample of 99 "normal" star-forming LAEs. In Paper I we also present a thorough assessment of the completeness and spurious source contamination in our catalog, based on simulated data. The completeness is used in §6 to estimate the Lyα luminosity function. In our sample of LAEs we expect a 4-10% contamination from spurious sources. The sample used in this work is presented

in Table 2.1.

2.3 LAE Sample

The 99 LAEs in the sample span a range in luminosities of $\log(L_{Ly\alpha}) = 42.42 - 44.03$, and have a median luminosity of $\log(\tilde{L}_{Ly\alpha}) = 43.03$. Figure 2.1 shows the survey 5σ limiting Lyα luminosity as a function of redshift, together with the luminosities and redshifts of all LAEs in the sample. The depth of the observations is variable across the survey area and dependent on the observing conditions, the airmass at which the observations were taken, the Galactic dust extinction towards different fields, and the instrumental configuration. Colors in Figure 2.1 correspond to the fraction of the total surveyed area for which the spectra reaches the corresponding limit in luminosity. While VIRUS-P has its lower throughput in the blue end of the wavelength range, the smaller luminosity distance at lower redshifts compensates for this fact, providing a relatively flat luminosity limit throughout the entire redshift range. As mentioned above, detailed simulations quantifying the completeness and spurious detection ratio for the whole survey are presented in Paper I. A good understanding of the completeness of the survey is essential in order to calculate the Lyα luminosity function. As shown in Paper I, the completeness at the 5σ flux limit shown in Figure 2.1 is 33%, reaching 50% at 5.5σ and 90% at 7.5σ.

The redshift distribution of LAEs in our sample is shown in Figure 2.2 (errorbars show Poisson statistical uncertainties). The detected galaxies

span a range in redshift of $2.079 < z < 3.745$, with a median redshift of $\tilde{z} = 2.811$, properly sampling the $1.9 < z < 3.8$ range over which they could be detected. Figure 2.2 also shows the predicted redshift distribution of LAEs in the Pilot Survey calculated by integrating the Gronwall et al. (2007) luminosity function of narrow-band selected LAEs at $z = 3.1$ above the Pilot Survey flux limits shown in Figure 2.1, and correcting for the survey completeness. The agreement is excellent at high redhsift ($z > 3$), but we observe a drop in the number of LAEs at lower redhsifts from what is predicted by a non-evolving luminosity function. Recent narrow-band studies of $z \sim 2$ LAEs show hints for both an increase (Guaita et al., 2010) and decrease (Nilsson et al., 2009) of the LAE number density from $z = 3$ to $z = 2$. As stated by the authors themselves, neither of these studies probe a large enough volume to allow for a significant detection of the evolution in the LAE number density. In our surveyed volume, which is a few times larger than the volumes surveyed in those studies, we find some evidence for a decrease in the number density of LAEs from $z \sim 4$ to $z \sim 2$, although as discussed in §6, the statistical uncertainties remain too large to make a definitive statement. In any case, this type of evolution is expected if the escape fraction of Lyα photons from galaxies decreases towards lower redshifts. In §7 we find evidence that this effect indeed occurs, which supports the observed drop in the LAE number density.

2.4 The UV slope of Lyman alpha emitters

The UV continuum slope has been shown to be a powerful tool for estimating the amount of dust extinction in star-forming galaxies in the local universe (Meurer et al., 1995, 1999) as well as at high redshift (Daddi et al., 2004; Bouwens et al., 2009; Reddy et al., 2010). Direct observations of the ultra-violet spectral energy distribution of local star-forming galaxies have demonstrated that in the 1000Å-3000Å range, they are very well described by a power-law spectrum of the form $f_\lambda \propto \lambda^\beta$ (Calzetti et al., 1994). Differential dust extinction (reddening) makes the power-law slope correlate well with the amount of dust extinction in galaxies.

Measuring the spectral slope of the UV SED of LAEs at $1.9 < z < 3.8$ provides a direct measurement of their dust content, and its evolution with time. Knowledge of the amount of dust extinction in LAEs allows us to correct UV measured $SFRs$. An unbiased measurement of the SFR in these objects is not only important regarding the star-formation properties of these galaxies, but can also be used, together with the observed Lyα luminosities, to estimate the escape fraction of Lyα photons from the ISM of these high redshift systems, and to study a possible evolution in this quantity.

2.4.1 Measurement of the UV continuum Slopes, UV Luminosities, and Lyα EWs

We identify continuum counterparts of spectroscopically detected LAEs in our sample using publicly available broad-band optical images sampling the

rest-frame UV SED of the objects. Multi-band aperture photometry is then used to measure their UV continuum slope (β) and UV luminosity as described below.

For the purpose of measuring β we use the B, r^+, i^+, and z^+ images of the COSMOS and GOODS-N fields presented in Capak et al. (2004) and Capak et al. (2007), the g, r, i, and z images of the XMM-LSS field from the Canada-France-Hawaii Telescope Legacy Survey (CFHTLS, Mellier et al., 2008) W1 field, and the g, i, and z MUNICS-Deep images presented in Paper I. The identification and association with broad-band counterparts of our emission line detected objects makes use of a maximum likelihood algorithm which is described in detail in Paper I. Briefly, our astrometric uncertainty and the typical surface density of galaxies as a function of continuum brightness is used to identify the most likely broad-band counterpart for each LAE. The possibility of the emission-line source having no counterpart in the broad-band imaging is also considered. This can happen if the source is fainter than the sensitivity of the images or if the source is spurious. The no counterpart option is adopted if the probability exceeds that of all other possible counterparts. Only 9 out of 99 (9%) objects show no broad-band counterparts. This number is in good agreement with the 4-10% contamination expected from spurious detections in our LAE sample (Paper I, §3), although these objects could in principle be real and have very high EWs. In Paper I we showed that only one of them has significantly high EW given the limits that can be put using the depth of the broad-band images, while the large majority (8/9) show

low signal-to-noise (S/N) detections (< 6.5) where the false detection ratio is the highest. For simplicity we omit these "no counterpart" sources from our analysis as we expect the large majority of them to be false detections. We also reject one other object (HPS-89) from our analysis because its broad-band counterpart photometry is catastrophically affected by a bright neighbor.

Fluxes are measured in optimal 1.4×FWHM diameter color apertures, and scaled to total fluxes for each object using the ratio between V-band (g-band for MUNICS) fluxes measured in the color aperture and aperture-corrected fluxes measured in a SExtractor (Bertin & Arnouts, 1996) defined Kron aperture (Gawiser et al., 2006a; Blanc et al., 2008). Any contribution from the measured Ly-alpha line to the broad-band fluxes is removed. While we do take into account IGM absorption when fitting for the UV slope, we decide to omit the U-band in the fits because in our redshift range the band includes the Lyman 912Å break. Since IGM absorption is expected to be stochastic, an average line-of-sight correction might not apply to single objects. This leaves us with a B-band through z-band SED for each object.

The approximate rest-frame wavelength range sampled by the above bands shifts from 1500Å-3000Å at $z = 1.9$ to 900Å-1900Å at $z = 3.8$, so only the B-band is affected by Lyman forest absorption at the higher redshift end of our range. Following a similar methodology as that described in Meurer et al. (1999) and Reddy et al. (2010), we compute the UV continuum slope for each object by fitting the rest-frame UV SED with a power-law spectrum of the form $f_\lambda \propto \lambda^\beta$ corrected for IGM absorption at the corresponding redshift of

each object using a Madau (1995) prescription. All available bands redwards the Lyman break are used to perform the fit. When an object is not detected in a particular band, we properly include the upper limit in flux given by the photometric uncertainty in the χ^2 minimization in order to not censor our data. The error in β is estimated from Monte Carlo simulations of 100 realizations of the UV SED, where the fluxes in each band are varied within their photometric errors. This fitting also provides the UV luminosities at 1216Å and 1500Å which are used to estimate the Lyα EW and the SFR, respectively. All these quantities are reported in Table 2.1. Figure 2.3 shows the UV continuum slope β as a function of redshift for the 89 objects having continuum counterparts.

In principle, the UV slope can depend not only on the amount of dust extinction, but also on the age, metallicity, and initial mass function (IMF) giving rise to the stellar population. Extensive work can be found in the literature regarding these effects on the observed UV slope of star-forming galaxies. Leitherer & Heckman (1995) showed that for both instantaneous bursts and constant star formation synthetic stellar populations, changes of the order of $\Delta\beta = \pm 0.2$ around a typical value of $\beta \sim -2.3$ are introduced by variations in age (1 Myr to 1 Gyr) and metallicity (0.1 $Z_\odot$ to 2 $Z_\odot$). They also find the UV slope to be largely insensitive to the assumed IMF. This result is in good agreement with the work of Bouwens et al. (2009), who demonstrate that the UV slope dependence on dust is dominant over that on age, metallicty and IMF. They use Bruzual & Charlot (2003) models to show that changes by

a factor of two in age and metallicity introduce changes of $\Delta\beta \lesssim 0.1$. Schaerer & Pelló (2005) also present a similar result. In Figure 1 of their paper it can be seen that for a range in ages of 1 Myr to 1 Gyr (encompassing the expected age range for LAEs), and metallicities between 1/50 $Z_\odot$ and solar, both constant SFR population synthesis models, and single bursts younger than 10 Myr (time over which they can produce significant Lyα emission) show variations in their UV slopes of $\Delta\beta = \pm 0.2$ ($\Delta E(B-V) = 0.04$). These systematics are smaller than the typical uncertainty in the measurement of β for LAEs in our sample. Therefore, by assuming a constant value for the intrinsic (dust-free) UV slope across our LAE sample, we can robustly estimate the amount of dust reddening directly from the observed values of β given an attenuation law.

The right axis of Figure 2.3 shows the corresponding value of the reddening $E(B-V)$, calculated assuming an intrinsic UV slope $\beta_0 = -2.23$ for a dust-free stellar population (Meurer et al., 1999), and a Calzetti et al. (2000) extinction law. The value of β_0 is derived from a fit to the relation between the IR to UV ratio and β in a sample of local starburst galaxies (Meurer et al., 1999), and reproduces the observed relation at $z \sim 2$ (Reddy et al., 2010). Although Reddy et al. (2010) found young (< 100 Myr) $z \sim 2$ galaxies to lie slightly below the Meurer et al. (1999) relation, and closer to that of Pettini et al. (1998), these two relations converge at low extinction and imply basically indistinguishable values for β_0. In order to take into account age and metallicity induced uncertainties in our error budget for the dust reddening, we sum in quadrature a systematic error of $\Delta\beta = \pm 0.2$ ($\Delta E(B-V) = 0.04$)

to the uncertainty in β, and propagate it into the error in $E(B-V)$. Measured values for the dust reddening and it associated uncertainty are reported in Table 2.1.

2.4.2 Dust Properties of LAEs and comparison to Previous Measurements

Our LAEs show a mean UV continuum slope $\langle\beta\rangle = -1.5 \pm 0.1$ (formal error on the mean) corresponding to a mean $\langle E(B-V)\rangle = 0.16 \pm 0.02$ (median $\tilde{E}(B-V) = 0.13$). The measured slopes span a relatively broad range of $-3 < \beta < +2$, with the large majority (83/89, 93%) of the objects having $\beta < 0$ ($E(B-V) < 0.45$). All objects with $\beta < \beta_0$ (i.e. bluer than the assumed intrinsic dust-free slope) are consistent with $\beta = \beta_0$ (i.e. $E(B-V) = 0$) within 1σ.

These slopes and reddenings are in rough agreement with previous measurements of narrow-band detected LAE broad-band colors. For $z = 2.1$ LAEs, Guaita et al. (2010) find a typical $(B-R) \simeq 0.2$ ($\beta = -1.5$ using equation 3 in Nilsson et al. (2009)) and a relatively uniform distribution in the $-0.5 < (B-R) < 1$ ($-3.3 < \beta < 0.7$) range. Similarly, at $z = 2.3$, Nilsson et al. (2009) find a median $(B-V) = 0.14$ corresponding to $\beta = -1.4$, with the bulk of their LAEs having $-3.0 < \beta < 2.0$. At $z = 2.2$ Hayes et al. (2010) used SED fitting to find that LAEs in their sample have a range in $E(B-V) = 0 - 0.4$. At higher redshifts, usually lower levels of extinction are measured. At $z = 3.1$ Nilsson et al. (2007) find $A_V = 0.26^{+0.11}_{-0.17}$ from

fitting the stacked SED of 23 LAEs in the GOODS-S field, corresponding to $E(B-V) = 0.06^{+0.03}_{-0.04}$ (assuming a Calzetti attenuation law). Verhamme et al. (2008), using Monte Carlo Lyα radiative transfer fitting of the line profiles of 11 $z \sim 3-5$ LBGs (8 of them also LAEs) from Tapken et al. (2007), find that the color excess spans a range of $E(B-V) = 0.05-0.2$. Gawiser et al. (2006a) report that the best-fit SED to the stacked optical photometry of $z = 3.1$ LAEs in their sample has $A_V = 0^{+0.1}_{-0.0}$, corresponding to $E(B-V) < 0.03$.

For comparison, similar ranges in β and $E(B-V)$ as those seen here have been measured for LBGs (e.g. Shapley et al., 2001; Erb et al., 2006; Reddy et al., 2008). Figure 2.4 shows the $E(B-V)$ distribution of LAEs in our sample, compared with that of UV continuum selected galaxies at $1.9 < z < 2.7$ (BX galaxies) and at $2.7 < z < 3.4$ (LBGs) from Erb et al. (2006) and Reddy et al. (2008). The $E(B-V)$ distributions for the continuum-selected galaxies are different from those presented in the original papers in that we have set all their $E(B-V) < 0$ values to zero for proper comparison with our sample. It can be seen that both the shape and median value of the $E(B-V)$ distribution of LAEs and BX/LBGs are relatively similar (medians are indicated by the dashed lines in Figure 2.4). This result, together with the fact that LAEs and BX/LBGs seem to overlap in the two-color BX/LBG selection diagram (Guaita et al., 2010; Gawiser et al., 2006a), implies that both populations have relatively similar spectral continuum properties in the UV. Nevertheless, Figure 2.4 shows an LAE distribution that is peaked at lower $E(B-V)$ than the BX/LBG distributions, and also that Lyα selection might

allow for the inclusion of some highly reddened objects, although the reality of these red LAEs will be questioned in the next section. These galaxies, if real, are excluded of UV-selected samples by construction, since the color cuts in those selections reject object with $E(B-V) \gtrsim 0.5$ (Daddi et al., 2004; Blanc et al., 2008).

The observed UV slopes imply that LAEs present low levels of dust extinction. One third (30/89) of the LAEs in our sample are consistent with being dust-free ($E(B-V) = 0$) to 1σ, with the fraction going up to 60% within the 2σ uncertainty. Still, a significant fraction of LAEs show non negligible amounts of dust. As will be shown in §5, dust in LAEs should not be neglected; doing so would strongly underestimate the SFR in these objects. Dust also plays a dominant role in setting the escape fraction of Lyα photons, as we will discuss in §5.4.

2.4.3 Evolution of the Dust Properties of LAEs

At first sight, Figure 2.3 shows different behaviors in the dust-content distribution of LAEs at the high and low redshift ends of our sample. At $z < 3$ we see the emergence of a small population of LAEs (6/89) with red UV slopes ($\beta > 0$). These objects, if real, could represent an interesting population of dusty star forming galaxies in which some physical mechanisms allows for the escape of Lyα photons. We have reasons to question the reality of these objects (see below). Furthermore, in this section we show that their presence does not affect the average properties of the LAE population which is dominated by

UV-blue LAEs.

To test for any evolution on the dust-content of LAEs with redshift we divided the sample in two redshift bins: low-z ($1.9 < z \leq 2.8$) and high-z ($2.8 < z < 3.8$). The division corresponds to the median redshift of the whole sample, and divides the survey volume in two roughly equal sub-volumes. The corresponding age of the universe at $z = 3.8$, 2.8, and 1.9 is $\sim$1.6, 2.3, and 3.4 Gyr. The median Lyα luminosity of the two sub-samples equals that of the whole sample ($\log L_{Ly\alpha}$ =43.0).

The mean UV slopes of the high and low redshift samples are shown in Figure 2.3. Error-bars show the formal error on the mean and the standard deviation for each sample including $\sim$68% of the objects. The mean value of $E(B-V)$ stays constant with values 0.16 ± 0.03 and 0.17 ± 0.02 for the low and high redshift bins respectively. The scatter around these values is large and the means are statistically consistent with each other, and with the mean of the full sample. Therefore, we do not detect any significant evolution in the average UV slope and dust reddening of LAEs from $z \sim 4$ to $z \sim 2$.

The lack of evolution in the mean dust-content of LAEs implies that this rare population of very high $E(B-V)$ objects emerging at $z < 3$, if real, does not affect the average properties of the overall population due to their reduced number. The dust content of the bulk of the LAE population remains relatively constant across the $2 < z < 4$ range.

Doubt regarding the validity of the UV slope measurements for these

objects, and their classification as LAEs arises from looking at the distribution of rest-frame Lyα EWs for our sample. Figure 2.5 shows the EW distribution for both UV-blue ($\beta < 0$) and UV-red ($\beta \geq 0$) LAEs together with the one for the whole sample. The Lyα EW is measured as described in §4.1, and hence can differ from the values presented in Paper I. It is evident from Figure 2.5 that UV-blue LAEs dominate the overall population since they present a practically indistinguishable EW distribution (well fitted by an exponential with an e-folding parameter $w_0 = 74 \pm 7$) from that of the full sample ($w_0 = 77 \pm 7$). UV-red LAEs on the other hand, in addition to being rare in numbers, present a very different distribution in rest-frame EW, characterized by the presence of many extremely high EW (> 500Å) objects. Two of these UV-red objects are in the MUNICS field where we lack deep X-ray data to reject AGNs from our sample (one of these sources shows significantly extended Lyα emission and is a good candidate for an extended Lyα nebula, or Lyα Blob as discussed in Paper I). The remaining four objects have low association probabilities (≤ 0.6) with their broad-band counterparts, casting doubt on the validity of our UV slope and EW measurements for these objects. Further follow-up observations are necessary to confirm the nature of these detections.

If real, these UV-red LAEs would have an extreme nature, being very dusty and highly star-forming. We remove these six objects from all the subsequent analysis, and for the rest of the paper we focus only on the results regarding the dominant UV-blue LAE population. It must be kept in mind that if these objects happen to be real LAEs, no strong evidence for a bi-

modality in the dust content or SFR of LAEs is found in our data. The $\beta > 0$ cut used to separate this population of objects is solely based on the fact that $\beta > 0$ objects are absent at $z > 3$ in our sample. After removing these objects from our sample, we find a mean dust-reddening for LAEs of $\langle E(B-V) \rangle = 0.13 \pm 0.01$, corresponding to an average dust attenuation of $\sim 70\%$ at 1500Å.

2.5 UV versus Lyα SFRs and the Escape Fraction of Lyα Photons

In this section we use the dust extinction values derived from the UV continuum slope in the previous section to estimate the dust-corrected SFR of LAEs in our sample. A comparison between the observed Lyα luminosity and the intrinsic Lyα luminosity implied by the dust-corrected SFR allows estimation of the escape fraction of Lyα photons from these galaxies. Throughout this analysis we have decided to neglect the effects of the IGM. As stated in §1, at these redshifts we expect attenuations for Lyα of no more than 5-25%, which is within our typical uncertainty for the Lyα luminosity. Furthermore, if outflows are common in LAEs, as many lines of evidence suggest, then IGM scattering at these redshifts may become even less important as most Lyα photons leave galaxies red-shifted from the resonance wavelength (see discussion and references in §1). We start by comparing the observed (not corrected for dust) $SFRs$ derived from the UV and Lyα luminosities, then introduce the dust corrections, and finally estimate the escape fraction of Lyα photons and

study how it relates to the amount of dust reddening.

2.5.1 Estimation of the Star Formation Rate and the observed $SFR(Ly\alpha)$ to $SFR(UV)$ ratio.

The UV monochromatic luminosity at 1500Å ($L_{\nu,1500}$) for each object is taken from the fits described in §4. In order to calculate the SFR we use a standard Kennicutt (1998a) conversion

$$SFR(UV)\ [\mathrm{M_\odot yr^{-1}}] = 1.4 \times 10^{-28} L_{\nu,1500} [\mathrm{erg\ s^{-1} Hz^{-1}}] \tag{2.1}$$

which assumes a Salpeter IMF with mass limits 0.1 to 100 $\mathrm{M_\odot}$. The Lyα derived $SFRs$ were calculated using the standard Kennicutt (1998a) conversion factor for Hα and assuming the intrinsic Lyα to Hα ratio of 8.7 from Case B recombination theory (Brocklehurst, 1971; Osterbrock & Ferland, 2006), so

$$SFR(Ly\alpha)\ [\mathrm{M_\odot yr^{-1}}] = 7.9 \times 10^{-42} \frac{L_{Ly\alpha}}{8.7} [\mathrm{erg\ s^{-1}}] \tag{2.2}$$

Figure 2.6 shows $SFR(Ly\alpha)$ versus $SFR(UV)$ for our 83 objects. Without accounting for dust we measure median $SFRs$ of 11 $\mathrm{M_\odot yr^{-1}}$ and 10 $\mathrm{M_\odot yr^{-1}}$ from UV continuum and Lyα respectively. Although these agree with what is typically quoted for LAEs in the literature, we consider them to be underestimated by roughly a factor of $\sim 3-4$ because of the lack of a dust extinction correction.

We observe a median ratio $SFR(Ly\alpha)/SFR(UV) = 0.83$. Single ob-

jects present a large scatter around the median, with values ranging from 0.2 to 5.9. Since the UV SFR conversion factor is valid for galaxies with constant star formation over 100 Myr or more, while the one for Lyα is valid at much younger ages of $\sim$ 10 Myr (Kennicutt, 1998a), young galaxies can have intrinsic $SFR(Ly\alpha)$ to $SFR(UV)$ ratios higher than unity. The dashed lines in Figure 2.6 show the allowed range for dust-free constant star-formation stellar populations with metallicities from 1/50 $Z_{\odot}$ to solar and ages from 1 Myr to 1 Gyr from Schaerer (2003). A Lyα escape fraction of less than unity can push objects above this range. All the objects in our sample show $SFR(Ly\alpha)$ to $SFR(UV)$ ratios (or roughly equivalently Lyα EWs), which are consistent within 1σ with those of normal stellar populations (i.e lower than ~ 4).

The observed median ratio between these two quantities is in rough agreement with previous measurements found in the literature. At $z \sim 2.1$, Guaita et al. (2010) measures a mean $SFR(Ly\alpha)$ to $SFR(UV)$ ratio of 0.66 for narrow-band selected LAEs, consistent with the 0.56 value measured by Nilsson et al. (2009) at $z \sim 2.3$. Gronwall et al. (2007) find LAEs at $z \sim 3.1$ to span a similar range in the $SFR(Ly\alpha)$-$SFR(UV)$ plane as the one observed here, and while they quote a mean ratio of 0.33, a revised value of ~ 1 is actually a better estimate for their sample [2]. Ouchi et al. (2008) measures a ratio of 1.2 in their $z \simeq 3.1$ sample of LAEs. Recently Dijkstra & Westra (2010) conducted a statistical study of the relation between these two quantities. Compiling a number of LAE samples at $3.0 \lesssim z \lesssim 6.5$, they find 68% of LAEs

[2]Caryl Gronwall, private communication

to show $SFR(Ly\alpha)/SFR(UV) = 0.9^{+1.6}_{-0.5}$, in agreement with our observations.

There is reason to expect evolution in $SFR(Ly\alpha)/SFR(UV)$ with redshift. First, if the dust content of galaxies changes with redshift, and Lyα and UV photons suffer different amounts of extinction, we should see a redshift dependence in the ratio. Also, if the Lyα line suffer from significant IGM absorption, the dependence of the IGM opacity with redshift should affect the $SFR(Ly\alpha)$ to $SFR(UV)$ ratio. In Figure 2.7 we present the $SFR(Ly\alpha)$ to $SFR(UV)$ ratio, as well as the rest-frame Lyα EW as a function of redshift. While these two quantities are roughly equivalent, $SFR(UV)$ is calculated from the UV monochromatic luminosity at 1500Å, while the EW uses the monochromatic luminosity at 1216Å, therefore the ratio between them has a mild dependence on the UV slope. Because of this dependence, we chose to present both quantities in Figures 2.7 and 2.8.

Over the $2 < z < 4$ range, we do not observe evolution at a significant level in the Lyα EW or the ratio between the Lyα and UV SFRs. For our low and high redshift bins we measure median EWs of 87 ± 63Å and 53 ± 26Å respectively (median absolute deviation errors). A Kolgomorov Smirnof (KS) test to the cumulative EW distributions for the low and high redshift sub-samples allows the hypothesis of them being drawn from the same parent distribution to 2σ. In terms of $SFR(Ly\alpha)/SFR(UV)$, the measured median ratios are 1.1 and 0.7 for the low and high redshift sub-samples. The fact that we do not observe a significant decrease in the typical EW of LAEs supports our assumption of neglecting IGM absorption in our analysis.

We also analyze the relation between $SFR(Ly\alpha)/SFR(UV)$ and the dust reddening $E(B-V)$ derived from the UV slope. If UV and Lyα photons suffer from similar amounts of extinction, the above ratio should be independent of the amount of dust present in the galaxy. This is indeed the case for our LAEs, as can be seen in Figure 2.8, where the relation for the two quantities (as well as that between EW and $E(B-V)$) is shown. Throughout the entire range $0 < E(B-V) < 0.45$ the ratio between Lyα and UV derived $SFRs$ stays flat with objects scattered around the median value. A similar behavior is seen for the EW.

2.5.2 Dust Corrected $SFRs$ and Estimation of the Lyα Escape Fraction

We now correct the UV luminosity of our objects using the values of $E(B-V)$ estimated in §4 and a Calzetti et al. (2000) attenuation law. This approach provides a better estimate of the true SFR in the galaxies. Figure 2.9 shows a comparison between the dust-corrected $SFR(UV)_{corr} = SFR(UV) \times 10^{(0.4 k_{1500} E(B-V))}$, and the uncorrected $SFR(Ly\alpha)$. Error-bars include the uncertainty in the dust correction which has been propagated from the uncertainty in the measurement of the UV continuum slope β. Note that the axes in Figure 2.9 are different from those in Figure 2.6. LAEs in our sample have a median dust-corrected $\tilde{SFR}(UV) = 34$ $M_{\odot}yr^{-1}$, a factor of ~ 3 higher than the uncorrected median value, and show intrinsic $SFRs$ ranging from 1 to 1500 $M_{\odot}yr^{-1}$.

The escape fraction of Lyα photons is given by the ratio between the Lyα derived SFR and the extinction corrected UV SFR.

$$\begin{aligned} f_{esc}(Ly\alpha) &= \frac{L(Ly\alpha)_{observed}}{L(Ly\alpha)_{intrinsic}} \\ &= \frac{SFR(Ly\alpha)}{SFR(UV) \times 10^{(0.4 k_{1500} E(B-V))}} \end{aligned} \tag{2.3}$$

Measured values of $f_{esc}(Ly\alpha)$ are reported in Table 2.1. Figure 2.10 presents the Lyα escape fraction of our LAEs as a function of redshift (black circles). A broad range in the escape fraction (2% to 100%) is observed. LAEs in our sample show a median escape fraction $\tilde{f}_{esc}(Ly\alpha) = 0.29 \pm 0.04$, and a mean escape fraction $\langle f_{esc}(Ly\alpha) \rangle = 0.55 \pm 0.08$ (formal error on the mean). All objects showing $f_{esc}(Ly\alpha) > 1$ are consistent with $f_{esc}(Ly\alpha) = 1$ to 1.5σ.

A recent study by Hayes et al. (2010) used a pair of optical and NIR narrow-band filters to sample the Lyα and Hα lines over the same volume. By comparing the Lyα and Hα luminosities of a sample of 38 LAEs at $z = 2.2$, they derived a lower limit of 0.32 for the average Lyα escape fraction of LAEs, a value consistent with our measured average. Another estimation of the Lyα escape fraction was done by Verhamme et al. (2008) using an independent method on their spectroscopic sample of 11 high-z galaxies (8 of which are LAEs). Fitting the Lyα emission line velocity profiles using Monte Carlo radiative transfer simulations yielded best-fit values for $f_{esc}(Ly\alpha)$ between 0.02

and 1, with a median value of 0.17, in good agreement with our observed median value. The agreement between these three independent estimations using a different set of techniques is encouraging.

A median (mean) escape fraction of $\sim$ 20% ($\sim$ 50%) is one order of magnitude higher than that adopted in the semi-analytical models of Le Delliou et al. (2005), in which a 2% escape fraction combined with a top-heavy IMF is used to match the output of the models to the observed Lyα and UV luminosity function of LAEs at different redshifts. We observe a much larger escape fraction, and our measured EWs can be explained by standard stellar populations with normal IMFs. Also, the large scatter seen in Figure 2.10 implies that using a single value of $f_{esc}(Ly\alpha)$ to model the LAE galaxy population is not a realistic approach.

It is important to remark that estimating the escape fraction directly from the observed $SFR(Ly\alpha)/SFR(UV)$ ratio, by assuming LAEs are dust-free galaxies, would imply a significant overestimation of its value. For example, the best-fit SED to the stacked optical photometry of $z = 3.1$ LAEs in Gawiser et al. (2006a), which has $A_V = 0^{+0.1}_{-0.0}$, implies a best-fit escape fraction of 0.8 (although the uncertainty in the fit allows for a escape fraction > 0.2, in agreement with our results). Similarly, the ratios measured by Ouchi et al. (2008), Nilsson et al. (2009), and Guaita et al. (2010) imply escape fractions in the 0.5 to 1.0 range if dust is not considered. As discussed above, if we were to completely neglect dust extinction we, would measure a value of 0.87 for our sample.

2.5.3 Evolution of the Lyα Escape Fraction in LAEs

No significant evolutionary trend is present across the $1.9 < z < 3.8$ range of our objects in Figure 2.10, where the median escape fractions for the two $1.9 < z < 2.8$ and $2.8 < z < 3.8$ redshift bins (red open stars in Figure 2.10) are consistent with the median for the whole sample. In order to investigate if the Lyα escape fraction of LAEs evolves over a larger baseline in cosmic time, we also show results found in the literature at a lower redshift. At higher redshifts the Lyα escape fraction for LAEs remains poorly constrained, although attempts to measure it exist in the literature (eg. Ono et al., 2010)

At low redshift Atek et al. (2009) performed optical spectroscopy on a sample of $z \simeq 0.3$ LAEs (Deharveng et al., 2008) and used the Hα luminosity, in combination with dust extinctions derived from the Balmer decrement, to estimate the Lyα escape fraction of these objects. A similar range in the escape fraction is observed for $z \simeq 0.3$ and $2 < z < 4$ LAEs, with the former showing values ranging from 0.03 to 1, implying that there has not been significant evolution in $f_{esc}(Ly\alpha)$ over the $\sim$8 Gyr from $z \sim 3$ to $z \sim 0.3$. At very high redshifts ($z = 5.7$ and 6.6) Ono et al. (2010) has estimated the Lyα escape fraction of a sample of a few hundred narrow-band selected LAEs using a similar method to the one used here, except that their intrinsic $SFRs$ were measured by SED fitting. Their escape fractions are consistent with our measured values at $2 < z < 4$, although their error-bars are large. Therefore we detect no significant evolution in $f_{esc}(Ly\alpha)$ over the $0.3 < z < 6.6$ range.

This lack of evolution in the Lyα escape fraction of LAEs must be in-

terpreted with caution, since nothing ensures that the LAE selection technique recovers the same galaxy populations at these very distant epochs in the universe. Furthermore, since the selection is based on the strength of the Lyα line relative to the the underlying continuum (i.e. the EW of the line), the technique will tend to favor galaxies with high Lyα escape fractions, as long as they satisfy the brightness cut of the survey, at any redshift. Therefore, the lack of evolution in $f_{esc}(Ly\alpha)$ cannot be interpreted as constancy in the physical conditions in the ISM of these galaxies. For example, while at low redshift the escape fraction is most likely dominated by dust absorption, at $z \sim 6$ it is most likely dominated by IGM attenuation.

2.5.4 The Relation between f_{esc}(Lyα) and Dust

As discussed in §1, a major subject of debate regarding the escape of Lyα photons from star-forming galaxies is the role played by dust. It is not clear whether the resonant nature of the transition produces Lyα photons to be extincted more, less, or in the same amount as continuum photons outside the resonance. For example, while Lyα photons should originate in the same regions as Hα photons, we have no reason to expect the extinction seen by Lyα photons to follow the nebular extinction relation $E(B-V)_{stars} = 0.44E(B-V)_{gas}$ seen for non-resonant hydrogen transitions in star-forming galaxies at $z = 0$ (Calzetti, 1997), since resonant scatter makes the optical paths seen by Lyα completely different from the one seen by other lines like Hα or Hβ. Furthermore, it has not been established if the above relation holds at high

redshift or not.

In order to test this issue we parameterize the ratio between the dust opacity seen by Lyα and that which continuum photons at the same wavelength would see in the absence of the transition. Following Finkelstein et al. (2008), we adopt the parameter $q = \tau_{Ly\alpha}/\tau_{\lambda=1216}$, where $\tau_\lambda = k_\lambda E(B-V)/1.086$ and k_λ is assumed to be a Calzetti et al. (2000) dust attenuation law. $E(B-V)$ is always taken to be the stellar color excess derived from the UV slope.

A value of $q \sim 0$ implies that Lyα photons suffer very little extinction by dust, as is expected in an extremely clumpy multi-phase ISM. Large values ($q \gg 1$) represent cases in which scattering of Lyα photons introduces a strong increase in the dust attenuation as is expected in a more homogeneous ISM. As discussed in §1, not only the structure of the ISM determines the value of q, but also the kinematics of the ISM, since favorable configurations (eg. an expanding shell of neutral gas which allows backscattering) can reduce the amount of dust extinction seen by Lyα photons. All these processes are coupled in determining the value of q, and discriminating between them requires a joint analysis of the UV, Lyα, and Hα luminosities, the dust extinction either from the shape of the UV continuum or from Balmer decrements, and the profiles of the latter two emission lines. Until such data exist, interpretation is difficult, but we can still gain insights about the escape of Lyα photons and the dust properties of LAEs from the measured value of q.

In Figure 2.11 we present the Lyα escape fraction versus the dust red-

dening $E(B-V)$ for our sample of LAEs. A clear correlation between the escape fraction and the amount of dust extinction is seen. Also shown are the expected correlations for different values of the parameter q. The LAE population falls along the $q = 1$ relation. The median for the whole sample is $\tilde{q} = 0.99 \pm 0.44$ (median absolute deviation error), implying that in most LAEs the Lyα emission suffers a very similar amount of dust extinction to that experienced by UV continuum light.

Our results show good agreement with those of Hayes et al. (2010). In their work, 5 out of 6 LAEs at $z = 2.2$ detected in both Lyα and Hα show escape fractions and dust reddenings consistent with the $q = 1$ relation. The same is true for the large majority of their LAEs with no Hα detections for which they could only provide lower limits to the escape fraction. Our LAEs at $2 < z < 4$ also occupy the same region in the $E(B-V)$ vs. $f_{esc}(Ly\alpha)$ plane as the low redshift LAEs ($z \simeq 0.3$ Atek et al., 2009) shown as green triangles in Figure 2.11. This implies that not only the Lyα escape fraction in LAEs does not evolve with redshift as shown in §5.3, but its dependence on the dust content of the ISM remains the same from $z = 4$ to 0.3.

The LAE selection criteria imply that these objects are chosen to be the galaxies with the largest Lyα escape fractions given their Lyα luminosities and dust content at any redshift. Most likely, a combination of ISM geometry and kinematics favors the escape of Lyα photons in these galaxies as compared to the common galaxy population at any redshift. Hence, when examining Figure 2.11 we should think of LAEs as the upper envelope of the escape

fraction distribution at any E(B-V). For example, Kornei et al. (2010) found that LBGs with Lyα emission typically lie below the $q = 1$ relation. In their work they parameterized the difference in the extinction seen by Lyα and continuum photons by the "relative escape fraction", $f_{esc,rel}$, which relates to q by the following relation

$$q = \frac{log(f_{esc,rel})}{0.4 k_{\lambda=1216} E(B-V)} \tag{2.4}$$

They find LBGs to have $\langle f_{esc,rel} \rangle = 0.27$ (which does not include LBGs showing Lyα in absorption). We present this relation for LBGs as a red line in Figure 2.11. This finding supports our previous point, namely that LAEs are the upper envelope to the overall galaxy population in the $E(B-V)$ vs. $f_{esc}(Ly\alpha)$ plane.

Our result should not be interpreted as evidence against the existence of a clumpy multiphase ISM in LAEs, since in the presence of a completely homogeneous ISM we expect $q > 1$. Nevertheless, our result indicates that either a clumpy ISM, a favorable kinematic configuration of the ISM, or a combination of both, can reduce the amount of dust seen by scattering Lyα photons only up to the point where they encounter the same level of dust opacity as the continuum. Since LAEs by definition will be the galaxies with the largest Lyα escape fractions at any value of $E(B-V)$, the absence of a significant number of points at low values of q in Figure 2.11 suggests that enhancement of the Lyα EWs due to clumpiness in the ISM is not a common process in galaxies.

2.6 The Lyα Luminosity Function

It has been well established in the literature that the Lyα luminosity function does not show significant evolution from $z = 3$ to 6 (Shimasaku et al., 2006; Tapken et al., 2006; Ouchi et al., 2008). On the other hand, a strong decrease of roughly one order of magnitude is seen in the abundance of LAEs from $z \sim 3$ down to $z \sim 0.3$ (Deharveng et al., 2008). At what point in cosmic time this decrease starts to take place, and how well it traces the SFR history of the universe, is unknown. Recently there have been reports of possible evolution in the number density of LAEs between $z \sim 3$ and $z \sim 2$ (Nilsson et al., 2009), but, as stated by the same authors, these results might be affected by cosmic sample variance over the surveyed volumes. Furthermore, Cassata et al. (2011) find no evolution in the luminosity function across these epochs in their sample of spectroscopically detected LAEs. The existence of evolution in the luminosity function (or number density) of LAEs down to these lower redshifts is still a subject of debate.

By examining the redshift distribution of our LAEs (Figure 2.2), we found indications that their number density might be decreasing towards lower redshifts ($z < 3$) in our sample (§3). In this section we measure the Lyα luminosity function of LAEs, and study any potential evolution down to $z \sim 2$. We restrict the measurement of the luminosity function to LAEs in the COSMOS and GOODS-N fields, which account for 81% (80/99) of the total sample. Both MUNICS and XMM-LSS lack deep X-ray data comparable to the one available in COSMOS and GOODS-N, so it is not possible to identify

AGNs in those fields.

2.6.1 Measurement of the Luminosity Function

To measure the luminosity function we adopt a $1/V_{max}$ formalism similar to the one used by Cassata et al. (2011). We compute the volume density of objects in bins of $\Delta log(L) = 0.125$ dex, as the sum of the inverse of the maximum volumes over which each object in the luminosity bin could have been detected in our survey. As discussed in §3, the depth of the observations is variable across the surveyed area. The whole survey covers 169 arcmin^2, corresponding to 60 VIRUS-P pointings. Each pointing was covered by six dithered observations, which accounts for 360 independent observations each reaching different depths. The noise spectrum for each IFU fiber in each of these observations is an output of our data processing pipeline, and can be directly translated into an effective line luminosity limit for Lyα at each redshift (see Figure 2.1).

For each object, V_{max} is given by

$$V_{max} = \sum_i V_{max,i} \tag{2.5}$$

where $V_{max,i}$ is the integral of the co-moving volume over all the redshifts at which the object could have been detected (i.e. where the luminosity limit is lower than the objects luminosity) for each observation i. Summing over the inverse of V_{max} for all objects in each luminosity bin then yields the luminosity function shown as open black circles in Figure 2.12.

As mentioned briefly in §3 and discussed extensively in Paper I, the effects of incompleteness are important over all luminosities in our survey. Completeness is a direct function of the S/N at which the emission line is detected in our spectra. Since the limiting luminosity is not constant at all redshifts (Figure 2.1), objects of the same luminosity can be detected with high significance, and hence high completeness, at certain redshifts and with low significance and low completeness at others. This is different than, for example, imaging surveys where objects are detected in a narrow redshift range, and the S/N is close to a unique function of the luminosity. In those cases, incompleteness becomes only important in low luminosity bins, where the objects flux approach the depth of the images[3]. In our case, we must account for incompleteness over the whole luminosity range if we want to get a proper estimate of the luminosity function.

In Paper I we present a detailed completeness analysis of our survey based on simulations of the recovery fraction of synthetic emission lines at different S/N in our spectra. Using these recovery fractions we correct the observed Lyα luminosity function calculated as described above. The resulting completeness-corrected luminosity function is shown by the red filled circles in Figure 2.12. Error-bars shows Poisson uncertainties only, and correspond to a lower limit for the error since they do not include cosmic variance, although Ouchi et al. (2008) show that for volumes such as the one surveyed here ($\sim 10^6$

[3]In reality, incompleteness in narrow-band emission line surveys is more complicated than this because of the non top-hat shape of narrow-band filters, and shows a dependence with the redshift of the sources; see the discussion in Gronwall et al. (2007).

Mpc^3), cosmic sample variance uncertainties are not significantly higher than Poisson errors.

We fit the observed Lyα luminosity function using a Schechter (1976) function of the following form

$$\phi(L)dL = \phi^*(L/L^*)^\alpha \; exp(-L/L^*) \; d(L/L^*) \tag{2.6}$$

Since the depth of our observations ($\sim 5 \times 10^{-17}$ erg s^{-1}cm^{-2} in line flux) is somewhat limited, we do not consider our data to be sufficiently deep to constrain the faint-end slope (α) of the luminosity function. We consider the best available constraint on α to come from the spectroscopic survey recently performed by Cassata et al. (2011). They measure $\alpha \simeq -1.7$ using a survey which reaches more than one order of magnitude deeper than ours in terms of limiting line flux ($\sim 1.5 \times 10^{-18}$ erg s^{-1}cm^{-2}). We take their measured α as our fixed fiducial value for the faint-end slope of the luminosity function, but also report results assuming $\alpha = -1.5$, since that is the value most commonly used in the literature (Gronwall et al., 2007; Ouchi et al., 2008). Our results do not depend significantly on the assumed value of α.

The best-fit Schechter luminosity function ($\alpha = -1.7$) is shown by the solid red line in Figure 2.12, and 1, 2, and 3σ confidence limits for the parameters are shown in Figure 2.13. The best fit parameters for $\alpha = -1.7$ and -1.5 are reported in the first two rows of Table 2.2.

2.6.2 Comparison with Previous Measurements

Figure 2.12 also shows the Lyα luminosity functions measured by several authors at similar redshifts. The overall agreement with previous measurements is good. The Lyα luminosity functions of van Breukelen et al. (2005); Gronwall et al. (2007); Ouchi et al. (2008); Hayes et al. (2010), and Cassata et al. (2011) measured at $2.3 < z < 4.6$, $z = 3.1$, $z = 3.1$, $z = 2.2$, and $1.95 < z < 3$ respectively, agree with our observed values to within $\sim 1\sigma$ (Poisson) at all luminosities. The Hayes et al. (2010) measurement shows better agreement with our data at the bright end of the luminosity function. This is in fact surprising, as their measurement was performed over a smaller volume (5.4×10^3 Mpc^3) and a fainter range in luminosities ($2 \times 10^{41} - 5 \times 10^{42}$ erg s^{-1}) than the other mentioned works.

Our best-fit Schechter function appears to be flatter than previous measurements over a similar range in luminosities. Figure 2.13 shows that this difference is because we derive a higher L^* and a lower ϕ^* than previous authors (except Hayes et al. (2010) who found a very similar value for ϕ^* but a larger value for L^*). The best-fit parameters measured by van Breukelen et al. (2005); Gronwall et al. (2007); Ouchi et al. (2008); Hayes et al. (2010), and Cassata et al. (2011) fall within our 2σ confidence contour. This last work is the only one of the mentioned luminosity function measurements in which $\alpha = -1.7$. For all the other measurements, the faint-end slope was either assumed or measured to be -1.5 except for van Breukelen et al. (2005) who used -1.6. For better comparison, Figure 2.13 also shows uncertainty contours for

our fit assuming $\alpha = -1.5$ (dotted contours). As mentioned above, the value of α does not change our results in any significant way.

The L^* and ϕ^* parameters are strongly correlated with each other, so the 2σ discrepancy with previous measurements is not surprising as it follows the sense of the correlation. Most importantly, we survey a very large volume and hence are able to find rare high luminosity objects. The luminosity functions derived in these studies typically stop at $\sim 10^{43}$ erg s^{-1}, while we find objects up to three times brighter luminosities. If we fit a Schechter function to only bins with $L(Ly\alpha) \leq 10^{43}$ erg s^{-1}, we obtain the luminosity function shown as a dashed red line in Figure 2.12, which is in much better agreement with previous measurements (black star in Figure 2.13 and third row in Table 2.2).

2.6.3 Evolution of the Lyα Luminosity Function

As mentioned above, evidence suggests that the Lyα luminosity function does not significantly evolve between $z \sim 3$ and $z \sim 6$. While at the high end of this redshift range ($z \gtrsim 5$) IGM absorption might become important and the lack of evolution might imply an increase in the intrinsic Lyα luminosity function (Cassata et al., 2011), at least between $z \sim 4$ and $z \sim 3$ the lack of intrinsic evolution seems well supported as changes in IGM transmission are negligible (Ouchi et al., 2008). We can extend these studies to lower redshifts and ask: Does the luminosity function show any significant evolution down to $z \sim 2$?

To test for possible evolution, we have again divided our sample in the two redshift bins defined in §4, one at low-redshift ($1.9 < z < 2.8$), and another one at high-redshift ($2.8 < z < 3.8$). We measure the luminosity function in each of these bins independently. The results are shown in Figure 2.12, best fit parameters are presented in Table 2.2, and 1σ confidence limits are shown in Figure 2.13. At $L(Ly\alpha) \leq 10^{43}$ erg s^{-1}, where cosmic variance is lower than at higher luminosities, the low-z luminosity function seems to be systematically lower than the high-z luminosity function by a factor about ~ 2, in agreement with what we observed in §3 when comparing the redshift distribution of our objects to the predictions for a non evolving luminosity function. Still, both the high-z and low-z luminosity functions fall within their mutual Poisson uncertainties, and there is overlap between the 1σ confidence limits in their best-fit Schechter parameters (Figure 2.13).

We conclude that we find indications for evolution in the luminosity function over the $2 \lesssim z \lesssim 4$ range, with a decrease towards lower redshifts, but only at a low significance level. Larger samples, such as the ones HETDEX will produce in its few firsts months of operation, will be required to confirm this. If real, this evolution implies that the large drop in the Lyα luminosity function, evident at $z \simeq 0.3$, starts to occur at $z > 2$. Another way of searching for evolution in the Lyα luminosity function is to integrate it, and compare the implied Lyα luminosity density at each redshift. This is the subject of the next section.

2.7 Evolution of the Lyα Luminosity Density and the Global Escape Fraction of Lyα Photons.

In §5.2 we measured the median escape fraction of Lyα photons at $2 < z < 4$ in LAEs to be $\sim 30\%$. This does not represent the median escape fraction of the whole galaxy population at those redshifts, since LAEs will, by definition, be biased towards having high $f_{esc}(Ly\alpha)$. On the other hand, we can integrate the Lyα luminosity function measured in the previous section to estimate the Lyα luminosity density ($\rho_{Ly\alpha}$) at these redshifts. Comparing this observed luminosity density with that predicted from the global SFR density (ρ_{SFR}) for the entire galaxy population provides an estimate of the global escape fraction of Lyα photons and its evolution with redshift. The above approach is equivalent to taking the ratio between the SFR density implied by the observed Lyα luminosity density using Equation 2.2 ($\rho_{SFR,Ly\alpha}$), and the total ρ_{SFR}. This method has been applied by Cassata et al. (2011). In this work we extend their analysis which included the Cassata et al. (2011) data at $2 < z < 6.6$, the measurement of Gronwall et al. (2007) at $z = 3.1$, and the data of Ouchi et al. (2008) at $z = 3.1$, 3.7, and 5.7. We add the HETDEX Pilot Survey data points at $1.9 < z < 3.8$, as well as the $z \sim 0.3$ LAE data from Deharveng et al. (2008) and Cowie et al. (2010), the $z = 2.2$ data of Hayes et al. (2010), the $z = 4.5$ measurement by Dawson et al. (2007), the measurement at $z = 5.7$ of Shimasaku et al. (2006), the $z = 6.5$ data from Kashikawa et al. (2006), the data of Ouchi et al. (2010) at z=6.6, and the $z = 7.7$ measurement of Hibon et al. (2010). A similar dataset has been

analyzed in this way in a recent submission by Hayes et al. (2011), although using a different set of Hα and UV luminosity functions at different redshifts to estimate the total SFR density.

The top panel in Figure 2.14 shows $\rho_{SFR,Ly\alpha}$ derived from the observed Lyα luminosity density using Equation 2.2. We present our results for the full sample and for the low-z and high-z bins of the HETDEX Pilot Survey (red, blue, and green filled circles), as well as the compilation of data points calculated from the Lyα luminosity functions at $0.3 < z < 7.7$ mentioned above (black filled circles). Vertical error-bars are estimated from the published uncertainties in L^* and ϕ^*, and horizontal error-bars show the redshift range of the different samples (omitted for narrow-band surveys). Also presented is the latest estimate of the total SFR density history of the universe from Bouwens et al. (2010a), which has been derived from the best to date collection of dust extinction corrected UV luminosity functions at a series of redshifts between 0 and 8, and shows a typical uncertainty of 0.17 dex (Bouwens et al., 2010a, and reference therein).

A source of systematic error in measuring the Lyα luminosity density comes from the choice of the luminosity limit down to which the integration of the luminosity function is performed. An excellent discussion on this issue can be found in Hayes et al. (2011). With the goal of estimating the volumetric Lyα escape fraction by comparison to the UV derived SFR density, we should ideally choose an integration limit consistent with the one used by Bouwens et al. (2010a) to integrate their UV luminosity functions. In this way

we can ensure both measurements are roughly tracing the same galaxies. In the case of Lyα and UV luminosity functions this is nontrivial, as the exact number will depend on the, mostly unconstrained, shape of the Lyα escape fraction distribution for galaxies as a function UV luminosity. In lack of a better choice, we follow the approach of Hayes et al. (2011), and integrate the Lyα luminosity functions down to the same fraction of L^* as the UV luminosity function were integrated ($0.06L^*_{z=3}$ in the case of Bouwens et al. (2010a)). For consistency with Hayes et al. (2011), and in order to allow for a better comparison with their results, we define this limit using the Gronwall et al. (2007) luminosity function at $z = 3.1$, for which the integration limit becomes $0.06L^*_{G07} = 2.66 \times 10^{41}$ erg s^{-1}. For all the data points in Figure 2.14 we also shows the same measurements obtained by integrating the luminosity functions down to zero luminosity (upper open circles). The unlimited integration typically overestimates the luminosity (SFR) density by $\sim 60\%$. This provides a notion of the maximum impact that the choice of this integration limit has on the measured value of the luminosity density.

A second source of systematic error in the above measurement comes from the role that IGM scattering has at reducing the observed Lyα flux of sources at very high redshifts. Although all our previous analysis neglected the effects of IGM scattering on the Lyα line, this approach was only well justified at our redshifts of interest ($z < 4$), where IGM scattering is negligible for our purposes (see discussion in §1 and §5). To study the escape of Lyα photons from galaxies across a larger redshift range, we should try to incorporate the

effect of the IGM, which is not negligible for the measurements at very high redshift ($z \sim 6$). As discussed in §1, the effects of the ISM and IGM kinematics in and around galaxies makes this correction very difficult (Dijkstra et al., 2007; Verhamme et al., 2008). To first order, we have applied a correction using the Madau (1995) average Lyα forest opacity, and assuming that only half of the Lyα line flux suffers this attenuation. The filled symbols in Figure 2.14 include this correction. Raw measurements done without applying this correction are also shown in Figure 2.14 as the open circles below each data point. While this correction can become large ($\sim$ 50%) at the highest redshifts, it impact is still within the 1σ uncertainties coming from the luminosity function measurements.

In accordance with the low significance hint of evolution presented in §6.3, in the $2 < z < 4$ range, all the estimates of $\rho_{SFR,Ly\alpha}$ agree with each other within 1σ. However, by examining the overall trend of the data points, and keeping in mind the ones at higher and lower redshifts, there are clearly indications for evolution in the SFR density derived from Lyα from $z \sim 7$ down to $z \sim 0.3$, with a steady decrease towards lower redshifts across the $2 < z < 4$ range. Although the uncertainties in the $2 < z < 4$ range are large, allowing any two datapoints to be consistent with each other, the overall trend implies a decrease in $\rho_{Ly\alpha}$ of roughly a factor of ~ 2 from $z = 4$ to 2. We stress the need for larger samples of LAEs at these redshifts to better constrain this evolution.

The bottom panel of Figure 2.14 shows the global average escape frac-

tion of Lyα photons, which is given by the ratio between $\rho_{SFR,Ly\alpha}$ and ρ_{SFR} at any given redshift. The average escape fraction derived from our Lyα luminosity function over the whole $1.9 < z < 3.8$ range is $(3.0^{+2.3}_{-1.2})\%$. Errors include 1σ uncertainties in the luminosity function parameters and the 0.17 dex uncertainty in the total SFR density from Bouwens et al. (2010a). For our $1.9 < z < 2.8$ and $2.8 < z < 3.8$ bins we derived a mean Lyα escape fraction for the overall galaxy population of $(2.0^{+2.0}_{-0.9})\%$ and $(4.3^{+10.3}_{-2.2})\%$ respectively. This amount of evolution is not statistically significant, but we believe it to be real in the context of the overall trend seen in Figure 2.14. It also does not contradict the lack of evolution in the escape fraction for LAEs observed in §5.2, since, as mentioned above, the LAE selection tends to identify galaxies with high $f_{esc}(Ly\alpha)$ at any redshift, independent of the value of the escape fraction of the total galaxy population. The median dust extinction of a factor of ~ 3 measured in §4.2 implies that LAEs contribute roughly 10% of the total star formation at $2 < z < 4$. This contribution rises to 80% by $z \sim 6$, implying that galaxies at these redshifts must have very low amounts of dust in their ISM, which is consistent with the very blue UV slopes of continuum selected galaxies at these high redshifts (Bouwens et al., 2010b; Finkelstein et al., 2010). The observed behavior is also consistent with the results of Stark et al. (2010), who find the fraction of LBGs showing high EW Lyα emission to roughly double from $z = 4$ to 6. A similar result was also reported by Ouchi et al. (2008), who measure a significant level of evolution in the UV luminosity function between their $z = 3.7$ and $z = 6.6$ samples of LAEs, which was not traced by the Lyα

luminosity function.

The above escape fractions are in agreement with the result of Hayes et al. (2010), who measured an overall Lyα escape fraction of $(5.3 \pm 3.8)\%$ at $z = 2.2$ by comparing the Lyα and Hα luminosity function of narrow-band selected emission line galaxies over the same co-moving volume. On the other hand, by applying the same method used here Cassata et al. (2011) measured an average escape fraction of $\sim$20% at $z = 2.5$. The difference is easily explained by the fact that the latter authors compared their observed Lyα derived SFR density (which agrees with our value) to the total SFR density uncorrected by dust, which underestimates the true value at these redshifts.

It is evident that a strong decrease in the Lyα escape fraction of galaxies occurred between $z \sim 6$, and $z \sim 2$. In order to quantify this decrease we fit the data points in the lower panel of Figure 2.14 using two different functional forms. First, we fit a power-law of the form

$$\log(f_{esc}(z)) = \log(f_{esc}(0)) + \xi \log(1 + z) \tag{2.7}$$

This is the same parametrization used by Hayes et al. (2011) to fit the history of the global Lyα escape fraction. Best fit parameters are presented in Table 2.3. In order to provide a quantitative assessment of the impact of systematic errors in the measurement, we not only fit our best estimates of the escape fraction at each redshift, but also the values calculated ignoring

the luminosity function integration limit, and the IGM correction. The best fitting power-laws for these three sets of data points are shown as dotted lines in Figure 2.14. For comparison with the results of Hayes et al. (2011), we should consider our raw measurement without including the effects of the IGM, as a correction of this type was not done in their work. They find best fit values of $\log(f_{esc}(0)) = -2.8 \pm 0.1$, and $\xi = 2.6 \pm 0.2$, in excellent agreement with our result.

While the power-law model provides a reasonable fit to the data, it seems to systematically overestimate the measured values of $f_{esc}(Ly\alpha)$ in the $2 < z < 5$ range, and underestimate them in the $5 < z < 8$ range. The data points in Figure 2.14 seem to indicate a sudden drop, or transition in the escape fraction between $z = 6$ and 2. A similar transition, in a coincident redshift range, is observed in the dust extinction derived from the UV slope of continuum selected galaxies (Bouwens et al., 2009). Given the important role that dust has at regulating the escape of Lyα photons, it would not be surprising if the dust content and the Lyα escape fraction of galaxies present a similar evolution with redshift. In order to quantify this behavior we also fit a *transition* model of the following form,

$$\log(f_{esc}(z)) = \frac{\log(f_{esc}(0))}{2} \, (1 - \tanh(\theta(z - z_{tr})) \tag{2.8}$$

where z_{tr} is the transition redshift at which the decrease in the escape fraction takes place ($f_{esc} = 1$ for $z \gg z_{tr}$), and the parameter θ determines the

sharpness of the transition. Best-fit parameters to the measured escape fraction at each redshift, and the values without IGM correction, and without a luminosity function integration limit are presented in Table 2.3. Our best-fit *transition* model, implies a very high Lyα escape fraction of $\sim 80\%$ at $z \sim 6$, which drops softly from $z \sim 6$ to $z \sim 2$, with a characteristic transition redshift at $z_{tr} = 4.0 \pm 0.5$, in order to reach a value of $\sim 1\%$ in the local universe.

By analyzing the values in Table 3, It can be seen that, given the current uncertainties, the IGM correction and the choice of the luminosity function integration limit do not induce major changes in the best-fit parameters, especially in the case of the power-law exponent. The largest effect is that of the integration limit on the escape fraction at $z = 0$. The reason for this is that low L^* values are measured for the Lyα luminosity functions at low redshift. Therefore, the integration limit lays closer to L^* at these redshifts, making the value of the luminosity density more dependent on it.

Equation 2.8 predicts the average Lyα luminosity of star-forming galaxies at any redshift given their average SFR, and it might prove useful for semi-analytic models of galaxy formation attempting to reproduce the Lyα luminosity function. However, the escape fraction shows a very large scatter for single objects, and it might be systematically different for galaxy populations selected using different methods. Therefore, this relation should be used with caution, and only in an statistical manner. Also, this equation is only valid over the redshift range in which observations are available, and to the extent that current uncertainties allow. For example, given the current uncer-

tainties, we do not consider the escape fraction to be properly constrained at $z > 6.6$. While it is tempting to interpret the slight drop seen in the last data point at $z = 7.7$ as a possible reduction in Lyα transmission due to the neutralization of the IGM as we walk into the end of re-ionization, the error-bars are too large to allow for any significant conclusions.

2.8 Conclusions

For a sample of LAEs at $1.9 < z < 3.8$, detected by means of blind integral field spectroscopy of blank extragalactic fields having deep broad-band optical imaging, we were able to measure the basic quantities SFR, $E(B-V)$, UV luminosity, Lyα EW, and $f_{esc}(Ly\alpha)$. From these quantities and the correlations observed between them we conclude:

- Over the $2 < z < 4$ range LAEs show no evolution in the average dust content of their ISM, parameterized by the dust reddening $E(B-V)$, and measured from the UV continuum slope. These objects show a mean $\langle E(B-V) \rangle = 0.13 \pm 0.01$, implying that dust absorbs $\sim 70\%$ of the UV photons produced in these galaxies. While one third of LAEs down to our luminosity limit are consistent with being dust-free, the level of dust extinction measured for the rest of the sample is significant, and should not be neglected.

- At $z < 3$, we see the possible appearance of a rare (6/89 objects) population of highly reddened ($E(B-V) > 0.45$) LAEs, typically showing

high Lyα EWs. Two of these objects are in the MUNICS field where we do not have deep X-ray data to reject AGNs from our sample. The remaining four objects show low association probabilities (≤ 0.6) with their broad-band counterparts, casting doubt on the validity of our UV slope and EW measurements. The presence of these objects in the sample does not affect significantly the average dust properties of LAEs at the low redshift end of our range. If real, these objects are of great interest since their presence could indicate that the fraction of dusty LAEs grows towards lower redshifts. Followup of these objects is necessary to confirm this.

- The Lyα EWs of LAEs in our sample are consistent with the expectations for normal stellar populations with metallicities within 1/50 $Z_{\odot}$ and solar. We do not find it necessary to invoke a top-heavy IMF, the presence of population III stars, or an enhancement of the EW due to a clumpy dust distribution in a multi-phase ISM, to explain the observed EWs.

- LAEs in our sample show a median uncorrected UV derived $SFR \simeq 11$ $M_{\odot}yr^{-1}$. Correcting the UV luminosities for dust extinction increases this median value to $SFR \simeq 34$ $M_{\odot}yr^{-1}$, implying that assuming LAEs to be dust-free galaxies can translate into large underestimates of their SFRs. The ratio between the observed (i.e. uncorrected for dust) UV and Lyα derived $SFRs$ shows a median value of 0.83. Neither this ratio, nor the Lyα EW, show significant evolution with redshift across the

$2 < z < 4$ range. These two quantities also show no dependence with $E(B-V)$, implying that the ratio between the amount of dust extinction seen by Lyα photons and that seen by UV photons is independent of the dust-content of the galaxies' ISM. This finding is at odds with the expectation of models in which a clumpy distribution of dust in a multi-phase ISM promotes the escape of Lyα photons over that of UV continuum photons. It also implies that some combination of ISM geometry and kinematics reduces the amount of extinction seen by Lyα photons from that expected in a static and homogeneous ISM, but only up to the point where it is similar to that experienced by continuum photons.

- The escape fraction of Lyα photons from LAEs, given by the ratio between the observed Lyα luminosity and that predicted from the dust-corrected UV SFR, shows a median value of 29%. A large scatter is seen around this number, with objects ranging from a few percent to 100%. Both the median value, and the range of observed escape fractions in LAEs, show no evolution across the $2 < z < 4$ range sampled by our objects, and does not seem to evolve all the way down to $z = 0.3$. Since LAE selection is biased to include objects of high escape fractions at any combination of dust content, redshift and survey limiting luminosity, it is not surprising that this parameter shows little or no evolution. This lack of evolution in LAEs does not imply that the Lyα escape fraction for the overall galaxy population is not evolving.

- The Lyα escape fraction of LAEs shows a clear correlation with $E(B-$

V). The correlation follows what is expected for a value of $q = 1$, where q is the ratio between the dust opacity seen by Lyα and that seen by continuum photons. This behavior is consistent with what is observed for LAEs at $z = 0.3$, implying that not only the value of the escape fraction, but also its dependence with dust content, do not evolve with redshift. While other galaxies not identified by the LAE selection can have $q > 1$, and show low Lyα EWs, lack of Lyα emission, and even Lyα in absorption, the lack of objects with $q \ll 1$ confirms that preferential escape of Lyα photons over continuum photons in the presence of a clumpy dust distribution is not a common process in galaxies.

We also measure the Lyα luminosity function across our redshift range. Integration of the luminosity function yields a measurement of the Lyα luminosity density in our sampled volume. Using our data, and a compilation of measurements of the Lyα luminosity function at different redshifts from the literature, we are able to trace the evolution of $\rho_{Ly\alpha}$ with redshift from $z = 0.3$ to $z = 7.7$. Comparing the observed value of $\rho_{Ly\alpha}$ with the expected density implied by the SFR history of the universe, allows a measurement of the evolution of the average Lyα escape fraction for the overall galaxy population in this redshift range. From these measurements we conclude the following:

- The observed Lyα luminosity function is well matched to previous measurements in the literature, especially in the $L(Ly\alpha) \leq 10^{43}$ erg s^{-1} range typically measured by previous studies. Given the large volume sampled

by the HETDEX Pilot Survey, we are able to find many objects above this luminosity. Both the redshift distribution and the luminosity function show hints of a decrease in the number density of LAEs of roughly a factor of 2 from $z = 4$ to 2, although this decrease is not statistically significant and larger samples are required before it can be confirmed. In any case, this decrease goes in the right direction and is consistent with what is expected from the observed drop in the Lyα escape fraction for the overall galaxy population.

- The Lyα luminosity density is observed to increase steadily from $z = 0.3$ to $z \simeq 2$, following the behavior of the SFR history of the universe. Over this range, the average Lyα escape fraction increases very slowly from $\sim 1\%$ to $\sim 5\%$. At $z \gtrsim 2$ the increase in $\rho_{Ly\alpha}$ starts to flatten, and a decline is observed around $z \sim 6$. This behavior is accompanied by a decrease in ρ_{SFR} immediately after $z = 2$, implying that over the $2 < z < 6$ range, the average Lyα escape fraction in galaxies increases steadily from the $\sim 5\%$ up to $\sim 80\%$ by $z = 6$. Current measurements of the luminosity function at higher redshifts do not constrain the behavior of the escape fraction beyond $z = 6.6$. This drop in the average escape fraction of Lyα photons with cosmic time is consistent with the increase in the dust-content of star forming galaxies, which is expected from the chemical enrichment of these objects as star formation proceeds, and is observed as a reddening in the UV slope of star forming galaxies towards lower redshifts (Bouwens et al., 2010b; Finkelstein et al., 2010)

- Equation 2.8 provides a useful analytical form which describes the history of the average Lyα escape fraction of galaxies as a function of redshift. This equation can prove useful to predict the expected average Lyα luminosity of galaxies in numerical simulations and semi-analytical models. The reader must keep in mind that galaxies do not show a single value of the escape fraction at any given redshift, but rather a relatively broad (and mostly unconstrained) distribution, so this equation can only be used in a statistical sense. It must also be kept in mind that the behavior of the escape fraction at $z > 6.6$ is still unconstrained.

These last few points have interesting consequences regarding the potential that observations of LAEs at very high redshifts ($z \geq 7$) have to detect the effects of cosmic re-ionization. Our results imply that at these redshifts, dust is no longer an important factor setting the average escape fraction of Lyα photons in galaxies. Therefore, a significant drop in the Lyα escape fraction could be more easily interpreted as being caused by an increased neutral fraction in the IGM.

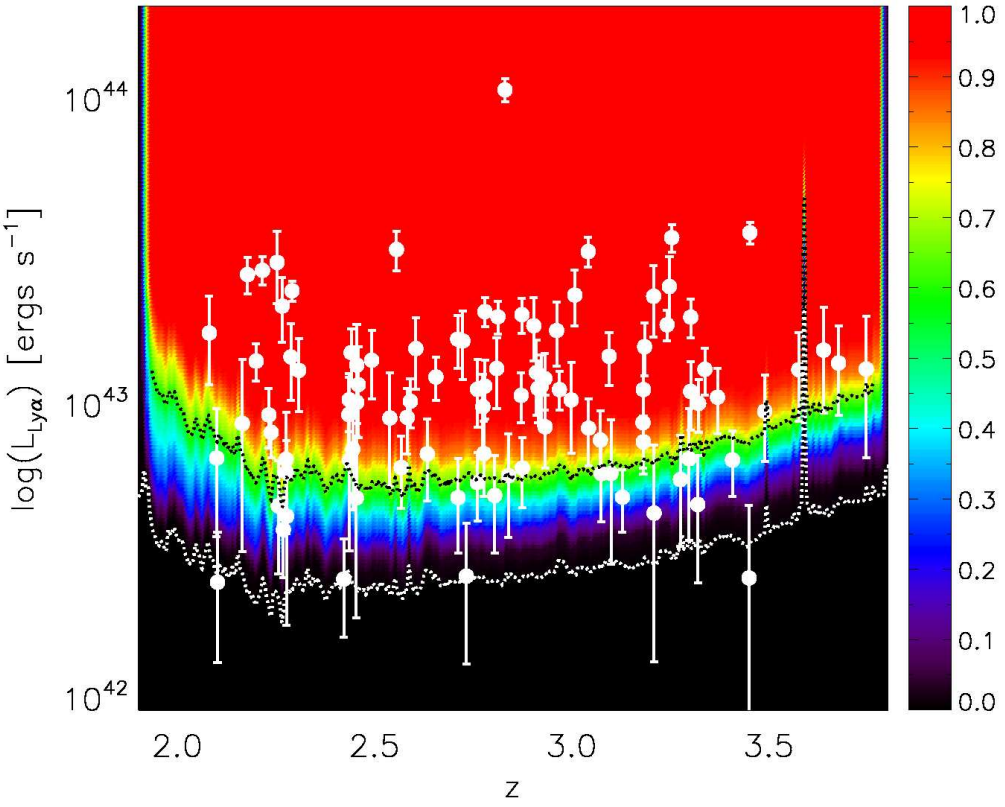

Figure 2.1 Limiting Lyα luminosity (5σ) as a function of redshift for the survey. The survey depth varies across the observed area due to changes in atmospheric transparency, Galactic extinction, and instrumental configuration. Hence, the background color indicates the fraction of the total survey area over which a given limit is reached. White points mark the redshift and Lyα luminosities (with error-bars) of the 99 objects classified as LAEs. The dotted black and white lines show the mean and best limits over the whole survey respectively. Even below this last limit, the completeness of the survey is not zero, explaining why we see 2 points below this curve.

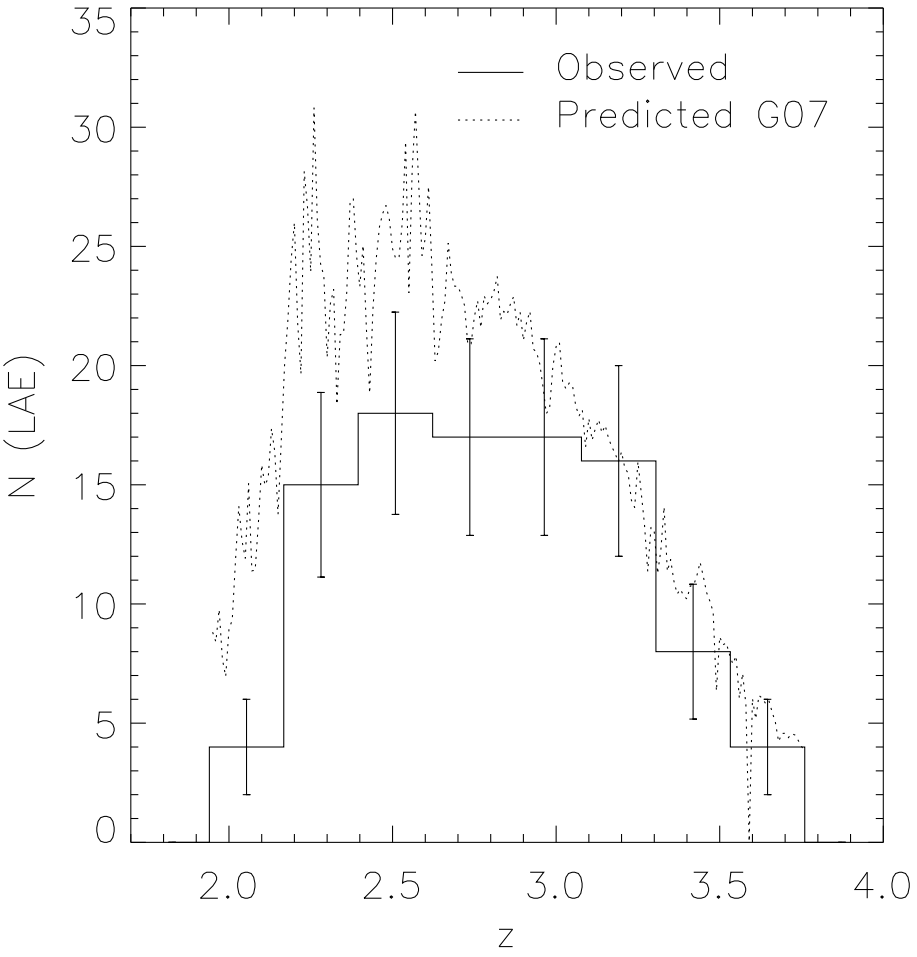

Figure 2.2 Redshift distribution of the 99 LAEs in the Pilot Survey (solid histogram). Error-bars represent Poisson uncertainties only. Also shown is the incompleteness-corrected predicted redshift distribution (dotted line) given by our flux limit and assuming the Gronwall et al. (2007) Lyα luminosity function with no evolution over $2 < z < 4$.

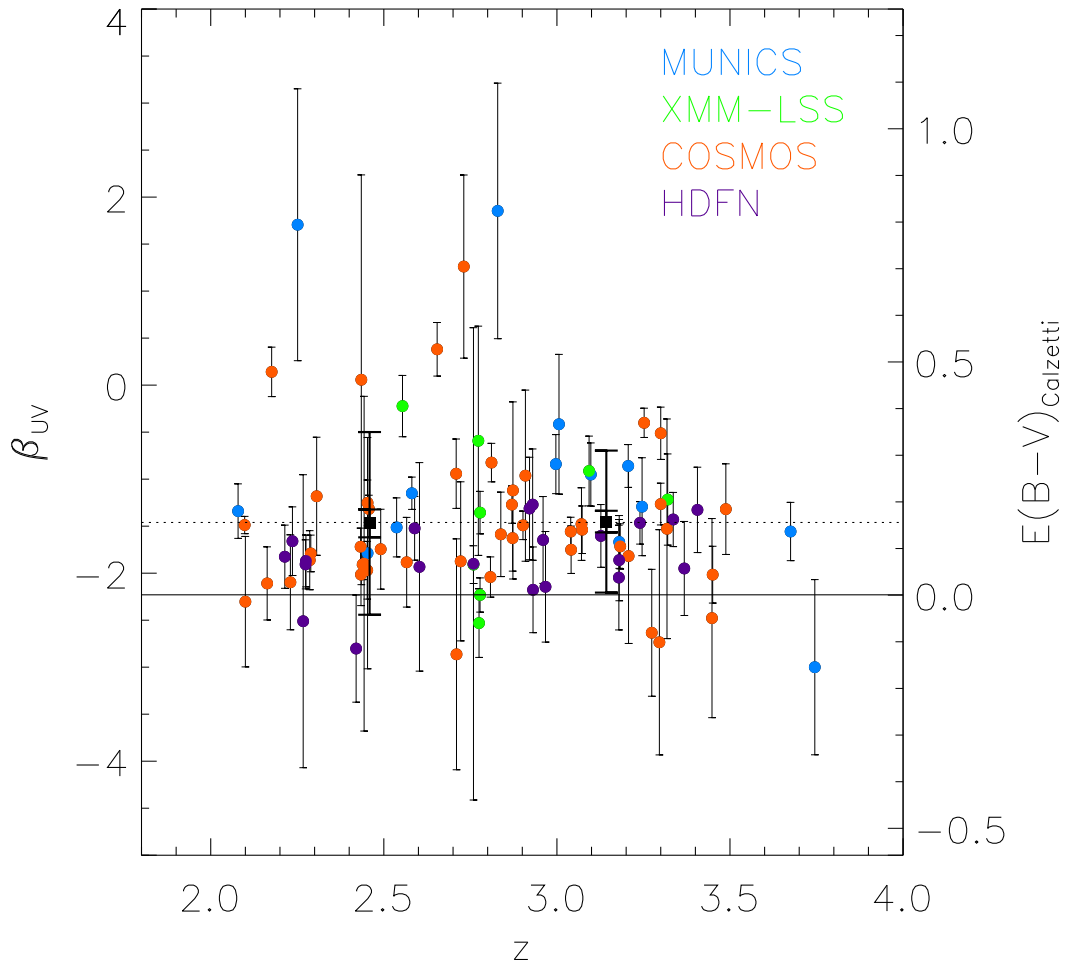

Figure 2.3 UV continuum slope as a function of redshift for the 89 LAEs with broad-band optical counterparts. Objects are color coded by field. The right axis shows the equivalent E(B-V) assuming a Calzetti et al. (2000) attenuation law. The horizontal lines mark the assumed intrinsic UV slope corresponding to a dust-free stellar population ($\beta_0 = -2.23$, solid line), and the mean for the whole sample (dotted line). Also shown are the mean UV slopes for two redshift bins at $1.9 < z < 2.8$ and $2.8 < z < 3.8$ (black squares), with two sets of error-bars corresponding to the standard deviation in β within each bin (large error-bars) and the formal error in the mean (small error-bars).

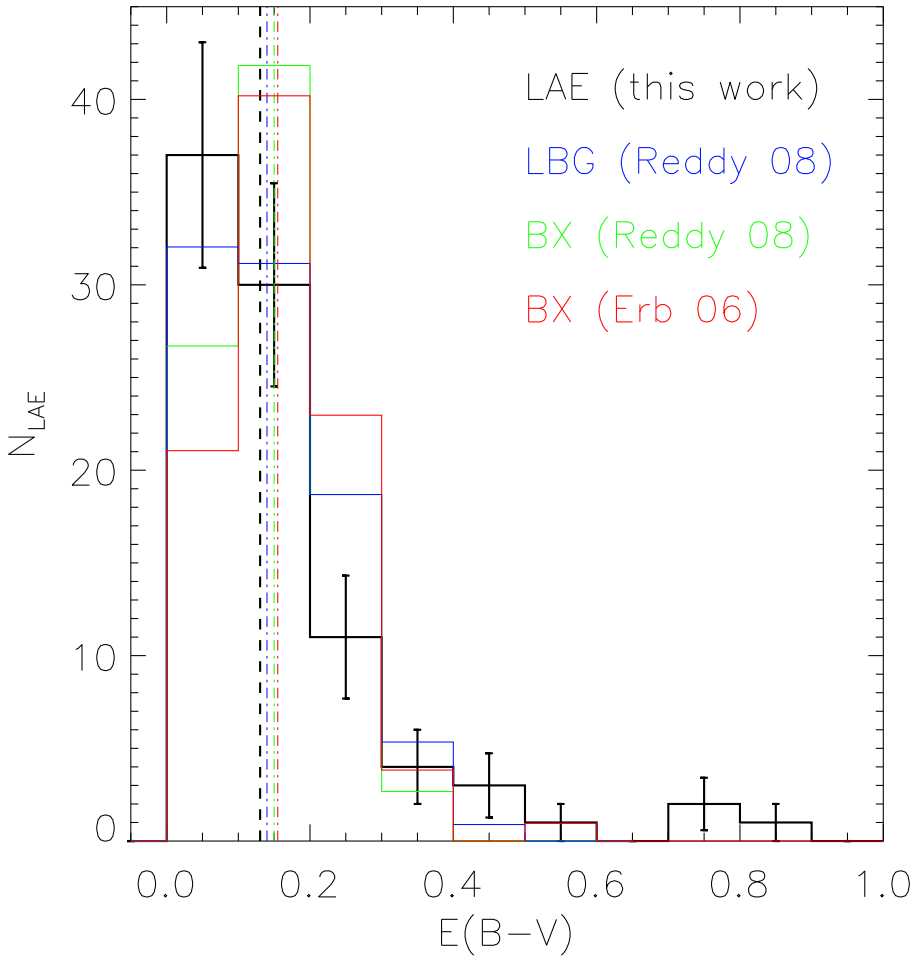

Figure 2.4 $E(B-V)$ distribution of LAEs in our sample (Poisson error-bars), together with that of BX/LBGs taken from Erb et al. (2006) and Reddy et al. (2008) (solid histograms). The median of each distribution is marked by the vertical dashed lines.

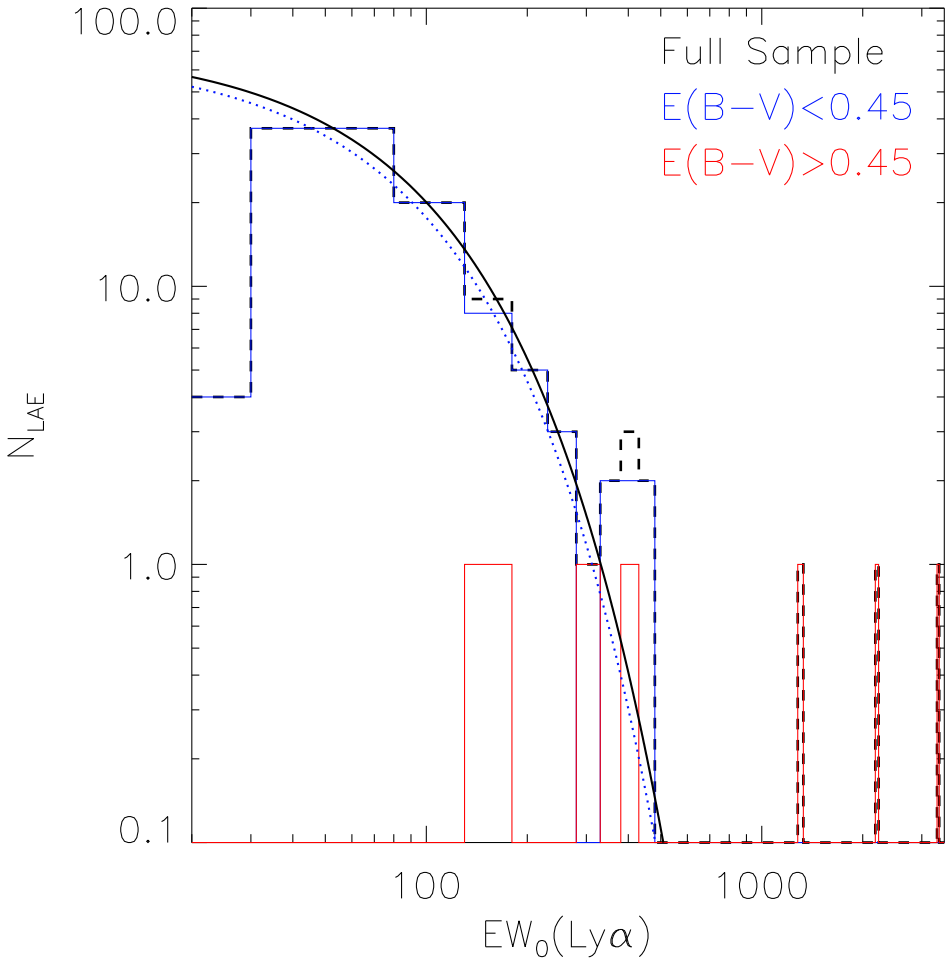

Figure 2.5 Rest-frame Lyα *EW* distribution of LAEs in our sample (dashed black histogram). The distributions for low ($E(B-V) < 0.45$) and high ($E(B-V) > 0.45$) reddening objects are shown (blue and red histograms respectively). Also shown are the best-fit exponential distribution ($N \propto \exp[-EW/w_0]$) to the whole sample ($w_0 = 77 \pm 7$Å, solid black line) and the low reddening sample ($w_0 = 74 \pm 7$Å, dotted blue line).

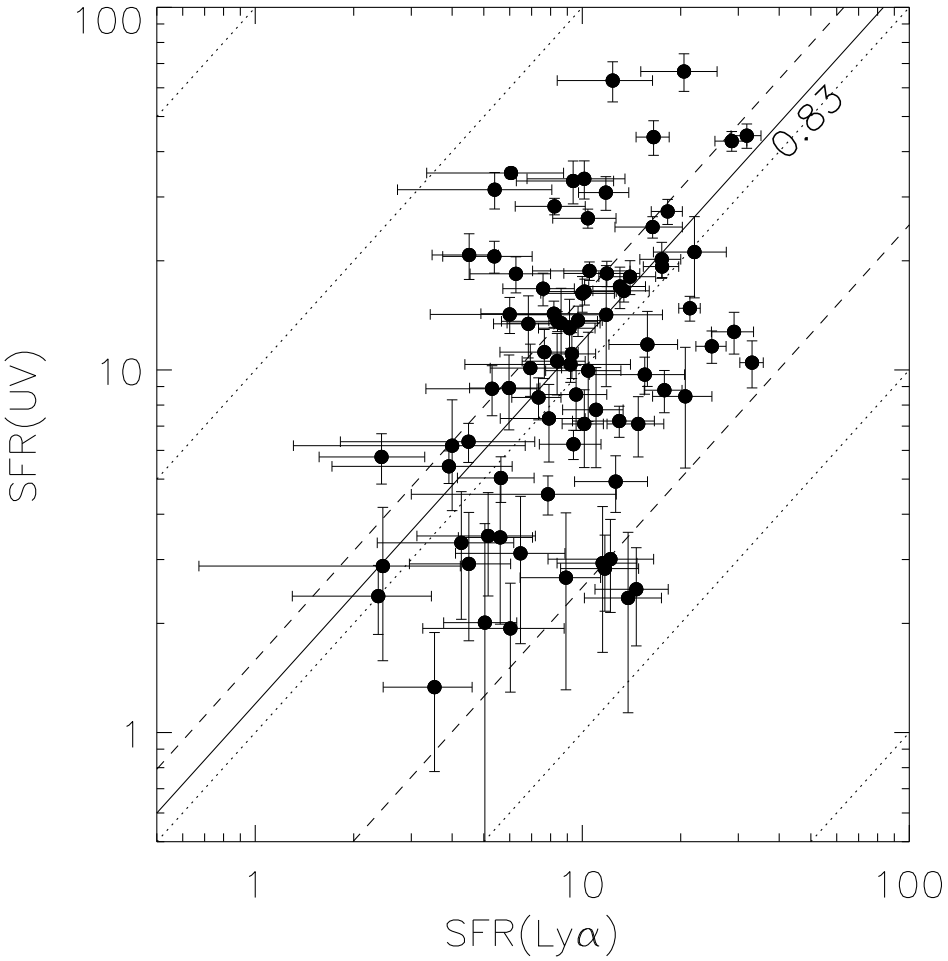

Figure 2.6 UV versus Lyα derived $SFRs$ for the 83 LAEs in the final sample. Values are not corrected for dust extinction. The solid line shows the median SFR(Lyα) to $SFR(UV)$ ratio of 0.83. The expected range for dust-free normal stellar populations is marked by the dashed lines. Dotted lines mark ratios of 0.01, 0.1, 1, 10, and 100.

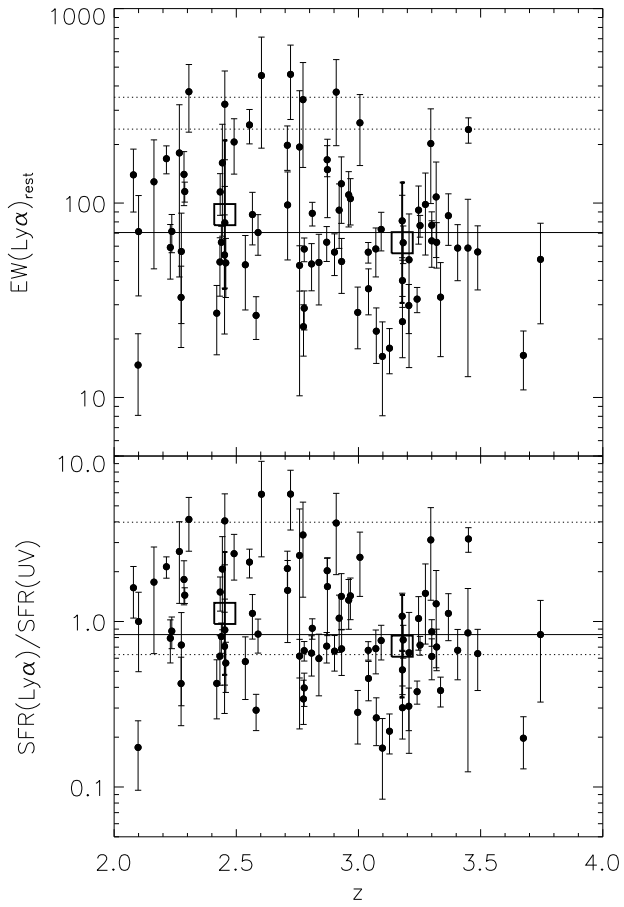

Figure 2.7 Rest-frame Lyα EW, and $SFR(Ly\alpha)$ to $SFR(UV)$ ratio (not corrected for dust) as a function of redshift. The median EW of 71Å and ratio of 0.83 are marked by solid horizontal lines. The dotted lines on the top panel indicate the maximum EW range for young normal stellar populations with metallicities between solar and one 1/50 solar from Schaerer (2003). Dotted lines in the bottom panel display the allowed range in the $SFR(Ly\alpha)$ to $SFR(UV)$ ratio for dust-free normal stellar populations. The open boxes show the median EW and ratio for the two redshift bins at $1.9 < z < 2.8$ and $2.8 < z < 3.8$.

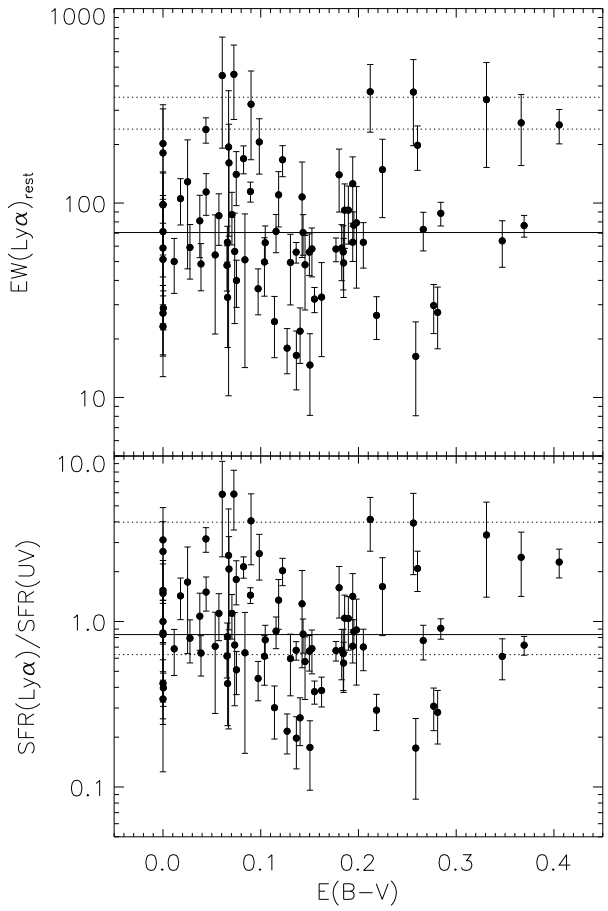

Figure 2.8 Rest-frame Lyα EW and $SFR(Ly\alpha)$ to $SFR(UV)$ ratio (not corrected for dust) as a function of E(B-V). Symbols are the same as in Figure 2.7.

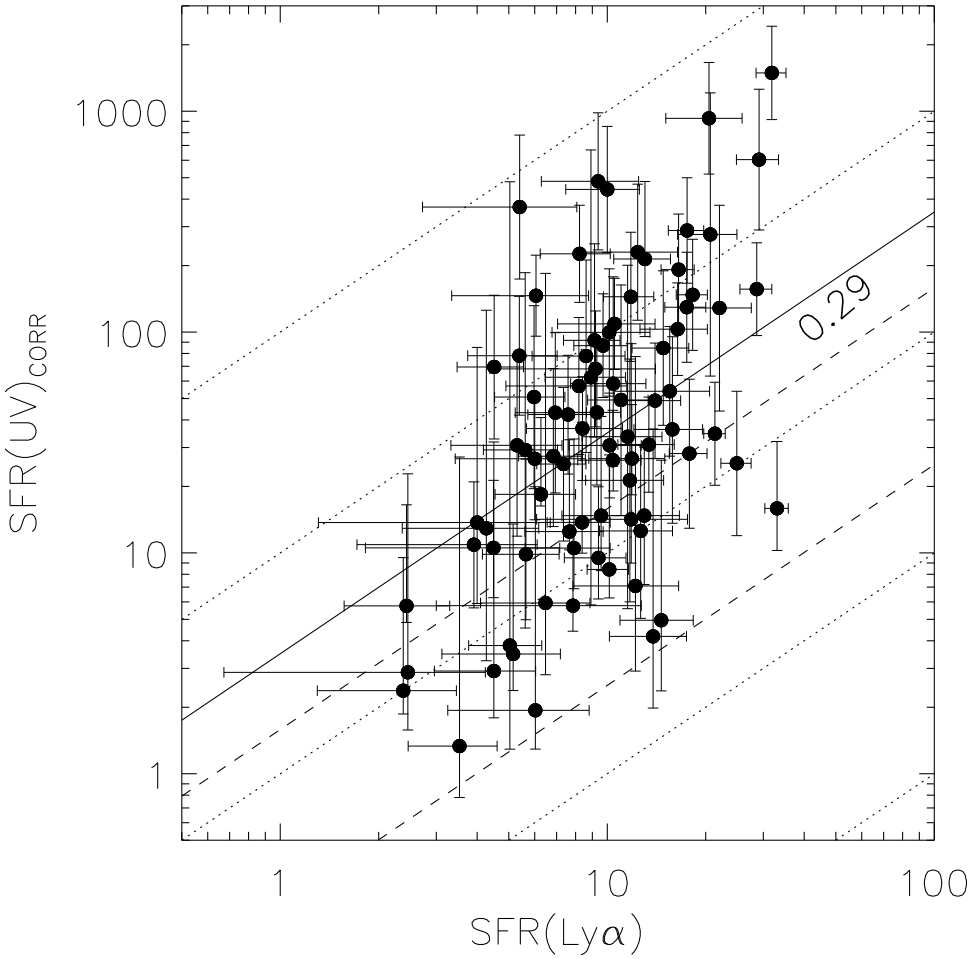

Figure 2.9 Same as Figure 2.6, but with $SFR(UV)$ corrected for dust. Errorbars include the uncertainty in the correction. The solid line marks the median escape fraction of 29%.

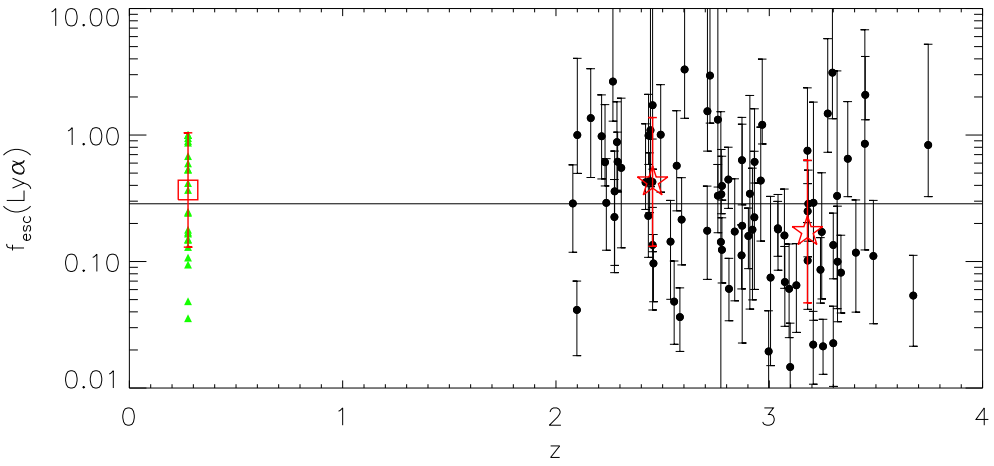

Figure 2.10 Escape fraction of Lyα photons as a function of redshift for the 83 LAEs in the final sample. The solid horizontal line denotes the median escape fraction of 29%. Also shown is the median escape fraction for the two redshift bins at $1.9 < z < 2.8$ and $2.8 < z < 3.8$ (open red stars), with errorbars corresponding to the standard deviation of $\log(f_{esc})$ within each bin. The escape fractions of LAEs at $z = 0.3$ with their median from Atek et al. (2009) (green triangles, red open square) are also displayed.

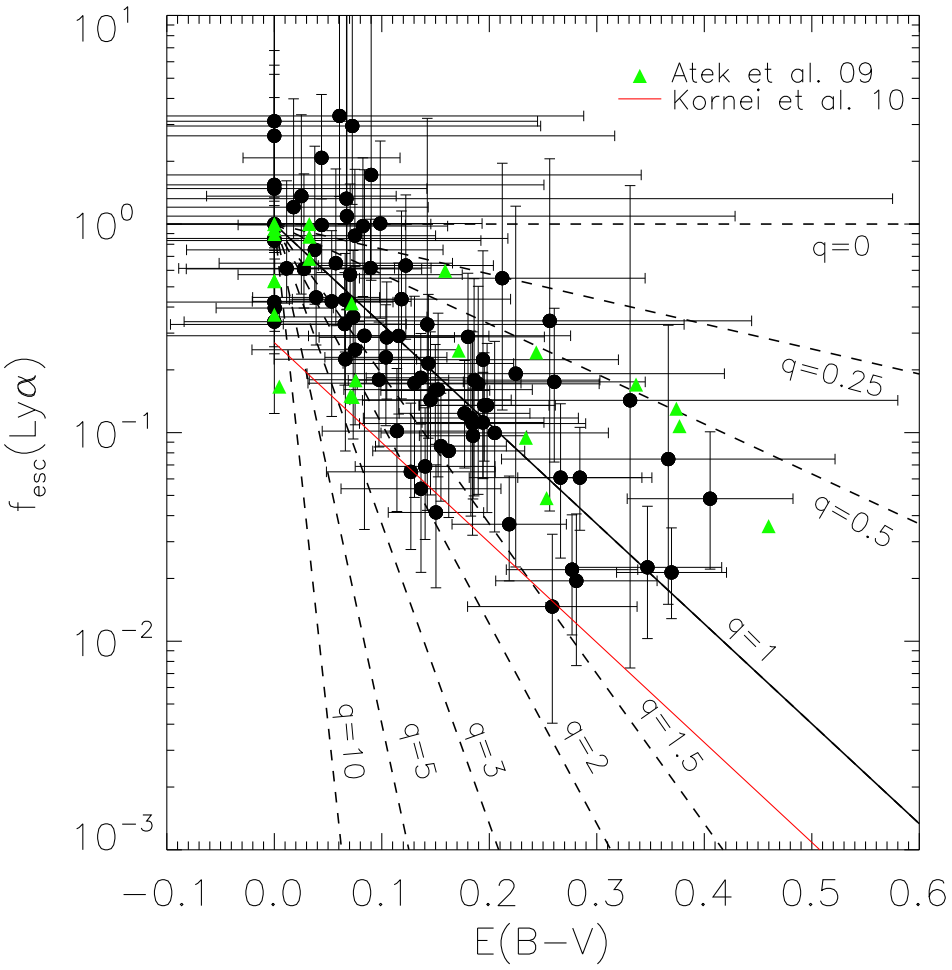

Figure 2.11 Lyα escape fraction as a function of E(B-V). Dashed lines show the expected correlation for different values of the parameter $q = \tau_{Ly\alpha}/\tau_{\lambda=1216}$. The red line displays the relation for LBGs showing Lyα in emmission from Kornei et al. (2010). Green triangles show the values for $z \simeq 0.3$ LAEs from Atek et al. (2009).

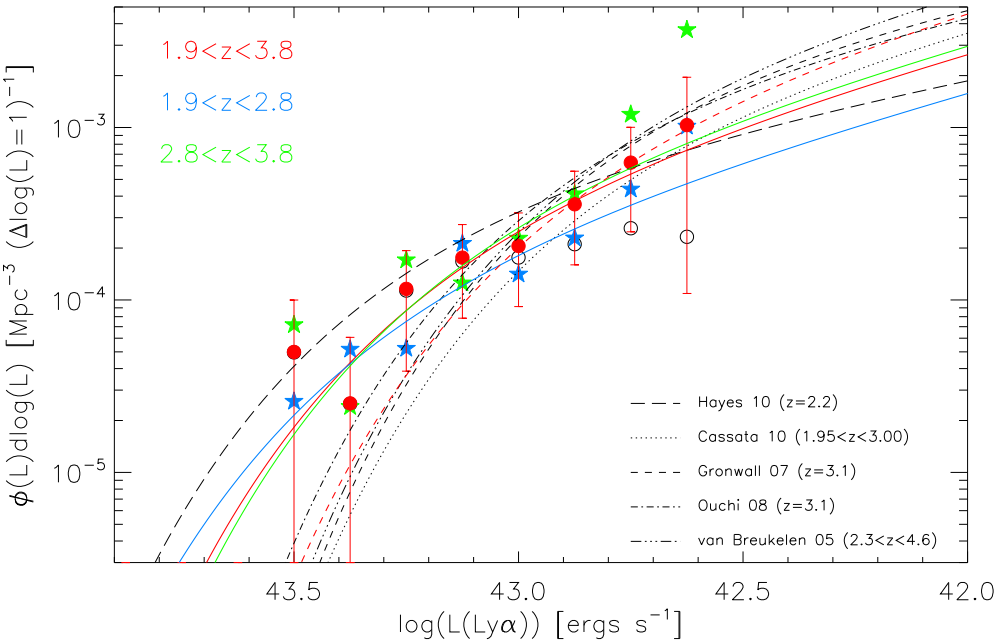

Figure 2.12 Lyα luminosity function of the HETDEX Pilot Survey sample of 80 LAEs in COSMOS and HDF-N, shown before and after applying the completeness correction (open black and filled red circles respectively). Poisson error-bars are included. Also displayed are the completeness corrected luminosity function for the two redshift bins at $1.9 < z < 2.8$ and $2.8 < z < 3.8$ (blue and green stars respectively), and the luminosity functions of van Breukelen et al. (2005); Gronwall et al. (2007); Ouchi et al. (2008); Hayes et al. (2010),and Cassata et al. (2011). Schechter fits to the full sample, as well as the low-z and high-z samples, are also presented (solid red, blue, and green curves respectively). The red dashed line denotes the best Schechter fit to the $L(Ly\alpha) \leq 10^{43}$erg s^{-1} bins.

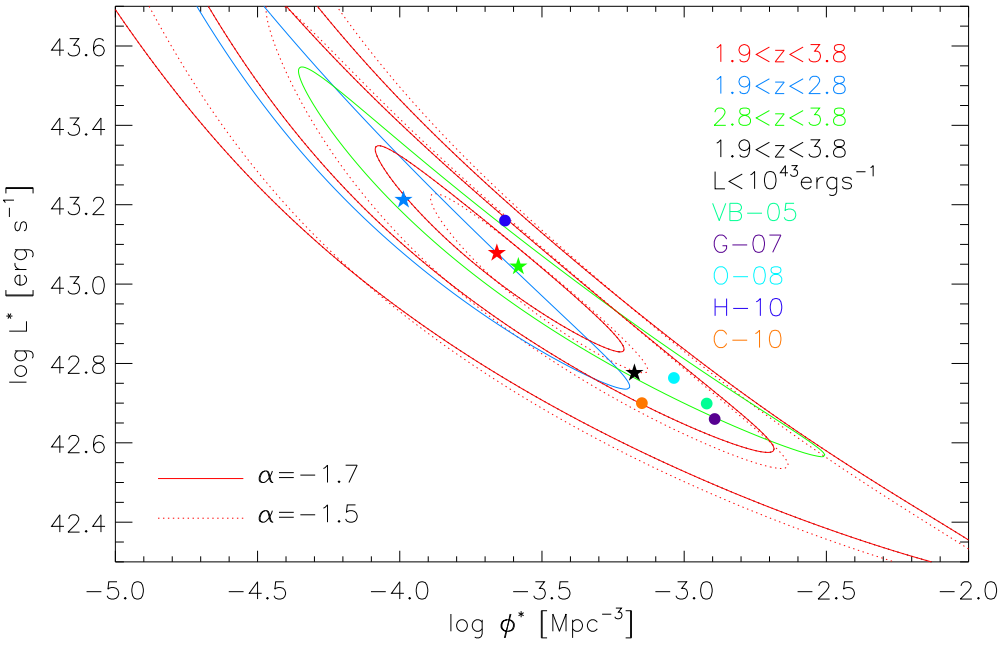

Figure 2.13 Contours show 1, 2, and 3σ confidence limits for the luminosity function parameters L^* and ϕ^*. Stars show our results for the full sample and the two redshift bins at $1.9 < z < 2.8$ and $2.8 < z < 3.8$. The parameters estimated by van Breukelen et al. (2005); Gronwall et al. (2007); Ouchi et al. (2008); Hayes et al. (2010), and Cassata et al. (2011) are also presented (filled circles).

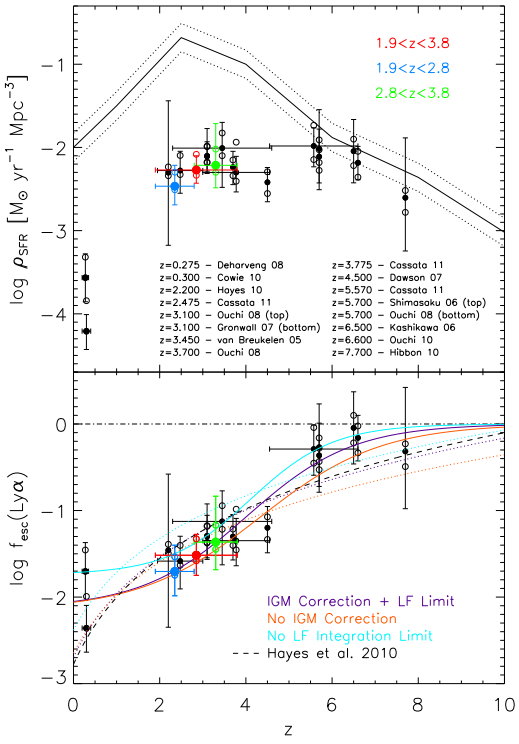

Figure 2.14 *Top panel:* SFR density (ρ_{SFR}) as a function of redshift. The solid and dotted lines show the total ρ_{SFR} from Bouwens et al. (2010a) and its typical uncertainty of 0.17 dex. Blue, green, and red filled circles show $\rho_{SFR,Ly\alpha}$ derived from the Lyα luminosity function in the two redshift bins at $1.9 < z < 2.8$ and $2.8 < z < 3.8$, as well as for the full sample. Black filled circles show the derived densities at different redshifts from the luminosity functions of van Breukelen et al. (2005); Shimasaku et al. (2006); Kashikawa et al. (2006); Gronwall et al. (2007); Dawson et al. (2007); Ouchi et al. (2008); Deharveng et al. (2008); Ouchi et al. (2010); Cowie et al. (2010); Hayes et al. (2010); Hibon et al. (2010), and Cassata et al. (2011). Raw values computed without applying an IGM correction are shown by the open circles below each measurement. Values computed integrating the Lyα luminosity functions all the way down to $L(Ly\alpha) = 0$ are shown by the open circles above each measurement. *Bottom panel:* Escape fraction of Lyα photons for the overall galaxy population, derived from the ratio between the Lyα derived $\rho_{SFR,Ly\alpha}$ and the total value at each redshift. The dashed line marks an escape fraction of 100%. Solid lines shows our best fit to the data given by Equation 2.8, while dotted lines show the best fit powerlaw functions. Purple, orange, and cyan colors indicate fits to the escape fraction measurements including an IGM correction and an integration limit for the luminosity function, ignoring the IGM correction, and ignoring the luminosity function integration limit respectively. The black dashed line shows the result of Hayes et al. (2011).

Table 2.1. Properties of HETDEX Pilot Survey LAEs

ID[a]	z	$L(Ly\alpha)$	$L_{\nu,1500\mathring{A}}$[b]	β	$E(B-V)$	$f_{esc}(Ly\alpha)$	$EW_0(Ly\alpha)$
		10^{42}erg s^{-1}	10^{28} erg s^{-1} Hz^{-1}		mag		Å
HPS-3	3.09	14.4±2.8	12.1±1.6	-0.9±0.4	0.27±0.08	$0.06^{+0.08}_{-0.04}$	73±16
HPS-6	2.78	20.1±2.2	19.5±1.6	-1.4±0.2	0.18±0.06	$0.12^{+0.10}_{-0.06}$	58±8
HPS-11	2.78	11.5±2.5	18.7±1.1	-2.2±0.2	0.00±0.05	$0.40^{+0.28}_{-0.09}$	28±6
HPS-13	3.32	10.1±2.0	9.3±1.9	-1.2±0.5	0.20±0.11	$0.10^{+0.17}_{-0.07}$	62±16
HPS-17	2.78	6.9±1.9	13.2±1.5	-2.5±0.4	0.00±0.08	$0.34^{+0.43}_{-0.10}$	23±6
HPS-22	2.77	9.8±2.7	1.9±1.0	-0.6±1.2	0.33±0.25	$0.14^{+1.39}_{-0.14}$	340±187
HPS-25	2.55	32.1±4.7	9.1±1.2	-0.2±0.3	0.41±0.08	$0.05^{+0.05}_{-0.03}$	252±50
HPS-34	2.76	11.2±2.8	11.7±1.0	-1.9±0.2	0.07±0.06	$0.33^{+0.25}_{-0.16}$	47±12
HPS-51	3.10	5.9±2.9	22.4±2.6	-1.0±0.3	0.26±0.08	$0.01^{+0.02}_{-0.01}$	16±8
HPS-53	3.57	13.0±4.2	-	-	-	-	-
HPS-62	2.08	17.1±5.5	6.9±0.8	-1.3±0.3	0.18±0.07	$0.29^{+0.29}_{-0.17}$	139±49
HPS-82	2.25	29.1±7.7	1.4±0.7	1.7±1.4	0.79±0.29	$0.01^{+0.11}_{-0.01}$	2213±1548
HPS-84	3.25	24.3±6.1	15.1±3.8	-1.3±0.5	0.19±0.11	$0.17^{+0.33}_{-0.12}$	91±30
HPS-89	2.54	14.4±3.0	-	-	-	-	-
HPS-91	3.00	10.3±3.4	23.7±3.2	-0.8±0.3	0.28±0.08	$0.02^{+0.02}_{-0.01}$	27±9
HPS-92	3.67	13.6±4.4	44.9±5.7	-1.6±0.3	0.14±0.07	$0.05^{+0.06}_{-0.03}$	16±5
HPS-93	2.26	20.9±5.0	-	-	-	-	-
HPS-95	2.45	13.4±4.8	2.1±0.6	-1.8±1.2	0.09±0.25	$1.72^{+17.09}_{-1.18}$	322±155
HPS-99	3.01	22.8±4.7	6.0±2.2	-0.4±0.7	0.37±0.16	$0.07^{+0.25}_{-0.06}$	258±102
HPS-109	3.21	22.5±5.9	47.5±5.6	-0.9±0.2	0.28±0.06	$0.02^{+0.02}_{-0.01}$	29±8
HPS-111	3.18	11.2±3.7	24.0±2.9	-1.7±0.3	0.11±0.07	$0.10^{+0.10}_{-0.06}$	24±8
HPS-124	3.74	13.0±6.3	10.1±3.7	-3.0±0.9	0.00±0.19	$0.83^{+4.39}_{-0.51}$	51±27
HPS-126	2.83	106.7±9.1	3.5±3.2	1.9±1.4	0.82±0.28	$0.01^{+0.10}_{-0.01}$	3338±3038
HPS-127	2.54	9.0±3.6	10.2±0.8	-1.5±0.3	0.15±0.08	$0.14^{+0.16}_{-0.09}$	48±19
HPS-142	2.58	9.1±2.2	20.2±1.1	-1.1±0.2	0.22±0.05	$0.04^{+0.03}_{-0.02}$	26±6
HPS-144	2.73	2.7±1.3	1.0±0.5	1.3±1.0	0.70±0.20	$0.00^{+0.01}_{-0.00}$	270±187
HPS-145	2.18	26.5±3.6	5.4±0.5	0.1±0.3	0.48±0.07	$0.03^{+0.03}_{-0.02}$	380±66
HPS-150	2.90	18.1±4.2	17.7±1.2	-1.5±0.2	0.15±0.05	$0.16^{+0.11}_{-0.07}$	55±13
HPS-153	2.71	16.3±3.2	5.1±1.0	-0.9±0.4	0.26±0.08	$0.18^{+0.22}_{-0.10}$	198±50
HPS-154	2.87	6.2±1.6	2.5±1.0	-1.1±0.9	0.22±0.19	$0.19^{+1.03}_{-0.17}$	148±64
HPS-160	2.43	6.6±3.2	0.4±0.4	0.1±2.2	0.46±0.44	$0.14^{+9.03}_{-0.15}$	1306±1732
HPS-161	3.25	35.1±3.7	31.6±2.4	-0.4±0.2	0.37±0.05	$0.02^{+0.01}_{-0.01}$	76±9
HPS-164	2.45	10.1±5.3	7.4±0.8	-1.3±0.2	0.20±0.06	$0.14^{+0.13}_{-0.09}$	79±42
HPS-168	3.45	36.4±3.0	7.5±1.1	-2.0±0.3	0.04±0.07	$2.08^{+2.10}_{-0.76}$	238±35
HPS-174	3.45	2.7±2.0	2.1±0.9	-2.5±1.1	0.00±0.22	$0.85^{+5.94}_{-0.73}$	58±45
HPS-182	2.43	10.4±2.2	4.5±0.4	-2.0±0.3	0.04±0.08	$0.99^{+1.11}_{-0.40}$	114±27
HPS-183	2.16	8.6±5.3	3.2±0.4	-2.1±0.4	0.03±0.09	$1.36^{+1.98}_{-0.90}$	128±82
HPS-184	3.21	4.4±3.0	4.4±1.5	-1.8±0.9	0.08±0.19	$0.29^{+1.53}_{-0.26}$	51±36
HPS-189	2.45	4.9±2.9	4.5±0.6	-2.0±0.3	0.05±0.07	$0.43^{+0.50}_{-0.31}$	54±32
HPS-190	2.28	6.0±1.6	-	-	-	-	-
HPS-194	2.29	23.5±1.8	10.6±0.8	-1.8±0.2	0.09±0.06	$0.62^{+0.44}_{-0.26}$	114±13
HPS-196	2.65	12.3±2.0	7.4±1.0	0.4±0.3	0.53±0.07	$0.01^{+0.01}_{-0.00}$	134±27
HPS-197	2.44	7.1±2.6	2.2±1.0	-1.9±1.8	0.07±0.36	$1.09^{+32.85}_{-0.70}$	160±93
HPS-205	2.91	12.7±3.5	2.1±0.9	-1.0±0.9	0.26±0.19	$0.34^{+1.71}_{-0.30}$	372±174
HPS-207	2.71	5.0±1.7	2.1±0.8	-2.9±1.2	0.00±0.25	$1.54^{+15.26}_{-0.80}$	97±46
HPS-210	3.49	9.5±3.0	9.6±2.4	-1.3±0.5	0.18±0.11	$0.11^{+0.19}_{-0.08}$	56±20

Table 2.1 (cont'd)

ID[a]	z	$L(Ly\alpha)$	$L_{\nu,1500\mathring{A}}$ [b]	β	$E(B-V)$	$f_{esc}(Ly\alpha)$	$EW_0(Ly\alpha)$
HPS-213	3.30	11.0±2.8	11.6±1.3	-0.5±0.3	0.35±0.07	$0.02^{+0.02}_{-0.01}$	63±17
HPS-214	3.30	6.6±3.1	1.4±0.5	-2.7±1.2	0.00±0.24	$3.11^{+28.94}_{-1.77}$	202±102
HPS-223	2.31	12.9±3.5	2.0±0.5	-1.2±0.6	0.21±0.13	$0.55^{+1.41}_{-0.42}$	373±142
HPS-229	3.04	31.6±3.5	30.5±1.9	-1.6±0.2	0.14±0.05	$0.18^{+0.12}_{-0.07}$	55±6
HPS-231	2.72	16.1±4.1	1.8±0.5	-1.9±0.8	0.07±0.18	$2.95^{+12.73}_{-1.71}$	459±190
HPS-244	2.10	2.6±1.2	1.7±0.4	-2.3±0.7	0.00±0.15	$1.00^{+3.04}_{-0.50}$	71±38
HPS-249	3.27	5.7±2.2	2.5±0.8	-2.6±0.7	0.00±0.14	$1.48^{+4.30}_{-0.75}$	98±44
HPS-251	2.29	14.3±4.0	5.2±0.5	-1.9±0.3	0.07±0.08	$0.88^{+0.95}_{-0.51}$	140±43
HPS-253	3.18	15.4±3.0	12.9±1.4	-1.7±0.2	0.10±0.06	$0.29^{+0.24}_{-0.14}$	62±13
HPS-256	2.49	13.9±3.5	3.5±0.6	-1.7±0.4	0.10±0.09	$1.01^{+1.49}_{-0.65}$	206±65
HPS-258	2.81	19.3±2.4	13.8±0.9	-0.8±0.2	0.28±0.06	$0.06^{+0.05}_{-0.03}$	88±12
HPS-263	2.43	9.2±3.0	9.7±0.6	-1.7±0.2	0.10±0.06	$0.23^{+0.18}_{-0.12}$	49±16
HPS-266	2.20	13.8±1.9	-	-	-	-	-
HPS-269	2.57	6.2±1.6	3.6±0.5	-1.9±0.5	0.07±0.10	$0.57^{+0.98}_{-0.32}$	87±26
HPS-273	3.64	15.0±5.7	-	-	-	-	-
HPS-274	2.87	10.7±2.0	9.8±0.9	-1.3±0.2	0.19±0.06	$0.11^{+0.08}_{-0.05}$	62±12
HPS-283	3.30	19.3±2.8	14.4±1.6	-1.3±0.2	0.20±0.06	$0.14^{+0.11}_{-0.06}$	76±13
HPS-286	2.23	9.2±2.0	7.6±1.5	-2.1±0.5	0.03±0.11	$0.61^{+1.13}_{-0.21}$	59±18
HPS-287	3.32	4.7±2.1	2.4±0.9	-1.5±1.2	0.14±0.24	$0.33^{+2.88}_{-0.29}$	107±55
HPS-288	3.04	8.4±2.1	12.0±1.2	-1.8±0.3	0.10±0.06	$0.18^{+0.16}_{-0.09}$	36±9
HPS-292	2.87	19.6±2.6	6.3±0.8	-1.6±0.4	0.12±0.08	$0.63^{+0.75}_{-0.35}$	166±30
HPS-296	2.84	5.8±2.2	6.3±1.0	-1.6±0.4	0.13±0.10	$0.17^{+0.28}_{-0.12}$	49±19
HPS-306	2.44	14.8±2.9	11.8±0.8	-1.9±0.2	0.07±0.05	$0.43^{+0.29}_{-0.19}$	62±13
HPS-310	3.07	7.6±1.9	7.2±1.2	-1.5±0.4	0.15±0.09	$0.16^{+0.21}_{-0.10}$	58±16
HPS-313	2.10	6.7±3.0	24.9±0.8	-1.5±0.1	0.15±0.04	$0.04^{+0.03}_{-0.02}$	14±6
HPS-314	2.63	6.9±2.1	-	-	-	-	-
HPS-315	3.07	5.9±1.8	14.7±1.5	-1.5±0.3	0.14±0.07	$0.07^{+0.06}_{-0.04}$	21±6
HPS-316	2.81	13.1±3.4	13.2±1.1	-2.0±0.2	0.04±0.06	$0.44^{+0.36}_{-0.18}$	48±13
HPS-318	2.46	11.6±3.8	13.4±0.8	-1.3±0.1	0.18±0.05	$0.10^{+0.07}_{-0.05}$	49±16
HPS-327	2.25	4.7±1.9	-	-	-	-	-
HPS-338	2.60	15.2±4.0	1.7±0.9	-1.9±1.1	0.06±0.23	$3.30^{+25.40}_{-1.94}$	452±260
HPS-341	2.93	8.4±2.3	8.0±1.2	-2.2±0.5	0.01±0.10	$0.61^{+1.00}_{-0.20}$	50±15
HPS-360	2.92	11.5±3.0	7.1±2.0	-1.3±0.5	0.19±0.12	$0.18^{+0.37}_{-0.13}$	91±33
HPS-370	3.18	8.7±2.5	5.2±1.3	-2.0±0.6	0.04±0.12	$0.75^{+1.61}_{-0.34}$	81±28
HPS-372	2.76	5.5±1.4	1.4±1.3	-1.9±2.5	0.07±0.51	$1.32^{+165.25}_{-0.94}$	194±183
HPS-373	2.91	11.3±2.6	-	-	-	-	-
HPS-389	2.59	10.2±1.9	7.9±1.1	-1.5±0.3	0.14±0.08	$0.21^{+0.25}_{-0.12}$	70±16
HPS-391	2.96	17.4±4.1	8.4±2.0	-1.6±0.5	0.12±0.10	$0.44^{+0.72}_{-0.29}$	110±34
HPS-395	2.27	6.6±2.8	10.2±1.2	-1.9±0.3	0.07±0.07	$0.22^{+0.22}_{-0.14}$	32±14
HPS-402	2.97	11.2±1.6	5.1±1.2	-2.1±0.6	0.02±0.13	$1.20^{+2.78}_{-0.36}$	105±28
HPS-403	3.18	7.5±1.6	9.6±1.9	-1.9±0.4	0.08±0.10	$0.25^{+0.38}_{-0.14}$	39±10
HPS-415	3.37	10.5±2.5	6.1±1.2	-2.0±0.5	0.06±0.11	$0.65^{+1.19}_{-0.32}$	86±25
HPS-419	2.24	8.1±1.4	6.0±0.8	-1.7±0.4	0.12±0.08	$0.29^{+0.36}_{-0.17}$	71±15
HPS-420	2.93	12.1±2.5	5.5±1.7	-1.3±0.6	0.19±0.13	$0.22^{+0.52}_{-0.16}$	125±47
HPS-426	3.41	6.6±1.6	6.4±1.5	-1.3±0.5	0.18±0.10	$0.12^{+0.19}_{-0.08}$	58±18
HPS-428	3.34	13.0±2.3	22.0±2.3	-1.4±0.3	0.16±0.07	$0.08^{+0.08}_{-0.04}$	32±16
HPS-434	2.27	3.9±1.2	1.0±0.4	-2.5±1.6	0.00±0.32	$2.65^{+51.32}_{-1.36}$	180±139
HPS-436	2.42	2.7±1.0	4.1±0.7	-2.8±0.6	0.00±0.12	$0.42^{+0.94}_{-0.16}$	27±10

Table 2.1 (cont'd)

ID[a]	z	$L(Ly\alpha)$	$L_{\nu,1500\mathring{A}}$ [b]	β	$E(B-V)$	$f_{esc}(Ly\alpha)$	$EW_0(Ly\alpha)$
HPS-447	3.13	5.0±1.1	14.8±2.1	-1.6±0.3	0.13±0.08	$0.06^{+0.07}_{-0.04}$	17±4
HPS-462	2.21	27.4±2.9	8.3±0.8	-1.8±0.3	0.08±0.08	$0.98^{+1.10}_{-0.53}$	169±27
HPS-466	3.24	18.2±2.1	31.3±3.4	-1.5±0.2	0.15±0.06	$0.09^{+0.07}_{-0.04}$	32±4
HPS-467	2.80	5.0±1.8	-	-	-	-	-
HPS-474	2.28	4.3±2.4	3.9±0.4	-1.9±0.3	0.07±0.07	$0.36^{+0.39}_{-0.27}$	56±32

[a]ID corresponds to that in Table 3 of Adams et al. (2011b). Equatorial coordinates and line fluxes are provided there.

[b]Dashes indicate objects with no broad-band counterpart.

Table 2.2. Lyα luminosity function Best Fit Schechter Parameters, Luminosity and SFR Density

Sample	α[a]	ϕ^*	L*	$\rho_{Ly\alpha}$	$\rho_{SFR,Ly\alpha}$
		10^{-4}Mpc^{-3}	10^{43}erg s^{-1}	10^{39}erg s^{-1}Mpc^{-3}	10^{-3}M$_\odot$yr^{-1}Mpc^{-3}
$1.9 < z < 3.8$	-1.7	$2.2^{+3.9}_{-1.3}$	$1.20^{+1.02}_{-0.52}$	$5.1^{+2.5}_{-1.6}$	$4.6^{+2.2}_{-1.4}$
$1.9 < z < 3.8$	-1.5	$2.9^{+4.4}_{-1.7}$	$1.01^{+0.67}_{-0.41}$	$4.3^{+2.0}_{-1.3}$	$3.9^{+1.8}_{-1.2}$
$1.9 < z < 3.8$, $L(Ly\alpha) \leq 10^{43}$	-1.7	$6.7^{+30.6}_{-5.9}$	$0.60^{+2.99}_{-0.33}$	$6.8^{+7.6}_{-2.7}$	$6.2^{+6.9}_{-2.5}$
$1.9 < z < 2.8$	-1.7	$1.0^{+5.4}_{-0.9}$	$1.63^{+9.46}_{-1.08}$	$3.4^{+2.7}_{-1.4}$	$3.1^{+2.4}_{-1.3}$
$2.8 \leq z < 3.8$	-1.7	$2.6^{+28.3}_{-2.2}$	$1.11^{+2.40}_{-0.74}$	$5.5^{+12.0}_{-2.6}$	$5.0^{+10.9}_{-2.3}$

[a]Fixed parameter

Table 2.3. Lyα Escape Fraction History Best Fit Paramenters

Function	Data Points	$\log(f_{esc}(0))$	ξ	z_{tr}	θ	χ^2_{red}
Power Law	IGM corr + LF limit	-2.7 ± 0.2	2.4 ± 0.3	-	-	1.1
	No IGM corr	-2.7 ± 0.2	2.2 ± 0.3	-	-	1.0
	No LF limit	-2.4 ± 0.2	2.2 ± 0.3	-	-	1.2
Transition	IGM corr + LF limit	-2.1 ± 0.3	-	4.0 ± 0.5	0.4 ± 0.1	0.41
	No IGM corr	-2.2 ± 0.3	-	4.3 ± 0.6	0.4 ± 0.1	0.38
	No LF limit	-1.7 ± 0.2	-	4.1 ± 0.4	0.5 ± 0.2	0.39

Chapter 3

The Spatially Resolved Star Formation Law from Integral Field Spectroscopy: VIRUS-P Observations of NGC 5194

We investigate the relation between the star formation rate surface density (Σ_{SFR}) and the mass surface density of gas (Σ_{gas}) in NGC 5194 (a.k.a. M51a, Whirlpool Galaxy). VIRUS-P integral field spectroscopy of the central 4.1 $\times$ 4.1 kpc^2 of the galaxy is used to measure Hα, Hβ, [NII]$\lambda\lambda$6548,6584, and [SII]$\lambda\lambda$6717,6731 emission line fluxes for 735 regions $\sim$170 pc in diameter. We use the Balmer decrement to calculate nebular dust extinctions, and correct the observed fluxes in order to measure accurately Σ_{SFR} in each region. Archival HI 21cm and CO maps with similar spatial resolution to that of VIRUS-P are used to measure the atomic and molecular gas surface density for each region. We present a new method for fitting the Star Formation Law (SFL), which includes the intrinsic scatter in the relation as a free parameter, allows the inclusion of non-detections in both Σ_{gas} and Σ_{SFR}, and is free of the systematics involved in performing linear correlations over incomplete data in logarithmic space. After rejecting regions whose nebular spectrum is affected by the central AGN in NGC 5194, we use the [SII]/Hα ratio to separate spectroscopically the contribution from the diffuse ionized gas (DIG) in the galaxy,

which has a different temperature and ionization state from those of H II regions in the disk. The DIG only accounts for 11% of the total Hα luminosity integrated over the whole central region, but on local scales it can account for up to a 100% of the Hα emission, especially in the inter-arm regions. After removing the DIG contribution from the Hα fluxes, we measure a slope $N = 0.82 \pm 0.05$, and an intrinsic scatter $\epsilon = 0.43 \pm 0.02$ dex for the molecular gas SFL. We also measure a typical depletion timescale $\tau = \Sigma_{HI+H_2}/\Sigma_{SFR} \approx 2$ Gyr, in good agreement with recent measurements by Bigiel et al. (2008). The atomic gas density shows no correlation with the SFR, and the total gas SFL in the sampled density range closely follows the molecular gas SFL. Integral field spectroscopy allows a much cleaner measurement of Hα emission line fluxes than narrow-band imaging, since it is free of the systematics introduced by continuum subtraction, underlying photospheric absorption, and contamination by the [NII] doublet. We assess the validity of different corrections usually applied in narrow-band measurements to overcome these issues and find that while systematics are introduced by these corrections, they are only dominant in the low surface brightness regime. The disagreement with the previous measurement of a super-linear molecular SFL by Kennicutt et al. (2007) is most likely due to differences in the fitting method. Our results support the recent evidence for a low, and close to constant, star formation efficiency (SFE=τ^{-1}) in the molecular component of the ISM. The data shows an excellent agreement with the recently proposed model of the SFL by Krumholz et al. (2009b). The large intrinsic scatter observed may imply the existence

of other parameters, beyond the availability of gas, which are important at setting the SFR.

3.1 Introduction

In the quest to achieve a thorough understanding of the processes involved in the formation and subsequent evolution of galaxies, we must first fully characterize the process of star formation under different environments in the ISM. During the last decade, major efforts have been made to characterize the variables involved in triggering star formation and setting the star formation rate (SFR) in galaxies. Kennicutt (1998a) showed that, integrating over the whole optical disk of galaxies, the star formation rate surface density (Σ_{SFR}), as measured by the Hα emission, tightly correlates with the total gas surface density (Σ_{HI+H_2}) over several orders of magnitude in SFR and gas density. The relation from Kennicutt follows a power-law form, with a slope $N = 1.4$. These types of correlations between Σ_{SFR} and Σ_{gas}, either atomic (Σ_{HI}), molecular (Σ_{H_2}), or total (Σ_{HI+H_2}), are usually known as Star Formation Laws (SFL, a.k.a. Schmidt Laws or Schmidt-Kennicutt Laws, after Schmidt, 1959, who first introduced the power-law parametrization to relate gas density and the SFR), and they show that the availability of gas is a key variable in setting the SFR.

Although the global SFL provides us with valuable insights on the role that gas density plays at setting the SFR, the measurement involves averaging over the many orders of magnitude in Σ_{gas} and Σ_{SFR} present in the ISM of

single galaxies, implying the loss of valuable information about the detailed physics that give rise to the SFL. Azimuthally averaged measurements of gas surface densities and the SFR have been used to conduct more detailed studies of the SFL across the disks of local galaxies. For example, Wong & Blitz (2002) measured, under the assumption of constant dust extinction, a slope of $N \approx 0.8$ for the molecular SFL, and $N \approx 1.1$ for the total gas SFL on a sample of seven molecule rich spirals, with a large scatter from galaxy to galaxy, and Schuster et al. (2007) measured $N = 1.4 \pm 0.6$ for the total gas SFL on NGC 5194. Azimuthally averaged profiles are also affected by averaging effects since Σ_{SFR} and Σ_{gas} can change by more than 2 orders of magnitude at constant galactocentric radius due to the presence of spiral structure. We refer the reader to Bigiel et al. (2008) for a thorough compilation of previous measurements of the SFL in local galaxies.

More recently two studies have been aimed at measuring the "spatially resolved" SFL throughout the disks of nearby galaxies. Kennicutt et al. (2007) used a combination of narrow-band Hα and 24μm photometry to estimate Σ_{SFR}, as well as 21cm and CO J=1-0 maps to measure Σ_{gas} for 257 star-forming regions, 520 pc in diameter, in the disk of NGC 5194. They measured slopes of $N = 1.37 \pm 0.03$ and $N = 1.56 \pm 0.04$ for the molecular and total gas SFL respectively. Bigiel et al. (2008) used far-UV and 24μm images to create a Σ_{SFR} map, and 21cm, CO J=2-1, and CO J=1-0 data to create Σ_{gas} maps of seven spiral galaxies and eleven late-type/dwarf galaxies. After convolving the maps to a common resolution of 750 pc, they performed a pixel-to-pixel analy-

sis and measured a molecular SFL with an average $N = 1.0 \pm 0.2$ for the normal spirals ($N = 0.84$ for NGC 5194). Both studies found a lack of correlation between the SFR and the atomic gas density, which saturates around a value of 10 $M_{\odot}pc^{-2}$. This value is thought to be associated with a density threshold for the formation of molecular gas, and is consistent with predictions from theoretical modeling of giant atomic-molecular complexes (Krumholz et al., 2009a). The total gas SFL is then driven by the correlation between the molecular gas density and the SFR, and the molecular fraction in the ISM. At the highest densities present in normal spiral galaxies ($\Sigma_{HI+H_2} = 50 - 1000$ $M_{\odot}pc^{-2}$) the ISM is mostly molecular and the total gas SFL closely follows the H_2 SFL. At densities lower than $10M_{\odot}pc^{-2}$ the total gas SFL gets much steeper due to a strong decrease of the molecular fraction. This behavior has been recently modeled by Krumholz et al. (2009b).

While spatially resolved studies of the SFL obtain consistent results on the behavior of the atomic gas, they disagree when it comes down to the molecular component. The Bigiel et al. (2008) measurement of a linear molecular SFL is consistent with a scenario in which star formation occurs at a constant efficiency inside GMCs, whose properties are fairly uniform across normal spiral galaxies (Blitz et al., 2007; Bolatto et al., 2008). This homogeneity in the properties of GMCs is expected if they are internally regulated by processes like stellar feed-back, and they are decoupled from their surroundings due to the fact of being strongly overpressured (Krumholz et al., 2009b). Kennicutt et al. (2007), on the other hand, measured a super-linear molecular SFL in

NGC 5194, which suggests an increasing SFE towards higher gas densities. Although the authors state that a super-linear slope ($N > 1$) is still consistent with a constant "efficiency" if the star-forming lifetimes of massive clouds were systematically lower than those of low-mass clouds, this is true only if the efficiency is defined as the ratio of the produced stellar mass over the available molecular gas mass, which is the classical definition used by galactic studies in the Milky Way. In this work, as well as in Bigiel et al. (2008), the efficiency is defined as SFE= $\Sigma_{SFR}/\Sigma_{gas}$, or the inverse of the depletion time, so shorter star formation timescales imply a higher SFE, and a super-linear SFL always translate in higher SFE at higher gas densities.

With the goal of investigating this issue, we have conducted the first measurement of the spatially resolved SFL using integral field spectroscopy. We mapped the Hα emission in the central 4.1×4.1 kpc^2 of the nearby face-on spiral galaxy NGC 5194 using the Visible Integral field Replicable Unit Spectrograph Prototype (VIRUS-P, Hill et al., 2008a). Hydrogen recombination lines are known to be good tracers of the SFR. Their intensity scales linearly with the ionizing UV flux in galaxies, which is dominated by the emission from massive stars (≥ 10 M$_\odot$) with typical lifetimes of < 20 Myr, hence they provide an almost instantaneous measurement of the SFR Kennicutt (1998b, and references therein).

Due to the small field of view of current integral field units (IFUs), typically less than 1 arcmin^2, 2D spectroscopic Hα mapping of nearby galaxies with large angular sizes has not been conducted efficiently in the past.

Instead, narrow-band imaging has been typically used to construct Hα based SFR maps. Hα narrow-band imaging suffers from contamination from the [NII]$\lambda\lambda$6548,6584 doublet, and is sensitive to systematic errors in continuum subtraction and the estimation of the strength of the Hα absorption in the underlying stellar spectrum. Spectroscopic measurements are free of all these sources of error, and hence provide a much cleaner measurement of Hα fluxes. A major part of this paper is dedicated to investigate these systematics in order to assess the validity of the typical corrections applied to narrow-band Hα images.

VIRUS-P is the largest field of view IFU in the world and it allows for efficient Hα mapping of nearby galaxies. The observations presented here were taken as part of the VIRUS-P Exploration of Nearby Galaxies (VENGA[1], Blanc et al. in preparation). VENGA is a large scale extragalactic IFU survey that will spectroscopically map large parts of the disks of $\sim$ 20 nearby spirals, to allow a number of studies on star-formation, structure assembly, stellar populations, gas and stellar dynamics, chemical evolution, ISM structure, and galactic feedback.

The VIRUS-P spectral map was used in combination with CO J=1-0 and HI 21cm intensity maps of NGC 5194 from the BIMA Survey of Nearby Galaxies, SONG (Helfer et al., 2003), and The HI Nearby Galaxy Survey, THINGS (Walter et al., 2008), to measure Σ_{SFR}, Σ_{H_2}, and Σ_{HI} in order to

[1]http://www.as.utexas.edu/~gblancm/venga.html

construct the spatially resolved SFL. In §2 and §3 we present the VIRUS-P observations and the data reduction and calibration methods. In §4 we describe the CO and 21cm data used to measure the molecular and atomic gas surface densities, as well as a HST NICMOS Paα image used to validate our dust extinction measurements. §5 presents the methods used to remove the stellar continuum and measure accurate nebular emission line fluxes, together with our dust extinction correction. The calculation of Σ_{gas} is described in §6. The rejection of regions whose nebular emission is affected by the central AGN in NGC 5194 is presented in §7. The correction to account for the contribution of the DIG to the Hα fluxes is described in §8. The resulting spatially resolved SFLs for the molecular, atomic and total gas are presented in §9, followed by a discussion on the implications of our results for narrow-band imaging surveys in §10. Finally we compare our results with previous measurements and theoretical predictions of the SFL in §11, and present our conclusions in §12.

Throughout this paper we assume a distance to NGC 5194 of 8.2 Mpc for consistency with Kennicutt et al. (2007). While Bigiel et al. (2008) used a slightly smaller distance of 8.0 Mpc, it is worth noticing that most of the results in this paper are based on surface densities, which are independent of distance, and thus are not affected by the assumed value. All values for Σ_{SFR} are in units of $M_{\odot}yr^{-1}kpc^{-2}$, and values of Σ_{gas} are in units of $M_{\odot}pc^{-2}$.

3.2 Observations

We obtained spatially resolved spectroscopy over the central 4.1×4.1 kpc^2 region of NGC 5194 on the night of April 4, 2008, using VIRUS-P on the 2.7m Harlan J. Smith telescope at McDonald Observatory. VIRUS-P with the VP-2 IFU bundle used in this work consists of a square array of 246 optical fibers which samples a $1.7' \times 1.7'$ field of view with a 1/3 filling factor. The fibers are 200μm in diameter, corresponding to 4.3″ on sky. The spectrograph images the spectrum of the 246 fibers on a 2048×2048 Fairchild Imaging CCD. Because of camera alignment issues, the spectrum of one fiber fell off the chip, reducing the number of usable fibers to 245.

The spectrograph was used in a red setup under which it samples a wavelength range of 4570-6820Å with a spectral resolution of ∼5.0Å (FWHM). This red setup allows us to sample both Hβ and Hα, and our resolution is high enough to resolve the Hα-[NII]$\lambda\lambda$6548,6893 complex. We took the data in 2x1 binning mode in the spectral direction which translates into a plate scale of 2.2 Åpixel^{-1}. Given the 1/3 filling factor of the IFU, three dithered exposures were necessary to sample the complete field of view.

We obtained four 20 minute exposures at each of the 3 dither positions, accounting for an effective exposure time of 80 minutes. Dither 1 was centered at α=13:29:52.69; δ=+47:11:43.0. Dithers 2 and 3 were offset from dither 1 by $\Delta\alpha = -3.6''$; $\Delta\delta = -2.0''$ and $\Delta\alpha = 0.0''$; $\Delta\delta = -4.0''$ respectively. Figure 3.1 shows the observed region in NGC 5194 as well as the position of the IFU fibers for the 3 dithers. Because of the extended nature of NGC 5194 no fibers

in the field of view sampled a blank region of the sky. This implied the need for off-source sky frames in between science frames. We obtained 5 minute sky exposures bracketing all science exposures. These were obtained 30′ North of NGC 5194. The typical seeing during the observations was 2.0".

Bias frames, comparison NeCd lamps, and twilight flats were taken at the beginning and end of the night. VIRUS-P is mounted on a two-degree of freedom gimble at the broken cassegrain focus of the telescope. The gimble keeps the spectrograph in a fixed gravity vector independent of the position of the telescope during the observations which translates into a practically complete lack of flexure in the spectrograph optical components. For this reason calibration frames intercalated with the science observations were not necessary.

The spectro-photometric standard Feige 34 was observed for the purpose of flux calibration (see §3.1). Standard observations were performed using a finer 6 position dither pattern which better samples the PSF of the star and ensures the collection of its total flux (see §3.1 and Figure 3.2).

The instrument is equipped with a guiding camera which images a $4.5' \times 4.5'$ field offset from the science field sampled by the IFU. The guiding camera is a 512×512 pixel Apogee unit equipped with a BV filter which allows broad-band photometric measurements of the stars in the field. During the night we saved a guider frame every 30 seconds in order to reconstruct changes in atmospheric transparency. The guider images are also used to establish the IFU astrometry. The relative offset, rotation and plate scales of the guider and

IFU fields have been precisely calibrated using observations of crowded fields in open clusters, so the pixel coordinates of stars in the guider frames provide us with coordinates for the center of all fibers in the IFU with an astrometric rms of $\sim 0.5''$.

In this way we obtained spectra for 735 regions $4.3''$ in diameter ($\sim$170 pc at the distance of NGC 5194), in the central region of the galaxy. The spectra reaches a median 5σ sensitivity in continuum flux density of 2.5×10^{-17} erg s^{-1}cm^{-2}Å^{-1}, which translates into a median signal-to-noise (S/N) ratio per resolution element of 95 (53 for the faintest fiber).

3.3 Data Reduction

Data reduction is performed using our custom pipeline VACCINE (Adams et al. in preparation). Individual frames are overscan and bias subtracted, and bad pixels are masked. We use the twilight flats to trace the peak of the spatial profile of the spectrum of all fibers on the chip, and extract the 2D spectrum of each fiber on the science frames, comparison lamp frames, and flats using a seven pixel aperture around the peak.

The extracted comparison lamp spectra are used to compute an independent wavelength solution for each fiber. We use 4th order polynomials to compute the wavelength solutions which show a typical rms of 0.2 Å ($\sim$0.1 pixel).

We correct the twilight flats for solar absorption lines and use them

to measure the shape and amplitude of the spatial profile of the fibers as a function of wavelength. This profile is given by the point spread function (PSF) of the fibers on chip in the spatial direction, and the relative instrumental throughput of each fiber as a function of wavelength. Dividing the twilight flats by this profile yields a pixel-to-pixel flat. We divide all science, sky, and spectro-photometric standard frames by both the fiber profile and the pixel-to-pixel flats. This removes any fiber-to-fiber and pixel-to-pixel variations in sensitivity.

A background frame is created for each science exposure by averaging the two bracketing 5 minute sky frames and scaling by the difference in exposure time. We estimate the sky spectrum for each fiber by fitting a non-uniform spline to the spectra of the 60 neighboring fibers on chip in the background frame. This spectrum is subtracted from each fiber in the science data.

In order to test the quality of our background subtraction algorithm we construct background frames for each of our sky exposures using the two closest of the other sky exposures. We then follow the same procedure to background subtract our sky frames. We observe residuals centered around zero in the background subtracted sky frames that are less than 1% of the galaxy continuum flux in the faintest fibers in our science data. The only exception are the regions of the spectra at the wavelength of the 4 brightest sky emission lines in our wavelength range in which the residuals can be considerably larger due to the fast time variability of these spectral features. These regions showing poor background subtraction are masked in our science data. At this

stage we combine individual exposures using a biweight (Beers et al., 1990).

Error maps including Poisson photon count uncertainties and read-noise are created for every fiber on each frame. We use these error maps together with the fiber profile to calculate the weights used for collapsing the 2D spectrum into a 1D spectrum. The flux in photo-electrons at each wavelength after collapsing is given by

$$f_\lambda = \frac{\sum_{i=1}^{7} \left(\frac{p_i}{e_i}\right)^2 G f_{\lambda,i}}{\sum_{i=1}^{7} \left(\frac{p_i}{e_i}\right)^2} \tag{3.1}$$

where p_i is the value of the fiber profile, G is the gain, f_i is the flux in ADUs in the combined background subtracted spectrum, and e_i is the corresponding error at each pixel as measured in the error map. This is equivalent to weighting the pixels by $(\mathrm{S/N})^2$. The sum is performed at every wavelength (column) over the the 7 pixel aperture used for extraction. The final product is a wavelength calibrated 1D spectrum of the area sampled by each of the 245 fibers on each of the 3 dither positions on the galaxy.

3.3.1 Flux Calibration

Flux calibration of IFU data can be challenging but, if proper care is taken, very accurate spectro-photometry can be achieved. This is mostly because of the lack of a wavelength dependent slit loss function. Atmospheric dispersion can change the position of a standard star in the field of view as a function of wavelength, but as long as the field is completely sampled by the

fibers the total flux of the star at all wavelengths is always collected. Also, photometry of stars in the guider images taken during the observations allows us to measure and correct for changes in atmospheric transparency during the night.

During the observation of standard stars, fibers in the IFU only sample a region of the star's PSF. Determining the fraction of the total flux collected by each fiber is essential in order to compute a proper instrumental sensitivity function by comparing each fiber spectrum to the total intrinsic spectrum of the star. This requires knowledge of the shape of the PSF as well as the distance from the PSF centroid to the center of each fiber.

The spectro-photometric standard star Feige 34 was observed using a 6 position dither pattern shown in the left panel of Figure 3.2. This tight pattern provides a better sampling of the PSF and ensures we collect the total flux of the star. We calculate the position of the centroid of the PSF relative to the fibers by taking the weighted average of the fibers positions in the field of view, using the measured flux in each of them as weights. This corresponds to the first moment of the observed light distribution.

The filled circles in the right panel of Figure 3.2 show the flux measured in each fiber as a function of its radial distance to the PSF center. This information can be used to reconstruct the shape of the star PSF at the moment of the observations. In order to do this, we assume a Moffat profile for the PSF and reconstruct its observed light distribution by summing the flux in 4.3" diameter circular apertures at the corresponding radial distance of each

fiber. The best-fitted PSF and its fiber sampled light distribution are shown by the solid and dashed curves in the right panel of Figure 3.2. It can be seen that the best-fitted model PSF, after being sampled by the fibers in our dither pattern, matches the measured flux remarkably. This PSF model allows us to know what fraction of the star total flux was measured by each fiber during the observations.

We normalize the spectrum of each fiber by the fraction of the total flux it sampled, and average this value for all fibers having a significant ($> 5\sigma$) flux measurement in order to obtain the star total instrumental spectrum. We correct the total spectrum by atmospheric extinction and use the Feige 34 measurement of Oke (1990) to construct our instrumental sensitivity function.

Relative variations in atmospheric transparency during the night are measured by performing aperture photometry on stars in the guider images. Observing conditions were confirmed to be very stable, with maximum variations in transparency of less than a 10%. All spectra in our science frames are corrected by this variations, atmospheric extinction, and flux calibrated using the instrumental sensitivity function.

It is important to notice that any difference in illumination or throughput between fibers was taken out during the flat-fielding process, so a common sensitivity function applies to all fibers. Our final product is a wavelength and flux calibrated spectrum for the 735 regions.

In order to estimate the systematic uncertainty in our flux calibration

we have compared sensitivity functions computed using different standard star observations taken as part of different observing programs with VIRUS-P. Comparison of 10 standards taken between September 2007 and June 2008 under different observing conditions show that after correcting for relative changes in atmospheric transparency (using photometry of stars in the guider images) the computed sensitivity functions show an rms scatter of less than 5%.

3.4 Other Data

3.4.1 THINGS HI Data

We use a combined 21 cm line intensity map of NGC 5194 from the Very Large Array (VLA) taken as part of The HI Nearby Galaxy Survey (THINGS[2]; Walter et al., 2008) to estimate the atomic gas surface density (Σ_{HI}). HI data for NGC 5194 was taken using the B, C, and D arrays during 2004 and 2005, with a combined on source integration time of $\sim$10 hours. The final co-added (B+C+D array) integrated intensity map has a robustly weighted beam size of $5.82'' \times 5.56''$, which is well matched to the $4.3''$ VIRUS-P fiber diameter convolved with the $2''$ seeing. The 1σ noise per 5.2 km s^{-1} channel is 0.44 mJy beam^{-1} corresponding to a atomic gas surface density of Σ_{HI}= 0.59 M$_\odot$ pc^{-2}. For more details on data products and data reduction see Walter et al. (2008).

[2]http://www.mpia.de/THINGS/Data.html

3.4.2 BIMA SONG CO Data

Molecular gas surface densities are measured using the CO J=1-0 intensity map of NGC 5194 from the Berkeley Illinois Maryland Array (BIMA) Survey of Nearby Galaxies (BIMA SONG[3]; Helfer et al., 2003). Zero spacing single dish data from the NRAO 12 m telescope was combined with the interferometric BIMA C and D array data, resulting in a map with a robust beam size of $5.8'' \times 5.1''$, well matched to the 21 cm map and the VIRUS-P spatial resolution. The corresponding 1σ noise is 61 mJy beam^{-1} in a 10 km s^{-1} channel or $\Sigma_{H_2} = 13$ M$_\odot$ pc^{-2}. For more details on the observations and the data reduction refer to Helfer et al. (2003).

3.4.3 HST NICMOS Paschen-α Data

The center of NGC 5194 was imaged in Paα by Scoville et al. (2001) using HST+NICMOS. A 3×3 mosaic covering the central $186'' \times 188''$ of the galaxy was imaged using the F187N and F190N narrow-band filters, sampling the Paα line and the neighboring stellar continuum respectively. In this work we use this continuum subtracted Paα image to measure emission line fluxes to check the validity of our dust extinction correction. The data reduction, mosaicking, flux calibration and continuum subtraction are described in Scoville et al. (2001) and Calzetti et al. (2005). The Paα image overlaps completely with the VIRUS-P pointing shown in Figure 3.1.

[3]http://nedwww.ipac.caltech.edu/level5/March02/SONG/SONG.html

3.5 Measurement of Emission Line Fluxes

We estimate the current Σ_{SFR} for each region by means of the Hα nebular emission luminosity. In this section we describe the methods used to separate the emission lines coming from ionized gas from the underlying stellar spectrum, measure emission line fluxes, and estimate the dust extinction in each region using the Hα/Hβ ratio.

3.5.1 Photospheric Absorption Lines and Continuum Subtraction

In galaxy spectra, both the Hα and Hβ emission lines sit on top of strong Balmer absorption lines characteristic of the photospheric stellar spectrum of young stars. Removing the contribution from these absorption lines is essential in order to estimate properly the emission line flux.

We use a linear combination of stellar template spectra to fit the absorption line spectrum of each region. The templates are high S/N, high resolution, continuum normalized spectra of a set of 18 stars from the Indo-U.S. Library of Coudé Feed Stellar Spectra (Valdes et al., 2004). Stars were chosen to span a wide range in spectral types and metallicities (A7 to K0, and [Fe/H] from -1.9 to 1.6).

The resolution of the templates is degraded to match the VIRUS-P 5.0Å spectral resolution. For each of the 735 regions, we mask the parts of the galaxy spectrum affected by emission lines and sky subtraction residuals from bright sky lines. The continuum at each wavelength is estimated using an iterative running median filter, and used to normalized the observed spectrum.

We use this masked, continuum normalized spectrum to fit the best linear combination of stellar templates for each region. Figure 3.3 shows the best-fitted template combinations in regions centered in Hβ, Mg b, and Hα for 3 regions in the galaxy. The bottom, middle and upper panels correspond to fibers with the lowest, median and highest S/N in their spectra respectively. For all 735 regions we obtain excellent fits to the underlying stellar spectrum. Figure 3.3 shows the importance of taking into account the effect of photospheric Balmer absorption lines when measuring Hα and Hβ fluxes. Ignoring the presence of the absorption features can introduce serious underestimations of the emission line fluxes. For Hα this effect can account for underestimations of up to 100% as will be shown in §10.

The best-fitted linear combination of stellar templates is scaled by the galaxy continuum and subtracted from the original spectrum in order to produce pure nebular emission line spectra for all fibers. Figure 3.4 shows the nebular spectrum of the same regions shown in Figure 3.3. After subtracting the stellar light, we are able to identify most well known emission features in galaxy spectra. Hβ, [OIII]$\lambda\lambda$4959,5007, [NII]$\lambda\lambda$,6548,6584, Hα and [SII]$\lambda\lambda$,6717,6731 are clearly seen in the spectra of all 735 regions. Visual inspection of Figure 3.4 shows that the [NII]$\lambda\lambda$,6548,6584/Hα ratio can change drastically from region to region. This effect can introduce systematic biases in narrow-band measured Hα fluxes if the ratio is assumed to be constant across the disk (Calzetti et al., 2005; Kennicutt et al., 2007). This issue will be discussed in detail in §10.

3.5.2 Emission Line Fluxes

We measure emission line fluxes by independently fitting Hβ, the Hα-[NII]$\lambda\lambda$,6548,6584 complex, and the [SII]$\lambda\lambda$,6717,6731 doublet. Although the lines in the Hα-[NII] complex are clearly resolved in our spectra, their wings show some level of overlap so we used a 3 Gaussian component model to fit these lines. Similarly a 2 Gaussian component model was used to fit the [SII] doublet. Hβ was fitted using a single Gaussian. These fits provide the total flux and its uncertainty of all the above lines for the 735 regions. All lines are detected with a significance higher than 3σ in all fibers. We measure a median and lowest S/N over all fibers of 109 and 15 for Hα, 29 and 4 for Hβ, 49 and 13 for [NII]λ6584, and 32 and 5 for [SII]λ6717. Emmision line fluxes of all lines for all fibers are given in Table 1, which is available in its entirety in the electronic edition of this paper.

3.5.3 Extinction Correction from the Balmer Decrement

The observed spectra is affected by differential extinction due to the presence of dust in the ISM of both NGC 5194 and the Milky Way. Before attempting to estimate SFRs from Hα fluxes, these have to be corrected for dust extinction. Failing to do so can introduce underestimations in the SFR of up to factors of $\sim$10 in the regions we are studying. The Balmer line ratio Hα/Hβ, as will be shown bellow, provides a good estimate of the dust extinction at the wavelength of the Hα line.

Assuming an intrinsic Hα/Hβ ratio of 2.87 (Osterbrock & Ferland,

2006), the observed ratio provides the extinction at the wavelength of Hα through the following equation,

$$A_{H\alpha} = -2.5 \log \left[\frac{[H\alpha/H\beta]_{obs}}{2.87} \right] \left(\frac{1}{1 - k(H\beta)/k(H\alpha)} \right) \tag{3.2}$$

where $[H\alpha/H\beta]_{obs}$ is the observed line ratio and $k(\lambda)$ is the extinction law. We assume a foreground MW extinction law as parameterized by Pei (1992). SMC and LMC laws were also tested (also using the Pei, 1992, parametrization), and no significant change was observed in the deduced extinction values (these 3 extinction laws are practically identical at these wavelengths). To correct for Galactic extinction towards NGC 5194 we use a value of $A_B = 0.152$, taken from Schlegel et al. (1998).

In order to test the reliability of our Balmer decrement extinction values, we compare our corrected Hα fluxes to corrected Paα fluxes. The hydrogen recombination Paα line at 1.87μm, although one order of magnitude fainter than Hα, is very weakly absorbed by dust, and hence provides an unbiased estimate of the intrinsic SFR even in highly extincted regions (Scoville et al., 2001). Most recent studies of spatially resolved star formation in nearby disk galaxies use recipes to account for dust obscured star formation which are ultimately linked to a calibration based on Paα (Calzetti et al., 2005; Kennicutt et al., 2007; Bigiel et al., 2008; Leroy et al., 2008). In particular, Calzetti et al. (2005) finds a tight linear correlation between the 24μm luminosity of star forming regions in NGC 5194 and their Pα luminosities, providing justification for the use of linear combinations of 24μm fluxes with either Hα or UV

fluxes to estimate the intrinsic SFR in the other mentioned works. In our case, if the extinction corrected Hα fluxes linearly correlate with the corrected Paα fluxes, following the intrinsic line ratio expected from recombination theory, then we can confirm that our extinction values have been properly estimated. In that case we can do without the IR data, and apply an extinction correction to the measured Hα fluxes which is solely based in the optical spectra.

We measure Pα fluxes for all 735 regions in the NICMOS F187N continuum subtracted narrow-band image (see §4.1), using apertures matching the size of the VIRUS-P fibers. Figure 3.5 shows extinction corrected Paα versus Hα fluxes for all regions showing 5σ detections of Paα emission in the NICMOS narrow-band image. Both lines have been corrected using the Balmer decrement derived extinction, and a MW extinction law. The solid line in Figure 3.5 shows the theoretical Hα/Paα=8.15 ratio taken from Osterbrock & Ferland (2006). The observed line ratios are in agreement with the theoretical value, and the scatter can be attributed mostly to measurement errors. This confirms that Hα fluxes, once corrected for dust obscuration using the Balmer decrement derived extinction, can provide an unbiased measure of the intrinsic SFR in the disks of normal face-on spirals.

3.6 Measurement of Gas Mass Surface Densities

In order to measure the atomic and molecular gas surface density at the position of each of the 735 regions under study, we measure integrated intensities in the THINGS 21 cm and the BIMA SONGS CO J=1-0 maps,

and translate them into gas surface densities using the calibrations presented below. The intensities are measured over an area equal to the beam size of each map. At each of the 735 fiber positions we perform aperture photometry on the 21 cm and CO maps, and measure the integrated gas intensity in apertures of effective radius $r_{\rm eff}=\sqrt{ab}/2$, where a and b are the major and minor axis of the beam of each map. This translates in an effective apperture diameter of $5.7''$ and $5.4''$ for the 21 cm and CO maps respectively, which is well matched to the VIRUS-P spatial resolution which is set by the convolution of a $4.3''$ diameter fiber and a $2''$ FWHM seeing disk.

To convert the 21 cm intensities in atomic hydrogen column densities we use the following relation adapted from Walter et al. (2008),

$$N_{HI} = 1.823 \times 10^{18} \left(\frac{T_B}{\rm K\ km\ s^{-1}\ sr} \right) {\rm cm}^{-2} \tag{3.3}$$

where T_B is the velocity integrated surface brightness temperature in the 21 cm map. To convert the CO J=1-0 intensities to H_2 column densities we use the CO to H_2 conversion factor X_{CO} from Bloemen et al. (1986) so,

$$N_{H_2} = 2.8 \times 10^{20} \left(\frac{T_b}{\rm K\ km\ s^{-1}\ sr} \right) {\rm cm}^{-2} \tag{3.4}$$

where T_B is the velocity integrated surface brightness temperature in the CO J=1-0 map. The X_{CO} factor used here was chosen for consistency with Kennicutt et al. (2007), and differs from the $X_{CO} = 2.0 \times 10^{20} (Kkms^{-1})^{-1}$ factor used by Bigiel et al. (2008). Current uncertainties in X_{CO} are of the

order of a factor of 2, and the true value depends on assumptions about the dynamical state of GMCs (Blitz et al., 2007). In any case, using a different X_{CO} can only introduce an offset in the normalization of the SFL and should not change its observed shape.

Finally, the atomic and molecular gas surface densities are derived from the column densities using the following relations,

$$\Sigma_{HI} = m_H N_{HI} \cos i \tag{3.5}$$

$$\Sigma_{H_2} = 2 m_H N_{H_2} \cos i \tag{3.6}$$

where m_H is the hydrogen atom mass and $i = 20°$ is the inclination of NGC 5194 as measured by Tully (1974). These correspond to hydrogen gas surface densities, and should be multiplied by a factor $\sim$1.36 to account for the mass contribution of helium and heavier elements. The measured atomic and molecular gas surface densities for all regions are given in Table 1.

3.7 Photoionization and shock-heating by the central AGN

The center of NGC 5194 hosts a weak active nucleus. The emission-line ratios in the narrow-line region around the AGN are consistent with those of typical Seyfert nuclei (Bradley et al., 2004, and references therein). X-ray *Chandra* observations show the nucleus and two extended emission components

extending $\sim 15''$ North and $\sim 7''$ South of it (Terashima & Wilson, 2001). Bipolar extended radio emission spatially coincident with the X-ray emission, as well as weak jet with a position angle of 158° connecting the nucleus with the southern radio lobe was observed by Crane & van der Hulst (1992) and further confirmed by Bradley et al. (2004). All the observations are consistent with the gas in the inner nuclear region ($r < 1''$) being dominantly photoionized by the central AGN, and the outer parts showing extended emission, arising from shock-heating by a bipolar outflow.

For the purpose of constructing the SFL, we want to exclude regions whose main source of ionization is not UV flux coming from massive star-formation. Regions in which the gas is photoionized by the AGN or shock-heated by the jet will emit in Hα and mimic star-formation.

In order to identify these regions we use emission-line ratio diagnostics commonly used to distinguish normal from active galaxies (Veilleux & Osterbrock, 1987; Kewley et al., 2001). Figure 3.6 shows the extinction corrected [NII]λ6584/Hα versus [OIII]λ5007/Hβ line ratios for all the regions. The solid and dotted lines mark the theoretical threshold separating AGNs from star-forming galaxies proposed by Kewley et al. (2001) and the ± 0.1 dex uncertainty in their modeling. To avoid the rejection of regions unaffected by AGN contamination which scatter above the threshold, we impose a double criteria. We flag as "AGN affected", all the region lying above the threshold, and at an angular distance of less than $15''$ (600 pc) from the nucleus of the galaxy. Filled triangles in Figure 3.6 correspond to the 17 regions complying

with both criteria. Open diamonds correspond then to the 718 regions unaffected by AGN contamination we will use to construct the SFL. Notice that none of these regions lie above the +0.1 dex model uncertainty dotted line, and that the ones lying above the threshold seem to follow the same sequence traced by the regions unaffected by AGN contamination below it. These fibers showing high line ratios but not associated with the central AGN fall in the inter-arm regions of the galaxy, and have a spectrum that is dominated by the DIG (§8).

Figure 3.7 shows a map of the [NII]λ6584/Hα line ratio. Regions flagged as "AGN affected" are marked with black crosses. It can be seen that they have high emission-line ratios typical of AGN, and that they fall in a region which is spatially coincident with the extended radio and X-ray emission observed around the nuclei. The "AGN affected" region is elongated in a similar direction to the measured PA=158° of the radio jet (Crane & van der Hulst, 1992; Bradley et al., 2004; Terashima & Wilson, 2001). Figure 3.7 clearly shows the enhanced line ratio in the inter-arm regions of NGC 5194. These high ratios originate in the DIG of the galaxy and are discussed in the following Section.

3.8 Contribution from the Diffuse Ionized Gas and Calculation of SFR Surface Densities

If we were to calculate Σ_{SFR} using the extinction corrected Hα flux observed on each region, we would be working under the assumption that all the emission observed in a given line of sight towards the galaxy has an

origin associated with ionizing flux coming from localized star-formation in the same region. This is not necessarily true in the presence of a diffuse ionized component in the ISM of the galaxy. The role of the diffuse ionized gas (DIG, a.k.a. warm ionized medium, WIM) as an important component of the ISM of star-forming disk galaxies in the local universe has been properly established during the last two decades (e.g. see reviews by Mathis 2000 and Haffner et al. 2009). The existence of a significant component of extra-planar ionized hydrogen in a galaxy requires that a fraction of the ionizing Lyman continuum photons generated in star forming regions in the disk escapes and travels large distances of the order of kiloparsecs before ionizing neutral hydrogen at large heights above the disk. These distances are one order of magnitude larger than the Strömgren radii associated with the most massive O stars, and the ionizing flux is thought to escape through super-bubbles in a complex hydrogen density and ionization distribution created by supernovae, stellar winds, and large scale ionization by OB associations (e.g. Dove et al. 2000).

Under these conditions a hydrogen atom emitting an Hα photon observed to come in the direction of a certain region of the galaxy is not necessarily required to have been ionized by locally produced UV photons in the same region. Hence the Hα flux measured in each region is the sum of the flux coming from locally star-forming H II regions in the disk, and a contribution from the DIG. In order to properly estimate Σ_{SFR} and the spatially resolved SFL we need to separate and subtract the DIG contribution from the observed Hα fluxes.

Low-ionization line ratios like [NII]λ6584/Hα and [SII]λ6717/Hα (hereafter [SII]/Hα) are observed to be greatly enhanced in the DIG, as compared to the typical values observed in H II regions (Reynolds, 1985; Hoopes & Walterbos, 2003). Recent results from The Wisconsin Hα Mapper (WHAM[4]) sky survey by Madsen et al. (2006) show that H II regions in the Milky Way have a typical $([SII]/H\alpha)_{HII}$=0.11 with a small rms scatter from region to region of only $\Delta([SII]/H\alpha)_{HII}$=0.03. On the other hand, high galactic latitude pointings sampling the DIG component show a mean $([SII]/H\alpha)_{DIG}$=0.34, with a large scatter from pointing to pointing of $\Delta([SII]/H\alpha)_{DIG}$=0.13. Figure 3.8 shows a histogram of the [SII]/Hα line ratios taken from Madsen et al. (2006) for H II regions and the DIG as measured by WHAM. It can be seen that the [SII]/Hα ratio provides a very useful tool to separate the contribution from the DIG and the disk H II regions in our spectra. The [NII]/Hα ratio, while still enhanced in the DIG as can be clearly seen in Figure 3.7, shows a much larger scatter both for H II regions and pointings towards the DIG, and does not provide such a clean separation as the [SII]/Hα ratio (see Figure 21 in Madsen et al. (2006)).

We model the measured Hα flux of each region as the sum of a contribution from H II regions plus a contribution from the DIG, so

$$\begin{aligned} f(H\alpha) &= f(H\alpha)_{HII} + f(H\alpha)_{DIG} \\ &= C_{HII} f(H\alpha) + C_{DIG} f(H\alpha) \end{aligned} \tag{3.7}$$

[4]http://www.astro.wisc.edu/wham/

where C_{HII} is the fraction of the total flux coming from local star-forming regions in the disk, and C_{DIG}=(1-C_{HII}). The observed [SII]/Hα ratio is then given by,

$$\frac{[SII]}{H\alpha} = Z' \left[C_{HII} \left(\frac{[SII]}{H\alpha} \right)_{HII} + C_{DIG} \left(\frac{[SII]}{H\alpha} \right)_{DIG} \right] \tag{3.8}$$

where $Z' = Z/Z_{MW}$ is the metallicity of NGC 5194 normalized to the Milky Way value. Figure 3.9 shows the observed [SII]/Hα ratio as a function of extinction corrected Hα flux. The left axis shows C_{HII} calculated assuming a value of $Z' = 1.0/1.5$. Bresolin et al. (2004) measured the oxygen and sulfur abundance gradient in NGC 5194 using multi-object spectroscopy of 10 H II regions spanning a large range in radii. Integrating his best-fitted oxygen abundance gradient out to a radius of 4.1 kpc provides an mean 12+log(O/H)=8.68, which is 1.55 times lower than the solar oxygen abundance measured by Grevesse et al. (1996). Although a large scatter is observed in the literature for both the solar oxygen abundance and the oxygen abundance in Milky Way H II regions (Grevesse et al., 1996; Allende Prieto et al., 2001; Shaver et al., 1983; Deharveng et al., 2000), it can be seen in Figure 3.9 that using a factor of 1.5 implies that the brightest Hα emitting regions in NGC 5194 are completely dominated by emission from H II regions in the disk, having $C_{HII} \sim 1$ with a scatter that is consistent with the intrinsic scatter of 0.03 measured in the Milky Way by Madsen et al. (2006). These brightest regions trace the spiral structure of the galaxy and are expected to

be H II region dominated since on high star-formation regions the disk should outshine the DIG by many orders of magnitude.

There is a clear correlation between C_{HII} and the Hα flux. The observed trend is consistent with the DIG dominating the spectrum of fainter Hα regions, and the H II regions in the disk outshining the DIG in the brightest ones. The scatter is large mostly because of intrinsic scatter in the line ratio (see Figure 3.8). In order to compute a robust DIG correction, we fit the C_{HII} values using the simple functional form,

$$C_{HII} = 1.0 - \frac{f_0}{f(H\alpha)} \; ; \quad (\text{for } f(H\alpha) > f_0) \tag{3.9}$$

where $f_0 = 3.69 \times 10^{-15}$ erg s^{-1}cm^{-2} is the flux at which the DIG contributes 100% of the emission, and hence $C_{HII} = 0$ for $f(H\alpha) \leq f_0$. The correction is shown as the red solid line in Figure 3.9. We multiply the extinction corrected Hα fluxes by the above correction factor in order to remove any contribution from the DIG in NGC 5194. It is worth noting that using Equation 3.9 to remove the DIG is equivalent to subtracting a constant DIG flux value f_0 for all regions with $f(H\alpha) > f_0$ (the large majority of the regions). Hence, the line ratio distribution presented in Figure 3.9 is very well fitted by a flat DIG component.

Figure 3.10 presents maps of the extinction corrected Hα emission line flux before and after the DIG correction is applied. It can be seen clearly how the Hα emission traces the spiral pattern of star-formation. The correction

leaves the Hα flux coming from the brightest star-forming regions practically unchanged, while removing the contribution from the DIG which dominates the observed spectrum in the inter-arm regions of the galaxy. The latter can also be appreciated in Figure 3.7, which shows an enhanced [NII]/Hα ratio typical of the DIG in the inter-arm regions, and normal H II region ratios throughout the spiral arms.

Integrating over the complete observed area, the DIG contributes only 11% of the total Hα flux. Previous photometric measurements of the diffuse ionized fraction in nearby spiral galaxies, including NGC 5194, yield median diffuse fractions of $\sim$50% (e.g. Ferguson et al., 1996; Hoopes et al., 1996; Greenawalt et al., 1998; Thilker et al., 2002; Oey et al., 2007). These studies are performed either by masking of H II regions or by discrete H II region photometry in Hα narrow-band images. Although it will be seen in §10 that the assumption of a constant [NII]/Hα ratio throughout the galaxy used to correct the narrow-band images in all the above studies can introduce overestimations of the DIG Hα brightness of up to 40%, this effect is small, and cannot account for the difference between our diffuse fraction and the typical values found in the literature. The difference is most likely due to the fact that our observations are limited to the highly molecular, and hence strongly star-forming central part of the galaxy. Our measured diffuse ionized fraction is then only a lower limit to the DIG contribution over the whole galaxy, since at larger radii the relative contribution from H II regions is expected to significantly decrease. Though the DIG contribution to the integrated Hα luminosity in

the central region of NGC 5194 could be small, on the small scales sampled by the VIRUS-P fibers the DIG can account for 100% of the observed Hα flux, especially in between the spiral arms where H II regions are rare. Given the clear dependence of the above correction with Hα flux, failing to correct for this effect introduces a bias in the SFL towards shallower slopes.

The corrected Hα emission-line fluxes are transformed into Hα luminosities using the assumed distance to NGC 5194 of 8.2 Mpc. Since the DIG is suspected to arise from UV photons escaping star forming regions in the disk, not accounting for these photons should introduces a systematic underestimation of the SFR. The challenge resides in our inability to tell from where in the disk these UV photons come from. To ameliorate this problem, we scale the Hα luminosities by a factor of 1.11, which is equivalent to assuming that the UV photons ionizing the DIG were originated in the star-forming regions in the disk proportionally to their intrinsic UV luminosities. These scaled luminosities ($L_{corr}(H\alpha)$) are used to estimate the SFR for each of the 718 regions. We use the calibration presented in Kennicutt (1998b), for which the SFR is given by,

$$\mathrm{SFR}\ [M_{\odot}yr^{-1}] = 7.9 \times 10^{-42} L_{corr}(H\alpha)\ [\mathrm{erg\ s^{-1}}] \tag{3.10}$$

The above calibration assumes a Salpeter IMF over the range of stellar masses 0.1-100 $M_{\odot}$. To convert to the Kroupa-type two-component IMF used in Bigiel et al. (2008), the SFR must be multiplied by a factor of 0.63.

The SFRs for individual regions are then converted to SFR surface densities (Σ_{SFR}). Following Kennicutt et al. (2007), we divide the SFR by the projected area on the sky of the 4.3″ (172 pc) diameter regions sampled by each fiber on the IFU, and multiply it by a factor of cos(20°) to account for the inclination of NGC 5194 (Tully, 1974). The star formation rate surface density for all regions is provided in Table 1.

3.9 The Spatially Resolved Star Formation Law

The observed relations between Σ_{SFR} and the gas surface densities of different components of the ISM (Σ_{HI}, Σ_{H_2}, and Σ_{HI+H_2}) are presented in Figures 3.11, 3.12 and 3.13. Error bars in gas surface densities correspond to the 1σ uncertainties given in §4.1 and §4.2. Error bars in the SFR surface density include a series of uncertainties that we proceed to describe. First we consider the uncertainty in the observed Hα fluxes. This comes from the fitting of the Hα line described in §5.2, which was performed considering the observational error in the spectrum (obtained from the error maps described in §3). Second, the uncertainty in the dust extinction correction is included by propagating the fitting errors of the observed Hα and Hβ fluxes through Equation 3.2. Finally, in order to account for the error associated with the DIG correction, we introduce a 20% uncertainty in Σ_{SFR}, consistent with the median scatter of the points in Figure 3.9 around the correction used. All these uncertainties are summed in quadrature to account for the error bars in Σ_{SFR}. We do not consider errors in the flux calibration which are expected to

be of $\sim$5%, nor in the CO to H_2 conversion factor. The later is currently highly uncertain and might change by up to a factor of 2 depending on assumptions about the dynamical state of GMCs (Blitz et al., 2007). In any case, these two sources of systematic errors enter the SFL as multiplicative factors. Hence, they can only introduce a bias in the normalization of the SFL, and should not affect the fitted values of the slope and the intrinsic scatter.

From Figure 3.11 it is clear that Σ_{SFR} shows a very poor correlation with Σ_{HI}, since regions having similar atomic gas budgets can have star formation activities that differ by more than 3 orders of magnitude. We observe an evident saturation in the atomic gas surface density at $\Sigma_{HI} \approx 10\ M_{\odot}pc^{-2}$. Also, there is a slight inversion in the sense of the correlation at high Σ_{SFR}, associated with the central part of the galaxy due to the presence of a minimum in the HI profile (Bigiel et al., 2008). These HI "holes" are common in the centers of spiral galaxies, and in them the ISM is fully dominated by molecular hydrogen while the atomic gas is almost completely depleted. The saturation at 10 $M_{\odot}pc^{-2}$ has been previously observed by Wong & Blitz (2002) using azimuthally averaged data, and further confirmed to be a widespread phenomena in normal spirals by Bigiel et al. (2008) using 2D spatially resolved measurements. It is thought to be related to a threshold in surface density at which a phase-transition from atomic to molecular gas occurs in the ISM (Krumholz et al., 2009a). Given the lack of correlation between Σ_{HI} and Σ_{SFR}, we do not attempt to fit a atomic gas SFL. We restrict our analysis to the modeling of the molecular and total gas correlations with the star-formation activity. These

correlations are usually well described by a power-law function(Schmidt, 1959; Kennicutt, 1998a).

It has been established that the observed rms dispersion about a power-law in these SFLs is much larger than the observational uncertainties (Kennicutt, 1998a; Kennicutt et al., 2007), implying the existence of significant intrinsic scatter of physical origin in the relations. However, previous works have not introduced this intrinsic scatter into the parameterization of the SFL, and authors restrict themselves to measure the scatter after fitting a power-law to the data. In this work, we incorporate the intrinsic scatter in the SFL, which we parameterize as:

$$\frac{\Sigma_{SFR}}{1\mathrm{M}_{\odot}\mathrm{yr}^{-1}\mathrm{kpc}^{-2}} = A\left(\frac{\Sigma_{gas}}{100\mathrm{M}_{\odot}\mathrm{pc}^{-2}}\right)^{N} \times 10^{\,\mathcal{N}(0,\epsilon)} \tag{3.11}$$

where A is the normalization factor, N is the slope, and $\mathcal{N}(0,\epsilon)$ is a logarithmic deviation from the power-law, drawn from a normal distribution with zero mean and standard deviation ϵ. The value of ϵ corresponds to the intrinsic scatter of the SFL in logarithmic space. The factor $10^{\,\mathcal{N}(0,\epsilon)}$ can be interpreted as changes of physical origin in the star-formation efficiency for different regions. We chose a pivot value for the normalization of $100\mathrm{M}_{\odot}\mathrm{pc}^{-2}$, which is roughly at the center of the distribution of measured Σ_{gas} values, in order to minimize the covariance between the slope and the normalization. When comparing the normalization factors derived here with other fits found in the literature, this must be taken into account. Most works quote nor-

malizations at $1M_{\odot}pc^{-2}$, while Bigiel et al. (2008) quotes normalizations at $10M_{\odot}pc^{-2}$.

Previous measurements of the spatially resolved SFL use different algorithms to fit a power-law to the data. Usually a linear regression in logarithmic space is performed, but methods differ in the treatment of error bars. Kennicutt et al. (2007) used a FITEXY algorithm (Press et al., 1989), which has the advantage of incorporating errors in both the ordinate and abscissa coordinates, although errors must be assumed to be symmetric in logarithmic space, which is not always the case. Bigiel et al. (2008) used an ordinary least-squares (OLS) bisector method (Isobe et al., 1990) giving the same weighting to every data point. Both methods have the disadvantage of not being able to incorporate upper limits in the minimization. Our data is mainly limited by the sensitivity of the CO intensity maps as can be seen in Figure 3.12, where 93 of the 718 regions unaffected by AGN contamination are undetected in CO and hence we can only provide upper limits for their molecular gas surface densities. This is also the case in the works mentioned above. As will be seen in §11, these upper limits contain important information regarding the slope of the spatially resolved SFL, and neglecting them biases the fits towards steeper slopes. We introduce and use a new method for fitting the SFL which is not affected by the above issues.

3.9.1 The Fitting Method

To fit our data we use a Monte Carlo (MC) approach combined with two-dimensional distribution comparison techniques commonly used in color-magnitude diagram (CMD) fitting (Dolphin et al., 2001). Our method allows us to include the regions not detected in the CO map (including the ones with negative measured fluxes), incorporate the intrinsic scatter in the SFL as a free parameter, and perform the fitting in linear space, avoiding the assumption of log-normal symmetric errors. In the following, we describe our fitting method.

For any given set of parameters $\{A, N, \epsilon\}$, we generate 200 Monte Carlo realizations of the data. To create each realization, we take the measured values of Σ_{gas} as the true values and calculate the corresponding true Σ_{SFR} using Equation 3.11, drawing a new value from $\mathcal{N}(0, \epsilon)$ for each point in order to introduce the intrinsic scatter. Regions for which we measure negative CO fluxes are assumed to have $\Sigma_{gas} = \Sigma_{SFR} = 0$. In order to account for observational errors, data points are then offset in Σ_{SFR} and Σ_{gas} by random quantities given by the observed measurement error for each data point. The uncertainty in Σ_{SFR} is largely dominated by the errors introduced in the dust extinction and DIG corrections. Since both corrections are multiplicative, we apply the random offsets as multiplicative factor drawn from a $\mathcal{N}(1, \sigma(\Sigma_{SFR})/\Sigma_{SFR})$ distribution. On the other hand, the error in Σ_{gas} is dominated by systematic offsets introduced during the combination and calibration of interferometric data. Accordingly, the random offsets in Σ_{gas} are introduced in an additive manner, using values drawn from a $\mathcal{N}(0, \sigma(\Sigma_{gas}))$ distribution. It is important

to notice that while for plotting purposes, Figures 3.11, 3.12, and 3.13 show upper limits in Σ_{gas} and Σ_{SFR}, in the fitting procedure the measured values of these data-points are used together with their usually large error bars.

Having the observed data points and the large collection of realizations of the data coming from the model, we need to compare the distribution of points in the Σ_{gas}-Σ_{SFR} plane in order to assess how well the model fits the data given the assumed parameters. To do so, we define a grid on the Σ_{gas}-Σ_{SFR} plane and count the number of data points falling on each grid element both in the data and in the 200 realizations. This method is adapted from Dolphin et al. (2001), and it is the equivalent to the construction of Hess diagrams used in CMD fitting. The grid covers all the observed data points, has a resolution of $\Delta\Sigma_{gas}$=156 $M_{\odot}pc^{-2}$ and of $\Delta\Sigma_{SFR}$=0.11 $M_{\odot}yr^{-1}kpc^{-2}$, and is shown in the left panel of Figure 3.14. A single extra grid element containing all the points in the Monte Carlo realizations falling outside the grid and zero observed data points is also included in the calculations below.

We average the number of points in each grid element for the 200 Monte Carlo realizations and call this "the model". In order to compare the model to the data we compute a χ^2 statistic of the following form:

$$\chi^2 = \sum_i \frac{(N_i - M_i)^2}{M_i} \tag{3.12}$$

Where the sum is over all the grid elements in the Σ_{gas}-Σ_{SFR} plane, N_i is the number of observed data points, and M_i is the number of model data points

in the grid element i. We sample a large three dimensional grid in parameter space with a resolution of $\Delta\log(A)$=0.018, ΔN=0.036, and $\Delta\epsilon$=0.011, centered around our best initial guesses for the different SFLs, and compute χ^2 for every combination of parameters in the cube.

To exemplify our method, the left panel in Figure 3.14 shows the observed molecular SFL in linear space, together with the best-fitted Monte Carlo model. Overlaid are all the grid elements, color-coded according with the density of points inside each of them. The top central panel shows the number of points in each grid element in the model versus the data for the best-fitted model, in this plot, deviations from the dashed line contribute to the χ^2 statistic. Also shown is the χ^2 for each parameter, marginalized over the other two. The best-fitted value for each parameter is obtained by fitting a quadratic function to the minimum χ^2 at each parameter value sampled. Uncertainties at the 1σ, 2σ, and 3σ levels are also shown in the plots. Notice that the sampled set of parameters showing the minimum χ^2 is always within 1σ of the best-fitted value deduced from the quadratic function fitting.

Thorough testing of the fitting method was carried out. The number of Monte-Carlo simulations is high enough for consecutive runs of the algorithm on the same data to produce best-fitted values for the parameters that show a scatter of less than 0.1σ. The best-fitted parameters are somewhat sensitive to the chosen grid spacing in the linear Σ_{gas}-Σ_{SFR} plane. Fitting of artificially generated data-sets drawn from known parameters, showed the grid resolution we use to be the best at recovering the intrinsic parameters with deviations

from the true values of less than 0.5σ.

3.9.2 Fits to the Molecular and Total Gas Star Formation Laws

We applied our method to fit the observed SFL in both molecular gas and total gas. The best-fitted SFLs are shown as solid lines in Figures 3.12 and 3.13, where the best-fitted parameters are also reported. For the molecular gas SFL we measure a slope $N = 0.82 \pm 0.05$, an amplitude $A = 10^{-1.29\pm0.02}$, and an intrinsic scatter $\epsilon = 0.43 \pm 0.02$ dex. In the central part of NCG 5194 we are sampling a density regime in which the ISM is almost fully molecular, hence the total gas SFL closely follows the molecular SFL and shows very similar best-fitted parameters. For the total gas SFL we obtain a slope $N = 0.85 \pm 0.05$, an amplitude $A = 10^{-1.31\pm0.02}$, and an intrinsic scatter $\epsilon = 0.43 \pm 0.02$ dex.

Of great interest is the large intrinsic scatter observed in the SFL. A logarithmic scatter of 0.43 dex implies that the SFR in regions having the same molecular gas surface density can vary roughly by a factor of $\sim$3. This is very important to keep in mind when using the SFL as a star-formation recipe in theoretical models of galaxy formation and evolution. Results from this type of modeling should be interpreted in an statistical sense, and we must always remind ourselves that SFRs predicted for single objects can be off by these large factors. The bottom left panel of Figure 3.14 is an striking reminder of the limitations involved in the use of SFLs as star-formation recipes in analytical and semi-analytical models. The large scatter observed is indicative of the existence of other parameters, besides the availability of molecular gas,

which are important in setting the SFR.

As will be discussed in §11, the fact that we measure a slightly sub-linear SFL is consistent recent results by Bigiel et al. (2008) and Leroy et al. (2008), as well as with recent theoretical modeling by Krumholz et al. (2009b), but in disagreement with the significantly super-linear molecular and total gas SFLs measured in NGC 5194 by Kennicutt et al. (2007). Our results imply depletion times for the molecular gas of $\tau \approx 2$ Gyr, which is roughly a factor of $\sim$100 longer than the typical free fall time of GMCs (McKee, 1999). These low efficiencies, of the order of 1% per free-fall time, are observed in a large range of spatial scales and densities in different objects. It is seen all the way from HCN emitting clumps, infrared dark clouds, and GMCs in the Milky Way to the molecular ISM in large scales in normal spiral galaxies and starburst, and is consistent with models in which star-formation is regulated by supersonic turbulence in GMCs, induced by feedback from star-formation itself (Evans et al., 2009; Krumholz & McKee, 2005).

3.10 Balmer Absorption and the N[II]/Hα Ratio, Implications for Narrow-Band Imaging

Narrow-band imaging is the most widely used method for conducting spatially resolved measurements of the Hα emission line in nearby galaxies. Images taken with a narrow-band filter centered at Hα, and either a broad-band or off-line narrow-band, are subtracted in order to remove the continuum in the on-line bandpass. The excess flux in the on-line narrow-band is expected

to map the nebular emission. Narrow-band filters have typical FWHMs of $\sim$70Å, and hence suffer from contamination from the [NII]$\lambda\lambda$,6548,6584 doublet. Also, narrow-band techniques cannot directly separate the nebular emission from the underlying photospheric absorption Hα. Corrections to account for these two factors are usually applied.

In order to correct for the underlying absorption, the continuum image is usually scaled before subtraction so selected regions in the galaxy, which are a priori expected to be free of Hα emission, show zero flux in the subtracted image. This is equivalent to correcting for a constant Hα absorption EW across the galaxy (assuming that the continuum level was reliably estimated, which might not be the case when broad-bands are used instead of off-line narrow-bands, since the spectral slope of the stellar continuum can vary significantly across the galaxy). The [NII] contamination is usually taken out by assuming a constant [NII]/Hα ratio across the whole galaxy, which together with the relative filter transmission at the wavelengths of the three lines, is used to compute a correction factor which is used to scale down the observed continuum subtracted narrow-band fluxes in order to remove the [NII] contribution. Integral-field spectroscopy is free of these two effects, since both the [NII] lines and the photospheric Hα absorption can be clearly separated from the Hα emission (see Figure 3.3). Thus, our observations provide an important check on the validity of the corrections typically applied in narrow-band studies, and the biases introduced by them.

Line ratios of [NII]λ6584/Hα=0.5 and [NII]λ6548/[NII]λ6584=0.335

are typically assumed For the [NII] correction (Calzetti et al., 2005). Based on these ratios, a perfect Hα filter (i.e. one with a constant transmission across the three lines) would measure a flux that is a factor of 1.67 higher than the Hα flux. Figure 3.15 shows the ([NII]λ6548+[NII]λ6584+Hα)/Hα ratio as a function of the extinction corrected Hα flux, as measured in the VIRUS-P spectra of all 718 star-forming regions. Although we measure a mean value of 1.65 (solid line), in good agreement with the predictions from the above line ratios (dashed line), it can be seen that the correction factor is a strong function of Hα flux. The fact that we observe an increasing [NII]/Hα ratio as we go to fainter Hα fluxes is consistent with the nebular emission in the faintest parts of the galaxy (mainly the inter-arm regions) being dominated by the DIG component of the ISM (see Figure 3.7 and §8).

The observed line ratios imply that assuming a constant NII/Hα ratio throughout the galaxy would introduce systematic overestimations of the Hα flux of up to 40% in the faintest regions, as well as systematic underestimations of up to 25% for the brightest regions. The effect is a strong function of Hα flux, and its magnitude is of the order of the typical uncertainties quoted for narrow-band photometry of star-forming regions in nearby galaxies. While in theory these systematic missestimations should bias a measurement of the slope of the SFL towards shallower values, the magnitude of the effect is ten times smaller than the intrinsic scatter in the SFL and the introduced bias is negligible.

Now lets look at the effects introduced by errors in the continuum

subtraction and estimation of the underlying Hα stellar absorption. When doing narrow-band imaging, the estimated value for the Hα absorption EW is coupled, and impossible to separate from the estimated continuum level. So overestimations of the absorption EW can be thought as underestimations of the subtracted continuum and viceversa. Black crosses in Figure 3.16 show the observed Hα emission flux (before dust extinction correction) versus the fractional difference between the Hα emission and absorption fluxes for all the regions unaffected by AGN contamination. The magnitude of the Hα absorption was measured in the best-fitted stellar continuum spectrum of each region, constructed as described in Section 5.1. The vertical axis in Figure 3.14 can be interpreted as the fraction of the true flux we would observe if the underlying absorption was not taken out from our measurement. Negative values correspond to regions in which the absorption EW is higher than the emission EW. We measure a fairly constant absorption EW, showing a median of -2.4Å, and rms scatter of 0.2Å between different regions. This supports the approximation of a constant Hα absorption EW on which narrow-band corrections are based. Not taking into account the absorption feature can translate into gross underestimations of the emission line fluxes. For the brightest regions the underestimation can be up to $\sim$50%, and for the faintest regions we could completely miss the presence of nebular emission, and observe pure absorption.

The red crosses in Figure 3.16 show the emission minus absorption fluxes corrected using a constant Hα absorption EW of -2.4Å. It can be seen

that, under the assumption of a constant absorption EW, true fluxes can be recovered with typical uncertainties of less than 20% if the correct value of the median EW is used. Green and blue crosses in Figure 3.16 correspond to the values that would be obtained if the continuum had been overestimated and underestimated by 10% respectively, or equivalently if the Hα absorption EW had been underestimated by -0.2Å and overestimated by +0.3Å. The orange and light blue crosses correspond to continuum misestimations of a 50% (-0.8Å, +2.4Å). These offsets are of the same order of magnitude as the typical uncertainties in the continuum subtraction of narrow-band images of nearby galaxies. It can be seen that a systematic misestimations can be introduced to the measured Hα fluxes, especially in the fainter regions. Similarly to the [NII] correction discussed above, this effect is a strong function of Hα flux and in this case can induce a significant change in the slope of the SFL if the estimated absorption (continuum level) is sufficiently off from the true value. A 10% error in the continuum level can introduce systematic misestimations of up to 30%, which is small compared to the intrinsic scatter in the SFL, but a 50% error in the estimation of the continuum can induce misestimations of the measured fluxes that are of the order of the SFL intrinsic scatter, and hence introduce a significant systematic bias to the SFL slope.

We perform a comparison of our spectroscopically measured Hα emission line fluxes to fluxes measured by performing photometry in 4.3$''$ diameter apertures at the positions of each of our fibers on the continuum-subtracted and absorption line corrected narrow-band image used by Calzetti et al. (2005)

and Kennicutt et al. (2007). We correct the narrow-band fluxes for [NII] contamination using the correction factors shown in Figure 3.13, scaled by 0.97 to account for the lower filter transmission at the [NII] lines. Figure 3.17 shows the comparison. In order to account for differences in flux calibration and photometry aperture effects, we scale the narrow-band fluxes by a factor of 1.25, given by the mean ratio between the VIRUS-P and narrow-band fluxes for regions with $f(H\alpha) > 10^{-14}$erg s^{-1}cm^{-2} (to the right of the dotted line in Figure 3.15). At high Hα emission fluxes the effects of errors in the continuum subtraction are much smaller than for the fainter regions, so we consider safe to scale the fluxes in order to match the bright end of the distribution, also the magnitude of the scaling factor is of the order of the combined uncertainties in flux calibration.

Narrow-band fluxes presented in Figure 3.17 should not be affected by previously discussed systematics introduced by [NII] corrections, since we used the spectroscopically measured ratios to correct them. On the other hand, they clearly show a systematic deviation, with narrow-band fluxes being lower than spectroscopic fluxes as we go to fainter regions. This is consistent with an overestimation of the continuum level by $\sim$30%, or equivalently and underestimation of the Hα absorption EW by -0.6Å, which is well within the uncertainties involved in the continuum subtraction of the narrow-band image (Calzetti private comunication). It is important to notice that in Kennicutt et al. (2007), the spatially resolved SFL was built by doing photometry on Hα bright star-forming knots (brighter than 3×10^{-15} erg s^{-1}cm^{-2}), which are less

affected by errors in the continuum subtraction than for example the inter-arm regions. Hence we do not expect this effect to significantly affect the slope of the SFL that they measure.

The above comparison stresses a very important point. Although very deep narrow-band imaging can be obtained using present day imagers, low surface-brightness photometry of nebular emission in these images is limited by uncertainties in the continuum subtraction and estimation of photospheric absorption. In this respect, integral field spectroscopy provides us with a less biased way of measuring faint nebular emission in nearby galaxies.

3.11 Comparison with Previous Measurements and Theoretical Predictions

In this section we compare our results to the recent measurements on the spatially resolved SFL in NGC5194 by Kennicutt et al. (2007) and Bigiel et al. (2008), and to the predictions of the theoretical model of the SFL proposed by Krumholz et al. (2009b).

We find an almost complete lack of correlation between the atomic gas surface density and the SFR surface density (Figure 3.10). This is in good agreement with the observation of both Kennicutt et al. (2007) and Bigiel et al. (2008), and confirms the fact that the SFR is correlated with the molecular gas density, and it is this correlation which drives the power-law part of the total gas SFL. At low gas surface densities ($< 20 M_{\odot} pc^{-2}$) the ISM of spiral galaxies stops being mostly molecular, and hence the shape of the total gas

SFL is driven by a combination of the molecular gas SFL and the ratio of molecular to atomic hydrogen.

As discussed in §1, Kennicutt et al. (2007) finds a super-linear slope of 1.37 for the molecular SFL in NGC5194, while Bigiel et al. (2008) measures a slightly sub-linear slope of 0.84. The first of these measurements is consistent with models in which the SFR is inversely proportional to the gas free-fall time in GMCs and the molecular gas surface density is proportional to the total gas density ($N = 1.5$, Kennicutt (1998a)), while the second is more consistent with models in which the SFR shows a linear correlation with the molecular gas density, product of star-formation taking place at a constant efficiency in GMCs. Hence, establishing the slope of the SFL is important in order to distinguish between different physical phenomena that give rise to it.

Figure 3.18 shows the molecular SFL measured as described in §9, together with the best-fitted SFL as measured by Kennicutt et al. (2007) and Bigiel et al. (2008). The results from the latter are adjusted to account for differences in the IMF assumed for calculating Σ_{SFR}, and the different CO-H_2 conversion factor used in the calculation of Σ_{H_2}.

Our best-fitted molecular SFL shows a considerably shallower slope than the one measured by Kennicutt et al. (2007). We consider the source of the disagreement to be a combination of two factors. First, as shown in §10, the narrow-band Hα fluxes used by Calzetti et al. (2005) and Kennicutt et al. (2007) might be underestimated at the faint end of the flux distribution due to small systematic errors in continuum subtraction, although the effect is small

(of the order of the intrinsic scatter in the SFL), and cannot account for the bulk of the difference observed in the SFL slope. The second factor, which we consider to be the main cause behind the disagreement, is the difference in the fitting methods used to adjust a power-law to the data. As mentioned in §9, Kennicutt et al. (2007) used a FITEXY algorithm to perform a linear regression to the data in logarithmic space, rejecting upper limits in Σ_{H2} from the fit, and not fitting for the intrinsic scatter in the SFL. The solid green line in Figure 3.17 shows the result of applying the same procedure to our data. The FITEXY method significantly overpredicts the slope of the SFL ($N = 1.9$), in large part due to the exclusion of the Σ_{H2} upper limits. These data-points, having large error bars in Σ_{gas} and clear detections in Σ_{SFR}, have a significant statistical weight in the Monte Carlo fit because of their large number. Another factor promoting the fitting of shallower slopes by our Monte Carlo method, is the fact that we included the intrinsic dispersion in the SFL as a scatter in Σ_{SFR}, hence the fit will tend to equalize the number of data-points above and below the power-law at any given Σ_{gas}. This is a consequence of the expectation for a causal relation between Σ_{gas} and Σ_{SFR}, with the SFR beeing a function of the gas density, and not viceversa.

Kennicutt et al. (2007) provide a table of their measured values for Σ_{SFR} and Σ_{HI+H_2} and their uncertainties, from which they recover a slope of $N = 1.56$ for the total gas SFL. We apply our Monte Carlo fitting method to their data, and find best-fitted values of $A = 10^{-1.23\pm0.03}$ for the amplitude, $\epsilon = 0.40 \pm 0.03$ for the intrinsic scatter, and a slope $N = 1.03 \pm 0.08$. This

shallower slope is a lot closer to our mesured value of $N = 0.85$, and the rest of the difference can be easily explained by the underestimation of the narrow-band Hα fluxes presented in Figure 3.17 and differences in the DIG correction. The two independent datasets show excellent agreement in the value of intrinsic scatter. The small difference of 0.08 dex in the amplitude can be attributed to the fact that Kennicutt et al. (2007) targeted active star-forming regions in their study, and hence their measurement of the SFL is most likely biased towards higher star-formation efficiencies than the one presented here.

On the other hand, we measure a molecular SFL which shows an excellent agreement with Bigiel et al. (2008) both in slope and normalization. The agreement is better than expected, given the differences in the methods used to measure Σ_{SFR} and fitting the SFL. Their SFR measurements are not based on extinction corrected hydrogen recombination lines as in Kennicut et al. and this work, but rather on a linear combination of space-based GALEX far-UV and *Spitzer* MIPS 24μm fluxes. Also, they do not correct their data in order to account for any contribution from the DIG. The fitting method used by Bigiel et al. (2008) is an OLS Bisector, and they also reject non detections in CO from the fit. The orange solid line shows the result of applying this fitting method to our data. Just as in the case of the FITEXY algorithm, the OLS Bisector yields a significantly higher slope ($N = 1.5$) than the Monte Carlo fit. The reasons for this are the same as for the FITEXY algorithm, that is, the inclusion of the upper limits in Σ_{H_2}, and the introduction of the intrinsic

scatter in Σ_{SFR} in our method. One possible explanation for the agreement could be the interplay between the lack of DIG correction and the difference in fitting methods. The first will tend to drive the slope to shallower values, while the second will steepen it. The combination of these two effects working in opposite directions might be behind the agreement between Bigiel et al. (2008) and this work.

Although the comparison is hard due to the systematics involved in the different methods, the bottom line is that we measure a slope that is consistent with the scenario proposed by Bigiel et al. (2008) and Leroy et al. (2008), in which star-formation takes place at a nearly constant efficiency in GMCs over a large range of environments present in galaxies. This is also in agreement with recent the findings of (Bolatto et al., 2008), who find that extragalactic GMCs in the Local Group, detected on the basis of their CO emission, exhibit remarkably uniform properties, with a typical mass surface density of roughly 85 $M_{\odot}pc^{-2}$.

Based on these concepts of uniformity of GMC properties, and good correlation between the SFR and the molecular gas density, Krumholz et al. (2009b) proposed a simple theoretical model to explain the observed total gas SFL. In their model, star formation takes place only in molecular gas, and the total gas SFL is determined by three factors. First, the fraction of the gas in molecular form is set by the balance between the formation of H_2 in the surface of dust grains, and the dissociation of molecules by the far-UV continuum in the Lyman-Werner bands (Krumholz et al., 2008, 2009a). This drives the

shape of the total gas SFL in the low density regime where the ISM is not fully molecular. Second, the star-formation efficiency inside GMCs is low, and it is set by turbulence driven feedback processes (Krumholz & McKee, 2005). These are responsible for the power-law behavior of the molecular SFL. Third, GMCs are decoupled from the surrounding ISM when their internal pressure is higher than external pressure. In this regime their structure is determined by internal feedback processes, and they show very uniform properties including an almost constant surface density of 85 $M_{\odot}pc^{-2}$ (Bolatto et al., 2008). When the galactic ISM pressure becomes higher than this value, the GMC surface density must increase accordingly in order to maintain pressure balance with the external ISM. This gives rise to a steepening of the slope of the molecular SFL at $\Sigma_{H_2} \geq 85 M_{\odot}pc^{-2}$. In summary, the total gas SFL in the model shows a different behavior in the low, intermediate, and high density regimes. At low densities its behavior is driven by the transition from an atomic to a molecular ISM. Beyond the point at which the ISM becomes almost fully molecular the total gas SFL follows closely the molecular SFL, which shows a steeper slope in the high density regime driven by the pressure balance between the galactic ISM and GMCs.

Figure 3.18 shows a comparison of our data and the Krumholz et al. (2009b) model. We have assumed $Z' = Z/Z_{MW} = 1.0/1.5$, consistently with the DIG correction applied in §8, and a clumpiness factor $c = 4$ to account for the effect that the averaging of Σ_{gas} introduces in the molecular fraction in the model. We observe an excellent agreement for both the atomic and molecular

gas, as well as for the total gas SFL. The gas density range sampled by our observations, and the scatter in SFL does not allow us to discern between the model and the simple power law fitted using the Monte Carlo method, stressing the need to extend our observations towards more extreme density environments.

3.12 Summary and Conclusions

We have performed the first measurement of the spatially resolved SFL in nearby galaxies using integral field spectroscopy. The wide field VIRUS-P spectroscopic map of the central 4.1×4.1 kpc^2 of NGC 5194, together with the HI 21cm map from THINGS, and the CO J=1-0 from BIMA SONG were used to measure Σ_{SFR}, Σ_{HI}, and Σ_{H_2} for 718 regions $\sim$170 pc in diameter throughout the disk of the galaxy.

In this paper we have presented our method for calculating Σ_{SFR} from the spectroscopically measured Hα emission line fluxes. We have shown that the observed Hα/Hβ ratio is a good estimator of the nebular dust extinction, at least at the levels of obscuration present in face-on normal spiral galaxies like NGC 5194.

We have also presented a new method for estimating the contribution of the DIG to the Hα emission line flux, which is based on the observed low-ionization line ratio [SII]/Hα, and the large differences seen in this line ratio between H II regions and pointings towards the DIG in the Milky Way. The use of line ratios to correct both for dust extinction and the DIG contribution

is possible only because of the use of integral field spectroscopy spanning a large wavelength range, which includes all these important emission lines.

One of the main goals of this work is to make use of these clean spectroscopic emission line measurements to study the systematics involved in narrow-band estimations of the Hα emission line flux of nearby galaxies. We showed that proper estimation of the continuum and of the underlying stellar absorption features is crucial in order to get an unbiased estimate of the Hα flux. Errors of the order of 30% in the estimation of these quantities can introduce systematic misestimations of the Hα emission line flux by up to a factor of 3 in the low surface brightness regime.

We also tested the assumption of a constant [NII]/Hα ratio throughout the galaxy, usually used to remove the [NII] doublet contamination from the narrow-band measured fluxes. We found that the [NII]/Hα ratio varies significantly throughout the galaxy, and shows a clear correlation with the Hα flux. The sense of the correlation implies a higher [NII]/Hα ratio in regions that are fainter in Hα (typically the inter-arm regions of the galaxy), and is consistent with the DIG dominating the nebular spectrum in these zones. Assuming a constant [NII]/Hα would introduce overestimations of the Hα flux of $\sim$40% in the inter-arm regions, and underestimations of $\sim$25% for the brightest star-forming regions in the spiral arms.

Integral field spectroscopy proves to be an extremely powerful tool for mapping the SFR throughout the disks of nearby galaxies, especially with the advent of large field of view IFUs like VIRUS-P. Spatially resolved spectral

maps, besides allowing us to measure emission line fluxes in a much more unbiased way than narrow-band imaging, also provides extensive information about the physical conditions throughout the disks of nearby spiral galaxies. The spectra allows the measurement of metallicities, stellar and gas kinematics, stellar populations, and star formation histories across galaxies. In a future study we will investigate the role that all these other quantities that can be extracted from our data play at setting the SFR.

We found that the SFR surface density shows a lack of correlation with the atomic gas surface density, and a clear correlation with the molecular gas surface density. Hence, the total gas SFL is fully driven by the molecular gas SFL in the density regimes sampled by our observations. The atomic gas surface density is observed to saturate at a value of $\sim$10 $M_{\odot}pc^{-2}$, at which a phase transition between atomic and molecular gas is thought to occur in the ISM.

A Monte Carlo method for fitting the SFL which is not affected by the systematics involved in performing linear correlations of incomplete data in logarithmic space was presented. Our method fits the intrinsic scatter in the SFL as a free parameter. Applying this method to our data yields slightly sub-linear slopes N of 0.82 and 0.85 for the molecular and total gas SFLs respectively.

Comparison with previous measurements of the spatially resolved SFL are somewhat challenging because of the different recipes used to estimate Σ_{SFR}, and the different fitting procedures used to derive the SFL parameters.

The slopes we measured are in disagreement with the results of Kennicutt et al. (2007), who measured a strongly super-linear slope for both the molecular component and the total gas. On the other hand, our results are in very good agreement with the slope measured for the molecular gas SFL in NGC 5194 by Bigiel et al. (2008). Our results are consistent with the scenario recently proposed by Bigiel et al. (2008) and Leroy et al. (2008) of a nearly constant SFE in GMCs, which is almost independent of the molecular gas surface density. The main argument to support this scenario is the observation of a close to linear correlation between the Σ_{SFR} and Σ_{gas} in the density ranges present in the ISM of nearby normal spiral galaxies.

On the other hand our results also show a very good agreement with the more complex scenario recently proposed by Krumholz et al. (2009b), in which the surface density of molecular gas grows with the molecular to atomic fraction at low densities ($\Sigma_{HI+H_2} \lesssim$10 M$_\odot$pc^{-2}), becomes constant at intermediate densities (10 M$_\odot$pc$^{-2} \lesssim \Sigma_{HI+H_2} \lesssim$100 M$_\odot$pc^{-2}), and increases linearly with the total gas density in the high density regime ($\Sigma_{HI+H_2} \gtrsim$100 M$_\odot$pc^{-2}). This, combined with an slightly sub-linear efficiency as a function of molecular gas surface density given by the balance between gravitational potential energy and turbulent kinetic energy originated by internal feedback, gives rise to the observed SFL. In their model, the total gas SFL has a super-linear slope $N = 1.33$ in the high density regime, gets shallower at intermediate densities showing a slope of $N = 0.67$, and steepens again at lower densities as the molecular to atomic gas fraction rapidly decreases. Our observations

sample the transition between the intermediate and high density regimes in the model. The intrinsic scatter in the SFL, together with our limited density dynamic range does not allow us to observe the predicted kink in the SFL directly, but our measured slope of 0.85 is very close to what we expect to measure in a region where we sample both the sub-linear and super-linear parts of the SFL predicted by Krumholz et al. model. A proper detection of the kink in the SFL predicted by Krumholz et al. (2009b) will require extending the dynamic range to higher gas surface densities.

A major success of the Krumholz et al. (2009b) model is the excellent agreement it shows with the observation with respect to the SFE, or equivalently to the gas depletion timescales. We observe very long depletion timescales of $\tau \approx 2$ Gyr, in good agreement with previous observations. This time is $\sim$100 longer than the typical GMC free-fall time. The good agreement between our observations and the Krumholz et al. model implies that this very low efficiency can be easily explained by models in which star-formation is self regulated through turbulence induced by internal mechanical feedback in GMCs.

An important result of this study is the large intrinsic scatter of 0.43 dex observed in both the molecular and total gas SFLs. This translates into a factor of $\sim$3 scatter in the SFR for regions having the same molecular gas availability, and it may indicate the existence of further parameters that are important in setting the SFR. It is worth mentioning that part of the intrinsic scatter in the SFL must come from the scatter in the SFR-L(Hα) calibration.

Charlot & Longhetti (2001) show that SFRs derived from Hα alone present a large scatter when compared to SFRs derived from full spectral fitting of the stellar populations and nebular emission of a sample of 92 nearby star-forming galaxies. Recently, the detection of widespread UV emission beyond the Hα brightness profile cutoff in the outer disks of many nearby galaxies (Gil de Paz et al., 2005; Thilker et al., 2005; Boissier et al., 2007) , has raised questions about the proportionality between the Hα emission and the SFR in the low star-formation regime. Incomplete sampling of the IMF in low-mass embedded clusters has been proposed to explain the discrepancy between Hα and UV surface brightness profiles (e.g. Pflamm-Altenburg & Kroupa, 2008). Under this scenario the Hα emission fails to tracing star-formation in low mass clusters where statistical fluctuations can translate into a lack of massive ionizing stars, and the SFR-L(Hα) becomes non-linear in the low star-formation regime (Pflamm-Altenburg et al., 2007), which might enhance the downward scatter in our SFL measurements. This issue is beyond the scope of the current paper, but we intend to investigate the implications of applying non-linear SFR-L(Hα) to our data in future works.

In this paper we have established the method for studying the spatially resolved SFL using wide integral field spectroscopy, and have set new constrains on important quantities like the slope, normalization, and intrinsic scatter of the SFL. As mentioned in §1, this data forms part of an undergoing large scale IFU survey of nearby galaxies. VENGA will map the disks of $\sim$20 nearby spiral galaxies to radius much larger than those sampled by the data

presented here. In the future, we will extend this type of study to a larger set of galaxies spanning a range in Hubble types, metallicities, and star-formation activities. This will help us to sample a larger dynamical range in gas surface densities. The later requires the observation of much denser environments, like the ones present in starburst galaxies, to extend the observed SFL to higher densities. Deeper CO observations that map the molecular gas out to large radii will be necessary to extend the sampled range to lower densities. This is of great importance, since a proper characterization of the shape of the total gas SFL is necessary in order to distinguish between different star-formation models.

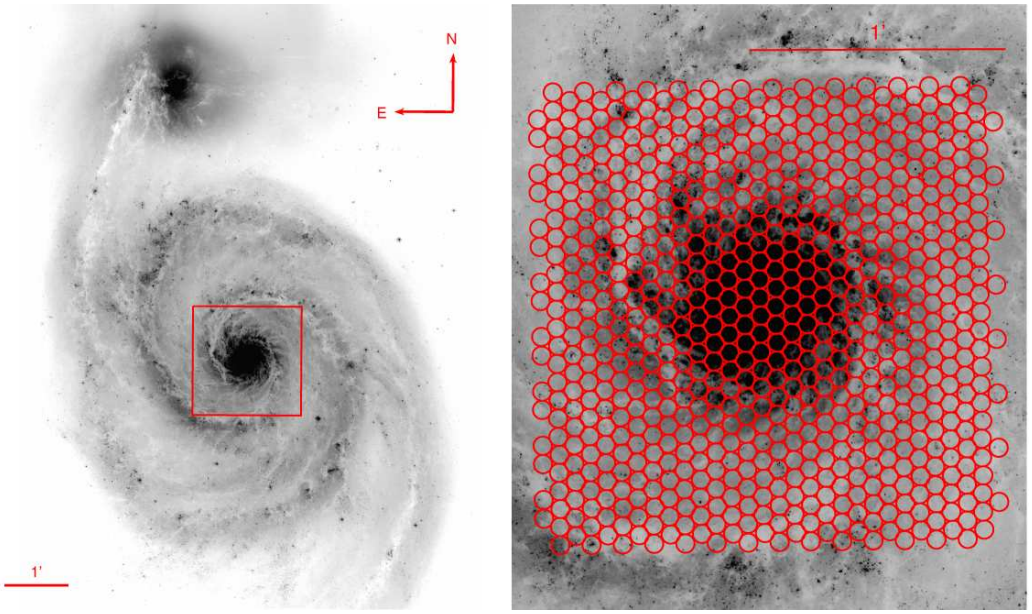

Figure 3.1 *Left:* HST+ACS V-band image of NGC5194 and its companion NGC 5195 (Mutchler et al., 2005). The central 4.1×4.1 kpc^2 region sampled by the $1.7' \times 1.7'$ VIRUS-P field of view is marked in red. *Right:* Map of the 738 regions sampled by VIRUS-P in the 3 dither positions. Each region has a diameter of $4.3''$ corresponding to $\sim$170 pc at the distance of NGC5194.

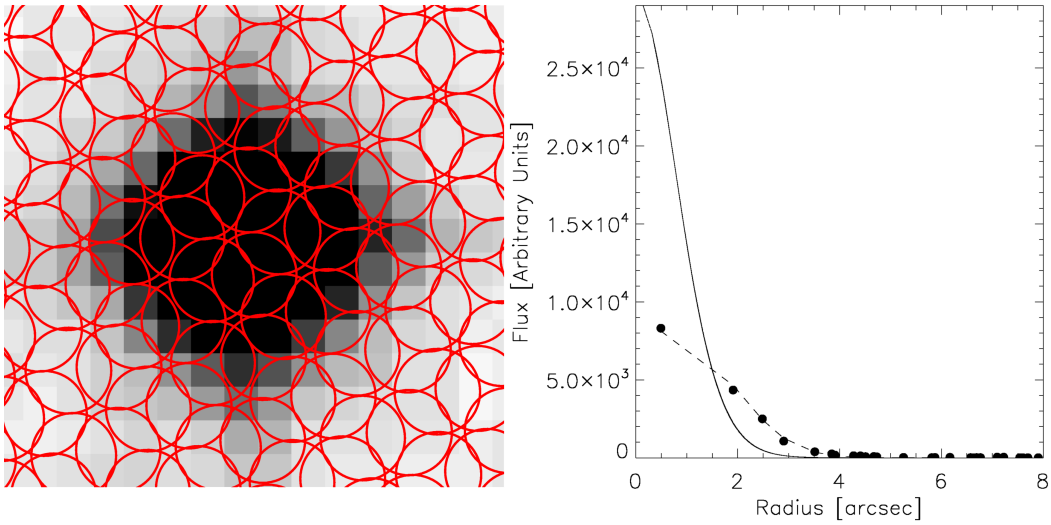

Figure 3.2 *Left:* DSS image of Feige 34. Superimpossed is the 6 dither position pattern used to observe spectro-photometric standard stars. *Right:* Flux measured by each fiber as a function of its distance to the PSF centroid (filled circles). Also shown are the best-fitted Moffat PSF (solid line), and its fiber-sampled light distribution (dashed line).

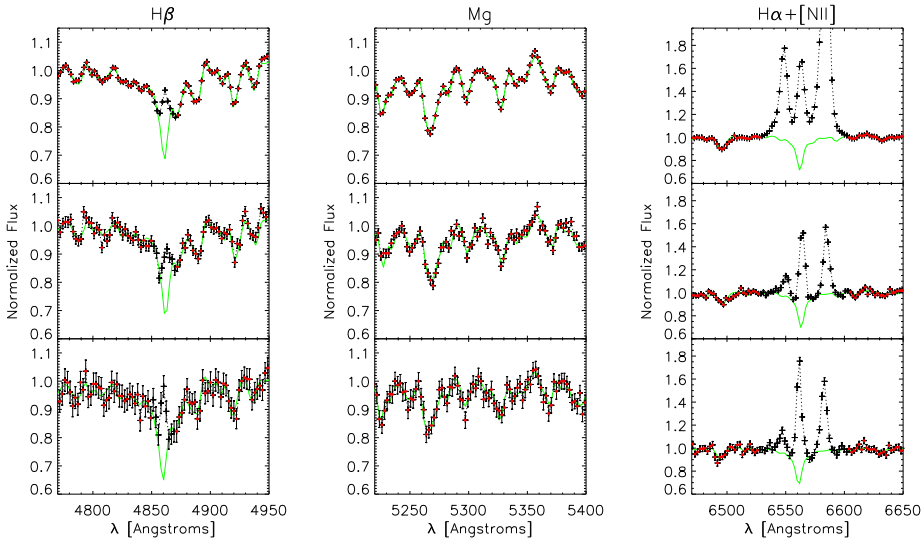

Figure 3.3 Continuum normalized spectra around the Hβ, MgII, and Hα features for 3 regions having the highest, median and lowest (top, middle, bottom) S/N per resolution element in the continuum. Crosses show the data with error bars. Red crosses mark the data points used to fit the best linear combination of stellar templates (green solid line). Black crosses were masked in the fit due to the presence of nebular emission.

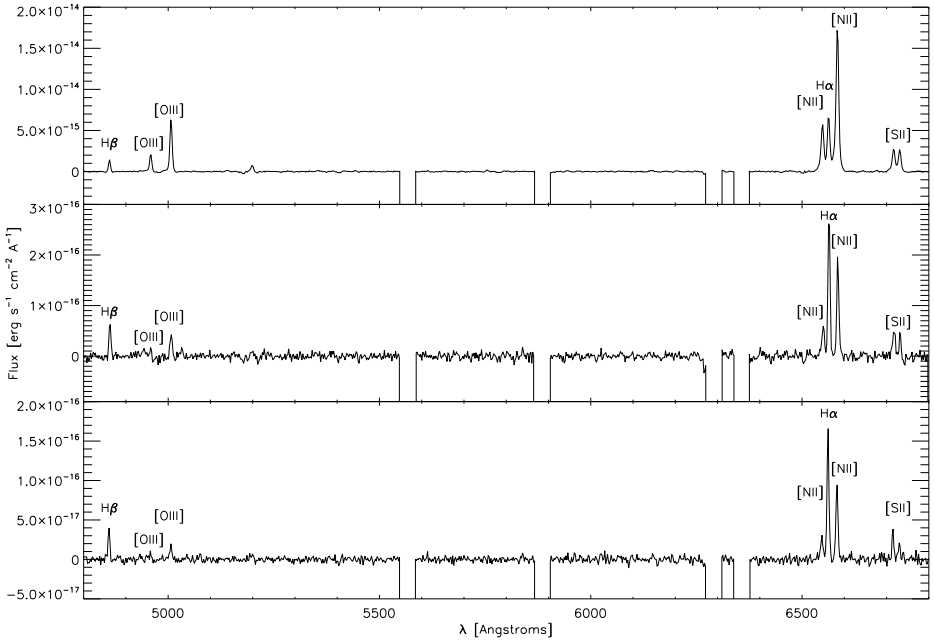

Figure 3.4 Nebular emission spectrum of the same regions shown in Figure 3.3, obtained by subtracting the best-fitted linear combination of stellar templates from the observed spectrum. Masked parts of the spectra correspond to the regions around strong night sky emission lines showing background subtraction residuals.

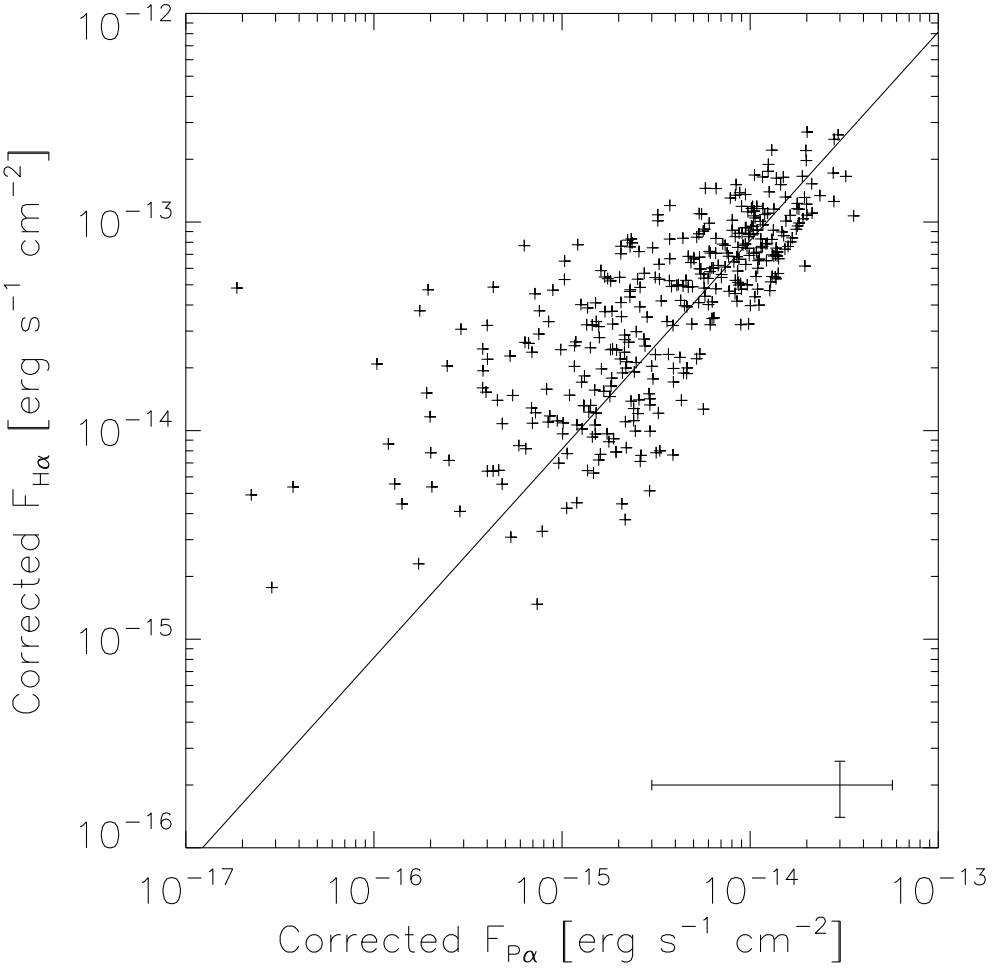

Figure 3.5 Hα versus Paα fluxes of all regions showing 5σ detections of Paα emission in the NICMOS narrow-band image. Fluxes are corrected for dust extinction using the Balmer decrement derived values. The solid line shows the Hα/Paα=8.15 ratio predicted by recombination theory. Median error bars for the corrected fluxes are shown.

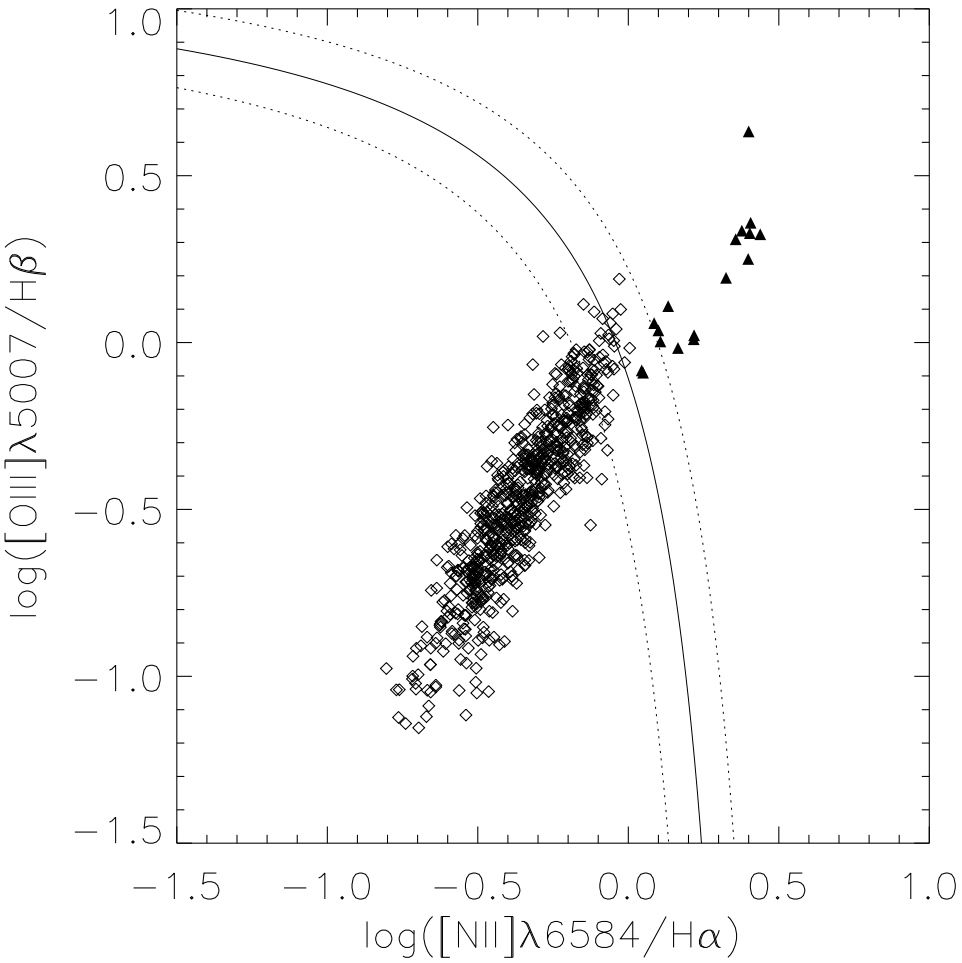

Figure 3.6 [NII]λ6584/Hα versus [OIII]λ5007/Hβ line ratio for the 735 regions. The solid line marks the theoretical threshold of Kewley et al. (2001) separating AGNs from star-forming galaxies. Dotted lines mark the $\pm$0.1 dex uncertainty in the threshold modeling. The 17 regions above the threshold and having angular distances to the galaxy nucleus of $< 15''$ are flagged as "AGN affected" and are shown as filled triangles. Open diamonds show the 718 regions unaffected by AGN contamination used to construct the SFL.

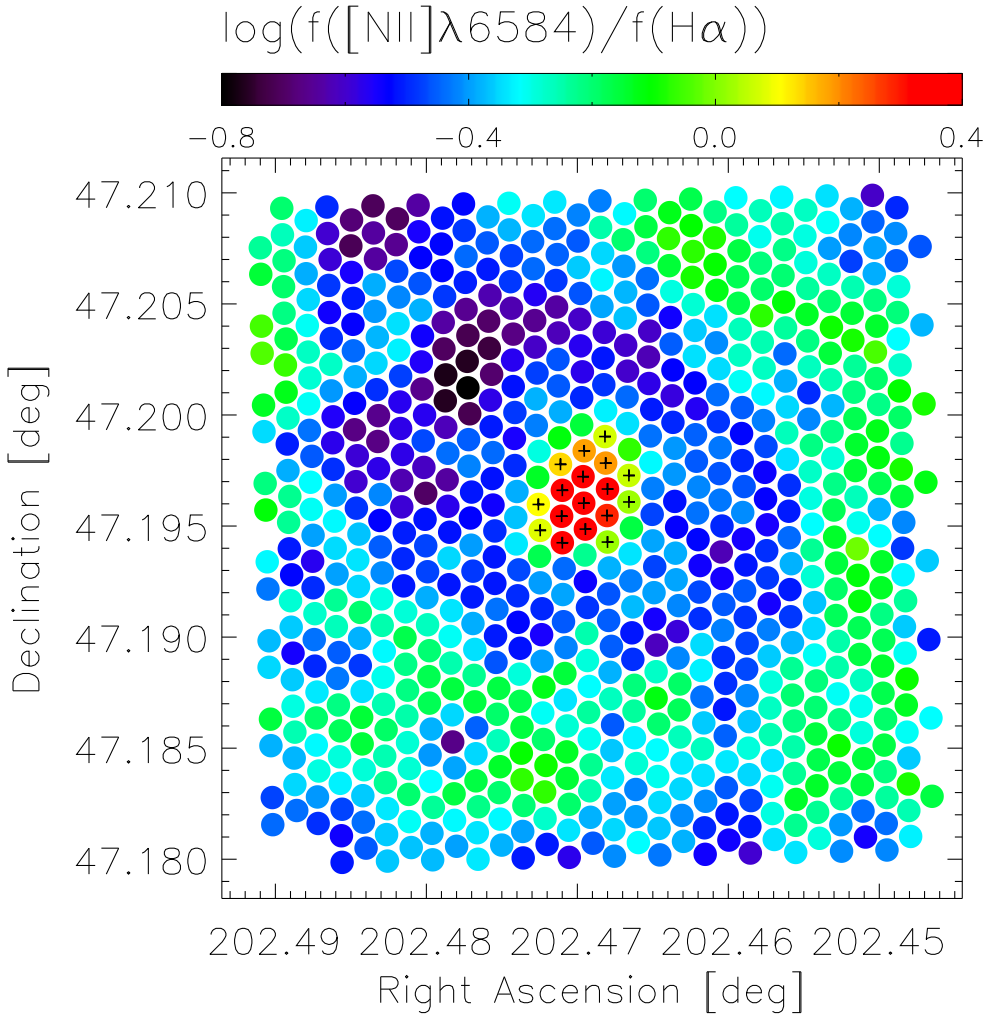

Figure 3.7 Map of the [NII]λ6584/Hα emission line ratio in the central region of NGC 5194. Regions flagged as "AGN affected" are marked by black crosses.

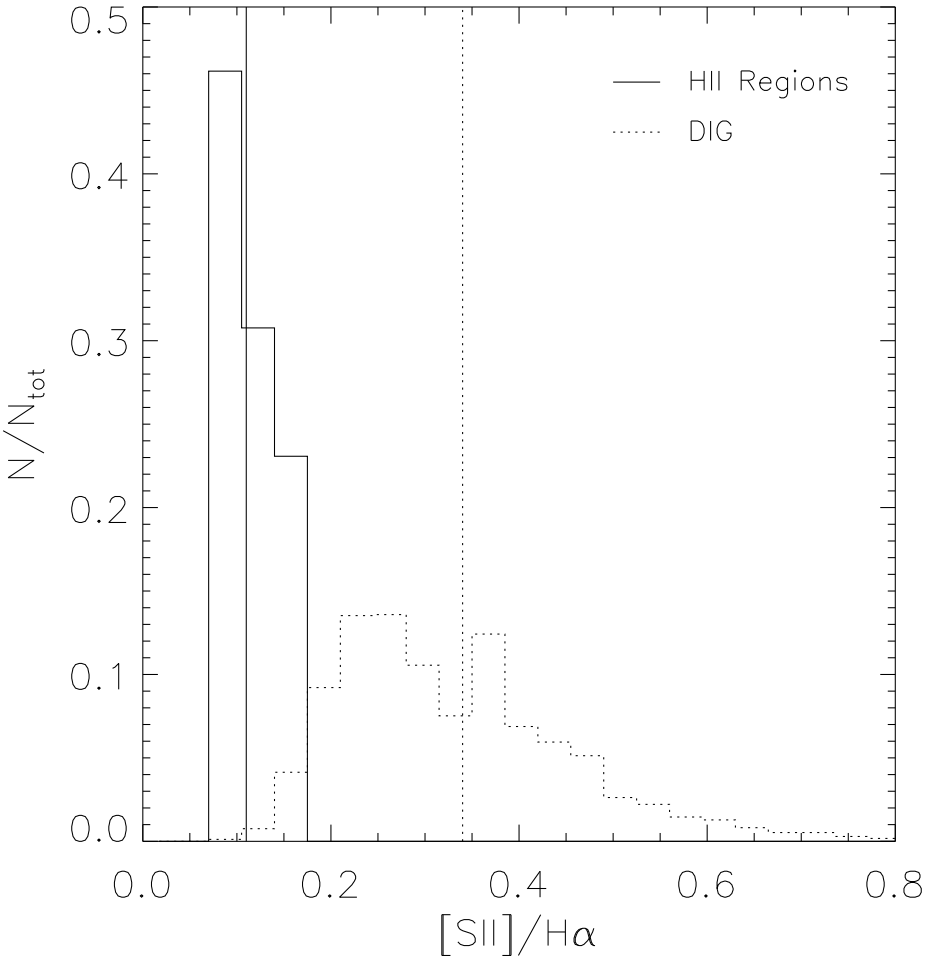

Figure 3.8 Histogram of the [SII]/Hα of H II regions (solid) and pointings towards DIG (dotted) in the Milky Way as measured by WHAM (Madsen et al., 2006). Vertical lines mark the mean values for the two distributions.

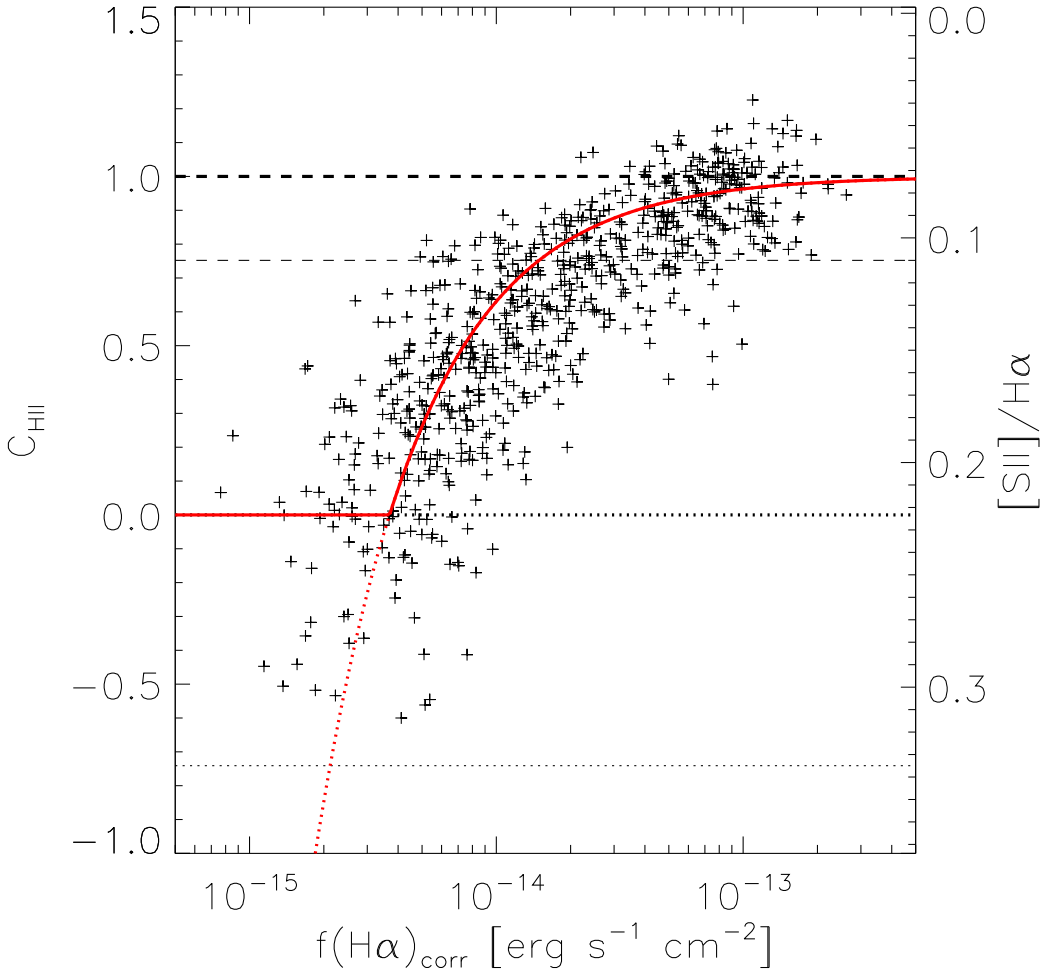

Figure 3.9 Observed [SII]/Hα emission line ratio for the 718 regions unaffected by AGN contamination. The thin dashed and dotted lines show the mean ratio observed in H II regions and pointings towards the DIG in the Milky Way respectively. The thick dashed and dotted lines show the former ratios scaled down by a factor $Z' = 1.0/1.5$. The left axis shows the fraction of the flux coming from H II regions in the disk given by Equation 3.8. The solid red curve shows the DIG correction applied to the data given by Equation 3.9, and the continuation of the function to fluxes lower than f_0 is marked by the dashed red line.

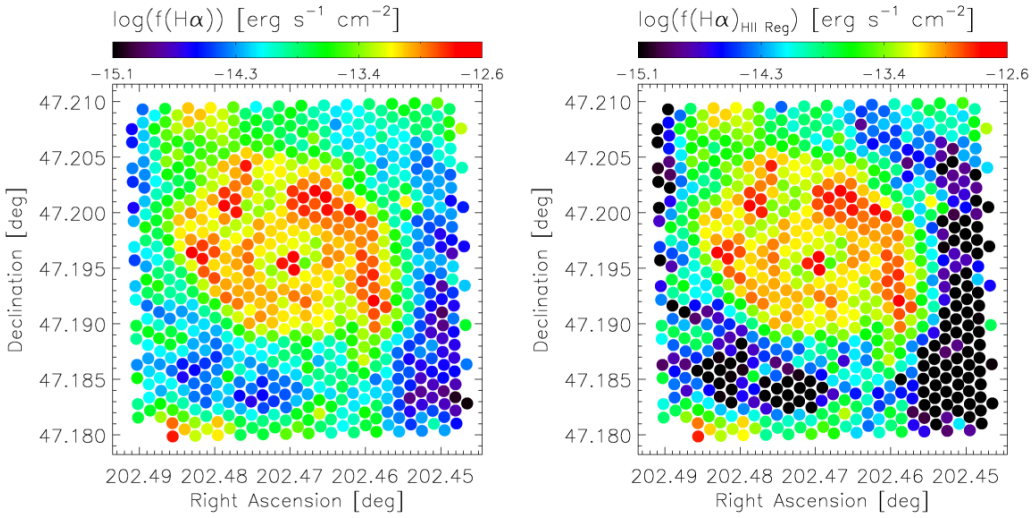

Figure 3.10 *Left:* Map of the extinction corrected Hα nebular emission flux in the central 4.1×4.1 kpc^2 of NGC 5194. *Right:* Same map after removing the DIG contribution to the Hα emission line flux, that is, showing only the flux coming from H II regions in the disk of NGC 5194.

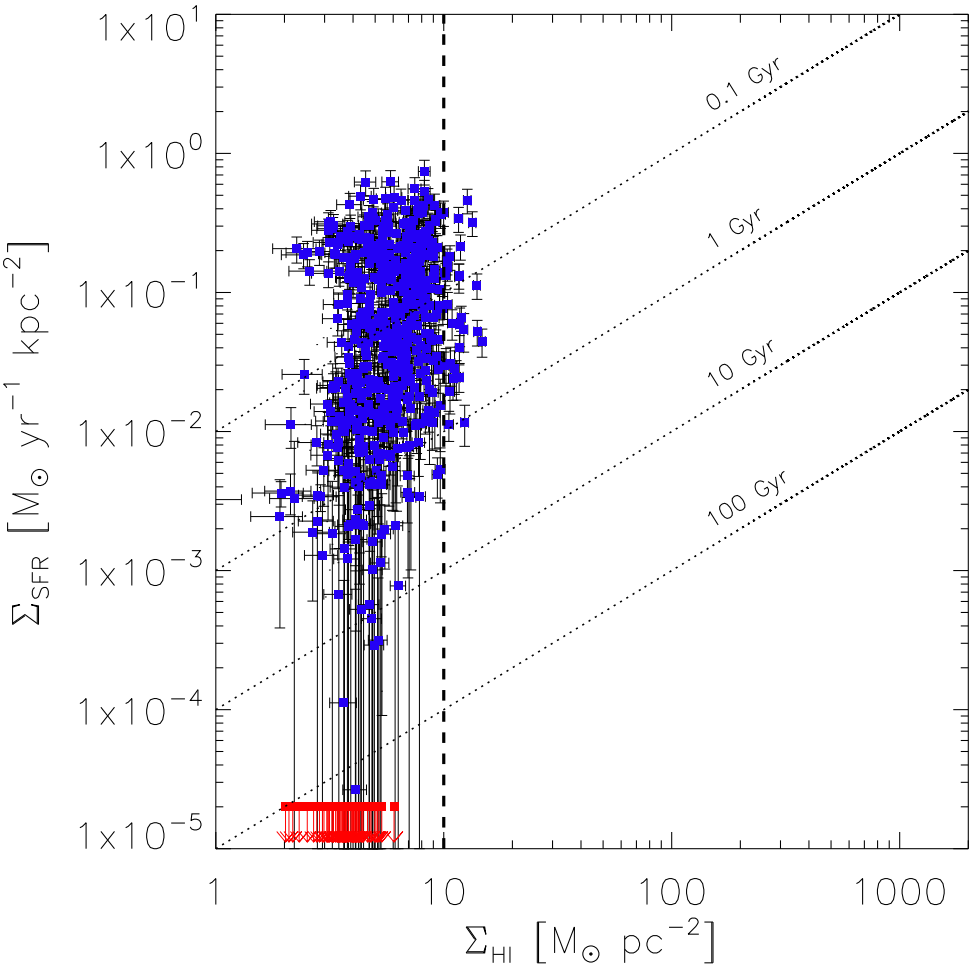

Figure 3.11 Atomic gas suface density versus SFR surface density for the 718 regions unaffected by AGN contamination. Upper limits in Σ_{SFR} correspond to regions with $C_{HII} = 0$. The vertical dashed line marks the HI to H_2 transition threshold at 10 $M_\odot pc^{-2}$. The diagonal dotted lines correspond to constant depletion timescales $\tau = \mathrm{SFE}^{-1}$ of 0.1, 1, 10 and 100 Gyr.

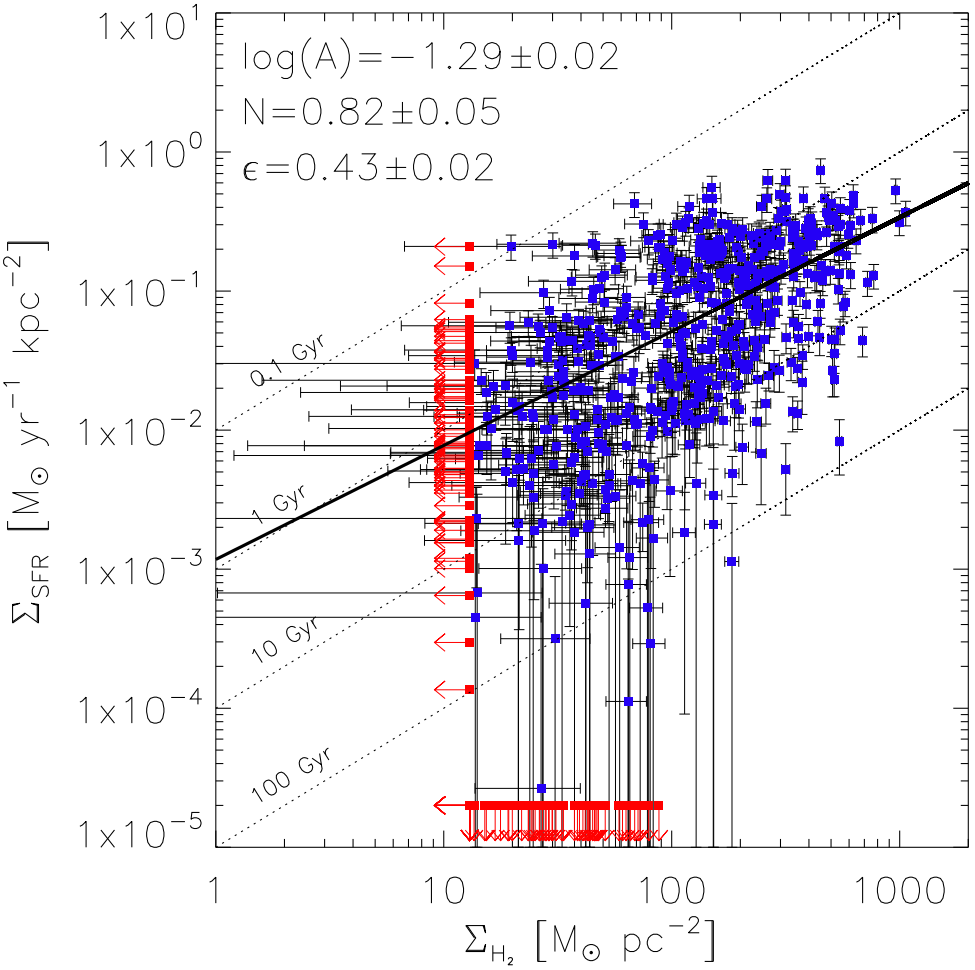

Figure 3.12 Molecular gas suface density versus SFR surface density for the 718 regions unaffected by AGN contamination. Upper limits in Σ_{SFR} correspond to regions with $C_{HII} = 0$. Upper limits in Σ_{H_2} correspond to regions with non-detection in CO at the 1σ level. The diagonal dotted lines correspond to constant depletion timescales $\tau = \mathrm{SFE}^{-1}$ of 0.1, 1, 10 and 100 Gyr. Also shown is the best-fitted power law from the Monte Carlo method (black solid line), and the best-fitted parameters.

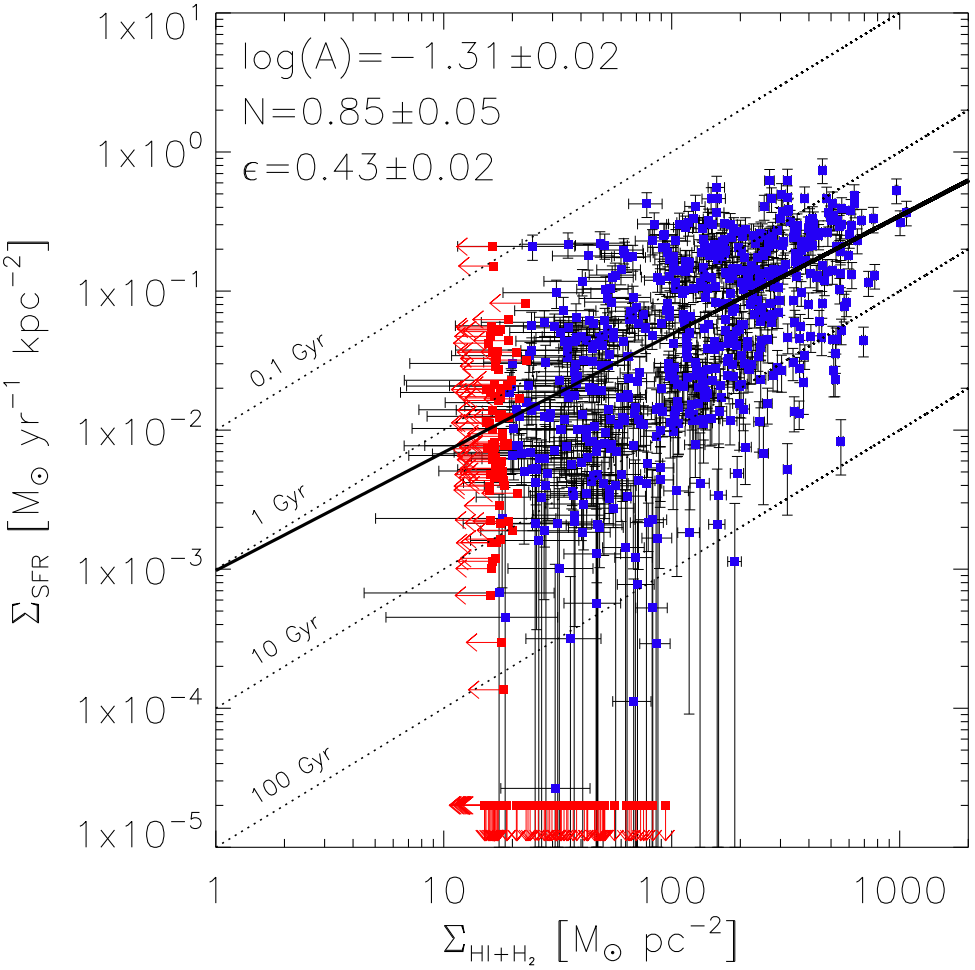

Figure 3.13 Total gas suface density versus SFR surface density for the 718 regions unaffected by AGN contamination. Upper limits in Σ_{SFR} correspond to regions with $C_{HII} = 0$. Upper limits in Σ_{HI+H_2} correspond to regions with non-detection in CO at the 1σ level. The diagonal dotted lines correspond to constant depletion timescales $\tau = \mathrm{SFE}^{-1}$ of 0.1, 1, 10 and 100 Gyr. Also shown is the best-fitted power law from the Monte Carlo method (black solid line), and the best-fitted parameters.

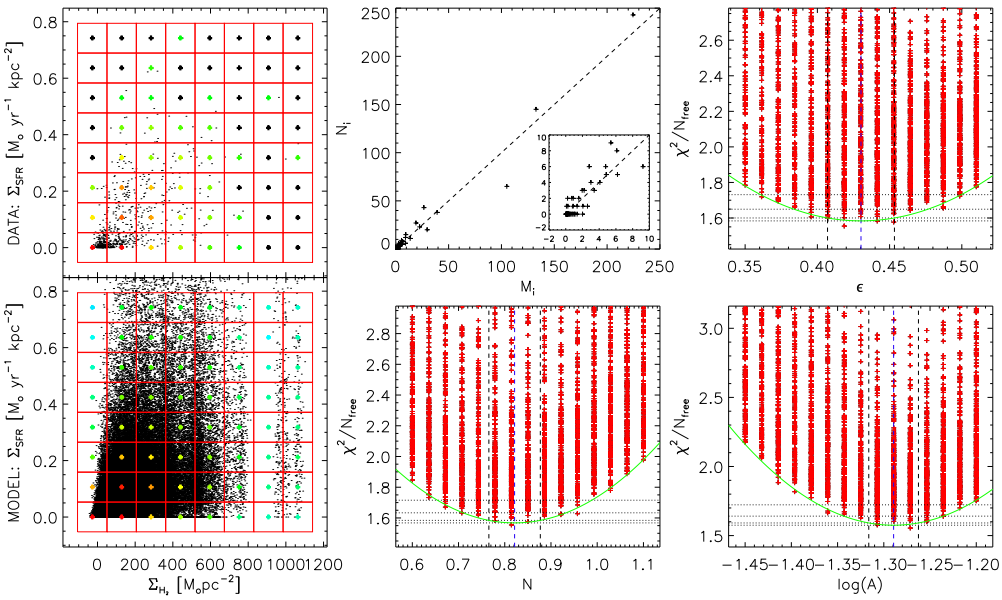

Figure 3.14 *Left:* The observed molecular SFL in linear space (top), together with the 200 Monte Carlo realizations of the data for the best-fitted parameters (bottom). The grid used to compare the model to the data is shown in red, and each box in the grid shows a cross, color-coded according to the number of points in the grid (with red corresponding to the highest value and black corresponding to zero). *Center-Top:* Number of data-points per grid elements in the model versus the data. *Center-Bottom and Right:* Reduced χ^2 for each of the three free parameter in the fit (A, N, and ϵ), marginalized over the other two parameters. Red crosses show the χ^2 obtained for each sampled combination of parameters. The best-fitted quadratic function to the minimum χ^2 is shown in green. The best-fitted χ^2, together with the 1σ, 2σ, and 3σ levels are shown as horizontal dotted lines. The blue and black vertical dashed lines marks the best-fitted parameter and its 1σ uncertainty respectively.

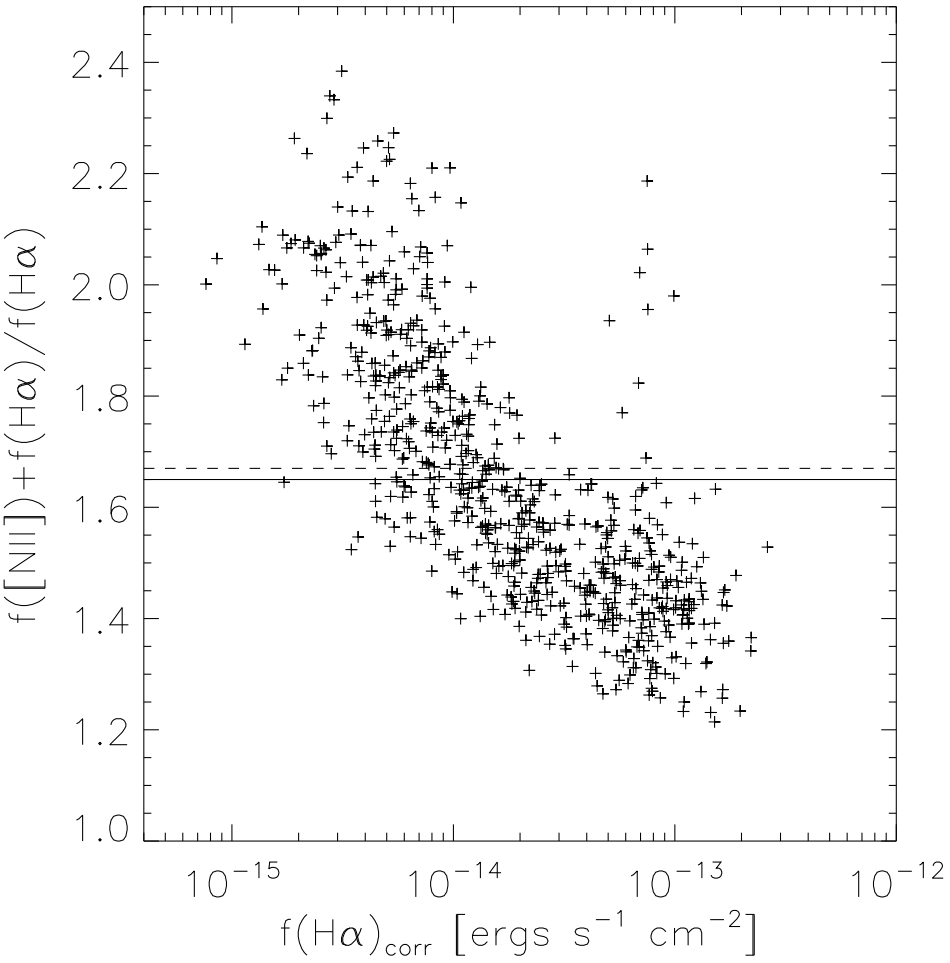

Figure 3.15 ([NII]λ6548+[NII]λ6584+Hα)/Hα ratio as a function of extinction corrected Hα flux for the 718 regions under study. The solid line marks the observed mean value of 1.65. The dashed line marks the 1.67 value expected by assuming line ratio of [NII]λ6584/Hα=0.5 and [NII]λ6548/[NII]λ6584=0.335.

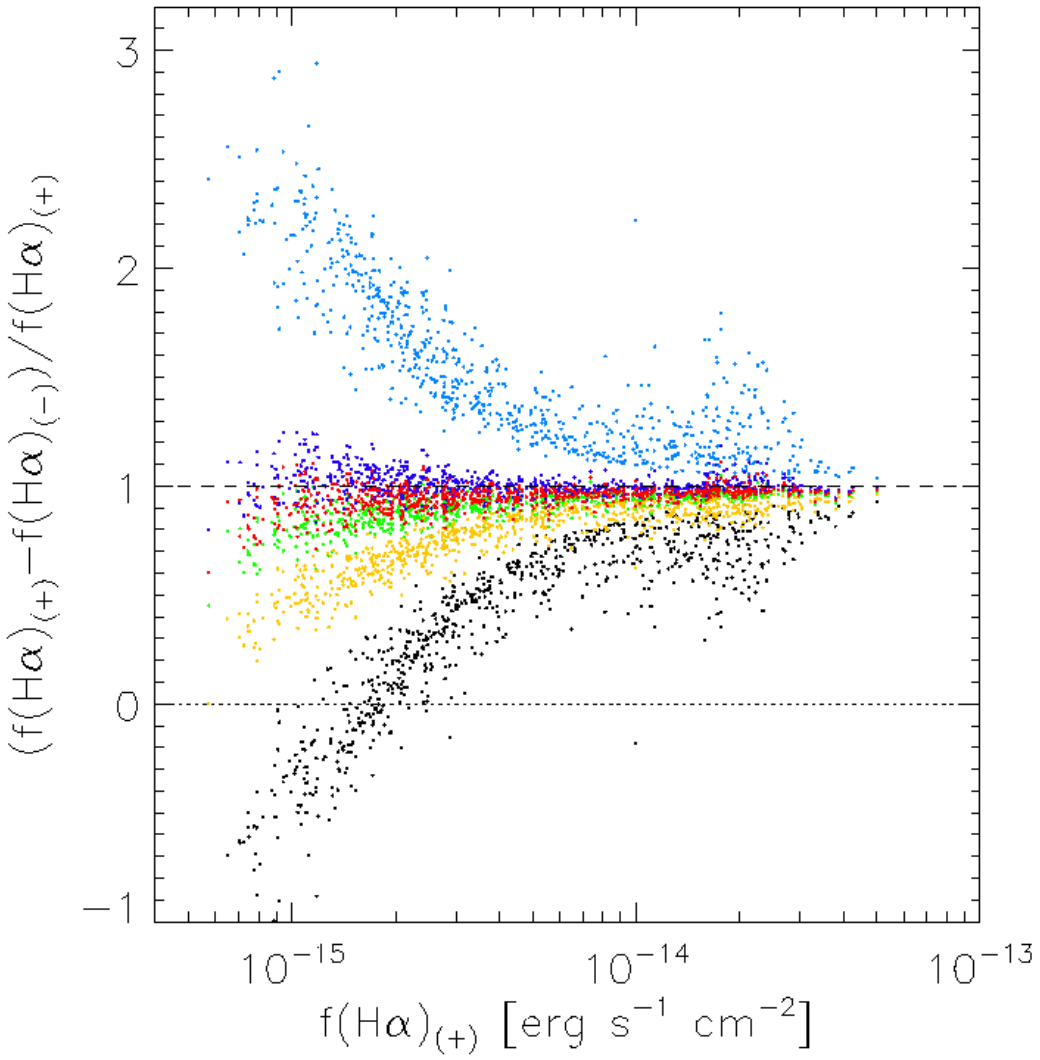

Figure 3.16 Bias introduced by the missestimation of the strength of the Hα absorption feature or equivalently of the continuum level. Black dots show show the fraction of the observed flux that we would observe if the stellar absorption was not considered at all. Red dots show the same fluxes corrected using a constant absorption EW=-2.4Å. Dark blue and green dots correspond to understimations and overestimations of the continuum by a 10%. Light blue and orange dots correspond to understimations and overestimations of the continuum by a 50%.

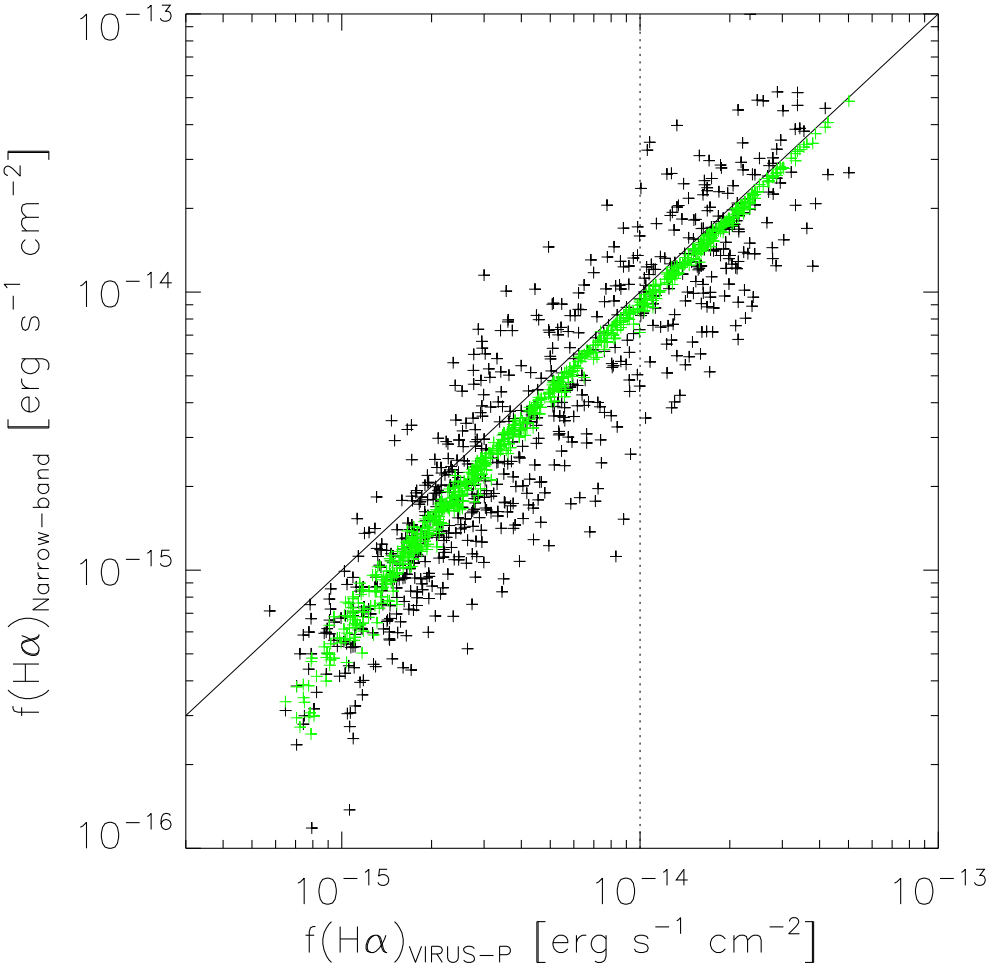

Figure 3.17 VIRUS-P observed Hα fluxes (before dust exticntion correction) versus Hα fluxes measured in the continuum subtracted image from Calzetti et al. (2005) (balck crosses). Data-points to the right of the vertical dotted line were used to scale the narrow-band fluxes in order to account for flux calibration and apperture discrepancies. The green crosses show the Hα fluxes that would have been measured by VIRUS-P if the continuum would have been overestimated by a 30% (see Figure 3.16).

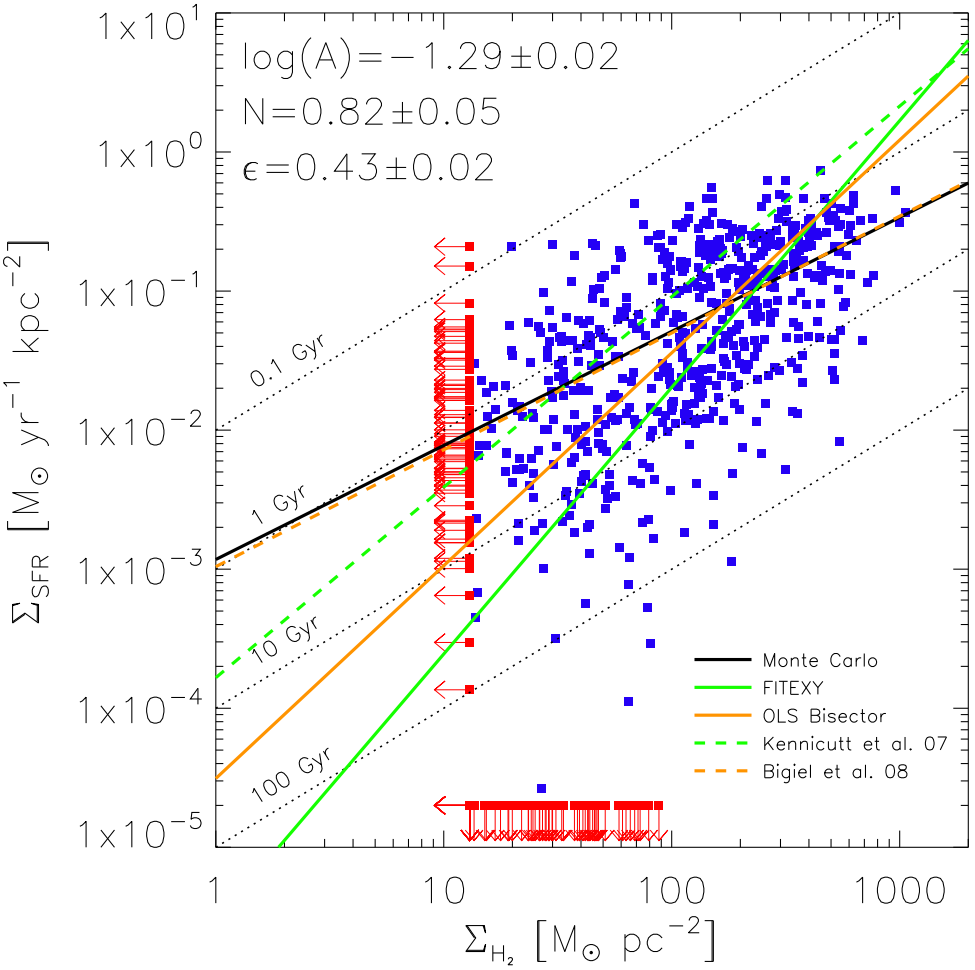

Figure 3.18 Molecular gas SFL as measured by VIRUS-P. Symbols are the same as in Figure 3.12. The black solid line shows our best fitted power-law obtained using the Monte Carlo method described in §9.1. Previous measurements by Kennicutt et al. (2007) and Bigiel et al. (2008) are shown as the green and orange dahsed lines respectively. Also shown are fits to our data (rejecting upper limits) using the FITEXY (solid green line) and OLS bisector (solid orange line) methods.

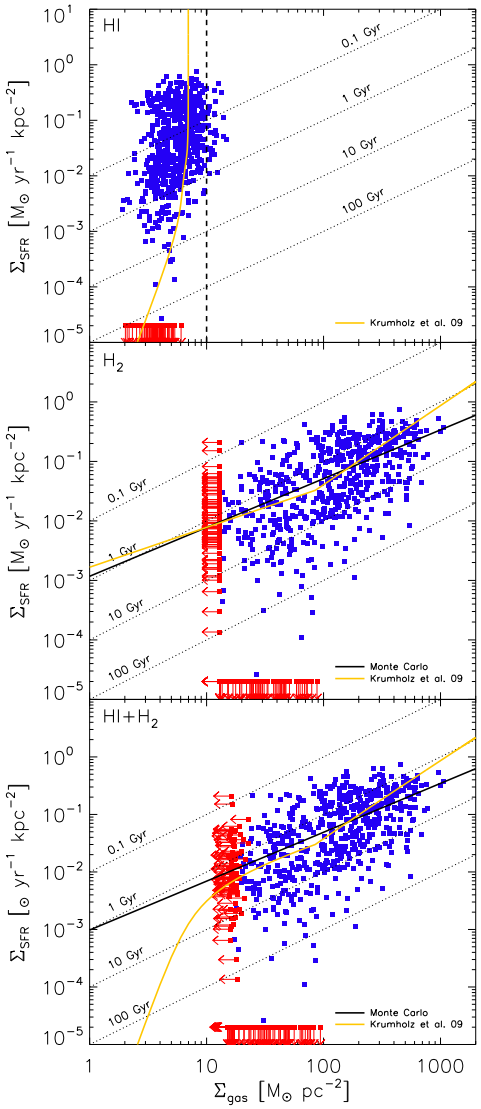

Figure 3.19 Comparison of the observed SFL for atomic gas (top), molecular gas (center), and total gas (bottom) and the theoretical model proposed by Krumholz et al. (2009b). Symbols are the same as in Figures 3.11, 3.12, and 3.12. The solid orange line show the Krumholz et al model for $Z' = 1.0/1.5$ and $c = 4$.

Table 3.1. Nebular Emission Line Fluxes, Gas Surface Densities, and SFR Surface Densities

ID	Equatorial Coordinates		Hβ	[NII]λ6548	Hα	[NII]λ6584	[SII]λ6717	[SII]λ6731	Σ_{H2}	Σ_{HI}	Σ_{SFR}
	α	δ			10^{-16} erg s^{-1}cm^{-2}				$M_{\odot}pc^{-2}$	$M_{\odot}pc^{-2}$	$M_{\odot}yr^{-1}kpc^{-2}$
1	13:29:48.11	+47:12:35.6	12.57±0.11	6.45±0.42	69.73±0.59	17.63±0.43	6.89±0.23	4.95±0.23	10.71±13.00	9.75±0.59	0.08181±0.01652
2	13:29:48.83	+47:12:35.5	4.22±0.41	4.94±0.46	29.44±0.54	13.90±0.48	4.77±0.43	3.12±0.43	127.44±13.00	12.25±0.59	0.05385±0.01664
3	13:29:49.55	+47:12:35.3	6.05±0.25	5.89±0.43	36.35±0.52	17.82±0.47	6.02±0.10	4.63±0.10	399.25±13.00	8.73±0.59	0.04681±0.01063
4	13:29:50.28	+47:12:35.2	4.78±0.25	4.42±0.53	27.71±0.59	13.85±0.55	4.11±0.10	3.02±0.10	174.20±13.00	10.05±0.59	0.02975±0.00752
5	13:29:51.00	+47:12:35.0	2.94±0.01	4.88±0.55	16.37±0.54	11.66±0.54	3.19±0.03	2.44±0.03	127.30±13.00	10.53±0.59	0.01123±0.00274
6	13:29:51.72	+47:12:34.8	4.75±0.04	5.77±0.29	24.74±0.31	16.43±0.30	4.64±0.10	2.99±0.10	131.55±13.00	7.08±0.59	0.01791±0.00369
7	13:29:52.44	+47:12:34.7	10.97±0.54	7.33±0.27	54.63±0.36	21.14±0.30	6.39±0.26	4.75±0.25	177.73±13.00	8.80±0.59	0.04645±0.01083
8	13:29:53.16	+47:12:34.5	4.62±0.48	4.20±0.44	27.62±0.50	13.26±0.47	4.30±0.48	2.47±0.45	168.82±13.00	8.98±0.59	0.03255±0.01115
9	13:29:53.89	+47:12:34.3	4.99±0.44	4.08±0.25	23.63±0.28	11.96±0.27	4.13±0.47	2.97±0.48	234.42±13.00	7.61±0.59	0.01148±0.00453
10	13:29:54.61	+47:12:34.2	14.64±0.58	7.49±0.53	77.49±0.77	23.63±0.59	8.51±0.27	6.00±0.27	156.60±13.00	10.39±0.59	0.08200±0.01802
11	13:29:55.33	+47:12:34.0	17.90±0.57	8.67±0.43	110.78±0.74	25.85±0.49	9.25±0.25	6.34±0.24	60.35±13.00	7.20±0.59	0.17611±0.03717
12	13:29:56.05	+47:12:33.9	26.21±0.65	9.79±0.27	151.56±0.50	29.99±0.32	9.70±0.11	6.57±0.10	19.73±13.00	4.79±0.59	0.20946±0.04325
13	13:29:56.78	+47:12:33.7	5.97±0.43	3.54±0.43	35.11±0.55	11.43±0.46	3.37±0.41	2.36±0.41	6.45±13.00	2.77±0.59	0.04218±0.01144
14	13:29:57.50	+47:12:33.5	1.65±0.35	3.13±0.11	9.08±0.08	6.03±0.08	2.10±0.08	1.49±0.08	65.49±13.00	3.78±0.59	0.00121±0.00489
15	13:29:47.74	+47:12:29.4	4.11±0.41	3.99±0.44	29.62±0.54	11.94±0.47	4.03±0.22	2.56±0.22	102.00±13.00	11.76±0.59	0.05899±0.01827
16	13:29:48.46	+47:12:29.2	5.33±0.48	4.19±0.26	30.08±0.31	11.94±0.27	3.97±0.46	2.94±0.49	116.73±13.00	10.70±0.59	0.03078±0.00962
17	13:29:49.18	+47:12:29.0	4.16±0.48	4.29±0.49	23.25±0.50	12.24±0.48	3.53±0.49	2.52±0.49	191.33±13.00	7.41±0.59	0.02067±0.00838
18	13:29:49.90	+47:12:28.9	4.46±0.54	4.26±0.55	24.35±0.58	12.58±0.57	4.03±0.04	2.92±0.04	107.58±13.00	5.40±0.59	0.02056±0.00859
19	13:29:50.62	+47:12:28.7	2.90±0.26	5.82±0.49	17.49±0.49	15.35±0.50	4.41±0.11	3.36±0.11	58.22±13.00	6.21±0.59	0.01711±0.00618
20	13:29:51.35	+47:12:28.6	2.66±0.49	4.35±0.29	13.53±0.29	12.24±0.30	4.35±0.30	2.49±0.27	127.99±13.00	5.12±0.59	0.00415±0.00540
21	13:29:52.07	+47:12:28.4	4.22±0.46	5.92±0.29	25.72±0.31	17.14±0.30	4.28±0.51	3.49±0.53	170.03±13.00	5.87±0.59	0.03125±0.01090
22	13:29:52.79	+47:12:28.2	8.83±0.52	5.32±0.52	45.38±0.66	16.26±0.56	5.23±0.26	3.87±0.28	207.98±13.00	6.75±0.59	0.04023±0.01007
23	13:29:53.51	+47:12:28.1	7.02±0.56	4.31±0.50	34.93±0.56	12.86±0.51	4.50±0.01	2.90±0.01	68.23±13.00	4.17±0.59	0.02578±0.00782
24	13:29:54.23	+47:12:27.9	6.14±0.29	5.20±0.13	36.11±0.14	12.94±0.12	4.55±0.54	3.15±0.55	207.04±13.00	6.91±0.59	0.04371±0.01007
25	13:29:54.96	+47:12:27.7	13.46±0.55	8.57±0.27	86.25±0.41	26.44±0.30	8.65±0.11	6.15±0.10	184.39±13.00	9.14±0.59	0.14613±0.03182
26	13:29:55.68	+47:12:27.6	24.96±0.64	9.80±0.52	123.07±0.88	27.29±0.59	9.88±0.51	7.15±0.50	96.32±13.00	7.04±0.59	0.11532±0.02399
27	13:29:56.40	+47:12:27.4	21.15±0.62	7.97±0.29	112.54±0.46	21.82±0.30	7.24±0.27	5.27±0.27	49.28±13.00	5.51±0.59	0.12542±0.02629
28	13:29:57.12	+47:12:27.2	2.91±0.36	3.66±0.38	22.94±0.43	10.45±0.39	3.18±0.42	2.06±0.38	72.04±13.00	4.81±0.59	0.05493±0.01943
29	13:29:57.84	+47:12:27.1	2.08±0.33	2.09±0.40	9.18±0.37	5.57±0.36	1.73±0.07	1.06±0.08	60.84±13.00	4.20±0.59	0.00000±0.00236
30	13:29:48.08	+47:12:22.9	3.63±0.42	2.67±0.24	19.55±0.26	8.28±0.25	3.43±0.10	1.96±0.09	152.16±13.00	9.14±0.59	0.01370±0.00621
31	13:29:48.80	+47:12:22.8	3.04±0.03	3.55±0.55	15.04±0.53	8.45±0.52	3.11±0.11	2.23±0.10	184.29±13.00	9.38±0.59	0.00489±0.00157
32	13:29:49.53	+47:12:22.6	3.53±0.03	4.25±0.30	19.03±0.30	12.46±0.30	4.32±0.11	2.75±0.11	63.33±13.00	5.10±0.59	0.01308±0.00278
33	13:29:50.25	+47:12:22.4	3.25±0.49	3.80±0.29	17.24±0.31	12.04±0.30	3.45±0.53	2.59±0.52	0.00±13.00	3.37±0.59	0.01004±0.00649
34	13:29:50.97	+47:12:22.3	2.70±0.10	4.70±0.55	14.63±0.55	12.60±0.56	3.20±0.27	2.04±0.27	14.38±13.00	6.89±0.59	0.00773±0.00251
35	13:29:51.69	+47:12:22.1	7.42±0.47	5.81±0.62	36.36±0.65	13.56±0.58	4.38±0.55	2.92±0.55	92.42±13.00	7.92±0.59	0.02603±0.00706
36	13:29:52.41	+47:12:21.9	6.47±0.30	5.37±0.04	31.56±0.05	15.43±0.04	4.42±0.11	2.77±0.11	106.36±13.00	5.23±0.59	0.02096±0.00507
37	13:29:53.14	+47:12:21.8	8.94±0.56	5.57±0.51	46.62±0.63	15.80±0.52	5.54±0.28	3.69±0.28	149.83±13.00	4.45±0.59	0.04334±0.01101
38	13:29:53.86	+47:12:21.6	14.87±0.60	9.17±0.58	73.39±0.78	24.92±0.62	7.90±0.55	5.91±0.55	105.98±13.00	6.14±0.59	0.06463±0.01434
39	13:29:54.58	+47:12:21.5	11.83±0.31	7.24±0.56	66.49±0.76	21.19±0.60	7.02±0.28	4.61±0.29	212.71±13.00	8.02±0.59	0.07998±0.01679
40	13:29:55.30	+47:12:21.3	11.02±0.53	8.10±0.54	62.21±0.72	22.01±0.58	7.32±0.11	5.07±0.11	179.39±13.00	8.19±0.59	0.07508±0.01720
41	13:29:56.03	+47:12:21.1	5.35±0.03	4.64±0.46	31.37±0.51	13.25±0.45	4.32±0.47	2.89±0.47	7.63±13.00	7.82±0.59	0.03639±0.00748
42	13:29:56.75	+47:12:21.0	8.48±0.51	5.24±0.26	50.10±0.35	16.97±0.29	5.69±0.26	3.86±0.25	61.97±13.00	5.18±0.59	0.06553±0.01595
43	13:29:57.47	+47:12:20.8	1.96±0.08	2.97±0.42	11.87±0.42	8.03±0.43	2.22±0.03	1.70±0.03	40.68±13.00	2.78±0.59	0.00834±0.00268
44	13:29:47.71	+47:12:16.6	1.53±0.41	2.39±0.27	10.92±0.26	7.11±0.26	2.12±0.46	1.31±0.49	81.06±13.00	7.17±0.59	0.01463±0.01362
45	13:29:48.43	+47:12:16.5	2.13±0.44	3.12±0.51	10.63±0.51	7.94±0.51	2.88±0.28	1.83±0.25	78.23±13.00	4.35±0.59	0.00053±0.00465
46	13:29:49.15	+47:12:16.3	3.57±0.48	4.68±0.54	17.90±0.55	13.74±0.55	4.19±0.50	3.21±0.51	41.67±13.00	3.46±0.59	0.00834±0.00539
47	13:29:49.87	+47:12:16.1	2.88±0.10	4.69±0.56	14.14±0.55	12.59±0.57	3.42±0.11	2.45±0.11	11.18±13.00	2.82±0.59	0.00370±0.00174
48	13:29:50.60	+47:12:16.0	6.90±0.52	6.18±0.56	37.54±0.64	17.50±0.58	5.19±0.11	3.34±0.11	0.00±13.00	4.22±0.59	0.03696±0.01033
49	13:29:51.32	+47:12:15.8	12.37±0.57	8.19±0.13	73.77±0.17	21.63±0.13	6.53±0.12	4.57±0.12	48.41±13.00	5.57±0.59	0.10399±0.02325
50	13:29:52.04	+47:12:15.7	25.53±0.71	20.67±0.37	132.87±0.51	58.85±0.43	16.06±0.14	14.06±0.15	99.08±13.00	2.58±0.59	0.14240±0.02970

Table 3.1 (cont'd)

ID	Equatorial Coordinates	Hβ	[NII]λ6548	Hα	[NII]λ6584	[SII]λ6717	[SII]λ6731	Σ_{H2}	Σ_{HI}	Σ_{SFR}
51	13:29:52.76 +47:12:15.5	17.55±0.63	8.64±0.32	99.61±0.47	25.19±0.35	7.92±0.62	5.24±0.58	94.15±13.00	3.84±0.59	0.12807±0.02747
52	13:29:53.48 +47:12:15.3	31.91±0.68	12.37±0.67	163.01±1.08	36.31±0.75	10.93±0.14	8.34±0.14	91.14±13.00	6.17±0.59	0.16962±0.03484
53	13:29:54.21 +47:12:15.2	105.49±1.09	35.08±0.67	501.26±1.43	101.41±0.83	27.16±0.38	20.98±0.37	151.51±13.00	7.44±0.59	0.46222±0.09298
54	13:29:54.93 +47:12:15.0	23.08±0.66	11.38±0.60	141.86±0.98	33.01±0.68	11.29±0.31	7.26±0.30	257.65±13.00	8.36±0.59	0.22487±0.04699
55	13:29:55.65 +47:12:14.8	8.25±0.49	9.65±0.54	56.70±0.69	26.75±0.59	8.89±0.52	6.48±0.51	215.44±13.00	6.27±0.59	0.10967±0.02617
56	13:29:56.37 +47:12:14.7	13.18±0.55	7.18±0.30	63.25±0.38	18.86±0.30	6.49±0.04	4.07±0.03	26.45±13.00	6.03±0.59	0.05035±0.01129
57	13:29:57.09 +47:12:14.5	3.21±0.41	3.70±0.49	18.44±0.51	9.33±0.49	2.95±0.09	1.97±0.10	20.06±13.00	3.09±0.59	0.01577±0.00748
58	13:29:57.82 +47:12:14.4	0.96±0.03	2.05±0.44	6.47±0.43	6.09±0.44	1.69±0.08	0.90±0.09	35.74±13.00	1.91±0.59	0.00244±0.00206
59	13:29:48.06 +47:12:10.2	1.83±0.40	3.43±0.10	10.61±0.11	10.08±0.11	3.42±0.04	2.09±0.03	41.95±13.00	5.31±0.59	0.00479±0.00670
60	13:29:48.78 +47:12:10.0	4.43±0.48	4.85±0.44	19.58±0.47	14.39±0.48	4.72±0.27	2.62±0.27	18.68±13.00	3.84±0.59	0.00508±0.00357
61	13:29:49.50 +47:12:09.9	6.98±0.04	3.74±0.28	33.41±0.33	12.40±0.30	4.06±0.28	2.49±0.26	9.03±13.00	3.75±0.59	0.02137±0.00434
62	13:29:50.22 +47:12:09.7	4.86±0.28	5.11±0.34	24.00±0.32	13.41±0.33	3.10±0.57	1.93±0.54	16.93±13.00	3.85±0.59	0.01401±0.00405
63	13:29:50.94 +47:12:09.5	12.46±0.61	8.64±0.62	59.86±0.77	27.93±0.69	7.67±0.04	5.02±0.04	0.00±13.00	2.96±0.59	0.04723±0.01109
64	13:29:51.67 +47:12:09.4	58.16±0.92	23.02±0.75	295.17±1.33	71.18±0.89	22.09±0.40	15.89±0.39	115.19±13.00	3.12±0.59	0.31111±0.06310
65	13:29:52.39 +47:12:09.2	35.95±0.84	22.21±0.80	210.78±1.21	65.77±0.92	20.49±0.43	13.35±0.40	165.21±13.00	4.72±0.59	0.30470±0.06276
66	13:29:53.11 +47:12:09.0	16.54±0.67	11.53±0.37	98.18±0.48	34.93±0.40	9.19±0.68	6.66±0.69	283.91±13.00	6.02±0.59	0.14039±0.03061
67	13:29:53.83 +47:12:08.9	17.90±0.65	9.28±0.36	94.99±0.48	26.10±0.38	7.14±0.66	4.62±0.66	138.33±13.00	5.71±0.59	0.10356±0.02229
68	13:29:54.55 +47:12:08.7	69.80±1.12	19.44±0.18	332.04±0.31	57.90±0.20	13.33±0.42	11.14±0.43	75.14±13.00	8.67±0.59	0.30342±0.06149
69	13:29:55.28 +47:12:08.6	11.87±0.54	7.38±0.29	75.56±0.41	21.49±0.32	7.10±0.54	4.91±0.54	424.89±13.00	5.93±0.59	0.12489±0.02779
70	13:29:56.00 +47:12:08.4	6.41±0.11	6.04±0.28	36.01±0.33	16.59±0.30	6.01±0.27	4.24±0.27	135.68±13.00	7.57±0.59	0.03844±0.00791
71	13:29:56.72 +47:12:08.2	3.68±0.03	4.31±0.11	21.22±0.12	11.73±0.12	4.34±0.53	3.00±0.51	39.64±13.00	5.71±0.59	0.01996±0.00404
72	13:29:57.44 +47:12:08.1	1.65±0.42	2.94±0.51	8.93±0.47	8.20±0.48	2.36±0.09	2.14±0.11	0.00±13.00	3.02±0.59	0.00065±0.00578
73	13:29:47.68 +47:12:03.9	2.65±0.25	2.69±0.11	10.88±0.10	8.92±0.10	2.51±0.25	1.42±0.22	13.58±13.00	3.73±0.59	0.00000±0.00139
74	13:29:48.40 +47:12:03.7	3.99±0.10	3.99±0.52	18.84±0.54	12.08±0.53	3.02±0.03	2.51±0.03	18.86±13.00	5.26±0.59	0.00692±0.00196
75	13:29:49.12 +47:12:03.6	21.85±0.60	13.81±0.51	127.65±0.79	41.67±0.59	10.76±0.29	8.06±0.28	37.46±13.00	5.51±0.59	0.17886±0.03730
76	13:29:49.85 +47:12:03.4	5.23±0.27	5.26±0.32	29.37±0.34	14.54±0.32	4.17±0.58	2.92±0.54	48.04±13.00	4.64±0.59	0.02933±0.00722
77	13:29:50.57 +47:12:03.3	13.72±0.60	11.67±0.35	92.03±0.45	34.34±0.38	10.55±0.33	7.27±0.32	59.66±13.00	4.04±0.59	0.17450±0.03844
78	13:29:51.29 +47:12:03.1	52.27±0.95	24.76±0.83	279.54±1.34	74.74±0.96	22.80±0.83	15.91±0.81	293.62±13.00	5.03±0.59	0.33123±0.06744
79	13:29:52.01 +47:12:02.9	45.60±0.94	31.76±0.93	258.87±1.35	95.92±1.09	27.18±0.49	20.77±0.48	507.32±13.00	4.69±0.59	0.35022±0.07165
80	13:29:52.73 +47:12:02.8	51.54±0.97	31.66±0.94	287.30±1.40	93.18±1.09	22.13±0.48	16.19±0.49	302.17±13.00	4.85±0.59	0.37422±0.07629
81	13:29:53.46 +47:12:02.6	14.38±0.73	11.71±0.73	81.39±0.84	34.69±0.78	9.00±0.44	6.02±0.42	198.96±13.00	6.67±0.59	0.10215±0.02346
82	13:29:54.18 +47:12:02.4	27.59±0.83	10.82±0.80	128.34±1.07	34.50±0.88	9.39±0.17	6.77±0.17	116.76±13.00	7.53±0.59	0.10491±0.02216
83	13:29:54.90 +47:12:02.3	53.17±0.84	19.84±0.38	331.38±0.72	57.59±0.44	19.71±0.15	13.89±0.15	150.05±13.00	7.46±0.59	0.55634±0.11268
84	13:29:55.62 +47:12:02.1	15.96±0.04	10.31±0.55	105.20±0.84	28.99±0.61	8.97±0.01	6.70±0.01	541.34±13.00	8.80±0.59	0.19294±0.03876
85	13:29:56.34 +47:12:01.9	24.62±0.69	12.27±0.62	123.21±0.92	36.61±0.71	12.27±0.32	9.32±0.32	82.01±13.00	6.94±0.59	0.11955±0.02505
86	13:29:57.07 +47:12:01.8	6.86±0.27	6.12±0.28	37.55±0.33	19.01±0.31	5.99±0.11	3.91±0.11	19.73±13.00	4.55±0.59	0.03766±0.00843
87	13:29:57.79 +47:12:01.6	2.30±0.42	2.75±0.45	9.66±0.47	7.42±0.46	2.67±0.11	1.42±0.08	5.61±13.00	3.66±0.59	0.00000±0.00260
88	13:29:48.03 +47:11:57.4	2.17±0.46	2.56±0.48	10.91±0.49	8.44±0.50	2.64±0.50	2.04±0.48	2.64±13.00	3.15±0.59	0.00101±0.00495
89	13:29:48.75 +47:11:57.3	3.46±0.03	3.25±0.11	14.67±0.11	9.16±0.11	2.73±0.44	2.54±0.49	6.70±13.00	5.33±0.59	0.00014±0.00027
90	13:29:49.47 +47:11:57.1	5.55±0.49	5.01±0.59	28.01±0.63	16.00±0.62	3.56±0.27	2.76±0.31	11.76±13.00	2.42±0.59	0.01956±0.00670
91	13:29:50.19 +47:11:57.0	31.60±0.05	18.98±0.61	192.13±0.95	59.01±0.71	17.93±0.37	13.14±0.36	176.44±13.00	4.48±0.59	0.30077±0.06025
92	13:29:50.92 +47:11:56.8	45.84±0.89	29.61±0.84	247.21±1.25	90.73±0.99	25.74±0.44	18.36±0.43	605.72±13.00	7.25±0.59	0.29722±0.06067
93	13:29:51.64 +47:11:56.6	38.93±1.04	27.17±1.10	221.49±1.38	83.86±1.23	19.65±0.23	14.92±0.22	550.31±13.00	5.72±0.59	0.29965±0.06225
94	13:29:52.36 +47:11:56.5	43.30±1.14	91.64±0.74	220.27±0.79	278.90±0.91	57.15±0.29	44.82±0.29	392.05±13.00	3.84±0.59	0.20632±0.04316
95	13:29:53.08 +47:11:56.3	43.47±1.08	55.62±1.20	213.43±1.39	171.49±1.42	36.72±0.65	27.61±0.67	143.95±13.00	5.23±0.59	0.20577±0.04258
96	13:29:53.80 +47:11:56.2	39.75±0.91	19.66±0.80	213.20±1.10	60.59±0.89	15.07±0.47	10.36±0.45	87.01±13.00	5.37±0.59	0.25174±0.05180
97	13:29:54.53 +47:11:56.0	19.26±0.72	13.40±0.79	105.76±0.97	38.36±0.85	10.29±0.16	6.79±0.16	134.66±13.00	4.34±0.59	0.12638±0.02732
98	13:29:55.25 +47:11:55.8	19.00±0.35	13.20±0.67	110.51±0.91	38.54±0.74	11.97±0.35	8.65±0.34	216.58±13.00	6.38±0.59	0.15191±0.03106
99	13:29:55.97 +47:11:55.7	47.55±0.76	14.66±0.32	213.11±0.57	45.70±0.37	14.98±0.59	11.68±0.58	378.85±13.00	7.82±0.59	0.16615±0.03371
100	13:29:56.69 +47:11:55.5	21.19±0.34	9.29±0.31	102.52±0.45	28.00±0.34	8.65±0.12	6.52±0.12	63.48±13.00	4.32±0.59	0.09002±0.01830

Table 3.1 (cont'd)

ID	Equatorial Coordinates	Hβ	[NII]λ6548	Hα	[NII]λ6584	[SII]λ6717	[SII]λ6731	Σ_{H2}	Σ_{HI}	Σ_{SFR}
101	13:29:57.41 +47:11:55.3	15.09±0.52	8.23±0.27	72.32±0.37	23.06±0.29	6.57±0.10	4.54±0.10	41.05±13.00	4.32±0.59	0.05891±0.01270
102	13:29:47.65 +47:11:51.2	2.08±0.41	4.55±0.62	9.41±0.47	8.06±0.48	1.87±0.41	1.54±0.46	45.82±13.00	2.94±0.59	0.00000±0.00322
103	13:29:48.38 +47:11:51.0	2.29±0.42	2.98±0.26	11.49±0.26	8.56±0.26	2.89±0.26	1.81±0.23	21.23±13.00	4.88±0.59	0.00161±0.00451
104	13:29:49.10 +47:11:50.8	4.52±0.11	5.10±0.61	24.66±0.60	13.74±0.58	4.24±0.55	2.67±0.53	0.00±13.00	6.11±0.59	0.02095±0.00474
105	13:29:49.82 +47:11:50.7	26.11±0.74	12.89±0.71	130.83±0.97	38.71±0.77	9.13±0.68	7.04±0.67	266.10±13.00	5.80±0.59	0.12798±0.02681
106	13:29:50.54 +47:11:50.5	33.12±0.78	22.43±0.68	194.78±0.99	68.60±0.79	19.04±0.16	13.58±0.16	388.08±13.00	8.64±0.59	0.28270±0.05824
107	13:29:51.26 +47:11:50.4	34.53±1.01	24.30±0.55	183.12±0.67	73.83±0.61	17.59±0.52	12.73±0.53	392.59±13.00	7.23±0.59	0.20921±0.04374
108	13:29:51.98 +47:11:50.2	26.39±0.64	47.93±0.77	124.07±0.75	151.90±0.89	21.18±0.10	16.31±0.10	260.16±13.00	4.42±0.59	0.09270±0.01939
109	13:29:52.71 +47:11:50.0	47.45±1.50	174.91±0.40	209.17±0.39	532.14±0.49	86.74±0.38	68.44±0.38	239.54±13.00	4.43±0.59	0.14016±0.02989
110	13:29:53.43 +47:11:49.9	45.16±1.16	54.17±1.31	213.57±1.47	164.07±1.51	30.65±0.67	22.39±0.67	153.47±13.00	4.10±0.59	0.18879±0.03918
111	13:29:54.15 +47:11:49.7	44.26±0.92	24.15±0.93	242.37±1.31	74.55±1.06	17.43±0.06	12.62±0.06	104.72±13.00	3.29±0.59	0.30160±0.06177
112	13:29:54.87 +47:11:49.5	41.37±0.77	16.17±0.72	198.66±1.10	45.77±0.79	13.42±0.38	9.42±0.37	141.08±13.00	4.97±0.59	0.18111±0.03696
113	13:29:55.59 +47:11:49.4	76.13±1.02	30.47±0.72	379.38±1.24	90.62±0.84	23.49±0.42	17.92±0.41	319.07±13.00	6.77±0.59	0.38663±0.07808
114	13:29:56.32 +47:11:49.2	23.41±0.64	11.13±0.61	130.04±0.91	33.53±0.67	11.15±0.13	7.69±0.13	109.58±13.00	6.82±0.59	0.16213±0.03382
115	13:29:57.04 +47:11:49.1	5.71±0.10	4.89±0.48	27.81±0.51	13.94±0.49	3.63±0.11	2.61±0.10	9.44±13.00	4.70±0.59	0.01705±0.00372
116	13:29:57.76 +47:11:48.9	3.55±0.36	4.69±0.49	18.33±0.49	11.76±0.48	3.83±0.40	2.51±0.40	27.71±13.00	4.88±0.59	0.01006±0.00468
117	13:29:48.00 +47:11:44.7	5.53±0.42	3.09±0.44	22.68±0.50	9.72±0.46	3.17±0.08	1.90±0.09	24.80±13.00	3.80±0.59	0.00489±0.00264
118	13:29:48.72 +47:11:44.6	3.33±0.23	3.97±0.56	16.91±0.54	11.78±0.54	3.50±0.03	2.44±0.04	9.04±13.00	5.95±0.59	0.00777±0.00323
119	13:29:49.44 +47:11:44.4	16.87±0.61	8.84±0.60	83.85±0.81	26.61±0.67	6.91±0.58	5.39±0.59	63.01±13.00	6.69±0.59	0.07672±0.01665
120	13:29:50.17 +47:11:44.2	22.48±0.64	20.71±0.68	157.02±0.98	63.22±0.80	17.64±0.66	12.42±0.65	405.33±13.00	9.21±0.59	0.33435±0.06978
121	13:29:50.89 +47:11:44.1	34.13±0.45	20.93±0.84	173.71±1.12	65.81±0.96	16.34±0.18	12.14±0.18	244.02±13.00	7.90±0.59	0.17990±0.03642
122	13:29:51.61 +47:11:43.9	52.87±1.09	29.90±1.12	269.89±1.41	93.14±1.24	20.07±1.14	14.65±1.09	111.63±13.00	3.26±0.59	0.28729±0.05880
123	13:29:52.33 +47:11:43.7	31.55±0.10	94.01±1.83	131.59±1.69	279.00±2.05	42.75±0.37	38.12±0.40	228.58±13.00	3.37±0.59	0.07390±0.01502
124	13:29:53.05 +47:11:43.6	53.33±1.59	297.73±2.31	312.51±2.48	863.73±2.83	110.81±0.14	122.21±0.16	184.59±13.00	2.61±0.59	0.40826±0.08647
125	13:29:53.78 +47:11:43.4	33.39±1.02	21.21±0.62	158.03±0.68	69.96±0.67	14.83±1.16	13.79±1.30	111.82±13.00	3.12±0.59	0.13715±0.02885
126	13:29:54.50 +47:11:43.3	40.50±0.89	19.78±0.88	214.77±1.23	65.14±1.00	16.71±0.47	13.42±0.48	200.35±13.00	4.56±0.59	0.24713±0.05075
127	13:29:55.22 +47:11:43.1	28.82±0.69	15.65±0.68	158.04±0.99	48.74±0.77	14.58±0.36	9.35±0.34	251.45±13.00	7.79±0.59	0.19359±0.03998
128	13:29:55.94 +47:11:42.9	24.83±0.69	13.15±0.65	132.91±0.93	40.00±0.73	11.76±0.14	8.57±0.13	347.01±13.00	10.39±0.59	0.15226±0.03181
129	13:29:56.66 +47:11:42.8	5.86±0.49	4.59±0.45	30.47±0.51	15.05±0.48	4.17±0.10	3.00±0.10	31.71±13.00	6.88±0.59	0.02439±0.00760
130	13:29:57.39 +47:11:42.6	3.87±0.37	4.09±0.50	17.72±0.49	10.82±0.48	3.74±0.47	2.04±0.44	7.14±13.00	4.63±0.59	0.00480±0.00322
131	13:29:47.63 +47:11:38.4	9.52±0.43	4.35±0.44	39.80±0.55	13.48±0.46	4.09±0.09	2.66±0.09	33.53±13.00	3.78±0.59	0.01771±0.00441
132	13:29:48.35 +47:11:38.3	2.37±0.38	3.31±0.45	10.41±0.45	10.57±0.48	2.58±0.41	1.98±0.45	0.00±13.00	2.68±0.59	0.00000±0.00272
133	13:29:49.07 +47:11:38.1	5.07±0.03	5.60±0.31	24.88±0.31	15.18±0.31	5.08±0.54	4.25±0.58	65.40±13.00	3.90±0.59	0.01461±0.00302
134	13:29:49.79 +47:11:38.0	19.41±0.60	13.51±0.61	121.07±0.88	40.05±0.70	12.92±0.33	8.35±0.31	364.64±13.00	7.48±0.59	0.19699±0.04146
135	13:29:50.51 +47:11:37.8	39.59±0.16	19.72±0.62	242.84±1.00	58.44±0.71	18.22±0.71	13.43±0.71	549.48±13.00	7.63±0.59	0.39052±0.07825
136	13:29:51.24 +47:11:37.6	20.90±0.73	15.59±0.81	109.13±0.97	46.04±0.88	10.33±0.42	7.67±0.41	197.14±13.00	5.35±0.59	0.11599±0.02490
137	13:29:51.96 +47:11:37.5	34.98±0.92	28.79±1.05	180.33±1.24	85.04±1.16	17.21±0.90	12.44±0.88	139.93±13.00	2.52±0.59	0.19285±0.04010
138	13:29:52.68 +47:11:37.3	51.78±1.16	47.95±1.33	233.74±1.47	144.48±1.48	26.86±0.72	21.64±0.75	59.76±13.00	2.43±0.59	0.18638±0.03835
139	13:29:53.40 +47:11:37.1	17.19±0.83	23.16±1.17	99.68±1.20	70.09±1.26	13.53±1.24	12.06±1.26	168.95±13.00	4.00±0.59	0.13487±0.03049
140	13:29:54.12 +47:11:37.0	47.97±0.95	25.67±0.96	242.75±1.27	75.80±1.06	17.55±0.97	14.20±0.99	224.21±13.00	4.11±0.59	0.25228±0.05157
141	13:29:54.84 +47:11:36.8	21.30±0.61	20.78±0.67	138.97±0.92	63.76±0.79	19.25±0.69	14.30±0.68	343.93±13.00	6.83±0.59	0.25237±0.05273
142	13:29:55.57 +47:11:36.7	24.93±0.67	13.33±0.63	126.29±0.89	40.60±0.71	11.85±0.13	9.69±0.14	342.97±13.00	9.15±0.59	0.12642±0.02639
143	13:29:56.29 +47:11:36.5	8.21±0.52	5.80±0.57	36.81±0.64	17.43±0.60	3.42±0.11	2.94±0.12	11.85±13.00	4.80±0.59	0.01996±0.00562
144	13:29:57.01 +47:11:36.3	21.35±0.54	8.52±0.27	92.11±0.40	25.37±0.30	7.98±0.26	5.33±0.26	23.49±13.00	4.13±0.59	0.05964±0.01244
145	13:29:57.73 +47:11:36.2	5.02±0.43	4.21±0.47	21.90±0.50	10.88±0.47	3.58±0.03	2.67±0.03	12.02±13.00	3.37±0.59	0.00650±0.00325
146	13:29:47.97 +47:11:32.0	2.02±0.39	2.53±0.48	8.95±0.44	6.90±0.45	2.18±0.01	1.16±0.01	0.00±13.00	3.57±0.59	0.00000±0.00286
147	13:29:48.69 +47:11:31.8	3.03±0.42	4.86±0.30	15.40±0.27	10.42±0.27	2.97±0.45	2.35±0.48	24.25±13.00	3.46±0.59	0.00620±0.00476
148	13:29:49.42 +47:11:31.7	11.43±0.46	5.93±0.54	59.45±0.69	18.85±0.58	6.73±0.55	4.56±0.53	195.48±13.00	6.85±0.59	0.05770±0.01285
149	13:29:50.14 +47:11:31.5	18.81±0.28	18.69±0.60	160.08±0.93	57.74±0.71	18.64±0.60	13.53±0.58	960.65±13.00	8.22±0.59	0.53224±0.10787
150	13:29:50.86 +47:11:31.3	27.28±0.73	16.59±0.78	134.51±0.97	46.95±0.84	11.53±0.05	10.57±0.06	210.28±13.00	6.90±0.59	0.12702±0.02649

Table 3.1 (cont'd)

ID	Equatorial Coordinates	Hβ	[NII]λ6548	Hα	[NII]λ6584	[SII]λ6717	[SII]λ6731	Σ_{H2}	Σ_{HI}	Σ_{SFR}
151	13:29:51.58 +47:11:31.2	18.39±0.72	13.89±0.79	103.37±0.96	43.01±0.88	10.07±0.05	8.05±0.06	206.44±13.00	8.99±0.59	0.13044±0.02837
152	13:29:52.30 +47:11:31.0	58.93±0.52	36.58±0.21	303.30±0.29	106.63±0.24	21.76±0.19	17.22±0.20	118.99±13.00	5.56±0.59	0.33033±0.06634
153	13:29:53.03 +47:11:30.9	20.57±0.78	15.60±0.92	113.46±1.07	47.69±1.00	9.54±0.06	8.00±0.07	259.97±13.00	5.49±0.59	0.13789±0.02985
154	13:29:53.75 +47:11:30.7	35.88±0.89	20.51±0.93	189.93±1.20	61.79±1.03	13.25±0.19	10.98±0.19	282.84±13.00	5.33±0.59	0.21648±0.04479
155	13:29:54.47 +47:11:30.5	27.25±0.66	18.74±0.70	172.92±1.01	54.67±0.80	15.27±0.69	11.13±0.71	349.80±13.00	5.45±0.59	0.29727±0.06134
156	13:29:55.19 +47:11:30.4	14.31±0.61	10.51±0.60	69.90±0.68	29.55±0.62	8.07±0.62	6.03±0.64	342.27±13.00	5.06±0.59	0.05939±0.01331
157	13:29:55.91 +47:11:30.2	5.58±0.04	4.39±0.13	24.51±0.13	12.78±0.12	2.62±0.03	2.75±0.04	37.86±13.00	4.25±0.59	0.00883±0.00180
158	13:29:56.64 +47:11:30.0	4.99±0.03	5.19±0.26	22.39±0.28	13.73±0.28	4.19±0.47	2.59±0.45	8.06±13.00	6.01±0.59	0.00798±0.00169
159	13:29:57.36 +47:11:29.9	5.69±0.43	4.69±0.49	21.51±0.50	11.65±0.48	4.11±0.49	2.51±0.44	7.33±13.00	4.75±0.59	0.00164±0.00196
160	13:29:47.60 +47:11:25.7	4.28±0.39	3.44±0.47	17.91±0.46	8.07±0.44	3.11±0.09	2.09±0.09	27.17±13.00	4.45±0.59	0.00212±0.00245
161	13:29:48.32 +47:11:25.5	2.61±0.33	2.13±0.43	9.94±0.43	6.92±0.44	1.95±0.19	1.11±0.20	16.81±13.00	4.01±0.59	0.00000±0.00155
162	13:29:49.04 +47:11:25.4	3.88±0.09	3.85±0.45	21.43±0.47	9.78±0.44	3.07±0.04	2.23±0.03	10.50±13.00	3.65±0.59	0.01740±0.00394
163	13:29:49.76 +47:11:25.2	24.73±0.49	15.88±0.55	127.44±0.84	49.25±0.66	15.52±0.29	11.00±0.28	545.04±13.00	5.31±0.59	0.13301±0.02726
164	13:29:50.49 +47:11:25.1	13.97±0.11	11.99±0.12	85.37±0.16	33.15±0.13	8.67±0.28	5.98±0.28	770.02±13.00	7.88±0.59	0.12930±0.02596
165	13:29:51.21 +47:11:24.9	20.78±0.64	9.97±0.69	100.89±0.86	26.74±0.71	7.16±0.14	5.45±0.14	132.53±13.00	8.17±0.59	0.08919±0.01891
166	13:29:51.93 +47:11:24.7	26.83±0.69	16.76±0.74	145.57±0.97	45.28±0.80	11.55±0.71	7.97±0.71	230.54±13.00	7.26±0.59	0.17315±0.03594
167	13:29:52.65 +47:11:24.6	27.68±0.71	26.81±0.80	144.18±0.99	84.22±0.93	19.92±0.78	16.96±0.79	309.30±13.00	5.95±0.59	0.15569±0.03233
168	13:29:53.37 +47:11:24.4	38.86±0.75	20.16±0.75	199.20±1.08	56.64±0.84	15.40±0.39	10.53±0.38	408.54±13.00	8.02±0.59	0.21135±0.04317
169	13:29:54.10 +47:11:24.2	40.76±0.72	22.78±0.63	214.34±0.95	67.59±0.73	19.47±0.15	15.09±0.15	339.39±13.00	4.34±0.59	0.24194±0.04924
170	13:29:54.82 +47:11:24.1	7.50±0.01	6.41±0.31	39.94±0.35	20.25±0.33	5.14±0.56	3.91±0.57	147.60±13.00	5.97±0.59	0.03781±0.00762
171	13:29:55.54 +47:11:23.9	4.65±0.45	5.00±0.46	21.70±0.48	15.32±0.51	3.57±0.03	2.86±0.04	5.03±13.00	5.19±0.59	0.00903±0.00424
172	13:29:56.26 +47:11:23.8	7.65±0.44	4.25±0.50	32.31±0.56	13.73±0.51	4.11±0.48	3.08±0.48	3.06±13.00	4.96±0.59	0.01291±0.00382
173	13:29:56.98 +47:11:23.6	8.33±0.43	4.98±0.40	35.92±0.48	13.52±0.43	4.72±0.09	3.15±0.09	0.00±13.00	8.44±0.59	0.01678±0.00443
174	13:29:57.70 +47:11:23.4	8.67±0.44	5.78±0.47	44.94±0.58	19.72±0.51	8.17±0.27	5.02±0.25	44.23±13.00	5.56±0.59	0.04064±0.00970
175	13:29:47.95 +47:11:19.3	1.61±0.35	2.32±0.45	7.06±0.40	5.31±0.41	1.64±0.38	0.91±0.39	43.73±13.00	4.22±0.59	0.00000±0.00243
176	13:29:48.67 +47:11:19.1	1.76±0.36	2.51±0.50	9.11±0.44	5.43±0.44	1.19±0.08	0.50±0.06	12.10±13.00	3.08±0.59	0.00000±0.00435
177	13:29:49.39 +47:11:18.9	4.26±0.44	4.92±0.54	20.75±0.53	12.73±0.53	3.32±0.03	2.72±0.03	34.88±13.00	3.68±0.59	0.01004±0.00476
178	13:29:50.11 +47:11:18.8	23.57±0.56	12.86±0.29	107.69±0.42	37.53±0.33	12.10±0.55	9.25±0.56	576.38±13.00	7.10±0.59	0.08253±0.01708
179	13:29:50.83 +47:11:18.6	6.21±0.10	6.12±0.52	39.51±0.61	19.14±0.56	5.56±0.29	4.24±0.29	438.05±13.00	4.98±0.59	0.06008±0.01244
180	13:29:51.55 +47:11:18.4	7.64±0.11	8.30±0.60	35.59±0.64	19.78±0.61	5.26±0.04	3.05±0.04	135.02±13.00	3.28±0.59	0.02147±0.00457
181	13:29:52.28 +47:11:18.3	10.04±0.04	8.02±0.62	53.17±0.70	22.68±0.65	5.14±0.12	4.07±0.12	192.15±13.00	5.54±0.59	0.05296±0.01076
182	13:29:53.00 +47:11:18.1	5.41±0.57	7.44±0.14	28.68±0.14	21.11±0.14	3.52±0.04	4.40±0.06	131.89±13.00	4.74±0.59	0.02381±0.00854
183	13:29:53.72 +47:11:18.0	7.79±0.50	6.46±0.51	34.07±0.55	18.09±0.53	4.46±0.29	4.11±0.36	102.26±13.00	3.65±0.59	0.01613±0.00478
184	13:29:54.44 +47:11:17.8	6.37±0.48	7.09±0.61	28.00±0.59	17.28±0.58	4.58±0.28	3.20±0.32	123.73±13.00	4.20±0.59	0.01163±0.00415
185	13:29:55.16 +47:11:17.6	4.15±0.03	3.60±0.52	17.27±0.54	12.18±0.54	2.73±0.04	1.97±0.04	0.00±13.00	3.96±0.59	0.00155±0.00089
186	13:29:55.89 +47:11:17.5	6.81±0.44	5.53±0.52	26.40±0.54	13.58±0.51	3.53±0.47	2.51±0.46	22.37±13.00	2.98±0.59	0.00527±0.00237
187	13:29:56.61 +47:11:17.3	7.72±0.41	5.69±0.25	42.28±0.31	16.19±0.26	5.58±0.23	3.72±0.23	36.71±13.00	5.60±0.59	0.04380±0.01050
188	13:29:57.33 +47:11:17.1	7.42±0.25	5.35±0.48	31.10±0.54	14.02±0.49	4.68±0.10	3.17±0.10	56.89±13.00	5.18±0.59	0.01165±0.00287
189	13:29:47.57 +47:11:13.0	1.69±0.02	2.25±0.03	7.50±0.03	5.74±0.03	1.46±0.37	1.37±0.40	29.01±13.00	3.51±0.59	0.00000±0.00018
190	13:29:48.29 +47:11:12.8	4.30±0.08	3.32±0.43	17.02±0.45	8.77±0.42	2.92±0.22	1.93±0.20	64.46±13.00	3.65±0.59	0.00011±0.00074
191	13:29:49.01 +47:11:12.6	2.72±0.40	2.68±0.47	10.90±0.46	7.17±0.45	2.11±0.09	1.63±0.09	11.86±13.00	3.28±0.59	0.00000±0.00216
192	13:29:49.74 +47:11:12.5	2.76±0.40	4.02±0.04	17.57±0.04	9.93±0.04	2.81±0.44	2.16±0.48	18.64±13.00	4.97±0.59	0.02077±0.00992
193	13:29:50.46 +47:11:12.3	16.93±0.47	10.78±0.50	99.58±0.73	30.99±0.56	9.72±0.49	7.50±0.49	472.23±13.00	7.73±0.59	0.13935±0.02913
194	13:29:51.18 +47:11:12.2	3.23±0.01	4.90±0.53	17.95±0.53	12.27±0.53	3.02±0.03	2.59±0.04	357.00±13.00	5.48±0.59	0.01315±0.00304
195	13:29:51.90 +47:11:12.0	5.03±0.03	4.71±0.11	21.64±0.12	12.92±0.12	3.22±0.04	1.94±0.03	74.45±13.00	3.83±0.59	0.00575±0.00118
196	13:29:52.62 +47:11:11.8	5.81±0.46	6.04±0.56	27.55±0.58	16.59±0.58	4.58±0.11	3.28±0.11	116.36±13.00	6.16±0.59	0.01519±0.00519
197	13:29:53.35 +47:11:11.7	6.52±0.45	6.16±0.52	33.17±0.58	16.89±0.55	4.36±0.11	3.85±0.11	97.39±13.00	2.44±0.59	0.02575±0.00723
198	13:29:54.07 +47:11:11.5	4.91±0.03	5.34±0.04	20.38±0.04	13.71±0.04	3.85±0.49	2.46±0.51	34.67±13.00	1.93±0.59	0.00361±0.00075
199	13:29:54.79 +47:11:11.4	6.94±0.45	4.93±0.51	27.49±0.55	12.57±0.51	4.31±0.03	3.20±0.04	18.83±13.00	3.10±0.59	0.00675±0.00270
200	13:29:55.51 +47:11:11.2	3.71±0.43	3.69±0.49	14.82±0.44	8.74±0.43	2.09±0.42	2.42±0.58	0.00±13.00	3.71±0.59	0.00000±0.00227

Table 3.1 (cont'd)

ID	Equatorial Coordinates	Hβ	[NII]λ6548	Hα	[NII]λ6584	[SII]λ6717	[SII]λ6731	Σ_{H2}	Σ_{HI}	Σ_{SFR}
201	13:29:56.23 +47:11:11.0	3.49±0.41	3.49±0.27	13.62±0.25	10.05±0.26	3.87±0.48	2.61±0.53	39.38±13.00	3.12±0.59	0.00000±0.00195
202	13:29:56.95 +47:11:10.9	4.28±0.39	4.38±0.45	18.54±0.47	12.48±0.47	3.74±0.03	2.41±0.03	98.38±13.00	6.97±0.59	0.00365±0.00277
203	13:29:57.68 +47:11:10.7	3.00±0.34	4.04±0.43	14.43±0.44	10.44±0.45	3.38±0.03	2.96±0.03	56.65±13.00	7.05±0.59	0.00335±0.00335
204	13:29:47.92 +47:11:06.5	2.13±0.18	2.88±0.41	9.43±0.36	6.76±0.36	1.96±0.08	1.72±0.09	32.92±13.00	5.35±0.59	0.00000±0.00142
205	13:29:48.64 +47:11:06.4	1.94±0.35	1.85±0.03	7.89±0.03	6.62±0.03	2.44±0.08	1.43±0.08	19.13±13.00	4.79±0.59	0.00000±0.00191
206	13:29:49.36 +47:11:06.2	2.28±0.03	2.56±0.24	11.09±0.24	6.59±0.22	2.56±0.23	1.53±0.25	30.78±13.00	5.16±0.59	0.00032±0.00057
207	13:29:50.08 +47:11:06.0	4.27±0.08	3.08±0.44	17.83±0.48	9.48±0.46	3.44±0.45	2.10±0.47	42.76±13.00	5.52±0.59	0.00199±0.00096
208	13:29:50.81 +47:11:05.9	4.58±0.21	4.61±0.44	25.40±0.50	14.40±0.47	4.72±0.24	3.39±0.24	515.89±13.00	5.17±0.59	0.02305±0.00567
209	13:29:51.53 +47:11:05.7	3.05±0.38	3.66±0.03	19.04±0.03	9.60±0.03	2.60±0.03	1.72±0.03	373.50±13.00	5.14±0.59	0.02214±0.00917
210	13:29:52.25 +47:11:05.6	5.90±0.09	5.25±0.52	29.48±0.55	13.15±0.51	4.11±0.25	3.17±0.26	126.22±13.00	5.06±0.59	0.02040±0.00438
211	13:29:52.97 +47:11:05.4	3.30±0.23	3.67±0.01	14.87±0.01	11.41±0.01	2.08±0.47	1.54±0.46	113.92±13.00	5.35±0.59	0.00183±0.00174
212	13:29:53.69 +47:11:05.2	2.81±0.03	3.07±0.09	11.92±0.11	9.91±0.11	2.81±0.03	1.67±0.03	40.77±13.00	2.02±0.59	0.00000±0.00024
213	13:29:54.41 +47:11:05.1	8.07±0.44	4.34±0.50	27.70±0.54	12.58±0.50	4.15±0.44	2.29±0.40	0.00±13.00	4.72±0.59	0.00214±0.00153
214	13:29:55.14 +47:11:04.9	7.25±0.24	6.04±0.12	28.12±0.12	11.35±0.11	3.49±0.03	2.18±0.03	37.35±13.00	5.24±0.59	0.00634±0.00169
215	13:29:55.86 +47:11:04.7	4.65±0.39	4.00±0.49	18.55±0.51	10.78±0.50	3.06±0.10	2.08±0.10	43.72±13.00	2.94±0.59	0.00129±0.00212
216	13:29:56.58 +47:11:04.6	5.33±0.39	5.17±0.04	25.04±0.04	13.24±0.03	3.93±0.10	3.53±0.10	24.72±13.00	4.41±0.59	0.01242±0.00417
217	13:29:57.30 +47:11:04.4	10.69±0.40	6.79±0.45	40.55±0.51	17.56±0.45	5.51±0.36	4.41±0.38	94.11±13.00	8.30±0.59	0.01271±0.00312
218	13:29:47.54 +47:11:00.2	1.73±0.34	1.04±0.37	5.73±0.39	4.96±0.41	1.09±0.01	0.39±0.01	42.75±13.00	3.82±0.59	0.00000±0.00102
219	13:29:48.27 +47:11:00.1	1.85±0.27	2.06±0.03	7.43±0.03	5.39±0.03	2.11±0.37	1.43±0.38	31.04±13.00	3.59±0.59	0.00000±0.00138
220	13:29:48.99 +47:10:59.9	2.17±0.03	2.72±0.43	7.76±0.41	5.85±0.42	2.37±0.03	1.89±0.03	47.03±13.00	3.63±0.59	0.00000±0.00045
221	13:29:49.71 +47:10:59.8	5.42±0.41	4.81±0.47	23.45±0.50	12.03±0.47	3.67±0.09	2.68±0.09	49.80±13.00	4.24±0.59	0.00739±0.00314
222	13:29:50.43 +47:10:59.6	8.41±0.41	4.46±0.45	34.22±0.53	12.15±0.47	5.02±0.47	2.92±0.44	0.00±13.00	4.48±0.59	0.01231±0.00339
223	13:29:51.15 +47:10:59.4	4.99±0.03	4.37±0.38	28.04±0.44	12.78±0.40	3.62±0.42	2.87±0.44	355.43±13.00	8.35±0.59	0.02763±0.00569
224	13:29:51.87 +47:10:59.3	19.34±0.46	11.43±0.48	82.98±0.67	32.33±0.54	7.29±0.24	5.49±0.23	547.74±13.00	6.95±0.59	0.05193±0.01084
225	13:29:52.60 +47:10:59.1	2.87±0.31	2.99±0.01	15.00±0.01	8.81±0.01	1.70±0.45	2.17±0.52	246.77±13.00	5.75±0.59	0.00680±0.00390
226	13:29:53.32 +47:10:58.9	1.75±0.01	2.64±0.25	8.86±0.24	7.94±0.26	1.70±0.45	1.64±0.44	63.03±13.00	3.35±0.59	0.00000±0.00057
227	13:29:54.04 +47:10:58.8	3.20±0.25	2.03±0.03	11.79±0.04	7.85±0.04	2.12±0.49	1.61±0.54	0.00±13.00	2.85±0.59	0.00000±0.00096
228	13:29:54.76 +47:10:58.6	2.62±0.38	3.95±0.49	13.66±0.48	9.85±0.49	3.31±0.47	2.32±0.48	21.42±13.00	4.12±0.59	0.00520±0.00483
229	13:29:55.48 +47:10:58.5	3.55±0.41	3.88±0.50	15.29±0.48	10.16±0.49	2.55±0.45	2.47±0.49	27.25±13.00	4.88±0.59	0.00101±0.00278
230	13:29:56.21 +47:10:58.3	5.83±0.09	5.29±0.48	29.49±0.52	13.32±0.49	5.35±0.46	2.98±0.45	99.16±13.00	6.58±0.59	0.02129±0.00453
231	13:29:56.93 +47:10:58.1	8.69±0.22	6.69±0.10	47.95±0.12	19.40±0.11	7.76±0.03	5.17±0.03	157.32±13.00	14.02±0.59	0.05210±0.01088
232	13:29:57.65 +47:10:58.0	14.15±0.48	8.04±0.52	55.94±0.61	19.28±0.52	8.50±0.49	7.13±0.51	266.52±13.00	11.67±0.59	0.02462±0.00551
233	13:29:47.89 +47:10:53.8	3.80±0.33	2.31±0.32	15.26±0.35	5.69±0.33	2.80±0.08	1.00±0.07	44.98±13.00	4.63±0.59	0.00000±0.00176
234	13:29:48.61 +47:10:53.6	5.98±0.20	3.01±0.36	23.64±0.39	9.51±0.36	3.00±0.20	2.36±0.20	40.23±13.00	4.20±0.59	0.00426±0.00140
235	13:29:49.33 +47:10:53.5	3.17±0.03	3.22±0.20	14.77±0.24	9.13±0.23	4.12±0.44	2.73±0.40	51.19±13.00	4.19±0.59	0.00274±0.00075
236	13:29:50.06 +47:10:53.3	19.79±0.49	9.43±0.49	80.35±0.65	25.19±0.51	9.25±0.26	7.14±0.26	55.21±13.00	5.92±0.59	0.04303±0.00903
237	13:29:50.78 +47:10:53.1	15.87±0.25	7.02±0.48	57.46±0.60	18.53±0.51	5.92±0.01	3.78±0.01	43.20±13.00	6.01±0.59	0.01923±0.00401
238	13:29:51.50 +47:10:53.0	3.74±0.35	4.64±0.47	23.08±0.48	10.30±0.44	2.84±0.41	2.58±0.48	281.26±13.00	9.51±0.59	0.02811±0.00928
239	13:29:52.22 +47:10:52.8	6.38±0.38	6.11±0.09	37.30±0.11	17.03±0.10	5.60±0.03	3.75±0.03	502.45±13.00	6.00±0.59	0.04479±0.01103
240	13:29:52.94 +47:10:52.7	4.56±0.35	4.29±0.42	26.16±0.49	12.35±0.45	4.66±0.23	3.14±0.23	296.67±13.00	6.68±0.59	0.02666±0.00793
241	13:29:53.67 +47:10:52.5	6.85±0.22	5.19±0.46	34.89±0.53	14.48±0.49	4.74±0.09	3.57±0.09	148.85±13.00	6.58±0.59	0.02763±0.00616
242	13:29:54.39 +47:10:52.3	4.48±0.03	4.51±0.09	28.35±0.11	13.52±0.10	4.58±0.43	3.87±0.43	238.76±13.00	6.79±0.59	0.03939±0.00791
243	13:29:55.11 +47:10:52.2	11.88±0.22	13.07±0.41	88.10±0.58	38.04±0.47	10.09±0.10	7.61±0.09	259.43±13.00	7.32±0.59	0.20999±0.04287
244	13:29:55.83 +47:10:52.0	10.87±0.36	11.86±0.42	67.86±0.55	30.93±0.47	9.97±0.10	7.81±0.10	283.06±13.00	9.58±0.59	0.10580±0.02258
245	13:29:56.55 +47:10:51.8	42.03±0.57	26.05±0.04	237.37±0.07	69.03±0.05	23.09±0.12	18.45±0.11	317.74±13.00	13.35±0.59	0.31654±0.06390
246	13:29:47.72 +47:12:33.6	10.94±0.44	5.78±0.47	49.70±0.62	16.08±0.50	5.90±0.09	4.05±0.08	0.00±13.00	10.02±0.59	0.03187±0.00731
247	13:29:48.44 +47:12:33.4	5.60±0.45	4.64±0.48	29.50±0.54	12.60±0.48	4.33±0.44	2.84±0.43	87.16±13.00	10.98±0.59	0.02422±0.00747
248	13:29:49.17 +47:12:33.2	4.29±0.45	5.85±0.26	28.44±0.30	15.93±0.28	5.85±0.10	3.53±0.09	255.17±13.00	8.80±0.59	0.04505±0.01465
249	13:29:49.89 +47:12:33.1	4.39±0.49	4.60±0.26	24.72±0.30	14.18±0.29	4.31±0.03	2.88±0.03	237.27±13.00	8.42±0.59	0.02317±0.00871
250	13:29:50.61 +47:12:32.9	3.40±0.26	4.46±0.53	18.19±0.55	11.57±0.54	3.78±0.27	2.58±0.26	114.88±13.00	8.90±0.59	0.01168±0.00435

Table 3.1 (cont'd)

ID	Equatorial Coordinates	Hβ	[NII]λ6548	Hα	[NII]λ6584	[SII]λ6717	[SII]λ6731	Σ_{H2}	Σ_{HI}	Σ_{SFR}
251	13:29:51.33 +47:12:32.8	2.84±0.48	4.58±0.30	15.66±0.29	12.14±0.29	2.91±0.10	1.76±0.09	95.40±13.00	6.01±0.59	0.00981±0.00713
252	13:29:52.05 +47:12:32.6	6.93±0.50	5.92±0.54	33.15±0.61	16.50±0.55	5.09±0.10	3.63±0.10	157.05±13.00	6.09±0.59	0.02106±0.00630
253	13:29:52.78 +47:12:32.4	7.44±0.50	5.87±0.28	42.80±0.33	16.75±0.29	4.91±0.10	3.66±0.10	183.79±13.00	8.66±0.59	0.05085±0.01305
254	13:29:53.50 +47:12:32.3	5.61±0.49	4.89±0.11	30.30±0.12	14.43±0.11	5.04±0.50	3.50±0.48	136.92±13.00	6.14±0.59	0.02721±0.00849
255	13:29:54.22 +47:12:32.1	7.04±0.47	5.17±0.26	36.06±0.31	15.39±0.28	5.24±0.10	3.84±0.09	216.76±13.00	6.47±0.59	0.02948±0.00796
256	13:29:54.94 +47:12:31.9	15.31±0.57	9.35±0.28	91.72±0.42	28.32±0.31	10.93±0.52	7.38±0.50	164.15±13.00	10.19±0.59	0.13331±0.02867
257	13:29:55.66 +47:12:31.8	29.03±0.70	11.65±0.56	164.38±0.99	32.63±0.64	10.66±0.54	7.80±0.53	30.10±13.00	4.97±0.59	0.21718±0.04483
258	13:29:56.39 +47:12:31.6	14.16±0.52	5.97±0.25	83.85±0.38	17.42±0.26	5.23±0.09	3.67±0.09	36.51±13.00	4.00±0.59	0.11749±0.02527
259	13:29:57.11 +47:12:31.5	3.69±0.39	3.29±0.22	19.32±0.24	9.32±0.22	3.11±0.22	1.97±0.18	57.86±13.00	3.95±0.59	0.01193±0.00533
260	13:29:47.35 +47:12:27.3	7.29±0.43	6.89±0.40	54.62±0.55	19.40±0.44	6.27±0.09	4.18±0.09	173.98±13.00	11.66±0.59	0.12956±0.03076
261	13:29:48.07 +47:12:27.1	4.42±0.45	3.99±0.49	25.95±0.55	10.70±0.49	4.14±0.46	3.09±0.47	116.83±13.00	11.15±0.59	0.02826±0.00976
262	13:29:48.79 +47:12:27.0	6.15±0.50	4.94±0.52	33.10±0.60	13.57±0.54	3.57±0.25	2.69±0.25	197.79±13.00	10.23±0.59	0.03038±0.00910
263	13:29:49.51 +47:12:26.8	3.41±0.50	3.82±0.28	18.98±0.29	11.93±0.29	3.86±0.42	2.75±0.45	101.06±13.00	6.25±0.59	0.01465±0.00793
264	13:29:50.23 +47:12:26.6	4.10±0.52	5.35±0.04	20.25±0.04	14.48±0.04	4.13±0.51	3.10±0.53	28.39±13.00	4.51±0.59	0.01015±0.00559
265	13:29:50.96 +47:12:26.5	2.48±0.49	4.68±0.30	14.81±0.30	13.25±0.31	3.11±0.50	2.53±0.53	54.66±13.00	6.16±0.59	0.01237±0.00930
266	13:29:51.68 +47:12:26.3	4.09±0.50	5.40±0.55	23.72±0.58	15.19±0.58	3.68±0.50	3.20±0.52	110.42±13.00	7.12±0.59	0.02406±0.00981
267	13:29:52.40 +47:12:26.2	6.62±0.51	5.72±0.56	37.35±0.64	17.09±0.58	5.34±0.29	3.42±0.27	186.25±13.00	6.02±0.59	0.04068±0.01142
268	13:29:53.12 +47:12:26.0	8.62±0.55	5.63±0.13	43.28±0.14	15.75±0.12	5.93±0.12	3.79±0.11	112.01±13.00	4.60±0.59	0.03547±0.00913
269	13:29:53.85 +47:12:25.8	8.04±0.12	6.21±0.34	44.43±0.36	15.19±0.32	4.71±0.55	3.25±0.58	76.47±13.00	5.60±0.59	0.04781±0.00977
270	13:29:54.57 +47:12:25.7	9.72±0.52	7.31±0.46	58.32±0.61	21.49±0.50	7.31±0.51	5.12±0.50	262.93±13.00	8.63±0.59	0.08112±0.01898
271	13:29:55.29 +47:12:25.5	13.35±0.54	8.37±0.45	78.41±0.66	23.60±0.50	8.81±0.27	5.94±0.26	147.66±13.00	8.55±0.59	0.10715±0.02347
272	13:29:56.01 +47:12:25.3	20.79±0.61	8.40±0.53	100.69±0.82	23.21±0.57	7.97±0.26	6.04±0.26	44.99±13.00	7.22±0.59	0.08841±0.01867
273	13:29:56.73 +47:12:25.2	11.09±0.27	5.78±0.40	63.83±0.59	16.68±0.44	6.98±0.25	3.95±0.23	89.71±13.00	6.03±0.59	0.08116±0.01693
274	13:29:57.46 +47:12:25.0	2.23±0.39	3.29±0.27	12.68±0.25	8.17±0.25	2.32±0.09	1.44±0.09	42.63±13.00	4.27±0.59	0.00707±0.00627
275	13:29:47.69 +47:12:20.8	2.89±0.43	3.50±0.51	17.12±0.50	9.21±0.49	3.02±0.09	1.93±0.09	188.39±13.00	9.65±0.59	0.01549±0.00832
276	13:29:48.42 +47:12:20.7	2.59±0.41	3.57±0.58	13.08±0.51	7.62±0.51	2.36±0.03	1.77±0.03	152.78±13.00	7.82±0.59	0.00341±0.00455
277	13:29:49.14 +47:12:20.5	3.10±0.26	4.30±0.57	17.88±0.57	10.69±0.56	2.92±0.03	2.44±0.04	99.97±13.00	5.73±0.59	0.01519±0.00557
278	13:29:49.86 +47:12:20.4	4.71±0.11	5.37±0.30	21.29±0.31	14.21±0.30	4.52±0.54	3.06±0.52	12.75±13.00	2.58±0.59	0.00734±0.00178
279	13:29:50.58 +47:12:20.2	2.87±0.49	4.82±0.57	17.18±0.56	13.56±0.56	3.40±0.11	2.34±0.11	0.00±13.00	4.39±0.59	0.01633±0.00980
280	13:29:51.30 +47:12:20.0	4.54±0.51	5.50±0.35	24.01±0.32	12.62±0.31	4.02±0.04	2.45±0.04	55.87±13.00	7.83±0.59	0.01796±0.00728
281	13:29:52.03 +47:12:19.9	10.25±0.32	7.24±0.60	52.94±0.72	22.91±0.65	6.25±0.52	3.98±0.51	115.02±13.00	5.09±0.59	0.04935±0.01068
282	13:29:52.75 +47:12:19.7	10.25±0.60	6.95±0.61	55.42±0.75	19.61±0.63	5.32±0.01	3.65±0.01	67.48±13.00	3.93±0.59	0.05878±0.01434
283	13:29:53.47 +47:12:19.5	16.08±0.13	8.83±0.62	82.82±0.83	23.03±0.63	7.29±0.12	5.21±0.12	149.21±13.00	6.92±0.59	0.08255±0.01670
284	13:29:54.19 +47:12:19.4	32.61±0.75	15.05±0.63	175.16±1.07	41.71±0.71	12.58±0.12	8.50±0.12	87.35±13.00	6.28±0.59	0.20566±0.04236
285	13:29:54.91 +47:12:19.2	11.32±0.54	6.72±0.12	62.09±0.15	21.05±0.13	7.06±0.27	5.10±0.27	283.38±13.00	9.24±0.59	0.06964±0.01585
286	13:29:55.64 +47:12:19.1	7.15±0.03	5.78±0.26	44.97±0.34	17.89±0.29	6.65±0.50	4.77±0.50	104.84±13.00	7.43±0.59	0.06782±0.01365
287	13:29:56.36 +47:12:18.9	10.83±0.52	7.41±0.52	67.17±0.73	21.20±0.56	6.39±0.10	4.95±0.11	45.49±13.00	5.84±0.59	0.10310±0.02342
288	13:29:57.08 +47:12:18.7	5.72±0.42	5.28±0.10	28.94±0.10	13.32±0.10	4.17±0.22	2.80±0.23	16.52±13.00	3.36±0.59	0.02074±0.00611
289	13:29:47.32 +47:12:14.6	5.12±0.49	4.09±0.43	26.39±0.49	11.47±0.45	3.88±0.10	2.97±0.10	132.31±13.00	8.96±0.59	0.01908±0.00684
290	13:29:48.04 +47:12:14.4	2.04±0.44	3.25±0.29	11.26±0.27	8.50±0.27	2.35±0.09	1.61±0.10	72.72±13.00	4.71±0.59	0.00414±0.00639
291	13:29:48.76 +47:12:14.2	3.03±0.50	3.90±0.51	13.79±0.52	11.71±0.54	4.48±0.11	2.84±0.10	10.28±13.00	3.91±0.59	0.00120±0.00396
292	13:29:49.49 +47:12:14.1	4.29±0.11	5.36±0.31	22.00±0.31	13.27±0.30	3.97±0.52	2.70±0.51	8.88±13.00	3.43±0.59	0.01386±0.00310
293	13:29:50.21 +47:12:13.9	6.97±0.53	7.82±0.59	37.61±0.64	21.49±0.61	6.27±0.11	4.20±0.12	1.25±13.00	3.38±0.59	0.03621±0.01021
294	13:29:50.93 +47:12:13.7	8.95±0.55	8.88±0.60	53.36±0.73	24.34±0.64	7.69±0.59	5.53±0.58	29.08±13.00	4.40±0.59	0.07230±0.01779
295	13:29:51.65 +47:12:13.6	31.04±0.74	15.10±0.68	167.23±1.06	42.13±0.76	12.35±0.13	9.04±0.13	58.81±13.00	2.85±0.59	0.19726±0.04073
296	13:29:52.37 +47:12:13.4	33.04±0.76	15.16±0.36	172.07±0.57	44.79±0.41	12.99±0.59	9.36±0.58	92.58±13.00	3.36±0.59	0.18792±0.03865
297	13:29:53.10 +47:12:13.3	32.71±0.75	14.23±0.58	167.91±0.94	40.86±0.65	12.23±0.57	9.03±0.56	161.62±13.00	3.93±0.59	0.17709±0.03648
298	13:29:53.82 +47:12:13.1	35.83±0.76	12.48±0.66	170.42±1.07	36.76±0.73	10.41±0.13	8.32±0.13	109.45±13.00	5.39±0.59	0.15048±0.03092
299	13:29:54.54 +47:12:12.9	66.00±0.53	19.18±0.38	296.48±0.71	57.12±0.44	15.78±0.15	11.24±0.14	162.04±13.00	8.56±0.59	0.23660±0.04749
300	13:29:55.26 +47:12:12.8	12.88±0.53	8.54±0.55	80.69±0.79	23.57±0.59	8.45±0.53	6.64±0.53	432.62±13.00	4.96±0.59	0.12904±0.02832

Table 3.1 (cont'd)

ID	Equatorial Coordinates	Hβ	[NII]λ6548	Hα	[NII]λ6584	[SII]λ6717	[SII]λ6731	Σ_{H2}	Σ_{HI}	Σ_{SFR}
301	13:29:55.98 +47:12:12.6	6.39±0.47	5.54±0.46	37.64±0.54	16.29±0.48	5.47±0.27	3.97±0.26	108.38±13.00	7.65±0.59	0.04619±0.01253
302	13:29:56.71 +47:12:12.4	7.68±0.49	5.22±0.51	44.95±0.64	14.81±0.54	4.72±0.50	3.65±0.51	19.51±13.00	4.74±0.59	0.05628±0.01415
303	13:29:57.43 +47:12:12.3	1.99±0.36	2.41±0.44	10.88±0.46	7.77±0.46	2.38±0.03	1.27±0.02	24.67±13.00	2.21±0.59	0.00329±0.00520
304	13:29:47.67 +47:12:08.1	4.73±0.43	4.32±0.52	20.09±0.54	11.01±0.52	3.73±0.47	2.66±0.50	45.08±13.00	5.32±0.59	0.00413±0.00288
305	13:29:48.39 +47:12:07.9	4.25±0.26	4.21±0.28	18.66±0.28	11.34±0.27	3.55±0.49	2.36±0.50	20.04±13.00	5.18±0.59	0.00419±0.00203
306	13:29:49.11 +47:12:07.8	4.94±0.50	6.25±0.29	30.58±0.32	17.29±0.31	5.30±0.28	3.96±0.28	42.23±13.00	3.80±0.59	0.04095±0.01311
307	13:29:49.83 +47:12:07.6	3.36±0.26	3.82±0.31	19.76±0.31	11.07±0.31	2.52±0.26	2.22±0.32	40.23±13.00	4.46±0.59	0.01916±0.00603
308	13:29:50.55 +47:12:07.5	9.41±0.59	7.17±0.33	50.94±0.39	23.62±0.36	6.51±0.60	4.70±0.65	0.00±13.00	3.38±0.59	0.05331±0.01328
309	13:29:51.28 +47:12:07.3	30.79±0.81	16.89±0.75	172.07±1.13	51.76±0.86	14.51±0.39	10.71±0.39	45.06±13.00	3.41±0.59	0.22108±0.04592
310	13:29:52.00 +47:12:07.1	72.99±1.04	36.84±0.77	426.43±1.40	108.86±0.94	34.23±0.90	23.94±0.87	264.15±13.00	4.54±0.59	0.62245±0.12583
311	13:29:52.72 +47:12:07.0	49.36±0.96	25.26±0.45	285.83±0.73	78.24±0.53	20.61±0.85	14.19±0.84	248.54±13.00	5.99±0.59	0.40562±0.08269
312	13:29:53.44 +47:12:06.8	15.77±0.68	10.46±0.39	87.97±0.48	30.01±0.41	8.02±0.61	6.68±0.65	231.51±13.00	7.63±0.59	0.10743±0.02371
313	13:29:54.16 +47:12:06.6	44.79±0.86	15.22±0.39	220.75±0.64	45.42±0.44	12.06±0.15	8.80±0.15	156.11±13.00	7.90±0.59	0.21495±0.04384
314	13:29:54.89 +47:12:06.5	47.26±0.84	16.72±0.37	277.57±0.68	47.43±0.42	15.67±0.14	11.63±0.14	119.31±13.00	7.76±0.59	0.40626±0.08258
315	13:29:55.61 +47:12:06.3	14.01±0.12	10.54±0.54	89.79±0.81	30.75±0.62	10.16±0.28	7.46±0.29	451.89±13.00	7.21±0.59	0.15269±0.03082
316	13:29:56.33 +47:12:06.2	6.75±0.11	5.62±0.29	39.42±0.34	16.68±0.31	5.84±0.29	4.25±0.28	43.17±13.00	7.03±0.59	0.04776±0.00980
317	13:29:57.05 +47:12:06.0	4.44±0.48	4.40±0.27	23.82±0.30	12.98±0.28	4.23±0.50	2.94±0.49	15.35±13.00	4.11±0.59	0.01865±0.00729
318	13:29:47.29 +47:12:01.8	2.48±0.41	3.05±0.47	10.90±0.49	9.38±0.50	2.69±0.10	2.25±0.10	25.17±13.00	4.00±0.59	0.00000±0.00289
319	13:29:48.01 +47:12:01.7	3.07±0.42	3.51±0.52	16.04±0.52	10.07±0.53	2.86±0.10	1.96±0.10	3.44±13.00	3.41±0.59	0.00794±0.00537
320	13:29:48.74 +47:12:01.5	7.56±0.50	6.32±0.28	45.68±0.35	19.80±0.31	5.65±0.51	3.62±0.50	12.68±13.00	6.15±0.59	0.06230±0.01567
321	13:29:49.46 +47:12:01.3	8.27±0.30	5.04±0.30	36.67±0.34	16.68±0.32	4.27±0.04	3.39±0.04	29.63±13.00	4.62±0.59	0.01905±0.00439
322	13:29:50.18 +47:12:01.2	12.85±0.60	9.90±0.34	80.03±0.43	28.85±0.37	9.51±0.63	6.50±0.61	82.76±13.00	3.87±0.59	0.12613±0.02818
323	13:29:50.90 +47:12:01.0	57.53±0.95	31.31±0.84	362.57±1.49	101.31±1.03	29.98±0.85	20.71±0.82	316.05±13.00	5.84±0.59	0.62502±0.12680
324	13:29:51.62 +47:12:00.9	49.36±0.86	31.67±0.83	301.50±1.26	95.73±0.97	25.54±0.50	19.39±0.50	625.62±13.00	6.06±0.59	0.48287±0.09814
325	13:29:52.35 +47:12:00.7	46.53±1.00	41.27±1.06	279.00±1.45	135.21±1.27	30.97±0.56	23.16±0.54	503.67±13.00	3.88±0.59	0.42796±0.08772
326	13:29:53.07 +47:12:00.5	30.04±0.91	21.10±0.97	160.55±1.22	67.76±1.10	15.19±0.52	9.88±0.51	165.90±13.00	4.82±0.59	0.18537±0.03900
327	13:29:53.79 +47:12:00.4	17.60±0.78	10.62±0.82	95.12±1.01	32.07±0.90	7.59±0.43	6.34±0.41	129.18±13.00	6.73±0.59	0.10834±0.02419
328	13:29:54.51 +47:12:00.2	59.31±0.92	21.37±0.76	337.09±1.39	65.22±0.89	19.40±0.16	14.87±0.16	142.33±13.00	6.49±0.59	0.46040±0.09328
329	13:29:55.23 +47:12:00.0	23.87±0.64	11.98±0.33	132.99±0.50	36.69±0.37	11.72±0.63	8.23±0.60	353.61±13.00	7.57±0.59	0.16733±0.03478
330	13:29:55.96 +47:11:59.9	41.18±0.74	15.85±0.60	223.94±1.13	49.62±0.72	16.70±0.13	12.13±0.12	343.95±13.00	8.29±0.59	0.27344±0.05567
331	13:29:56.68 +47:11:59.7	18.06±0.62	7.78±0.58	86.23±0.81	24.28±0.64	7.83±0.12	6.44±0.12	59.69±13.00	6.30±0.59	0.07161±0.01545
332	13:29:57.40 +47:11:59.5	4.25±0.45	4.06±0.25	22.12±0.28	12.21±0.27	3.41±0.46	2.99±0.50	21.41±13.00	3.96±0.59	0.01479±0.00610
333	13:29:47.64 +47:11:55.4	2.71±0.09	2.77±0.42	13.00±0.43	8.10±0.43	2.77±0.24	1.47±0.23	24.88±13.00	2.66±0.59	0.00189±0.00128
334	13:29:48.36 +47:11:55.2	2.54±0.46	2.69±0.48	11.79±0.49	8.83±0.50	2.97±0.48	1.90±0.51	3.44±13.00	4.27±0.59	0.00000±0.00384
335	13:29:49.08 +47:11:55.1	3.85±0.51	4.48±0.31	19.44±0.31	12.31±0.31	3.07±0.01	2.17±0.01	16.13±13.00	4.14±0.59	0.01028±0.00589
336	13:29:49.80 +47:11:54.9	16.23±0.13	10.87±0.54	97.95±0.74	34.46±0.61	11.20±0.63	8.23±0.62	114.18±13.00	3.90±0.59	0.14547±0.02931
337	13:29:50.53 +47:11:54.7	26.68±0.74	21.20±0.67	164.56±0.92	62.75±0.76	18.66±0.40	13.26±0.40	478.00±13.00	6.19±0.59	0.26464±0.05512
338	13:29:51.25 +47:11:54.6	37.58±0.98	28.04±1.00	214.11±1.32	86.96±1.14	19.85±0.20	14.43±0.20	537.17±13.00	7.10±0.59	0.29020±0.06017
339	13:29:51.97 +47:11:54.4	32.98±1.12	50.17±1.19	176.35±1.25	159.09±1.36	28.23±0.28	22.02±0.28	377.28±13.00	4.98±0.59	0.20496±0.04356
340	13:29:52.69 +47:11:54.2	48.49±1.25	122.50±1.51	223.57±1.57	370.68±1.87	73.22±1.46	56.36±1.44	274.75±13.00	4.29±0.59	0.16700±0.03498
341	13:29:53.41 +47:11:54.1	41.96±0.93	34.31±1.13	207.28±1.37	108.41±1.29	22.04±0.24	17.68±0.25	163.30±13.00	5.29±0.59	0.20234±0.04163
342	13:29:54.14 +47:11:53.9	28.58±0.84	19.83±0.89	146.14±1.12	53.93±0.97	15.44±0.88	10.15±0.88	7.47±13.00	3.60±0.59	0.15130±0.03178
343	13:29:54.86 +47:11:53.8	18.64±0.64	12.58±0.60	103.20±0.79	38.82±0.68	12.29±0.15	8.89±0.15	145.29±13.00	4.49±0.59	0.12551±0.02684
344	13:29:55.58 +47:11:53.6	28.19±0.77	14.18±0.73	153.87±1.03	41.34±0.80	10.68±0.05	7.97±0.05	340.57±13.00	8.18±0.59	0.18615±0.03880
345	13:29:56.30 +47:11:53.4	33.87±0.39	15.55±0.55	173.72±0.89	45.11±0.63	15.13±0.13	11.12±0.13	149.39±13.00	5.76±0.59	0.18320±0.03696
346	13:29:57.02 +47:11:53.3	10.88±0.56	6.16±0.54	50.38±0.66	18.08±0.58	5.38±0.12	3.76±0.11	20.01±13.00	3.82±0.59	0.03431±0.00832
347	13:29:47.26 +47:11:49.1	2.85±0.42	3.09±0.45	11.36±0.46	8.92±0.47	3.27±0.46	2.00±0.47	17.73±13.00	3.23±0.59	0.00000±0.00220
348	13:29:47.99 +47:11:48.9	3.02±0.43	3.75±0.55	11.65±0.48	8.20±0.48	2.08±0.43	1.79±0.46	24.19±13.00	3.42±0.59	0.00000±0.00204
349	13:29:48.71 +47:11:48.8	4.20±0.42	3.60±0.52	17.70±0.54	11.04±0.54	3.43±0.27	2.35±0.24	10.41±13.00	6.21±0.59	0.00221±0.00271
350	13:29:49.43 +47:11:48.6	10.86±0.60	7.02±0.65	56.35±0.75	18.68±0.67	5.36±0.63	3.69±0.60	70.22±13.00	6.36±0.59	0.05384±0.01300

Table 3.1 (cont'd)

ID	Equatorial Coordinates	Hβ	[NII]λ6548	Hα	[NII]λ6584	[SII]λ6717	[SII]λ6731	Σ_{H2}	Σ_{HI}	Σ_{SFR}
351	13:29:50.15 +47:11:48.4	28.07±0.16	19.00±0.73	162.95±1.05	57.61±0.85	16.58±0.05	11.87±0.05	360.90±13.00	8.76±0.59	0.22794±0.04579
352	13:29:50.87 +47:11:48.3	27.40±0.84	19.85±0.87	156.75±1.12	61.93±0.98	14.93±0.18	12.05±0.19	296.47±13.00	9.36±0.59	0.21168±0.04454
353	13:29:51.60 +47:11:48.1	42.58±1.12	28.40±1.06	225.65±1.28	87.55±1.18	14.41±0.24	14.07±0.25	241.53±13.00	4.27±0.59	0.25977±0.05390
354	13:29:52.32 +47:11:48.0	37.33±1.42	138.72±0.41	173.52±0.38	415.76±0.48	61.96±0.12	56.24±0.13	224.74±13.00	5.25±0.59	0.12995±0.02848
355	13:29:53.04 +47:11:47.8	55.96±1.55	168.53±0.42	229.88±0.40	524.63±0.51	80.07±1.84	69.68±1.90	188.11±13.00	3.48±0.59	0.13137±0.02765
356	13:29:53.76 +47:11:47.6	40.37±1.07	26.97±1.16	194.01±1.37	81.63±1.26	18.08±0.23	13.12±0.24	97.93±13.00	3.62±0.59	0.17701±0.03683
357	13:29:54.48 +47:11:47.5	36.33±0.82	19.82±0.81	198.38±1.16	62.10±0.93	18.11±0.18	12.42±0.17	179.44±13.00	4.21±0.59	0.24338±0.05006
358	13:29:55.21 +47:11:47.3	89.74±0.56	28.12±0.82	417.85±1.49	84.12±0.95	22.30±0.42	17.58±0.43	150.82±13.00	5.65±0.59	0.36640±0.07348
359	13:29:55.93 +47:11:47.1	58.72±0.82	50.58±0.78	387.70±1.38	154.31±1.02	33.34±0.39	31.02±0.40	449.98±13.00	8.23±0.59	0.74227±0.14998
360	13:29:56.65 +47:11:47.0	9.45±0.52	6.40±0.12	44.38±0.14	18.07±0.12	4.81±0.11	3.59±0.11	13.66±13.00	6.44±0.59	0.03018±0.00749
361	13:29:57.37 +47:11:46.8	3.72±0.41	3.65±0.43	19.08±0.45	11.80±0.43	3.51±0.44	2.62±0.45	41.83±13.00	4.16±0.59	0.01065±0.00517
362	13:29:47.61 +47:11:42.6	6.74±0.44	4.17±0.47	27.39±0.53	10.82±0.47	3.71±0.45	2.91±0.47	15.45±13.00	4.26±0.59	0.00772±0.00292
363	13:29:48.33 +47:11:42.5	5.13±0.44	3.98±0.49	21.57±0.52	11.16±0.49	3.26±0.03	2.01±0.03	8.67±13.00	3.83±0.59	0.00493±0.00291
364	13:29:49.06 +47:11:42.3	5.28±0.49	4.91±0.58	29.95±0.62	15.08±0.59	4.77±0.58	3.38±0.57	39.16±13.00	5.83±0.59	0.03103±0.00997
365	13:29:49.78 +47:11:42.2	26.50±0.70	14.46±0.36	148.82±0.52	42.61±0.40	13.50±0.14	9.15±0.14	246.76±13.00	7.80±0.59	0.19200±0.03983
366	13:29:50.50 +47:11:42.0	33.69±0.72	22.86±0.74	205.13±1.10	66.43±0.85	20.27±0.39	14.28±0.39	493.56±13.00	9.20±0.59	0.32277±0.06617
367	13:29:51.22 +47:11:41.8	39.43±0.81	19.47±0.93	196.75±1.21	58.81±1.00	15.01±0.47	10.88±0.47	155.69±13.00	5.19±0.59	0.19598±0.04017
368	13:29:51.94 +47:11:41.7	32.94±1.13	41.25±1.15	176.62±1.22	127.54±1.28	22.35±0.26	16.98±0.28	89.24±13.00	2.26±0.59	0.20656±0.04395
369	13:29:52.67 +47:11:41.5	87.16±1.78	471.86±2.88	500.68±3.47	1285.67±3.37	174.67±2.06	193.44±2.25	207.82±13.00	2.06±0.59	0.63109±0.12990
370	13:29:53.39 +47:11:41.3	25.32±1.12	48.56±1.41	120.76±1.37	155.17±1.59	24.67±1.39	23.80±1.46	123.87±13.00	3.99±0.59	0.09322±0.02132
371	13:29:54.11 +47:11:41.2	53.74±1.02	28.88±1.04	270.79±1.40	88.11±1.15	21.51±0.54	15.13±0.54	184.13±13.00	3.12±0.59	0.27995±0.05713
372	13:29:54.83 +47:11:41.0	28.17±0.76	16.09±0.78	155.53±1.04	47.83±0.85	13.15±0.76	10.39±0.79	196.34±13.00	6.78±0.59	0.19340±0.04027
373	13:29:55.55 +47:11:40.9	36.04±0.70	23.11±0.67	218.17±1.08	69.65±0.80	21.88±0.35	16.03±0.35	484.93±13.00	11.61±0.59	0.33958±0.06932
374	13:29:56.27 +47:11:40.7	8.34±0.56	6.23±0.12	41.21±0.14	18.20±0.13	4.86±0.57	4.13±0.58	33.12±13.00	7.71±0.59	0.03173±0.00844
375	13:29:57.00 +47:11:40.5	7.62±0.48	5.38±0.51	38.11±0.59	15.70±0.53	4.61±0.25	2.60±0.24	31.87±13.00	5.94±0.59	0.02952±0.00780
376	13:29:47.24 +47:11:36.4	3.54±0.41	2.25±0.43	17.44±0.46	7.88±0.43	2.20±0.08	1.21±0.05	26.05±13.00	4.44±0.59	0.00714±0.00440
377	13:29:47.96 +47:11:36.2	3.04±0.42	2.74±0.41	10.20±0.39	7.74±0.39	3.00±0.10	1.46±0.09	15.37±13.00	3.50±0.59	0.00000±0.00128
378	13:29:48.68 +47:11:36.0	2.88±0.09	3.37±0.54	14.48±0.52	10.59±0.52	3.30±0.03	2.26±0.03	8.49±13.00	2.97±0.59	0.00478±0.00179
379	13:29:49.40 +47:11:35.9	9.26±0.29	7.71±0.56	54.54±0.68	23.45±0.61	7.69±0.12	4.48±0.12	178.90±13.00	5.85±0.59	0.07174±0.01538
380	13:29:50.12 +47:11:35.7	20.19±0.56	15.29±0.60	145.37±0.90	45.51±0.68	14.04±0.31	9.50±0.32	758.47±13.00	7.35±0.59	0.33097±0.06894
381	13:29:50.85 +47:11:35.6	41.81±0.82	21.45±0.79	222.63±1.17	65.02±0.91	17.84±0.17	11.43±0.16	270.26±13.00	7.09±0.59	0.25906±0.05294
382	13:29:51.57 +47:11:35.4	30.83±0.73	18.59±0.90	160.49±1.13	55.41±0.97	13.68±0.88	8.80±0.84	202.74±13.00	4.99±0.59	0.17437±0.03602
383	13:29:52.29 +47:11:35.2	44.05±1.06	31.56±1.16	222.43±1.37	94.91±1.26	18.12±1.12	14.46±1.16	79.04±13.00	3.16±0.59	0.22918±0.04732
384	13:29:53.01 +47:11:35.1	48.67±1.08	29.74±1.07	239.68±1.25	88.74±1.15	15.52±0.08	11.06±0.08	134.17±13.00	3.84±0.59	0.23391±0.04807
385	13:29:53.73 +47:11:34.9	37.10±0.97	23.38±0.23	203.39±0.28	71.37±0.25	14.85±0.55	11.80±0.58	246.45±13.00	3.53±0.59	0.25203±0.05220
386	13:29:54.46 +47:11:34.7	29.90±0.75	20.20±0.01	173.50±0.01	58.71±0.01	13.90±0.78	11.62±0.79	272.34±13.00	4.74±0.59	0.24306±0.05018
387	13:29:55.18 +47:11:34.6	29.06±0.67	20.00±0.59	162.57±0.85	56.20±0.67	17.61±0.67	12.80±0.66	542.89±13.00	7.39±0.59	0.20882±0.04300
388	13:29:55.90 +47:11:34.4	11.22±0.56	6.95±0.61	51.64±0.70	20.59±0.64	4.65±0.04	3.64±0.05	47.75±13.00	5.45±0.59	0.03477±0.00837
389	13:29:56.62 +47:11:34.2	9.66±0.49	6.72±0.47	42.33±0.54	17.52±0.49	4.12±0.49	3.27±0.51	28.70±13.00	3.44±0.59	0.02282±0.00572
390	13:29:57.34 +47:11:34.1	11.16±0.47	5.58±0.11	50.78±0.13	15.57±0.11	5.00±0.10	3.63±0.11	11.06±13.00	3.99±0.59	0.03289±0.00749
391	13:29:47.58 +47:11:29.9	3.68±0.40	2.38±0.45	13.20±0.45	7.94±0.45	2.32±0.21	1.60±0.18	19.27±13.00	4.14±0.59	0.00000±0.00152
392	13:29:48.31 +47:11:29.8	2.57±0.38	2.80±0.09	10.55±0.10	8.50±0.10	2.90±0.25	2.15±0.23	8.89±13.00	4.11±0.59	0.00000±0.00209
393	13:29:49.03 +47:11:29.6	4.85±0.45	3.50±0.49	28.19±0.58	12.50±0.54	3.97±0.11	2.83±0.11	24.13±13.00	3.84±0.59	0.03082±0.00992
394	13:29:49.75 +47:11:29.4	32.30±0.34	21.01±0.63	209.18±1.04	60.53±0.73	18.77±0.62	13.36±0.60	603.19±13.00	8.03±0.59	0.37882±0.07631
395	13:29:50.47 +47:11:29.3	19.75±0.33	16.08±0.64	128.76±0.89	46.22±0.73	13.14±0.64	11.08±0.65	644.15±13.00	7.97±0.59	0.23257±0.04731
396	13:29:51.19 +47:11:29.1	20.80±0.15	14.61±0.75	110.60±0.91	43.55±0.82	11.41±0.39	8.66±0.40	170.64±13.00	8.35±0.59	0.12289±0.02477
397	13:29:51.92 +47:11:28.9	36.86±0.18	28.43±0.48	183.22±0.59	80.62±0.52	18.80±0.44	13.63±0.44	158.08±13.00	9.06±0.59	0.18022±0.03611
398	13:29:52.64 +47:11:28.8	33.45±0.83	20.60±0.90	171.70±1.13	57.32±0.97	12.85±0.76	9.68±0.76	244.56±13.00	5.04±0.59	0.18121±0.03752
399	13:29:53.36 +47:11:28.6	34.09±0.83	21.48±0.19	186.20±0.25	59.92±0.21	13.99±0.75	10.52±0.76	300.82±13.00	8.69±0.59	0.22784±0.04696
400	13:29:54.08 +47:11:28.5	26.50±0.71	17.87±0.76	141.15±0.97	53.69±0.84	13.04±0.75	8.97±0.72	351.04±13.00	5.28±0.59	0.16046±0.03342

Table 3.1 (cont'd)

ID	Equatorial Coordinates	Hβ	[NII]λ6548	Hα	[NII]λ6584	[SII]λ6717	[SII]λ6731	Σ_{H2}	Σ_{HI}	Σ_{SFR}
401	13:29:54.80 +47:11:28.3	12.81±0.30	12.83±0.56	76.85±0.67	36.51±0.61	10.76±0.13	8.30±0.13	276.19±13.00	6.34±0.59	0.11031±0.02284
402	13:29:55.53 +47:11:28.1	6.39±0.11	6.24±0.59	31.72±0.63	16.95±0.62	4.07±0.57	2.85±0.65	66.82±13.00	4.12±0.59	0.02231±0.00481
403	13:29:56.25 +47:11:28.0	5.08±0.45	5.18±0.52	21.03±0.53	13.97±0.53	3.86±0.01	1.74±0.01	10.13±13.00	5.41±0.59	0.00402±0.00280
404	13:29:56.97 +47:11:27.8	6.11±0.43	4.35±0.47	22.75±0.50	12.37±0.48	3.72±0.46	2.63±0.47	0.00±13.00	7.01±0.59	0.00190±0.00187
405	13:29:47.21 +47:11:23.6	16.81±0.47	7.45±0.44	72.22±0.65	22.76±0.50	7.03±0.43	5.09±0.42	10.06±13.00	6.32±0.59	0.04395±0.00936
406	13:29:47.93 +47:11:23.5	2.56±0.38	2.32±0.21	8.73±0.22	6.04±0.23	1.98±0.02	2.21±0.03	28.82±13.00	3.97±0.59	0.00000±0.00117
407	13:29:48.65 +47:11:23.3	2.90±0.09	3.49±0.51	12.93±0.47	7.67±0.46	1.82±0.46	1.47±0.43	0.22±13.00	3.91±0.59	0.00000±0.00104
408	13:29:49.38 +47:11:23.1	6.17±0.24	5.91±0.52	38.00±0.60	16.51±0.54	5.32±0.50	4.49±0.50	48.02±13.00	4.12±0.59	0.05279±0.01183
409	13:29:50.10 +47:11:23.0	45.86±0.66	29.64±0.54	251.35±0.94	87.33±0.67	23.84±0.60	17.91±0.58	997.09±13.00	6.66±0.59	0.31377±0.06347
410	13:29:50.82 +47:11:22.8	10.15±0.27	7.97±0.59	54.35±0.69	25.21±0.64	6.15±0.12	4.97±0.12	360.30±13.00	6.23±0.59	0.05601±0.01187
411	13:29:51.54 +47:11:22.7	30.36±0.37	13.10±0.36	151.02±0.51	37.23±0.39	8.58±0.04	6.60±0.05	131.27±13.00	6.58±0.59	0.14692±0.02965
412	13:29:52.26 +47:11:22.5	22.56±0.68	14.09±0.71	117.04±0.92	42.48±0.79	11.04±0.37	7.63±0.38	237.14±13.00	5.15±0.59	0.12327±0.02600
413	13:29:52.98 +47:11:22.3	25.60±0.67	17.95±0.72	138.21±0.96	54.14±0.81	14.50±0.37	11.06±0.38	340.97±13.00	7.07±0.59	0.16199±0.03370
414	13:29:53.71 +47:11:22.2	28.37±0.70	14.79±0.38	139.97±0.51	43.39±0.42	10.71±0.69	7.22±0.68	245.33±13.00	3.85±0.59	0.13273±0.02745
415	13:29:54.43 +47:11:22.0	13.86±0.48	10.98±0.62	68.42±0.72	32.13±0.67	8.10±0.12	6.88±0.14	270.02±13.00	4.52±0.59	0.05953±0.01294
416	13:29:55.15 +47:11:21.8	6.09±0.49	4.62±0.53	24.62±0.57	16.12±0.57	3.60±0.10	3.31±0.12	30.41±13.00	5.94±0.59	0.00562±0.00291
417	13:29:55.87 +47:11:21.7	6.72±0.46	5.26±0.52	28.46±0.56	14.15±0.53	4.34±0.49	2.79±0.49	38.58±13.00	3.59±0.59	0.01018±0.00358
418	13:29:56.59 +47:11:21.5	8.27±0.43	5.73±0.49	42.64±0.57	15.39±0.50	4.68±0.46	3.23±0.44	28.39±13.00	6.40±0.59	0.03743±0.00907
419	13:29:57.32 +47:11:21.4	13.80±0.43	6.33±0.48	63.90±0.65	18.33±0.52	6.28±0.48	4.24±0.47	32.13±13.00	6.25±0.59	0.04635±0.00999
420	13:29:47.56 +47:11:17.2	1.75±0.01	3.06±0.52	7.74±0.43	6.51±0.42	1.82±0.33	1.51±0.38	30.00±13.00	5.04±0.59	0.00000±0.00075
421	13:29:48.28 +47:11:17.0	1.90±0.34	2.72±0.47	10.69±0.43	6.08±0.42	1.74±0.07	1.27±0.08	53.10±13.00	3.66±0.59	0.00398±0.00532
422	13:29:49.00 +47:11:16.9	2.37±0.08	2.65±0.47	11.00±0.46	7.11±0.48	1.91±0.40	1.47±0.39	23.47±13.00	2.52±0.59	0.00000±0.00114
423	13:29:49.72 +47:11:16.7	5.33±0.45	5.06±0.50	25.52±0.53	13.55±0.52	4.58±0.11	3.26±0.10	99.57±13.00	4.39±0.59	0.01382±0.00501
424	13:29:50.44 +47:11:16.5	18.87±0.52	10.97±0.01	98.07±0.02	32.38±0.01	9.58±0.46	6.65±0.46	537.23±13.00	8.08±0.59	0.10206±0.02131
425	13:29:51.17 +47:11:16.4	3.85±0.24	5.06±0.32	20.85±0.29	14.24±0.29	4.13±0.04	2.00±0.04	259.00±13.00	3.90±0.59	0.01553±0.00449
426	13:29:51.89 +47:11:16.2	6.71±0.50	6.99±0.59	29.18±0.61	18.89±0.61	4.53±0.56	2.85±0.51	146.23±13.00	3.72±0.59	0.01202±0.00422
427	13:29:52.61 +47:11:16.0	7.65±0.50	7.39±0.64	39.29±0.64	19.65±0.62	5.33±0.14	3.36±0.11	111.73±13.00	5.37±0.59	0.03330±0.00888
428	13:29:53.33 +47:11:15.9	5.35±0.48	6.94±0.59	24.72±0.59	19.19±0.61	4.31±0.56	3.24±0.58	103.38±13.00	3.75±0.59	0.01124±0.00459
429	13:29:54.05 +47:11:15.7	5.10±0.46	6.28±0.51	24.13±0.50	17.27±0.51	4.38±0.53	3.21±0.55	68.35±13.00	3.23±0.59	0.01190±0.00473
430	13:29:54.78 +47:11:15.6	4.36±0.44	5.19±0.04	19.40±0.04	14.04±0.04	3.24±0.01	2.57±0.01	20.90±13.00	3.62±0.59	0.00521±0.00332
431	13:29:55.50 +47:11:15.4	3.58±0.41	4.88±0.58	17.24±0.51	10.97±0.51	2.89±0.10	1.65±0.10	0.00±13.00	3.35±0.59	0.00612±0.00408
432	13:29:56.22 +47:11:15.2	6.95±0.23	4.97±0.48	30.26±0.54	14.21±0.50	4.79±0.09	3.29±0.10	37.28±13.00	3.49±0.59	0.01290±0.00314
433	13:29:56.94 +47:11:15.1	7.09±0.43	6.05±0.50	29.89±0.54	14.30±0.49	4.58±0.47	3.46±0.46	51.06±13.00	7.50±0.59	0.01106±0.00350
434	13:29:47.18 +47:11:10.9	5.28±0.08	3.95±0.42	20.71±0.44	10.37±0.41	3.12±0.37	2.28±0.38	74.59±13.00	4.27±0.59	0.00216±0.00082
435	13:29:47.90 +47:11:10.7	2.46±0.08	2.60±0.44	10.26±0.41	6.88±0.42	2.20±0.39	1.80±0.42	21.95±13.00	3.27±0.59	0.00000±0.00077
436	13:29:48.63 +47:11:10.6	3.58±0.23	3.24±0.46	12.92±0.45	8.15±0.45	2.94±0.03	1.66±0.03	43.22±13.00	4.04±0.59	0.00000±0.00097
437	13:29:49.35 +47:11:10.4	2.40±0.36	2.81±0.47	11.51±0.47	7.30±0.46	2.14±0.43	2.57±0.61	13.75±13.00	4.84±0.59	0.00045±0.00342
438	13:29:50.07 +47:11:10.3	6.01±0.09	5.42±0.48	32.07±0.54	14.36±0.49	5.22±0.50	3.34±0.47	95.40±13.00	7.00±0.59	0.02835±0.00596
439	13:29:50.79 +47:11:10.1	7.88±0.42	7.20±0.48	43.00±0.58	19.53±0.53	5.99±0.48	4.27±0.47	687.43±13.00	6.18±0.59	0.04431±0.01070
440	13:29:51.51 +47:11:09.9	3.14±0.40	4.78±0.54	19.30±0.53	12.87±0.53	4.11±0.51	2.90±0.52	196.67±13.00	4.76±0.59	0.02145±0.00924
441	13:29:52.24 +47:11:09.8	11.52±0.27	6.96±0.53	59.95±0.68	21.36±0.57	5.49±0.03	4.31±0.04	84.94±13.00	5.53±0.59	0.05842±0.01223
442	13:29:52.96 +47:11:09.6	5.45±0.43	5.36±0.52	25.32±0.54	13.66±0.52	3.90±0.27	2.46±0.28	141.90±13.00	5.62±0.59	0.01207±0.00439
443	13:29:53.68 +47:11:09.4	3.97±0.03	5.22±0.54	17.46±0.51	12.60±0.51	3.58±0.27	2.73±0.25	52.38±13.00	0.81±0.59	0.00324±0.00111
444	13:29:54.40 +47:11:09.3	11.83±0.43	6.61±0.52	46.69±0.61	17.06±0.54	4.90±0.03	3.47±0.03	8.57±13.00	3.11±0.59	0.01868±0.00435
445	13:29:55.12 +47:11:09.1	7.96±0.45	4.26±0.43	27.55±0.47	11.78±0.44	3.46±0.48	2.58±0.52	13.94±13.00	4.09±0.59	0.00232±0.00158
446	13:29:55.84 +47:11:09.0	3.66±0.09	4.07±0.55	13.74±0.49	9.29±0.49	2.75±0.03	2.40±0.04	38.59±13.00	2.77±0.59	0.00000±0.00070
447	13:29:56.57 +47:11:08.8	4.02±0.37	4.38±0.43	16.84±0.41	11.61±0.42	4.20±0.24	2.18±0.23	59.09±13.00	3.66±0.59	0.00143±0.00228
448	13:29:57.29 +47:11:08.6	4.62±0.36	4.71±0.24	21.20±0.25	12.30±0.25	4.62±0.09	3.45±0.09	40.31±13.00	7.10±0.59	0.00789±0.00329
449	13:29:47.53 +47:11:04.4	4.67±0.36	2.78±0.44	14.12±0.41	6.33±0.41	2.23±0.37	1.14±0.38	87.91±13.00	6.05±0.59	0.00000±0.00081
450	13:29:48.25 +47:11:04.3	1.95±0.35	2.60±0.44	7.83±0.40	5.74±0.41	2.18±0.03	1.56±0.03	26.25±13.00	5.12±0.59	0.00000±0.00188

Table 3.1 (cont'd)

ID	Equatorial Coordinates	Hβ	[NII]λ6548	Hα	[NII]λ6584	[SII]λ6717	[SII]λ6731	Σ_{H2}	Σ_{HI}	Σ_{SFR}
451	13:29:48.97 +47:11:04.1	2.93±0.03	4.08±0.49	12.30±0.45	8.72±0.45	2.70±0.21	1.65±0.21	23.54±13.00	4.42±0.59	0.00000±0.00073
452	13:29:49.70 +47:11:04.0	5.58±0.41	3.73±0.38	24.13±0.43	11.41±0.41	3.62±0.43	2.59±0.47	49.55±13.00	4.97±0.59	0.00790±0.00319
453	13:29:50.42 +47:11:03.8	4.00±0.37	3.75±0.23	21.05±0.26	10.04±0.25	3.01±0.09	2.12±0.09	81.47±13.00	4.18±0.59	0.01416±0.00534
454	13:29:51.14 +47:11:03.6	5.08±0.37	5.70±0.42	30.07±0.45	14.42±0.41	4.86±0.09	2.84±0.09	516.69±13.00	6.85±0.59	0.03533±0.00974
455	13:29:51.86 +47:11:03.5	3.59±0.20	4.61±0.11	19.37±0.11	10.47±0.10	2.32±0.09	2.37±0.10	339.47±13.00	4.98±0.59	0.01354±0.00382
456	13:29:52.58 +47:11:03.3	3.42±0.42	3.66±0.27	15.33±0.26	9.51±0.28	2.81±0.46	1.86±0.52	152.12±13.00	6.12±0.59	0.00210±0.00314
457	13:29:53.30 +47:11:03.2	2.18±0.20	3.79±0.59	11.18±0.49	9.47±0.51	2.07±0.01	1.29±0.01	37.46±13.00	3.24±0.59	0.00184±0.00254
458	13:29:54.03 +47:11:03.0	2.85±0.43	4.11±0.47	13.36±0.44	10.19±0.44	2.88±0.09	2.47±0.10	0.00±13.00	3.23±0.59	0.00155±0.00369
459	13:29:54.75 +47:11:02.8	7.69±0.43	4.88±0.54	30.00±0.54	12.56±0.50	3.39±0.01	2.56±0.01	2.39±13.00	5.47±0.59	0.00774±0.00266
460	13:29:55.47 +47:11:02.7	4.60±0.42	2.82±0.45	18.06±0.49	9.81±0.48	2.84±0.22	1.89±0.24	41.98±13.00	4.71±0.59	0.00057±0.00213
461	13:29:56.19 +47:11:02.5	4.16±0.38	4.34±0.50	19.65±0.49	10.58±0.48	3.63±0.45	2.34±0.42	31.16±13.00	3.43±0.59	0.00767±0.00379
462	13:29:56.91 +47:11:02.3	5.55±0.33	4.98±0.44	22.95±0.45	11.97±0.43	3.63±0.21	2.45±0.22	79.50±13.00	9.65±0.59	0.00534±0.00228
463	13:29:47.16 +47:10:58.2	2.56±0.34	2.23±0.54	7.24±0.39	5.02±0.43	1.50±0.02	1.37±0.03	27.88±13.00	3.07±0.59	0.00000±0.00064
464	13:29:47.88 +47:10:58.0	2.33±0.17	2.21±0.23	8.87±0.21	5.33±0.21	2.24±0.40	2.24±0.49	46.50±13.00	3.71±0.59	0.00000±0.00076
465	13:29:48.60 +47:10:57.8	2.51±0.36	2.49±0.44	9.83±0.40	5.95±0.41	2.21±0.38	1.12±0.41	26.36±13.00	3.47±0.59	0.00000±0.00177
466	13:29:49.32 +47:10:57.7	2.17±0.37	3.44±0.50	10.38±0.43	7.89±0.45	2.57±0.08	2.17±0.10	68.79±13.00	4.25±0.59	0.00000±0.00346
467	13:29:50.04 +47:10:57.5	11.46±0.43	7.86±0.48	51.61±0.58	17.90±0.49	6.22±0.10	4.16±0.09	6.42±13.00	3.92±0.59	0.03266±0.00734
468	13:29:50.76 +47:10:57.4	8.53±0.23	4.86±0.41	33.37±0.46	13.30±0.42	4.12±0.22	3.56±0.23	82.59±13.00	6.65±0.59	0.00989±0.00233
469	13:29:51.49 +47:10:57.2	5.75±0.37	5.92±0.24	34.94±0.29	16.13±0.26	4.82±0.23	3.14±0.22	445.63±13.00	9.49±0.59	0.04597±0.01166
470	13:29:52.21 +47:10:57.0	16.24±0.46	9.94±0.48	70.85±0.64	29.35±0.53	7.14±0.25	4.87±0.24	519.78±13.00	5.97±0.59	0.04473±0.00951
471	13:29:52.93 +47:10:56.9	3.10±0.22	3.58±0.49	13.98±0.46	9.36±0.47	2.97±0.44	2.21±0.44	183.82±13.00	5.25±0.59	0.00114±0.00184
472	13:29:53.65 +47:10:56.7	2.85±0.38	3.47±0.28	12.78±0.25	8.38±0.25	2.61±0.45	1.96±0.43	79.25±13.00	3.40±0.59	0.00000±0.00283
473	13:29:54.37 +47:10:56.5	3.16±0.40	3.49±0.26	15.74±0.26	9.83±0.26	3.31±0.44	2.40±0.47	36.41±13.00	3.81±0.59	0.00587±0.00427
474	13:29:55.09 +47:10:56.4	3.93±0.38	4.28±0.46	20.78±0.49	12.59±0.48	3.53±0.24	2.87±0.27	47.46±13.00	5.38±0.59	0.01411±0.00557
475	13:29:55.82 +47:10:56.2	5.29±0.23	5.22±0.48	26.42±0.52	12.67±0.49	4.34±0.40	3.09±0.41	53.91±13.00	5.95±0.59	0.01718±0.00432
476	13:29:56.54 +47:10:56.1	14.98±0.25	9.94±0.48	74.22±0.63	25.77±0.51	9.03±0.10	6.64±0.10	244.23±13.00	11.94±0.59	0.06607±0.01352
477	13:29:57.26 +47:10:55.9	8.81±0.40	6.88±0.03	46.46±0.04	17.45±0.03	7.09±0.40	5.53±0.41	231.83±13.00	14.72±0.59	0.04439±0.01015
478	13:29:47.50 +47:10:51.7	2.41±0.34	2.22±0.37	10.44±0.38	5.05±0.37	1.76±0.02	1.90±0.03	41.73±13.00	4.13±0.59	0.00000±0.00233
479	13:29:48.22 +47:10:51.6	11.12±0.40	5.03±0.09	45.53±0.11	13.17±0.09	5.02±0.38	3.75±0.39	39.82±13.00	3.70±0.59	0.02034±0.00462
480	13:29:48.95 +47:10:51.4	5.54±0.38	3.68±0.41	19.51±0.45	10.35±0.42	3.98±0.41	3.14±0.42	65.80±13.00	4.00±0.59	0.00000±0.00138
481	13:29:49.67 +47:10:51.2	7.18±0.23	4.77±0.09	28.05±0.11	13.13±0.10	5.02±0.43	3.95±0.45	14.20±13.00	5.83±0.59	0.00657±0.00170
482	13:29:50.39 +47:10:51.1	28.19±0.54	11.66±0.52	99.69±0.71	28.95±0.55	9.53±0.04	7.08±0.04	38.68±13.00	6.29±0.59	0.03853±0.00796
483	13:29:51.11 +47:10:50.9	12.17±0.48	6.44±0.51	43.82±0.58	18.69±0.53	3.96±0.01	2.85±0.01	47.22±13.00	6.56±0.59	0.01186±0.00301
484	13:29:51.83 +47:10:50.7	6.33±0.39	5.93±0.46	33.83±0.52	16.93±0.48	6.04±0.09	4.48±0.10	333.67±13.00	6.82±0.59	0.03068±0.00800
485	13:29:52.55 +47:10:50.6	10.66±0.41	8.68±0.45	62.21±0.59	22.30±0.48	8.26±0.39	5.66±0.39	448.81±13.00	7.59±0.59	0.08154±0.01781
486	13:29:53.28 +47:10:50.4	12.63±0.10	7.13±0.48	58.58±0.61	18.58±0.50	7.07±0.47	4.81±0.48	168.79±13.00	7.88±0.59	0.04174±0.00847
487	13:29:54.00 +47:10:50.3	7.95±0.23	5.43±0.44	40.48±0.55	17.39±0.49	5.87±0.09	4.47±0.10	230.78±13.00	8.42±0.59	0.03378±0.00731
488	13:29:54.72 +47:10:50.1	10.01±0.40	10.12±0.25	66.20±0.33	27.38±0.27	6.93±0.09	6.77±0.09	459.87±13.00	8.09±0.59	0.11841±0.02580
489	13:29:55.44 +47:10:49.9	25.07±0.26	22.56±0.11	130.56±0.16	57.73±0.13	17.02±0.49	14.62±0.51	496.56±13.00	10.12±0.59	0.14000±0.02817
490	13:29:56.16 +47:10:49.8	22.14±0.49	17.89±0.51	136.01±0.78	48.55±0.59	16.40±0.50	12.67±0.50	383.70±13.00	11.84±0.59	0.21482±0.04414
491	13:29:48.10 +47:12:31.3	6.02±0.45	4.56±0.50	29.58±0.54	10.82±0.47	3.50±0.03	2.61±0.03	36.97±13.00	10.65±0.59	0.01937±0.00601
492	13:29:48.82 +47:12:31.2	4.63±0.10	5.80±0.30	28.08±0.31	14.24±0.28	4.94±0.48	3.06±0.47	192.62±13.00	9.30±0.59	0.03456±0.00727
493	13:29:49.54 +47:12:31.0	3.68±0.03	4.71±0.55	22.70±0.58	13.45±0.56	4.98±0.45	3.57±0.45	213.36±13.00	6.82±0.59	0.02727±0.00588
494	13:29:50.27 +47:12:30.8	4.60±0.52	5.05±0.31	23.99±0.31	14.37±0.30	3.75±0.26	2.55±0.27	133.67±13.00	6.91±0.59	0.01712±0.00710
495	13:29:50.99 +47:12:30.7	2.27±0.49	4.63±0.33	14.07±0.29	11.65±0.29	3.71±0.28	2.60±0.27	114.05±13.00	6.22±0.59	0.01315±0.01048
496	13:29:51.71 +47:12:30.5	3.36±0.49	5.43±0.04	19.00±0.04	13.67±0.04	4.10±0.57	2.66±0.51	125.76±13.00	4.67±0.59	0.01563±0.00818
497	13:29:52.43 +47:12:30.4	5.32±0.48	6.46±0.31	29.29±0.32	17.44±0.30	5.33±0.26	3.99±0.28	209.26±13.00	6.93±0.59	0.02754±0.00879
498	13:29:53.16 +47:12:30.2	7.33±0.53	5.09±0.30	40.37±0.35	15.05±0.30	5.13±0.04	3.56±0.04	95.44±13.00	6.39±0.59	0.04197±0.01125
499	13:29:53.88 +47:12:30.0	4.58±0.10	4.76±0.47	30.24±0.53	13.09±0.48	5.17±0.51	3.87±0.52	172.97±13.00	4.94±0.59	0.04804±0.01019
500	13:29:54.60 +47:12:29.9	9.26±0.53	6.95±0.29	58.15±0.38	19.68±0.30	7.01±0.50	5.38±0.52	218.21±13.00	8.32±0.59	0.09057±0.02144

Table 3.1 (cont'd)

ID	Equatorial Coordinates	Hβ	[NII]λ6548	Hα	[NII]λ6584	[SII]λ6717	[SII]λ6731	Σ_{H2}	Σ_{HI}	Σ_{SFR}
501	13:29:55.32 +47:12:29.7	14.99±0.56	9.43±0.29	91.76±0.43	26.18±0.31	9.85±0.27	7.22±0.27	98.59±13.00	7.93±0.59	0.14036±0.03025
502	13:29:56.04 +47:12:29.5	37.18±0.82	14.99±0.65	193.77±1.10	44.73±0.74	12.19±0.32	8.62±0.31	46.22±13.00	4.62±0.59	0.21320±0.04381
503	13:29:56.77 +47:12:29.4	8.71±0.47	4.88±0.49	51.43±0.64	13.32±0.49	4.77±0.22	4.04±0.25	71.26±13.00	4.30±0.59	0.06757±0.01596
504	13:29:57.49 +47:12:29.2	1.93±0.34	3.67±0.51	11.62±0.44	6.68±0.41	1.80±0.19	1.93±0.21	63.40±13.00	4.44±0.59	0.00777±0.00676
505	13:29:47.73 +47:12:25.0	7.55±0.47	5.38±0.25	45.20±0.33	16.29±0.27	2.96±0.06	2.93±0.09	233.57±13.00	10.88±0.59	0.06022±0.01483
506	13:29:48.45 +47:12:24.9	5.72±0.48	3.81±0.46	30.01±0.52	10.24±0.45	3.60±0.03	2.77±0.03	164.59±13.00	11.35±0.59	0.02458±0.00776
507	13:29:49.17 +47:12:24.7	4.11±0.50	4.41±0.58	20.78±0.58	11.03±0.56	2.88±0.45	2.27±0.47	129.34±13.00	8.66±0.59	0.01187±0.00608
508	13:29:49.89 +47:12:24.6	3.21±0.27	4.89±0.31	20.47±0.31	13.38±0.31	4.35±0.28	3.55±0.29	33.50±13.00	4.06±0.59	0.02630±0.00820
509	13:29:50.61 +47:12:24.4	3.19±0.51	5.14±0.31	16.85±0.31	13.96±0.31	4.31±0.11	3.81±0.11	0.62±13.00	5.18±0.59	0.00942±0.00665
510	13:29:51.34 +47:12:24.2	3.01±0.29	4.89±0.58	16.66±0.57	12.44±0.57	4.01±0.04	2.55±0.04	90.69±13.00	7.90±0.59	0.01133±0.00503
511	13:29:52.06 +47:12:24.1	7.91±0.29	6.85±0.51	53.07±0.63	21.46±0.54	6.57±0.11	3.82±0.10	104.51±13.00	6.95±0.59	0.09622±0.02095
512	13:29:52.78 +47:12:23.9	6.97±0.30	6.27±0.62	34.25±0.65	15.47±0.60	3.70±0.11	1.95±0.10	182.87±13.00	4.09±0.59	0.02417±0.00583
513	13:29:53.50 +47:12:23.7	11.89±0.60	8.15±0.32	65.01±0.41	24.05±0.34	7.86±0.56	6.16±0.57	92.69±13.00	4.72±0.59	0.07284±0.01675
514	13:29:54.22 +47:12:23.6	10.09±0.61	8.01±0.05	54.56±0.05	17.32±0.04	6.24±0.32	4.68±0.32	136.93±13.00	7.65±0.59	0.05764±0.01407
515	13:29:54.95 +47:12:23.4	12.74±0.12	7.76±0.52	76.02±0.78	23.18±0.59	7.98±0.27	4.99±0.25	272.46±13.00	8.71±0.59	0.10756±0.02178
516	13:29:55.67 +47:12:23.3	8.75±0.51	6.43±0.54	51.25±0.69	17.85±0.56	6.51±0.51	4.58±0.50	89.13±13.00	8.28±0.59	0.06593±0.01599
517	13:29:56.39 +47:12:23.1	11.95±0.55	7.60±0.55	62.22±0.72	17.68±0.56	6.21±0.26	4.05±0.24	43.78±13.00	7.12±0.59	0.06114±0.01395
518	13:29:57.11 +47:12:22.9	5.13±0.10	4.76±0.50	27.36±0.55	11.63±0.49	3.65±0.03	2.88±0.03	33.45±13.00	4.32±0.59	0.02259±0.00490
519	13:29:57.83 +47:12:22.8	1.93±0.42	3.01±0.54	9.09±0.45	6.78±0.45	2.34±0.03	1.62±0.03	71.14±13.00	4.09±0.59	0.00000±0.00371
520	13:29:48.07 +47:12:18.6	2.68±0.45	3.86±0.29	16.30±0.27	10.47±0.27	3.41±0.11	2.28±0.10	100.69±13.00	5.49±0.59	0.01567±0.00920
521	13:29:48.80 +47:12:18.4	2.85±0.11	3.71±0.36	14.24±0.29	9.32±0.29	3.34±0.11	1.36±0.10	84.18±13.00	4.78±0.59	0.00438±0.00160
522	13:29:49.52 +47:12:18.3	3.03±0.44	5.40±0.64	15.90±0.57	12.96±0.58	4.08±0.11	2.62±0.10	47.80±13.00	3.11±0.59	0.00802±0.00571
523	13:29:50.24 +47:12:18.1	2.86±0.47	4.51±0.61	16.07±0.57	11.47±0.56	4.82±0.56	3.03±0.53	0.00±13.00	2.94±0.59	0.01123±0.00759
524	13:29:50.96 +47:12:17.9	3.85±0.27	5.02±0.51	24.55±0.53	13.35±0.50	3.57±0.04	2.63±0.03	28.41±13.00	6.49±0.59	0.03347±0.00922
525	13:29:51.68 +47:12:17.8	8.37±0.61	8.19±0.36	51.04±0.39	18.31±0.34	5.30±0.59	4.22±0.59	90.08±13.00	4.69±0.59	0.07269±0.01880
526	13:29:52.41 +47:12:17.6	11.57±0.62	10.04±0.35	66.22±0.42	27.66±0.37	8.56±0.33	5.46±0.31	50.72±13.00	3.78±0.59	0.08330±0.01943
527	13:29:53.13 +47:12:17.5	21.81±0.72	10.99±0.15	122.82±0.21	28.58±0.15	9.09±0.13	6.28±0.13	96.01±13.00	5.46±0.59	0.15762±0.03337
528	13:29:53.85 +47:12:17.3	25.62±0.72	12.28±0.63	151.00±1.05	36.13±0.71	10.64±0.32	7.30±0.31	158.08±13.00	6.67±0.59	0.21794±0.04548
529	13:29:54.57 +47:12:17.1	40.42±0.82	16.60±0.58	209.22±1.03	46.44±0.66	14.42±0.13	10.40±0.13	158.51±13.00	8.92±0.59	0.22752±0.04655
530	13:29:55.29 +47:12:17.0	7.86±0.27	7.95±0.13	51.10±0.15	21.95±0.13	6.75±0.11	5.64±0.11	291.65±13.00	6.89±0.59	0.08517±0.01826
531	13:29:56.02 +47:12:16.8	7.11±0.11	6.81±0.30	43.83±0.35	17.73±0.30	6.13±0.03	4.58±0.04	58.02±13.00	7.22±0.59	0.06253±0.01276
532	13:29:56.74 +47:12:16.6	10.68±0.55	7.28±0.50	65.47±0.66	19.19±0.51	6.76±0.28	4.85±0.28	27.42±13.00	3.78±0.59	0.09732±0.02245
533	13:29:57.46 +47:12:16.5	2.97±0.09	4.13±0.27	14.45±0.24	9.15±0.24	2.62±0.09	1.77±0.10	51.01±13.00	2.13±0.59	0.00373±0.00122
534	13:29:47.70 +47:12:12.3	4.21±0.27	3.95±0.13	17.09±0.11	8.54±0.11	3.02±0.10	2.44±0.10	64.43±13.00	6.31±0.59	0.00078±0.00143
535	13:29:48.42 +47:12:12.1	2.17±0.49	4.47±0.52	11.73±0.46	10.15±0.48	3.51±0.51	2.03±0.50	23.85±13.00	4.22±0.59	0.00400±0.00662
536	13:29:49.14 +47:12:12.0	3.94±0.04	5.34±0.32	20.77±0.31	13.23±0.30	3.69±0.11	3.09±0.12	21.16±13.00	3.19±0.59	0.01392±0.00293
537	13:29:49.86 +47:12:11.8	4.81±0.55	5.56±0.62	21.64±0.60	12.50±0.59	3.02±0.11	2.26±0.11	6.09±13.00	3.74±0.59	0.00751±0.00450
538	13:29:50.59 +47:12:11.7	11.33±0.53	7.86±0.62	58.40±0.76	23.27±0.66	6.95±0.31	4.70±0.31	0.00±13.00	3.18±0.59	0.05522±0.01274
539	13:29:51.31 +47:12:11.5	14.50±0.63	12.17±0.59	90.05±0.78	32.71±0.63	10.19±0.65	6.27±0.62	56.44±13.00	3.47±0.59	0.14226±0.03145
540	13:29:52.03 +47:12:11.3	41.00±0.85	20.20±0.77	211.88±1.22	53.95±0.85	15.96±0.73	11.44±0.73	100.66±13.00	3.44±0.59	0.22968±0.04706
541	13:29:52.75 +47:12:11.2	23.54±0.74	12.74±0.73	125.00±1.02	34.50±0.78	10.04±0.37	6.66±0.36	198.54±13.00	4.20±0.59	0.13986±0.02959
542	13:29:53.47 +47:12:11.0	29.34±0.16	13.51±0.69	152.00±1.07	38.20±0.77	11.87±0.36	8.88±0.35	110.17±13.00	4.71±0.59	0.16270±0.03270
543	13:29:54.20 +47:12:10.8	56.76±0.93	19.33±0.73	288.84±1.36	52.89±0.83	14.81±0.15	11.47±0.15	137.54±13.00	6.84±0.59	0.30614±0.06215
544	13:29:54.92 +47:12:10.7	33.38±0.84	11.81±0.39	160.65±0.57	31.92±0.40	9.73±0.35	7.37±0.36	181.12±13.00	6.28±0.59	0.14519±0.03006
545	13:29:55.64 +47:12:10.5	7.62±0.44	8.72±0.49	49.98±0.60	24.20±0.53	7.46±0.52	6.15±0.55	337.71±13.00	6.02±0.59	0.08516±0.02036
546	13:29:56.36 +47:12:10.4	6.21±0.52	5.07±0.31	34.14±0.34	12.70±0.30	3.53±0.26	3.55±0.29	56.56±13.00	8.09±0.59	0.03371±0.00995
547	13:29:57.08 +47:12:10.2	2.94±0.44	3.77±0.30	16.52±0.28	9.27±0.27	3.39±0.10	1.80±0.09	30.31±13.00	3.45±0.59	0.01184±0.00703
548	13:29:57.81 +47:12:10.0	1.54±0.40	3.22±0.54	7.93±0.48	7.76±0.49	3.17±0.51	1.80±0.49	0.00±13.00	2.18±0.59	0.00000±0.00476
549	13:29:48.05 +47:12:05.9	2.79±0.49	3.51±0.29	14.47±0.28	9.67±0.27	2.97±0.04	2.27±0.03	11.26±13.00	4.94±0.59	0.00593±0.00585
550	13:29:48.77 +47:12:05.7	5.53±0.52	5.82±0.56	27.24±0.60	15.89±0.57	4.74±0.11	2.66±0.10	29.97±13.00	5.26±0.59	0.01722±0.00635

Table 3.1 (cont'd)

ID	Equatorial Coordinates	Hβ	[NII]λ6548	Hα	[NII]λ6584	[SII]λ6717	[SII]λ6731	Σ_{H2}	Σ_{HI}	Σ_{SFR}
551	13:29:49.49 +47:12:05.5	6.98±0.53	5.22±0.04	37.06±0.05	15.66±0.04	4.90±0.13	2.83±0.12	58.67±13.00	5.47±0.59	0.03393±0.00952
552	13:29:50.21 +47:12:05.4	5.36±0.48	7.15±0.40	33.37±0.36	17.01±0.34	4.26±0.59	2.88±0.59	44.17±13.00	4.06±0.59	0.04621±0.01369
553	13:29:50.93 +47:12:05.2	20.79±0.73	13.83±0.74	129.11±1.02	39.11±0.80	11.14±0.38	8.11±0.36	0.00±13.00	3.28±0.59	0.20858±0.04449
554	13:29:51.66 +47:12:05.1	59.12±1.02	30.17±0.78	343.35±1.32	93.25±0.93	27.30±0.90	19.79±0.88	298.50±13.00	4.32±0.59	0.49247±0.10006
555	13:29:52.38 +47:12:04.9	55.06±1.00	36.13±0.50	321.45±0.79	107.51±0.60	31.14±0.83	22.98±0.80	378.08±13.00	4.93±0.59	0.46587±0.09475
556	13:29:53.10 +47:12:04.7	27.99±0.87	16.40±0.45	142.01±0.60	51.01±0.51	14.13±0.18	9.27±0.18	272.60±13.00	7.12±0.59	0.14400±0.03034
557	13:29:53.82 +47:12:04.6	17.94±0.76	12.39±0.82	104.51±1.02	32.42±0.86	8.78±0.05	5.69±0.05	177.08±13.00	7.71±0.59	0.14354±0.03160
558	13:29:54.54 +47:12:04.4	66.23±0.99	19.91±0.43	354.50±0.79	56.04±0.47	17.73±0.78	11.89±0.76	68.62±13.00	9.12±0.59	0.42373±0.08572
559	13:29:55.27 +47:12:04.2	28.14±0.69	13.24±0.14	167.69±0.23	37.16±0.15	12.56±0.32	8.95±0.31	433.94±13.00	7.63±0.59	0.24944±0.05144
560	13:29:55.99 +47:12:04.1	13.31±0.55	9.38±0.58	76.00±0.79	25.19±0.63	8.62±0.56	5.99±0.56	174.10±13.00	7.57±0.59	0.09670±0.02137
561	13:29:56.71 +47:12:03.9	8.56±0.57	6.43±0.58	46.07±0.70	18.65±0.62	6.16±0.12	4.36±0.11	50.19±13.00	5.59±0.59	0.04654±0.01209
562	13:29:57.43 +47:12:03.7	2.66±0.45	3.93±0.52	14.18±0.52	11.09±0.52	3.49±0.49	2.07±0.41	0.00±13.00	3.45±0.59	0.00661±0.00599
563	13:29:47.67 +47:11:59.6	2.39±0.45	3.64±0.48	12.50±0.45	8.51±0.44	2.48±0.51	1.33±0.39	5.09±13.00	2.85±0.59	0.00396±0.00560
564	13:29:48.39 +47:11:59.4	3.09±0.49	4.51±0.58	14.58±0.53	10.29±0.54	3.35±0.50	1.91±0.49	1.51±13.00	4.58±0.59	0.00286±0.00436
565	13:29:49.12 +47:11:59.3	9.68±0.30	6.48±0.59	49.36±0.71	19.47±0.61	4.62±0.11	3.30±0.11	29.06±13.00	4.67±0.59	0.04368±0.00947
566	13:29:49.84 +47:11:59.1	9.42±0.61	7.28±0.36	53.68±0.40	20.79±0.36	5.09±0.63	3.95±0.62	34.60±13.00	3.42±0.59	0.06481±0.01616
567	13:29:50.56 +47:11:58.9	26.31±0.76	22.57±0.40	194.36±0.61	65.20±0.47	18.90±0.39	15.26±0.39	316.12±13.00	5.55±0.59	0.47247±0.09838
568	13:29:51.28 +47:11:58.8	41.98±0.93	25.18±0.91	238.19±1.34	77.32±1.05	21.25±0.47	16.45±0.48	674.85±13.00	6.86±0.59	0.32094±0.06591
569	13:29:52.00 +47:11:58.6	39.68±0.93	34.63±0.59	233.67±0.77	109.30±0.70	26.10±0.23	19.85±0.24	510.09±13.00	4.91±0.59	0.34238±0.07041
570	13:29:52.73 +47:11:58.4	43.64±1.09	56.61±0.67	233.14±0.78	171.88±0.79	35.97±0.25	27.15±0.26	288.68±13.00	3.78±0.59	0.27375±0.05654
571	13:29:53.45 +47:11:58.3	30.05±0.97	19.72±0.86	161.30±1.10	62.24±0.97	14.84±0.20	10.50±0.20	149.46±13.00	5.77±0.59	0.18819±0.03978
572	13:29:54.17 +47:11:58.1	20.28±0.84	12.98±0.90	110.51±1.07	35.08±0.94	8.66±0.18	7.12±0.18	50.87±13.00	5.59±0.59	0.13024±0.02861
573	13:29:54.89 +47:11:58.0	32.07±0.76	15.92±0.72	187.44±1.14	45.85±0.81	15.34±0.15	9.97±0.15	194.68±13.00	5.72±0.59	0.26797±0.05525
574	13:29:55.61 +47:11:57.8	17.14±0.60	10.27±0.61	112.97±0.91	30.39±0.68	9.80±0.04	6.38±0.04	516.67±13.00	9.01±0.59	0.20797±0.04442
575	13:29:56.34 +47:11:57.6	63.27±0.93	21.25±0.73	278.27±1.29	60.07±0.84	19.71±0.72	13.06±0.69	132.29±13.00	6.44±0.59	0.21092±0.04272
576	13:29:57.06 +47:11:57.5	12.65±0.04	6.93±0.52	59.14±0.65	22.35±0.54	6.53±0.54	3.74±0.49	32.88±13.00	4.36±0.59	0.04321±0.00874
577	13:29:57.78 +47:11:57.3	4.74±0.46	3.74±0.28	20.59±0.28	9.57±0.26	3.01±0.24	1.91±0.22	11.77±13.00	4.75±0.59	0.00532±0.00323
578	13:29:48.02 +47:11:53.1	2.92±0.10	3.15±0.27	11.09±0.27	8.76±0.27	3.44±0.03	2.29±0.04	28.13±13.00	3.26±0.59	0.00000±0.00056
579	13:29:48.74 +47:11:53.0	4.53±0.48	3.50±0.53	19.58±0.56	10.45±0.54	2.79±0.10	2.48±0.10	12.10±13.00	5.33±0.59	0.00434±0.00338
580	13:29:49.46 +47:11:52.8	6.68±0.12	7.28±0.65	41.73±0.70	19.49±0.64	5.87±0.13	4.41±0.13	39.09±13.00	4.35±0.59	0.06117±0.01276
581	13:29:50.18 +47:11:52.6	25.73±0.72	18.10±0.73	167.80±1.07	54.63±0.83	18.31±0.65	12.45±0.62	412.26±13.00	6.89±0.59	0.30664±0.06393
582	13:29:50.91 +47:11:52.5	27.52±0.86	18.63±0.87	168.03±1.17	60.36±0.99	15.50±0.87	10.76±0.85	433.07±13.00	8.15±0.59	0.26418±0.05562
583	13:29:51.63 +47:11:52.3	30.54±0.08	25.45±1.16	172.37±1.38	85.38±1.32	17.10±0.24	14.26±0.26	402.65±13.00	5.26±0.59	0.22666±0.04553
584	13:29:52.35 +47:11:52.2	37.65±0.28	94.75±0.34	174.61±0.34	290.33±0.41	54.01±1.53	43.83±1.58	327.95±13.00	4.79±0.59	0.13020±0.02615
585	13:29:53.07 +47:11:52.0	43.85±1.26	102.59±0.83	208.75±0.85	306.80±0.99	63.93±0.80	48.03±0.81	192.07±13.00	4.32±0.59	0.16736±0.03534
586	13:29:53.79 +47:11:51.8	44.45±1.07	25.61±0.60	231.01±0.75	75.21±0.64	17.64±0.23	12.78±0.22	89.55±13.00	3.78±0.59	0.25470±0.05249
587	13:29:54.52 +47:11:51.7	22.81±0.80	17.57±0.87	127.49±1.08	49.96±0.94	13.88±0.84	10.73±0.87	115.70±13.00	3.88±0.59	0.16112±0.03445
588	13:29:55.24 +47:11:51.5	42.32±0.81	18.93±0.75	229.98±1.22	57.26±0.86	15.61±0.15	11.53±0.15	131.04±13.00	5.40±0.59	0.28067±0.05730
589	13:29:55.96 +47:11:51.3	36.60±0.43	19.59±0.71	204.10±1.13	55.20±0.81	15.86±0.14	12.03±0.14	396.88±13.00	7.74±0.59	0.26293±0.05307
590	13:29:56.68 +47:11:51.2	15.01±0.62	8.36±0.55	71.08±0.68	23.59±0.57	7.38±0.51	5.59±0.53	25.92±13.00	4.71±0.59	0.05587±0.01248
591	13:29:57.40 +47:11:51.0	7.09±0.27	6.25±0.50	36.13±0.53	15.36±0.47	4.07±0.49	3.88±0.51	44.55±13.00	4.50±0.59	0.02915±0.00666
592	13:29:47.64 +47:11:46.8	3.15±0.45	3.85±0.54	10.73±0.48	7.84±0.47	2.31±0.42	1.66±0.45	15.14±13.00	3.80±0.59	0.00000±0.00145
593	13:29:48.37 +47:11:46.7	3.55±0.44	4.38±0.29	16.79±0.28	9.68±0.27	2.84±0.10	1.92±0.09	7.68±13.00	5.16±0.59	0.00503±0.00399
594	13:29:49.09 +47:11:46.5	4.17±0.52	4.88±0.64	23.78±0.62	12.43±0.61	3.61±0.01	2.25±0.01	7.25±13.00	6.72±0.59	0.02290±0.00958
595	13:29:49.81 +47:11:46.4	21.10±0.73	11.98±0.73	116.09±0.97	34.51±0.78	8.72±0.14	6.10±0.14	212.27±13.00	6.80±0.59	0.14037±0.02999
596	13:29:50.53 +47:11:46.2	31.26±0.77	26.08±0.81	204.11±1.18	77.98±0.95	22.17±0.43	15.96±0.41	313.65±13.00	9.99±0.59	0.37610±0.07768
597	13:29:51.25 +47:11:46.0	43.30±1.05	26.01±1.10	233.20±1.41	71.80±1.18	16.22±1.03	14.11±1.07	204.80±13.00	5.73±0.59	0.27902±0.05761
598	13:29:51.98 +47:11:45.9	28.88±1.15	49.12±0.81	137.59±0.79	154.86±0.92	22.64±1.41	21.31±1.49	112.87±13.00	3.47±0.59	0.10724±0.02380
599	13:29:52.70 +47:11:45.7	88.76±2.02	462.58±2.91	519.94±2.89	1315.30±3.54	204.99±2.67	242.63±2.96	246.51±13.00	3.81±0.59	0.68499±0.14161
600	13:29:53.42 +47:11:45.5	35.58±1.28	77.54±1.60	167.10±1.58	227.92±1.84	39.07±1.52	30.51±1.53	141.07±13.00	3.62±0.59	0.12787±0.02797

Table 3.1 (cont'd)

ID	Equatorial Coordinates	Hβ	[NII]λ6548	Hα	[NII]λ6584	[SII]λ6717	[SII]λ6731	Σ_{H2}	Σ_{HI}	Σ_{SFR}
601	13:29:54.14 +47:11:45.4	49.70±1.06	26.40±1.06	267.84±1.45	78.55±1.17	18.50±0.22	14.21±0.22	141.91±13.00	3.19±0.59	0.32252±0.06609
602	13:29:54.86 +47:11:45.2	34.31±0.82	17.78±0.81	183.87±1.15	50.12±0.89	14.08±0.41	10.84±0.43	148.35±13.00	5.38±0.59	0.21525±0.04443
603	13:29:55.59 +47:11:45.1	59.09±0.48	31.59±0.17	337.29±0.29	88.33±0.20	24.04±0.16	18.38±0.15	469.65±13.00	8.53±0.59	0.46524±0.09336
604	13:29:56.31 +47:11:44.9	19.38±0.63	11.32±0.57	100.65±0.75	33.73±0.61	8.72±0.32	7.12±0.33	95.77±13.00	7.62±0.59	0.10483±0.02232
605	13:29:57.03 +47:11:44.7	5.42±0.25	5.09±0.29	25.38±0.30	12.88±0.29	4.06±0.27	3.34±0.27	15.56±13.00	5.90±0.59	0.01256±0.00334
606	13:29:57.75 +47:11:44.6	3.15±0.03	4.28±0.47	13.45±0.43	10.96±0.44	3.16±0.09	2.47±0.10	29.87±13.00	3.82±0.59	0.00000±0.00072
607	13:29:47.99 +47:11:40.4	4.83±0.43	4.12±0.52	19.43±0.52	9.71±0.48	3.01±0.03	2.01±0.03	43.63±13.00	3.82±0.59	0.00208±0.00236
608	13:29:48.71 +47:11:40.2	3.42±0.03	5.38±0.57	16.19±0.55	12.35±0.56	2.81±0.03	3.07±0.03	0.00±13.00	3.64±0.59	0.00454±0.00146
609	13:29:49.43 +47:11:40.1	11.38±0.59	9.45±0.64	71.72±0.80	26.51±0.68	8.82±0.13	5.39±0.13	126.49±13.00	6.67±0.59	0.11519±0.02654
610	13:29:50.16 +47:11:39.9	26.88±0.68	19.39±0.69	190.79±1.08	55.33±0.79	15.39±0.35	11.06±0.34	628.39±13.00	8.14±0.59	0.42378±0.08761
611	13:29:50.88 +47:11:39.8	29.24±0.79	19.07±0.45	168.89±0.59	51.74±0.49	13.99±0.17	9.93±0.17	259.86±13.00	7.00±0.59	0.23397±0.04860
612	13:29:51.60 +47:11:39.6	31.79±0.96	23.81±0.91	168.01±1.09	70.01±1.01	14.89±0.21	10.71±0.22	132.25±13.00	3.31±0.59	0.18951±0.03981
613	13:29:52.32 +47:11:39.4	39.14±1.20	70.19±0.33	185.84±0.33	206.95±0.38	39.17±0.32	32.13±0.33	122.09±13.00	1.38±0.59	0.14704±0.03126
614	13:29:53.04 +47:11:39.3	38.53±1.29	152.04±0.40	169.43±0.36	425.89±0.47	70.71±0.12	72.96±0.13	119.88±13.00	3.13±0.59	0.11109±0.02394
615	13:29:53.77 +47:11:39.1	29.92±1.03	25.72±1.18	162.62±1.33	77.57±1.28	16.13±1.18	11.15±1.12	167.12±13.00	4.50±0.59	0.19537±0.04165
616	13:29:54.49 +47:11:38.9	39.72±0.93	27.21±0.86	200.26±1.10	81.93±0.97	18.87±0.50	16.21±0.52	192.39±13.00	4.93±0.59	0.20455±0.04217
617	13:29:55.21 +47:11:38.8	26.40±0.68	21.40±0.38	180.01±0.56	62.14±0.44	19.23±0.70	14.59±0.68	477.56±13.00	9.68±0.59	0.36437±0.07532
618	13:29:55.93 +47:11:38.6	17.52±0.66	11.08±0.15	82.50±0.18	29.71±0.15	8.68±0.62	6.10±0.63	111.89±13.00	9.05±0.59	0.06565±0.01428
619	13:29:56.65 +47:11:38.4	6.02±0.04	4.77±0.56	30.59±0.61	14.09±0.57	3.57±0.11	2.34±0.11	14.60±13.00	5.12±0.59	0.02284±0.00480
620	13:29:57.38 +47:11:38.3	12.97±0.27	7.23±0.46	62.80±0.59	19.73±0.47	5.93±0.27	3.78±0.25	1.15±13.00	4.35±0.59	0.05111±0.01061
621	13:29:47.62 +47:11:34.1	4.34±0.41	4.24±0.50	16.58±0.48	8.14±0.45	2.88±0.45	1.51±0.37	33.49±13.00	3.49±0.59	0.00000±0.00191
622	13:29:48.34 +47:11:34.0	2.08±0.34	4.18±0.30	10.29±0.25	8.29±0.26	2.41±0.46	1.94±0.45	4.31±13.00	3.73±0.59	0.00000±0.00340
623	13:29:49.06 +47:11:33.8	4.46±0.47	5.53±0.63	25.06±0.60	13.67±0.58	3.49±0.57	2.97±0.54	60.61±13.00	3.94±0.59	0.02346±0.00868
624	13:29:49.78 +47:11:33.6	13.71±0.30	12.26±0.04	103.06±0.06	35.09±0.05	10.58±0.57	7.05±0.56	593.61±13.00	8.37±0.59	0.25522±0.05229
625	13:29:50.50 +47:11:33.5	24.47±0.65	16.27±0.69	164.32±1.01	47.79±0.77	14.34±0.15	9.27±0.14	525.32±13.00	7.11±0.59	0.32042±0.06650
626	13:29:51.23 +47:11:33.3	23.96±0.75	17.17±0.81	124.17±1.01	51.69±0.90	12.09±0.79	8.66±0.81	278.45±13.00	6.83±0.59	0.13103±0.02772
627	13:29:51.95 +47:11:33.1	36.17±0.91	24.82±1.00	190.56±1.24	73.37±1.10	16.18±0.97	12.63±1.00	147.02±13.00	6.43±0.59	0.21489±0.04451
628	13:29:52.67 +47:11:33.0	56.87±1.10	27.53±1.12	287.14±1.48	84.50±1.24	17.36±0.24	12.43±0.23	146.83±13.00	3.91±0.59	0.29882±0.06101
629	13:29:53.39 +47:11:32.8	29.38±0.96	23.80±1.10	171.15±1.31	70.49±1.20	12.50±0.07	9.10±0.07	236.59±13.00	4.43±0.59	0.24191±0.05120
630	13:29:54.11 +47:11:32.7	38.49±0.93	22.06±0.53	205.50±0.67	63.90±0.57	14.41±0.20	11.37±0.20	268.56±13.00	3.65±0.59	0.23981±0.04946
631	13:29:54.84 +47:11:32.5	22.09±0.64	15.50±0.68	153.56±0.99	48.13±0.78	14.58±0.68	10.50±0.68	397.47±13.00	5.66±0.59	0.32333±0.06754
632	13:29:55.56 +47:11:32.3	17.03±0.35	9.04±0.58	81.77±0.72	25.54±0.60	6.83±0.13	5.95±0.14	226.11±13.00	5.44±0.59	0.06832±0.01412
633	13:29:56.28 +47:11:32.2	9.04±0.54	5.85±0.56	39.97±0.66	18.18±0.60	4.32±0.01	4.34±0.01	33.99±13.00	4.19±0.59	0.02157±0.00585
634	13:29:57.00 +47:11:32.0	10.02±0.50	5.98±0.47	45.72±0.55	14.88±0.47	5.06±0.26	3.28±0.25	2.63±13.00	3.87±0.59	0.02882±0.00704
635	13:29:57.72 +47:11:31.8	6.58±0.25	4.42±0.11	29.26±0.12	11.18±0.11	3.84±0.10	2.64±0.11	24.44±13.00	4.93±0.59	0.01325±0.00321
636	13:29:47.96 +47:11:27.7	3.48±0.44	2.68±0.25	10.17±0.24	6.40±0.23	2.97±0.25	0.85±0.21	8.69±13.00	3.70±0.59	0.00000±0.00084
637	13:29:48.69 +47:11:27.5	3.59±0.45	3.71±0.04	15.27±0.04	10.46±0.04	2.46±0.24	2.16±0.25	14.02±13.00	3.46±0.59	0.00067±0.00279
638	13:29:49.41 +47:11:27.3	9.65±0.52	8.76±0.60	61.67±0.72	20.90±0.60	7.94±0.52	5.99±0.50	108.57±13.00	5.36±0.59	0.10076±0.02351
639	13:29:50.13 +47:11:27.2	46.50±0.37	30.70±0.66	266.40±1.15	88.93±0.82	25.96±0.65	19.58±0.63	1063.21±13.00	7.72±0.59	0.36817±0.07396
640	13:29:50.85 +47:11:27.0	19.98±0.65	13.01±0.70	112.47±0.91	37.21±0.76	9.56±0.67	7.51±0.67	225.74±13.00	7.29±0.59	0.14324±0.03039
641	13:29:51.57 +47:11:26.9	23.12±0.71	14.07±0.79	130.57±1.00	37.62±0.82	10.37±0.17	7.43±0.16	147.73±13.00	10.35±0.59	0.16938±0.03571
642	13:29:52.30 +47:11:26.7	34.56±0.79	24.37±0.87	186.12±1.13	67.32±0.95	18.26±0.45	13.67±0.45	227.93±13.00	5.77±0.59	0.22050±0.04541
643	13:29:53.02 +47:11:26.5	29.82±0.82	22.06±0.82	159.52±0.98	56.84±0.85	13.44±0.18	9.77±0.17	348.26±13.00	8.45±0.59	0.18449±0.03846
644	13:29:53.74 +47:11:26.4	37.93±0.81	23.57±0.83	211.54±1.17	64.45±0.93	17.27±0.43	12.97±0.42	339.07±13.00	7.05±0.59	0.27301±0.05598
645	13:29:54.46 +47:11:26.2	23.79±0.66	18.45±0.70	126.40±0.94	53.29±0.80	15.06±0.69	11.69±0.69	301.70±13.00	6.07±0.59	0.14180±0.02964
646	13:29:55.18 +47:11:26.0	8.66±0.30	9.06±0.65	41.80±0.69	23.79±0.65	5.95±0.04	4.31±0.04	91.44±13.00	5.67±0.59	0.03017±0.00679
647	13:29:55.90 +47:11:25.9	5.20±0.50	4.19±0.51	21.92±0.57	12.83±0.57	3.64±0.10	2.55±0.11	0.00±13.00	3.83±0.59	0.00528±0.00329
648	13:29:56.63 +47:11:25.7	5.81±0.10	5.22±0.51	22.83±0.53	13.10±0.51	4.33±0.26	2.99±0.24	0.00±13.00	7.99±0.59	0.00352±0.00111
649	13:29:57.35 +47:11:25.6	7.50±0.45	5.03±0.45	31.66±0.48	14.31±0.44	4.37±0.10	3.17±0.10	11.69±13.00	6.19±0.59	0.01240±0.00377
650	13:29:47.59 +47:11:21.4	4.70±0.36	3.87±0.54	16.14±0.47	8.27±0.45	2.90±0.44	1.84±0.48	37.42±13.00	5.20±0.59	0.00000±0.00121

Table 3.1 (cont'd)

ID	Equatorial Coordinates	Hβ	[NII]λ6548	Hα	[NII]λ6584	[SII]λ6717	[SII]λ6731	Σ_{H2}	Σ_{HI}	Σ_{SFR}
651	13:29:48.31 +47:11:21.2	1.91±0.39	4.29±0.15	7.90±0.09	5.69±0.10	1.73±0.03	1.42±0.04	24.62±13.00	4.03±0.59	0.00000±0.00220
652	13:29:49.03 +47:11:21.1	3.07±0.03	3.71±0.57	15.58±0.51	7.90±0.50	3.20±0.11	2.42±0.10	1.27±13.00	3.81±0.59	0.00630±0.00177
653	13:29:49.75 +47:11:20.9	9.53±0.03	10.80±0.57	60.54±0.69	27.44±0.60	8.42±0.53	6.68±0.53	365.44±13.00	4.75±0.59	0.09724±0.01964
654	13:29:50.48 +47:11:20.7	33.30±0.62	17.38±0.61	149.93±0.91	49.39±0.69	13.67±0.32	10.15±0.31	721.94±13.00	7.50±0.59	0.11502±0.02352
655	13:29:51.20 +47:11:20.6	10.53±0.54	9.26±0.67	57.44±0.73	22.63±0.66	5.62±0.32	4.37±0.31	167.78±13.00	4.58±0.59	0.06276±0.01473
656	13:29:51.92 +47:11:20.4	15.14±0.13	10.96±0.64	85.97±0.82	28.58±0.70	6.16±0.31	5.56±0.35	202.24±13.00	4.37±0.59	0.10930±0.02209
657	13:29:52.64 +47:11:20.2	11.93±0.13	12.54±0.75	64.94±0.80	34.49±0.77	7.66±0.36	6.10±0.39	238.48±13.00	5.32±0.59	0.07192±0.01466
658	13:29:53.36 +47:11:20.1	14.48±0.34	12.18±0.69	77.71±0.81	31.96±0.73	8.23±0.13	6.11±0.14	231.95±13.00	4.71±0.59	0.08511±0.01770
659	13:29:54.09 +47:11:19.9	17.61±0.54	11.56±0.57	87.93±0.72	31.14±0.61	8.62±0.64	6.64±0.65	174.63±13.00	3.45±0.59	0.08186±0.01736
660	13:29:54.81 +47:11:19.8	6.34±0.50	6.58±0.62	28.70±0.62	16.85±0.61	5.06±0.58	3.03±0.60	86.77±13.00	4.70±0.59	0.01372±0.00479
661	13:29:55.53 +47:11:19.6	4.87±0.25	5.11±0.30	20.71±0.30	12.96±0.29	4.38±0.59	2.11±0.51	40.96±13.00	4.31±0.59	0.00471±0.00189
662	13:29:56.25 +47:11:19.4	10.81±0.27	6.89±0.54	53.26±0.65	17.89±0.55	5.60±0.26	3.39±0.25	34.38±13.00	3.57±0.59	0.04378±0.00926
663	13:29:56.97 +47:11:19.3	10.91±0.26	6.62±0.51	54.60±0.63	17.60±0.52	5.26±0.48	3.67±0.49	32.82±13.00	7.22±0.59	0.04709±0.00990
664	13:29:57.70 +47:11:19.1	7.15±0.45	6.11±0.53	34.58±0.57	15.83±0.51	5.36±0.47	3.50±0.46	97.47±13.00	4.93±0.59	0.02329±0.00636
665	13:29:47.94 +47:11:14.9	1.90±0.35	3.01±0.51	8.23±0.42	5.87±0.42	1.96±0.24	1.20±0.22	19.99±13.00	2.98±0.59	0.00000±0.00238
666	13:29:48.66 +47:11:14.8	3.50±0.03	3.99±0.13	16.05±0.10	8.12±0.10	2.73±0.03	1.47±0.03	34.10±13.00	2.88±0.59	0.00340±0.00074
667	13:29:49.38 +47:11:14.6	2.82±0.46	4.23±0.30	13.12±0.28	8.66±0.28	2.48±0.01	1.71±0.01	0.00±13.00	3.43±0.59	0.00114±0.00379
668	13:29:50.10 +47:11:14.5	8.73±0.48	8.24±0.31	49.40±0.34	19.64±0.30	5.82±0.04	3.79±0.03	198.32±13.00	7.22±0.59	0.05766±0.01371
669	13:29:50.82 +47:11:14.3	8.82±0.41	7.77±0.12	53.83±0.14	20.46±0.12	5.70±0.11	3.98±0.11	564.64±13.00	6.27±0.59	0.07739±0.01745
670	13:29:51.55 +47:11:14.1	2.68±0.40	5.95±0.59	17.13±0.55	13.70±0.57	3.48±0.11	1.83±0.11	133.49±13.00	3.26±0.59	0.02045±0.01023
671	13:29:52.27 +47:11:14.0	5.65±0.43	7.75±0.63	33.47±0.63	18.92±0.62	5.15±0.04	4.18±0.04	110.42±13.00	5.44±0.59	0.04066±0.01134
672	13:29:52.99 +47:11:13.8	7.80±0.27	7.33±0.56	38.35±0.56	18.21±0.54	5.16±0.56	3.64±0.58	92.11±13.00	4.45±0.59	0.02835±0.00640
673	13:29:53.71 +47:11:13.6	4.12±0.25	6.16±0.59	20.64±0.57	14.49±0.56	3.90±0.11	3.42±0.13	70.86±13.00	2.14±0.59	0.01121±0.00364
674	13:29:54.43 +47:11:13.5	4.44±0.26	6.86±0.60	21.21±0.55	15.42±0.56	5.42±0.58	3.21±0.61	47.79±13.00	3.37±0.59	0.00960±0.00320
675	13:29:55.15 +47:11:13.3	4.60±0.46	5.47±0.60	17.12±0.54	11.90±0.54	3.45±0.04	2.29±0.04	0.00±13.00	3.44±0.59	0.00000±0.00198
676	13:29:55.88 +47:11:13.1	3.59±0.42	3.10±0.53	15.91±0.51	9.22±0.50	3.23±0.03	1.76±0.03	3.55±13.00	3.07±0.59	0.00225±0.00311
677	13:29:56.60 +47:11:13.0	4.29±0.10	4.68±0.47	20.52±0.46	12.96±0.45	3.94±0.25	3.54±0.26	80.52±13.00	5.44±0.59	0.00902±0.00221
678	13:29:57.32 +47:11:12.8	5.69±0.44	4.95±0.46	23.12±0.47	12.05±0.43	4.24±0.47	3.07±0.47	53.13±13.00	6.93±0.59	0.00479±0.00259
679	13:29:47.56 +47:11:08.6	3.37±0.19	2.69±0.46	12.98±0.43	6.53±0.41	1.70±0.34	1.31±0.32	72.67±13.00	4.74±0.59	0.00000±0.00101
680	13:29:48.28 +47:11:08.5	3.18±0.37	3.22±0.43	12.34±0.38	6.49±0.36	2.78±0.42	1.43±0.41	45.88±13.00	4.41±0.59	0.00000±0.00176
681	13:29:49.01 +47:11:08.3	2.51±0.41	4.09±0.56	11.81±0.48	8.57±0.48	2.77±0.52	2.33±0.50	5.15±13.00	4.93±0.59	0.00030±0.00361
682	13:29:49.73 +47:11:08.2	2.96±0.36	3.96±0.45	16.72±0.44	9.70±0.43	3.23±0.04	1.95±0.03	22.06±13.00	5.70±0.59	0.01249±0.00627
683	13:29:50.45 +47:11:08.0	8.11±0.45	6.20±0.51	44.44±0.59	16.25±0.51	5.16±0.03	3.71±0.03	317.27±13.00	5.53±0.59	0.04670±0.01132
684	13:29:51.17 +47:11:07.8	3.85±0.41	5.03±0.11	23.32±0.11	13.41±0.11	4.81±0.04	2.70±0.03	507.74±13.00	6.07±0.59	0.02682±0.00949
685	13:29:51.89 +47:11:07.7	4.71±0.44	5.39±0.30	26.65±0.30	12.97±0.29	4.79±0.54	2.74±0.50	127.12±13.00	3.87±0.59	0.02625±0.00862
686	13:29:52.61 +47:11:07.5	5.65±0.45	5.65±0.04	24.33±0.04	12.60±0.04	3.91±0.27	1.98±0.27	119.83±13.00	7.10±0.59	0.00784±0.00328
687	13:29:53.34 +47:11:07.4	4.00±0.44	4.49±0.55	17.15±0.52	11.50±0.52	4.08±0.57	2.44±0.48	79.25±13.00	2.79±0.59	0.00227±0.00293
688	13:29:54.06 +47:11:07.2	4.57±0.42	5.36±0.12	22.18±0.11	12.74±0.11	3.22±0.24	2.53±0.28	3.31±13.00	2.46±0.59	0.01126±0.00456
689	13:29:54.78 +47:11:07.0	22.47±0.30	8.19±0.56	92.29±0.75	20.13±0.55	6.09±0.50	4.36±0.50	0.00±13.00	4.79±0.59	0.05259±0.01070
690	13:29:55.50 +47:11:06.9	4.25±0.43	4.99±0.33	17.82±0.28	9.61±0.27	2.76±0.03	2.70±0.04	21.26±13.00	3.91±0.59	0.00213±0.00258
691	13:29:56.22 +47:11:06.7	4.20±0.25	4.67±0.29	14.52±0.26	10.64±0.27	3.21±0.48	2.34±0.48	7.51±13.00	2.09±0.59	0.00000±0.00085
692	13:29:56.95 +47:11:06.5	5.72±0.42	6.27±0.55	25.80±0.53	12.75±0.49	4.83±0.10	3.30±0.09	69.46±13.00	5.86±0.59	0.01102±0.00395
693	13:29:57.67 +47:11:06.4	9.21±0.41	8.11±0.47	49.48±0.57	21.26±0.50	8.51±0.10	5.80±0.10	111.83±13.00	8.32±0.59	0.05041±0.01149
694	13:29:47.91 +47:11:02.2	2.07±0.18	3.24±0.56	7.43±0.42	4.74±0.41	1.66±0.41	1.59±0.41	51.09±13.00	4.98±0.59	0.00000±0.00078
695	13:29:48.63 +47:11:02.0	2.22±0.36	2.48±0.25	8.07±0.23	5.81±0.23	2.01±0.03	1.98±0.03	27.11±13.00	3.95±0.59	0.00000±0.00137
696	13:29:49.35 +47:11:01.9	2.34±0.32	2.84±0.51	11.70±0.46	7.20±0.46	2.62±0.42	1.90±0.48	82.92±13.00	4.11±0.59	0.00167±0.00345
697	13:29:50.07 +47:11:01.7	5.71±0.03	5.01±0.12	24.65±0.11	11.22±0.10	2.79±0.09	2.66±0.10	0.39±13.00	3.77±0.59	0.00821±0.00166
698	13:29:50.80 +47:11:01.6	4.79±0.40	5.13±0.53	21.60±0.50	10.12±0.47	3.37±0.25	3.50±0.25	204.13±13.00	6.27±0.59	0.00755±0.00349
699	13:29:51.52 +47:11:01.4	4.97±0.40	5.32±0.53	22.45±0.50	11.62±0.47	3.35±0.09	2.05±0.09	544.35±13.00	7.75±0.59	0.00832±0.00357
700	13:29:52.24 +47:11:01.2	5.53±0.43	3.98±0.48	22.86±0.52	10.98±0.49	2.87±0.10	2.78±0.10	316.47±13.00	5.09±0.59	0.00522±0.00277

Table 3.1 (cont'd)

ID	Equatorial Coordinates	Hβ	[NII]λ6548	Hα	[NII]λ6584	[SII]λ6717	[SII]λ6731	Σ_{H2}	Σ_{HI}	Σ_{SFR}
701	13:29:52.96 +47:11:01.1	3.07±0.42	4.49±0.49	13.58±0.44	10.05±0.45	2.45±0.03	1.84±0.04	80.43±13.00	4.96±0.59	0.00029±0.00300
702	13:29:53.68 +47:11:00.9	2.03±0.35	3.67±0.53	9.17±0.48	8.24±0.51	2.13±0.42	1.74±0.62	0.00±13.00	2.32±0.59	0.00000±0.00275
703	13:29:54.41 +47:11:00.7	3.43±0.43	4.57±0.58	13.08±0.50	9.34±0.50	2.84±0.24	2.33±0.24	0.00±13.00	3.60±0.59	0.00000±0.00197
704	13:29:55.13 +47:11:00.6	4.48±0.42	4.56±0.49	20.43±0.52	10.22±0.49	3.43±0.03	1.84±0.03	51.86±13.00	5.11±0.59	0.00700±0.00364
705	13:29:55.85 +47:11:00.4	4.44±0.42	4.17±0.27	18.39±0.27	11.23±0.28	3.41±0.48	2.55±0.51	33.04±13.00	4.30±0.59	0.00218±0.00248
706	13:29:56.57 +47:11:00.3	5.42±0.42	4.90±0.50	27.73±0.53	13.41±0.50	5.28±0.49	3.72±0.49	81.95±13.00	8.68±0.59	0.02005±0.00625
707	13:29:57.29 +47:11:00.1	5.75±0.38	5.74±0.49	26.10±0.48	11.91±0.45	4.26±0.09	2.87±0.09	167.90±13.00	12.36±0.59	0.01164±0.00382
708	13:29:47.53 +47:10:55.9	1.72±0.33	1.76±0.43	7.05±0.41	4.08±0.38	1.16±0.38	0.71±0.37	47.71±13.00	3.15±0.59	0.00000±0.00189
709	13:29:48.26 +47:10:55.8	4.11±0.20	2.85±0.22	16.46±0.24	6.15±0.21	2.61±0.41	2.16±0.45	26.71±13.00	4.09±0.59	0.00003±0.00106
710	13:29:48.98 +47:10:55.6	2.88±0.38	2.99±0.11	11.10±0.09	6.79±0.09	2.25±0.23	2.16±0.25	58.72±13.00	4.35±0.59	0.00000±0.00171
711	13:29:49.70 +47:10:55.4	5.25±0.25	4.47±0.50	21.01±0.51	10.98±0.48	3.95±0.46	2.63±0.46	36.32±13.00	4.74±0.59	0.00294±0.00157
712	13:29:50.42 +47:10:55.3	26.54±0.53	12.53±0.51	104.37±0.74	32.41±0.57	10.82±0.10	8.70±0.11	29.94±13.00	5.42±0.59	0.05438±0.01122
713	13:29:51.14 +47:10:55.1	6.44±0.41	4.42±0.43	29.18±0.47	11.67±0.42	3.02±0.22	2.70±0.24	197.55±13.00	8.59±0.59	0.01418±0.00428
714	13:29:51.87 +47:10:54.9	13.01±0.44	11.07±0.48	81.83±0.68	33.45±0.55	7.76±0.46	5.75±0.47	609.42±13.00	7.48±0.59	0.13224±0.02818
715	13:29:52.59 +47:10:54.8	8.04±0.37	6.70±0.26	43.93±0.31	18.75±0.27	4.72±0.44	3.38±0.43	358.98±13.00	6.02±0.59	0.04570±0.01047
716	13:29:53.31 +47:10:54.6	2.88±0.20	3.87±0.04	17.39±0.03	9.59±0.03	2.82±0.43	1.79±0.46	161.05±13.00	4.37±0.59	0.01715±0.00506
717	13:29:54.03 +47:10:54.5	4.32±0.40	3.93±0.48	21.83±0.51	10.76±0.49	2.36±0.22	2.40±0.26	118.86±13.00	5.39±0.59	0.01291±0.00510
718	13:29:54.75 +47:10:54.3	4.98±0.39	5.06±0.04	27.34±0.04	13.55±0.03	4.40±0.10	2.81±0.09	122.45±13.00	6.03±0.59	0.02471±0.00734
719	13:29:55.47 +47:10:54.1	7.15±0.41	6.67±0.52	34.46±0.55	17.52±0.50	4.57±0.46	3.85±0.46	143.77±13.00	6.78±0.59	0.02292±0.00607
720	13:29:56.20 +47:10:54.0	9.37±0.44	8.08±0.48	55.89±0.61	21.04±0.52	6.85±0.25	4.71±0.25	237.72±13.00	9.90±0.59	0.07623±0.01733
721	13:29:56.92 +47:10:53.8	20.86±0.50	12.54±0.51	108.04±0.74	35.85±0.58	12.11±0.28	8.47±0.27	232.93±13.00	13.99±0.59	0.11255±0.02331
722	13:29:57.64 +47:10:53.6	11.97±0.49	8.87±0.56	55.84±0.63	20.52±0.54	7.68±0.11	6.64±0.12	149.69±13.00	11.71±0.59	0.03993±0.00905
723	13:29:47.88 +47:10:49.5	3.02±0.33	3.32±0.25	14.79±0.22	5.84±0.21	2.69±0.03	2.04±0.03	67.32±13.00	4.11±0.59	0.00432±0.00332
724	13:29:48.60 +47:10:49.3	7.69±0.35	5.00±0.47	27.64±0.48	11.01±0.42	3.05±0.37	2.26±0.39	39.55±13.00	2.79±0.59	0.00349±0.00155
725	13:29:49.33 +47:10:49.1	4.89±0.20	4.58±0.24	21.44±0.26	10.14±0.23	3.74±0.03	2.96±0.03	21.49±13.00	4.74±0.59	0.00627±0.00191
726	13:29:50.05 +47:10:49.0	22.24±0.51	9.43±0.28	90.66±0.37	23.29±0.28	11.00±0.50	8.63±0.52	48.86±13.00	6.78±0.59	0.05047±0.01047
727	13:29:50.77 +47:10:48.8	21.34±0.11	8.72±0.51	75.94±0.67	21.97±0.54	8.50±0.50	6.42±0.49	9.80±13.00	4.32±0.59	0.02734±0.00553
728	13:29:51.49 +47:10:48.7	7.83±0.24	6.76±0.11	35.09±0.12	13.44±0.11	3.89±0.46	2.82±0.43	137.13±13.00	6.31±0.59	0.01843±0.00407
729	13:29:52.21 +47:10:48.5	9.18±0.43	8.46±0.11	53.41±0.13	21.39±0.11	7.54±0.48	5.57±0.49	270.16±13.00	6.48±0.59	0.06794±0.01537
730	13:29:52.93 +47:10:48.3	19.24±0.49	10.79±0.29	92.92±0.38	25.44±0.29	8.98±0.28	6.35±0.26	388.25±13.00	9.59±0.59	0.08024±0.01671
731	13:29:53.66 +47:10:48.2	13.86±0.27	7.83±0.52	61.63±0.65	19.43±0.54	6.39±0.10	5.01±0.11	109.20±13.00	8.40±0.59	0.03963±0.00823
732	13:29:54.38 +47:10:48.0	6.47±0.03	6.67±0.03	35.22±0.04	16.97±0.04	6.15±0.10	3.64±0.09	375.70±13.00	7.95±0.59	0.03417±0.00685
733	13:29:55.10 +47:10:47.9	16.88±0.10	19.21±0.29	107.20±0.40	47.21±0.32	12.99±0.03	12.43±0.04	584.48±13.00	10.65±0.59	0.18048±0.03620
734	13:29:55.82 +47:10:47.7	21.93±0.45	20.03±0.30	117.25±0.42	52.41±0.34	20.01±0.49	14.68±0.49	393.95±13.00	11.66±0.59	0.13270±0.02718
735	13:29:56.54 +47:10:47.5	45.01±0.34	30.84±0.62	278.79±1.05	87.46±0.74	30.04±0.13	22.94±0.13	261.48±13.00	12.69±0.59	0.45990±0.09233

Chapter 4

The VIRUS-P Exploration of Nearby Galaxies (VENGA): Survey Design, Data Processing, and First Results on NGC0628

We present the survey design, data reduction and spectral analysis pipelines, and first results, of the VIRUS-P Exploration of Nearby Galaxies (VENGA). VENGA is a large-scale extra-galactic IFU survey, which maps the bulges, bars and large parts of the disks of 30 nearby massive spiral galaxies. The targets are chosen to span a wide range in Hubble type, star formation activity, morphology, and inclination. For these galaxies, the VENGA data will provide 2D maps of the star formation rate (SFR), kinematics and chemical abundances of gas and stars, dust extinction, stellar populations, and other quantities derived from the stellar continuum and nebular emission line spectrum at optical wavelengths (3600Å-6800Å). The uniqueness of the VIRUS-P large field of view allows the mapping of these extended sources to be performed. VENGA will allow us to correlate all these important quantities throughout the different environments present in galactic disks, allowing the conduction of a large number of studies in star formation, structure assembly, galactic feedback, and ISM properties in star-forming galaxies. Using the VENGA data on the face-on spiral NGC0628, we derive the presence of a

previously unknown active galactic nuclei (AGN) in the center of the galaxy. We also make use of emission line diagnostics, to study the contribution from the diffuse ionized gas (DIG) component of the ISM to the observed nebular spectrum. Finally, we measure the nebular oxygen abundance in HII regions across the disk of NGC0628, study its spatial distribution, and measure its radial gradient, and its impact on the star formation efficiency of molecular gas in different regions of the galaxy.

4.1 Introduction

In ΛCDM cosmology, the formation and evolution of galaxies takes place in gravitational potential wells in the dark matter distribution (DM halos). Gas accretion into these halos and merging processes ultimately trigger star formation giving rise to galaxies (Blumenthal et al., 1984). Although consensus has been reached concerning this picture, the baryonic physics behind galaxy formation in the centers of DM halos are still aggressively debated. The triggering of star formation and the variables that set the star formation rate (SFR) (Kennicutt, 1998a; Leroy et al., 2008; Krumholz et al., 2009b; Tan, 2010), the contribution from different types of feedback processes (AGN, supernovae, stellar radiation, Kauffmann et al., 1999; Croton et al., 2006; Thompson, 2008), as well as the impact of gas accretion from the inter-galactic medium (IGM, Dekel et al., 2009), at regulating the gaseous budget, structure, chemical composition, and kinematics of the ISM, and the role that major and minor mergers as well as secular evolution processes play at shaping galaxies

(Toomre & Toomre, 1972; Kormendy & Kennicutt, 2004), are the main current areas of research. All these processes play a major role in determining how galaxies evolve through cosmic time, building up their stellar mass and shaping their present day structure.

The detailed manner in which the above physical phenomena (star formation, gas accretion, feedback, interactions, and secular evolution) proceed, ultimately determines the morphology, kinematics, stellar populations, chemical structure, ISM density and ionization structure, and star formation history (SFH) of a galaxy. We can study these processes by obtaining spatially resolved measurements of quantities like the SFR, stellar and gas kinematics, stellar populations, chemical abundances (both gas phase and photospheric), atomic and molecular gas surface densities, etc., studying the correlations between them, and testing current theoretical models describing the above phenomena. Wide field optical integral field spectroscopy allows the measurement of many of these quantities in nearby galaxies. IFU maps, combined with multi-wavelength broad band photometry and sub-mm and radio maps of the same galaxies are powerful datasets to study galaxy evolution.

Integral field spectroscopy of nearby galaxies has been somewhat limited in the past, mostly due to the small field-of-view of available integral field units (IFUs). During the last decade, a new generation of wide field integral field spectrographs like SAURON on the 4.2m William Herschel Telescope (Bacon et al., 2001), PPAK on the 3.5m at Calar Alto Observatory (Kelz et al., 2006), SparsePak on the WIYN 3.5m telescope (Bershady et al., 2004), and

VIRUS-P on the 2.7m Harlan J. Smith telescope at McDonald Observatory (Hill et al., 2008a), have opened the path to study nearby systems subtending large angular diameters on the sky.

Early survey of nearby galaxies using IFUs mostly focused on studying the kinematics and stellar populations of early type systems. These include the SAURON Survey (Bacon et al., 2001; de Zeeuw et al., 2002), and its extension, the Atlas3D Survey (Cappellari et al., 2011) which by now have mapped hundreds of elliptical and lenticular galaxies. Wide field IFU studies of later type disk galaxies include the work of Ganda et al. (2006) who used SAURON to observe the central regions of 18 nearby late-type spirals, the Disk Mass Project (Bershady et al., 2010) which used SparsePak and PPAK to measure Hα velocity fields for 146 face-on spirals, and stellar kinematics for a subset of 46 objects, with the aim of constraining the distribution of stellar mass and dark matter in disk galaxies, and the PPAK IFS Nearby Galaxies Survey (PINGS, Rosales-Ortega et al., 2010), which maps the disks of 17 nearby disk galaxies. The PPAK IFU is currently being used to conduct the Calar Alto Legacy Integral Field Area survey (CALIFA, Sánchez et al., 2010), a massive project mapping ~ 600 galaxies of all Hubble types, selected based on their angular size and distance (in order for them to fill the PPAK field-of-view). A number of IFU studies of galaxies have also been done at high redshift ($1 < z < 3$), where target size is well suited to the small fields of view of IFUs in 10m class telescopes (e.g. Genzel et al., 2006; Förster Schreiber et al., 2006; Law et al., 2007; Wright et al., 2007; Lemoine-Busserolle et al.,

2010; Lemoine-Busserolle & Lamareille, 2010).

In this work, we present the VIRUS-P Exploration of Nearby Galaxies (VENGA), an IFU survey of 30 nearby spirals, which uses VIRUS-P (currently the largest field-of-view IFU in the world) to spectroscopically map large portions of the disks of these objects. The sample spans a wide range in Hubble types, SFRs, and morphologies, including galaxies with classical and pseudo-bulges, as well as barred and unbarred objects. Ancillary multi-wavelength data exists for many of the targets. This includes HST optical and near-IR imaging with ACS and NICMOS, Spitzer mid-IR and far-IR imaging with IRAC and MIPS, near-UV and far-UV imaging from GALEX, and far-IR HERSCHEL data. Also, both CO and HI 21cm maps, are available for most of the sample. VENGA's potential lies in a combination of wide spatial coverage, good spatial resolution, and depth. The large $1.7' \times 1.7'$ field-of-view available, allows us to typically sample each system out to $\sim 0.7R_{25}$ by tiling only a couple of VIRUS-P pointings. The size of the VIRUS-P optical fibers ($4.235''$ in diameter) samples physical scales of 300 pc at the median distance of our targets, and makes it very sensitive to low-surface brightness emission. In VENGA we aim to obtain spectra with a median $S/N = 40$ per fiber per spectral resolution element, which will permit good measurements of the velocity field, and stellar and nebular spectral features, at the native spatial resolution over most of the data-cube on every galaxy.

The VENGA data will be used to conduct an extensive set of studies on star-formation, structure assembly, stellar populations, gas and stellar dynam-

ics, chemical evolution, ISM structure, and galactic feedback. The data will also provide the best local universe control sample for IFU studies of high-z galaxies. The survey is designed with the following science goals in mind:

- Study the process of star-formation on galactic scales, including the correlations between the SFR and the star formation efficiency (SFE) with other parameters like gas and stellar surface density, metallicity, galaxy dynamics, and stellar populations. The ultimate goal is understand what are the relevant parameters setting the SFR across different environments within galaxies.

- Investigate the assembly of the central spheroidal stellar components of disk galaxies. This includes characterizing the dynamics, stellar populations, and chemical abundances of classical and pseudo-bulges in spiral galaxies, and comparing them to those of the disk, in order to constrain their star-formation history and understand their origin. The goal is to distinguishing between different evolutionary paths that might give rise to these structures (secular evolution, galaxy-galaxy interactions).

- Provide detailed observations of bar induced radial gas inflows into the central parts of disk galaxies. These observations include studying the velocity field of ionized gas and stars in the regions influenced by the presence of bars, and also the effect of bar induced shocks in the ISM on the local star formation efficiency.

- Construct two-dimensional maps of the stellar and gas phase metallicity on spiral galaxies. These maps will allow the study of radial abundance gradients measured with exquisite detail, the dispersion in abundances as a function of galactocentric radius, and to look for deviations from axisymmetry in the metallicity distribution. Comparing these measurements to chemical evolution models will help constrain the chemical enrichment, gas accretion, and star-formation history of disk galaxies in the local universe.

- Using nebular emission line diagnostics to unveil the nature of the ionizing sources in different parts of the disks of spirals. Including the study of low luminosity AGN, and their impact on the physical conditions of the gas in the central parts of galaxies. The spectra will also allow the study of the diffuse ionized gas (DIG) in the ISM, including measuring its density, ionization state and temperature. In particular, on the two edge-on systems, we will also be able to constrain the ionization structure and kinematics of the DIG as a function of distance above the mid-plane. All these studies will provide insight regarding the different feedback processes at play in star-forming disk galaxies.

- Studying the distribution of stellar mass and dark matter in spiral galaxies, by using a combination of the VENGA gas and stellar velocity fields and constraints on the M/L ratio from stellar populations. The data should allow us, in principle, to set constraints on the shape of the dark

matter halo density profile on these systems, which we can use to test the predictions of ΛCDM models.

In §4.2 we present the survey design, including a description of the VENGA sample and the observing strategy adopted to conduct the survey. We present the VIRUS-P observations in §4.3. In particular, we present the VENGA data obtained on the face-on Sc galaxy NGC0628, which we use throughout this work to show examples of our reduction and analysis techniques. The data processing pipeline, and construction of the final VENGA data-products (i.e. reduced and calibrated spectral data-cubes), is presented in §4.4, followed by a description of the techniques used to fit the spectra, measure stellar and gas kinematics, and extract emission line fluxes (§4.5). In $4.6 we present preliminary results regarding the presence of a low-luminosity AGN in the center of NGC0628, the contribution to the nebular spectrum of the extra-planar DIG, the nebular oxygen abundance gradient, and the impact of metallicity on the star formation efficiency across the galaxy. Finally, we present our conclusions in §4.7. Throughout the paper we adopt a standard set of ΛCDM cosmological parameters, $H_o = 70$ km s^{-1}Mpc^{-1}, $\Omega_M = 0.3$, and $\Omega_\Lambda = 0.7$ (Dunkley et al., 2009).

4.2 Survey Design

In this section we present and characterize the VENGA sample, and we discuss the main physical properties of the target galaxies, including their

stellar masses (M_*) and SFRs. We also describe the observing strategy and the instrumental configurations used to execute the survey.

4.2.1 The VENGA Sample

Table 4.1 presents the galaxies that are being observed as part of VENGA, and lists their main properties. Targets were chosen to span a wide range in Hubble types, from S0 to Sd, a wide range in inclinations, from face-on to edge-on systems, and they include both barred and unbarred objects. The sample also spans a wide range in right ascension, in order to allow observations to be carried out throughout the whole year, and all objects have declinations $\delta > -10$ deg, to make them accessible from McDonald Observatory. Figure 4.1 presents Digitized Sky Survey (DSS[1]) cutouts for all the galaxies in VENGA. Overlaid are the $1.7' \times 1.7'$VIRUS-P pointings observed on each galaxy. While VENGA is designed to map the galaxies out to $\sim 0.7R_{25}$, for NGC3198, NGC4569, NGC4826, NGC5055, and NGC7731, only a central pointing was observed due to observing time constraints.

Since one of the goals of VENGA is to study the origin and properties of stellar spheroids in the inner parts of disk galaxies, we included objects showing both classical bulges and pseudo-bulges (Kormendy & Kennicutt, 2004, and references therein). To distinguish between these two types of stellar

[1]The Digitized Sky Surveys were produced at the Space Telescope Science Institute under U.S. Government grant NAG W-2166. The images of these surveys are based on photographic data obtained using the Oschin Schmidt Telescope on Palomar Mountain and the UK Schmidt Telescope. The plates were processed into the present compressed digital form with the permission of these institutions.

structures, we adopt a criteria based on the Sersic index of the spheroidal component (n_B). Following the results of Fisher & Drory (2008) we adopt a limit of $n_B = 2$. We consider classical bulges those with $n_B > 2$, and pseudo-bulges those with with $n_B < 2$. Table 4.2 presents the bulge-to-total light fractions (B/T) and n_B values for 18 of the 30 VENGA galaxies taken from Dong & De Robertis (2006), Fisher & Drory (2008), and Weinzirl et al. (2009). Of the galaxies for which we found Sersic index measurements in the literature, 50% would be classified as classical bulges and 50% as pseudo-bulges using the $n_B = 2$ criterion.

In order to understand how well the galaxies in our sample represent the overall population of star forming galaxies in the local universe, we compare their stellar mass and SFR distributions to that of $\sim 10^5$ star forming galaxies at $z < 0.2$ from the Sloan Digital Sky Survey (SDSS, York et al., 2000) MPA/JHU[2] catalog of star formation rates (Brinchmann et al., 2004). For the VENGA galaxies, we estimate M_* from the K-band luminosity, by assuming a mass-to-light ratio of $\Upsilon_K = 0.42$ (Vallejo et al., 2002). The K-band luminosities are computed using the distances reported in Table 4.1, and the total K-band apparent magnitudes from the 2MASS Large Galaxy Atlas (LGA, Jarrett et al., 2003), except for NGC1042, NGC3147, NGC3949, NGC5981, NGC7479, and NGC7331, which are not included in the LGA, so their magnitudes were taken from the 2MASS Extended Source Catalog (Jarrett et al., 2000). We do not correct the luminosity for dust extinction, but we expect

[2]http://www.mpa-garching.mpg.de/SDSS/index.html

this effect to be small (at the $\sim$10% level at the wavelength of the K-band).

We were able to find integrated SFR measurements in the literature for 24 of the 30 galaxies in the VENGA sample. These were taken from Lee et al. (2009), Kennicutt et al. (2003), and Thilker et al. (2007), in that order of preference when multiple measurements were found. The stellar mass and SFR of the VENGA galaxies is reported in Table 4.3. Figure 4.2 shows the VENGA and SDSS galaxies on the M_* versus SFR plane. Our sample spans a range in SFR from 0.2 to 39 $M_\odot$ yr^{-1}, and is distributed in this parameter similarly to the overall population. In term of stellar mass, the VENGA galaxies span the range between 4×10^8 $M_\odot$ and $3\times10^{11}M_\odot$, but with 87% (26/30) of the sample having $M_* > 10^{10}$. By comparing the stellar mass distribution to that of the SDSS star forming galaxies it is evident that our sample is biased towards the high-mass end of the local population. VENGA is primarily a survey of massive spiral galaxies, and dwarf systems are therefore not well represented in the sample.

Finaly, it is important to characterize the spatial resolution we can achieve with VIRUS-P at the distance of each of our targets. Table 4.1 reports the phisycal scale in pc corresponding to one arcsecond on sky at the distance of each galaxy. Given the 4.235″ diameter of the VIRUS-P IFU fibers on the sky, we achieve a spatial resolution between 80 pc, for the closest galaxy (NGC6503), and 1020 pc for the furthest (NGC5981). The distribution of spatial resolutions achievable for all galaxies is presented in Figure 4.3. The median spatial resolution for the whole sample is 300 pc.

4.2.2 Observing Strategy

The VIRUS-P IFU is a square array of 246 optical fibers (each 4.235" in diameter) which sample a $1.7' \times 1.7'$ field-of-view (FOV) with a 1/3 filling factor. Three dithers provide full coverage of the FOV. The instrument images the spectra of the 246 fibers on a 2k×2k Fairchild Instruments charged-coupled device (CCD) with 15 μm pixels. The CCD electronics deliver 3.6-4.3 e^- read-noise depending on the read-out mode used. Each fiber spectra has an approximately gaussian spatial profile of ∼5 pixels FWHM, and fibers are stacked vertically on the CCD approximately 8 pixels appart from each other, making cross-talk between fibers essentialy negligible.

To obtain full coverage of the FOV, for each VIRUS-P pointing we observe 3 dithers at relative positions $(\Delta\alpha, \Delta\delta) = (0.0'', 0.0'')$, $(-3.6'', -2.0'')$, and $(0.0'', -4.0'')$ from the origin. Therefore, at each pointing we obtain individual spectra for 738 independent spatial resolution elements. Depending on the angular size of the targets we observe 1, 2, or 3 pointings on each galaxy (see Figure 4.1 and last column in Table 4.1) usually providing full coverage of the central part of the galaxies, and a typical sampling of the outer disk out to 0.7 R_{25}. Overall the VENGA survey consists of 60 individual pointings, composed of 3 dithers each, amounting for spectra of $\sim 44,000$ independent regions (typically a few 100pc in diameter) across the disks of the 30 galaxies in the sample.

The spectral range on VIRUS-P can be adjusted between 3600Å and 6800Å. The instrument has a set of volume phase holographic gratings which

provide different spectral resolutions and wavelength coverage. For VENGA, we use the lowest resolution setup whith spectral resolutions between 4.5 and 5.5Å FWHM (depending on the position of the spectrum on the CCD), and coverage of a spectral window ∼2200Å wide. We observe each galaxy in a blue setup (3600Å-5800Å) and a red setup (4600Å-6800Å), therefore obtaining full spectral coverage in the 3600Å-6800Å range. All the data is taken in 1×1 binning mode, which translates into a spectral dispersion of ~ 1.11 Å pixel^{-1}, except for some early observations of the central pointing of NGC5194 which where taken with 2×1 binning in the spectral direction (Blanc et al., 2009).

In terms of depth, the goal of VENGA is to obtain spectra that reaches a median $S/N \sim 40$ in continuum per spectral resolution element per fiber across each galaxy. This allows us to take full advantage of the instrument spatial resolution (given by the fiber size) throughout most of the maps, with only some measurements requiring spatial binning in the outer edges of the targets. Relative exposure times for different galaxies where scaled using their average B-band surface brightness within R_{25}, taken from the RC3 catalog (de Vaucouleurs et al., 1991, Table 4.1), and typically range from 45 min to 3 hr per dither.

4.3 Observations

The VENGA survey is still in the phase of data acquisition. Observations of all targets in the red spectral setup started in April 2008 and were completed in July 2010. Blue setup observations started in September 2010,

and we expect them to be completed around the end of 2011. Table 4.4 lists all the observing runs we have conducted as part of VENGA, the instrumental setup used, the number of nights observed, and the galaxies for which data was obtained.

As mentioned above, typical exposure times for each dither range from 45 min to 3 hr, typically divided in shorter exposures of 15 to 25 min to allow for cosmic ray rejection. When conditions were not phtometric, we went above these target exposure times to ensure reaching the desired depth. Because of the large angular diamter of our targets, during most observations the VIRUS-P IFU never samples regions of blank sky. Therefore, off source sky exposures are necessary to measure and subtract the sky spectum from the science data. We obtain 5 min sky frames bracketing each science exposure. The off-source frames are taken 30' north of each galaxy, and have been checked to not have extended sources in them. All observations are performed at an airmass $\chi > 2$.

Bias frames, arc lamps, and twighlight flats are obtained at the beginning and end of each night. For the red setup we use a combination of Ne+Cd comparison lamps, and the for the blue setup we use Hg+Cd. These combinations of lamps provide a good set of strong lines over the full spectral range of each setup, allowing for proper wavelength calibration with minimal extrapolation towards the CCD edges.

During most nights we obtain data for one or two spectro-photometric standard stars, using the six-position fine dithering pattern presented in Blanc

et al. (2009). As described below, standard star spectra are used to perform the relative flux calibration, while the absolute flux level is calibrated against broad-band images.

During some observing runs, the spectra of 1 to 3 out of the 246 fibers fall off the CCD due to camera and grating alignment issues. This translates in a lack of spectra for 1 to 3 fibers at the corner of the field-of-view, which does not affect the data significantly.

4.3.1 NGC0628 Data

In particular, in this paper we present the red-setup data over 3 VIRUS-P pointings on the face-on Sc galaxy NGC0628. The central coordinates of the three pointings are given in Table 4.5. The data was taken on the nights of the 8-9 of November 2008, 9-15 of November 2009, and 9-21 of December 2009. Observing conditions were variable between different runs and within different nights during the same observing run, ranging from photometric to partly cloudy conditions with atmospheric transparency down to ∼60%. The seeing (as measured from a gaussian fit to the guide-star in the co-focal guider camera of the instrument) ranged between 1.5″ and 4.0″ (FWHM), with a median of 2.0″.

Table 4.5 presents a summary of the red setup data used for NGC0628, after rejecting 7/109 (6%) frames which showed either bad pointing problems or catastrophic sky subtraction problems (see §4.4.4 and §4.4.6). For each dither in each pointing on the galaxy, we list the total on-source exposure

time, the number of frames, the average seeing of the frames, and the median atmospheric transparency (as measured in §4.4.6). Pointing 3 was observed under particularly bad conditions so it was revisited.

4.4 Data Reduction and Calibration

Data reduction is performed using the VACCINE pipeline for VIRUS-P data (Adams et al., 2011b), in combination with a series of custom built IDL routines. In this section we describe the data processing, and the techniques used for background subtraction, extraction of the 1D spectra, creation of the data-cubes[3], and calibration in wavelength, and flux (both in the relative and absolute sense). We also discuss the astrometry of our data. Both the astrometry and absolute flux calibration are based on the comparison of reconstructed images from the VIRUS-P IFU spectra to broad-band images of the galaxies.

4.4.1 Basic CCD Processing, Cosmic Ray Rejection, and Fiber Tracing

All individual frames (bias, flats, arcs, sky, and science) are overscan subtracted. We combine all the ovserscan subtracted bias files for each observing run (usually ~ 100) to create an image of any residual bias structure, which is subtracted from all the flat, arc, sky, and science frames.

We use the LA-Cosmic laplacian cosmic ray identification algorithm of

[3]We use a loose definition of *data-cube*, and unless stated otherwise we use the word *data-cube* to reffer to row-stacked spectra (RSS) files in the format described in §4.4.7

van Dokkum (2001), to identify and mask cosmic rays in the science images. We tunned the algorithm to be robust enough to identify most cosmic rays in the science frames while making sure real emission lines were not being masked. Any residual cosimc rays not identify in this pass, or the unmasked wings of elongated cosmic rays hitting the detector at very oblique angles are removed from the data when different frames are combined (§4.4.6).

Twilight flats are used to trace the spectrum of each fiber on the CCD. VIRUS-P is mounted on a gimble attached to the broken Cassegrian focus of the 2.7m telescope. The gimble keeps the spectrograph at a constant gravity vector, making flexure effects on the optical path of the instrument negligible. Thanks to this, with VIRUS-P there is no need to obtain calibrations at the same time and telescope position of the science data. We have observed sihfts in the positions of fibers on the CCD (at the 0.1 pixel level) when large changes in temperature ocurr. VACCINE corrects for these small offsets during the flat-fielding stage to properly remove the spatial PSF of each fiber from the 2D spectra. These offsets do not affect the tracing of the fibers used for extraction. This is because we use discrete pixel apertures centered around the pixel containing the traced centroid to extract the 2D spectrum of each fiber. Therefore, only very rarely a ~ 0.1 pixel shift can modify which pixels are chosen as part of the extraction aperture. In any case, to minimize all the above effects, for both the tracing and flat-fielding of each night's data we use the set of twilight-flats which is closest in temperature to the average temperature at which the science data is taken. Most of the time this means

the twilight-flats taken at dawn are used.

As mentioned above, we extract the 2D spectrum of each fiber in the science, sky, arc, and flat frames using a 5 pixel aperture centered around the pixel containing the centroid of the fiber's spatial profile. Using a discrete pixel instead of a fractional pixel aperture centered on the trace centroid itself, avoids having to re-sample the data and conserves the noise properties of individual pixels. At this stage in the reduction, VACCINE constructs a formal error map which accounts for both read-noise and Poisson uncertainty for each pixel in the 2D spectrum of each fiber. This map is properly propagated throughout the rest of the reduction (assuming gaussian uncertainties), and is used to produce the weights used when combining and collapsing spectra from different frames, and to create the final flux error spectrum for each fiber.

4.4.2 Wavelength Calibration and Characterization of the Instrumental Spectral Resolution

Arc lamp frames for each night are combined to produce a master arc. VACCINE is typically able to automatically fit and match ~ 20 emission lines in the line list. We fit the wavelength solution for each fiber independently using a 4th order polyinomial. Residuals in the wavelength solution with an r.m.s. dispersion of $\sigma_\lambda \simeq 0.1$ Å, or a tenth of a pixel (~ 6 km s^{-1} at 5000Å) are typically observed.

We also use the emission lines in the master arc frame to characterize the spectral resolution as a function of wavelength for each fiber. We measure

the FWHM of non-blended arc lines by performing single gaussian fits. By fitting a second order polynomial to the measured FWHM values across the spectral direction for each fiber, we create a robust map of the instrumental spectral resolution (FWHM_{ins}) of each fiber as a function of wavelength. Good knowledge of the resolution is essential at the time of fitting galaxy spectra with linear combinations of empirical or synthetic templates, which must be convolved to the same resolution of the data in order to extract meaningful line-of-sight velocity distributions (LOSVD) from the fits.

The VIRUS-P instrumental resolution is typically observed to change smoothly as a function of position on the detector, with values ranging from $\mathrm{FWHM}_{ins} = 4.4$ Å ($\sigma_{ins} = 112$ km s^{-1} at 5000Å) to $\mathrm{FWHM}_{ins} = 5.8$Å ($\sigma_{ins} =$ 148 km s^{-1} at 5000Å). No variation in the instrumental spectral resolution is observed between observing runs.

4.4.3 Flat Fielding

The flat-fielding process in VACCINE is used to divide out three different effects from the data: (1) the relative fiber-to-fiber throughput, (2) the profile of the fiber PSF on the detector across the spatial direction, and (3) the CCD pixel-to-pixel variations in quantum efficiency. First, VACCINE removes the signal coming from the solar spectrum from the combined twilight-flat (§4.4.1). For each fiber, this is achieved by fitting a bspline to the twilight spectra of a set of 60 neighbouring fibers which share a similar spectral resolution, and then normalizing the observed fiber by this combined high S/N

spectrum (see Adams et al., 2011b). Since each fiber provides an independent wavelength sampling of the observed spectrum, combining data from a large set of neighbouring fibers effectively yields a sub-pixel sampled twilight spectrum which after being fit by the bspline can be evaluated at the exact wavelength scale of the fiber of interest.

From the resulting normalized flat, VACCINE creates a fiber profile flat by runing a median smoothing kernel across the spectral direction. This new frame contains only the relative fiber-to-fiber througput and the fiber spatial profile. Dividing the original flat by this smoothed version yields a pixel-to-pixel flat that is applied to the data.

As mentioned in §4.4.1, small, sub-pixel, temperature induced offsets in the fiber positions on the CCD are sometimes present in the data. This can translate into systematic errors when removing the spatial profile of the fibers, if the data is divided by a flat-field that is offset from the data in the spatial direction. Errors can be particularly large at the edges of fibers where the data values are divided by smaller numbers than at the fiber's core. These offsets must be corrected for, in order to remove the fiber PSF across the spatial direction. VACCINE traces each fiber in the science and sky frames (after running a 30 pixel boxcar filter across the spectral direction to ensure a high S/N measurement of the fiber centroid), and computes an offset with respect to the fiber centroid in the flat. These offsets are used to resample the smoothed fiber profile using an optimal sinc-interpolation method in order to align it with the data. We divide the science and sky frames by this resampled smoothed

flat frame, therefore removing all the effects mentioned at the beggining of this section.

4.4.4 Sky Subtraction

The sky spectrum is measured by combining information from the two off-source sky exposures taken before and after each science frame. In Blanc et al. (2009) we simply averaged the before and after off-source frames to create the sky frame used for background subtraction. While this method worked well on the NGC5194 data presented there, those observations were taken far from twilight, and under very stable and dark conditions. We have found that when conditions are not optimal (e.g. close to twilight, when clouds are present, or near moon-rise or moon-set) the sky brightness can change non-linearly with time, making the simple averaging of bracketing background frames insuficient to produce an adecuate sky subtraction. We have adopted a more sophisticated method to estimate and subtract the sky spectrum from our data, which makes use of all the temporal information we can extract regarding the variability of the sky brightness as a function of wavelength, from all the sky frames obtained throughout each night.

As an example, Figure 4.4 shows the raw (i.e. not flux calibrated) sky spectrum measured from the 13 off-source sky frames taken during the night of November 7th, 2008. The spectra is color coded by UT time, with purple at the beginning of the night and red at the end of the night. The elevated brightness and blue color of the spectrum at the beginning of the night is

due to the first quarter moon. Moonset at McDonald Observatory on that date occurred at UT=8.47 hr, and can be clearly seen as a sharp drop in the sky brightness, specially at blue wavelengths. For this night, the darkest skies occurred between 9 hr and 10 hr UT. This is followed by a monotonous increase in sky brightness, which is steeper at redder wavelengths. This brightening and reddening is due to both the approachment of twilight and the fact that the observations were being done at increasing airmass.

To trace these changes, we divide the spectra in 500 bins in wavelength (roughly corresponding to a spectral resolution element), and measure the median sky brightness in each bin for every frame. Figure 4.5 shows the relative change in sky brightness across this specific night for three different wavelengths near the blue end, middle, and red end of the spectrum. Measurements for each sky frame are shown as filled circles. For reference, the black open diamonds show the average change in brightness integrated across the whole spectrum. The trends described above are clearly seen. Vertical dashed lines mark the beginning and end of observations of the same galaxy. The discontinuity in the sky brightness at these times is expected since the telescope is pointed at a different direction. We reffer to each of these sections of the night as "observing blocks".

For all observing blocks in every night of the survey, we fit the sky brightness in the different wavelengths bins, as a function of time using a cubic spline (color solid curves in Figure 4.5). This allows us to evaluate, at any wavelength and UT time within the observing block, a correction factor

by which the nearest sky frames must be multiplied in order to reconstruct the sky spectrum at the time of interest. Since the correction factors computed for the 500 wavelength bins are inherently noisy, we fit them as a function of wavelength using a fifth order polynomial. This allows us to multiply the sky frames by a smooth function of wavelength, without introducing further noise in the observed sky spectrum.

We apply the above procedure to correct the before and after background frames to the UT time of the science frames. We then average the two corrected frames to create a single background file for each science exposure. Sky subtraction is performed by VACCINE using this composite corrected sky. The method used by VACCINE to subtract the sky is analog to the bspline algorithm used to remove the solar spectrum from the twilight flats (see §4.4.3). Briefly, for each fiber in the science exposure, the sky spectra of a set of neighboring fibers in the background frame is simultaneously fit using a bspline, and then subtracted. As mentioned above, this procedure greatly benefits from the sub-pixel sampling of the sky obtained by combining information from different fibers having different wavelength samplings of the sky spectrum.

The quality of the sky subtraction in VENGA is excelent. We typically see sky subtraction residuals that are fully consistent with Poisson plus read-noise uncertainties. Larger residuals usually appear at the wavelengths of the 4 brightest sky emission lines in our wavelength range. This is mostly due to the fast time variability of these spectral features, which is independent of the

variability of the sky continuum taken into account by our corrections. These regions showing poor background subtraction are masked during the analysis of our science data. Rarely (less than 5% of the frames in the case of the red-setup data on NGC0628), when observations are taken under extremely bad observing conditions (usually combinations of clouds and moon, or clouds and closeness to twighlight), obvious residuals in the sky subtraction can be observed in the sky-subtracted science exposures. We reject these frames from the dataset.

4.4.5 Spectrophotometric Flux Calibration

We use observations of spectrophotometric standard stars from Massey et al. (1988) and Oke (1990) to calibrate the VENGA spectra. The method used to construct sensitivity curves from the IFU observations of standard stars is described in Blanc et al. (2009). The only difference with the approach taken in that previous work, is that in VENGA, standards are only used to perform the relative flux calibration as a function of wavelength. The absolute scale of the calibration comes from a comparison to broad-band optical images of the VENGA galaxies, which is described in the following section.

We calculate sensitivity curves for all standard stars taken during each observing run. These curves are normalized to a common scale, and are then averaged to create a master sensitivity curve for the run. All the science frames obtained during each observing run are multiplied by this curve to convert them to units of erg s^{-1} cm^{-2} $Å^{-1}$. The error maps for each frame

are also scaled accordingly. By looking at the dispersion between different sensitivity curves within each month, we estimate a typical uncertainty in the relative flux calibration of $\sim 5\%$.

4.4.6 Astrometry and Absolute Flux Calibration

The pointing of VIRUS-P is done using an offset guider camera which images a $4.5' \times 4.5'$ field $\sim 9'$ north of the IFU science field. A precise astrometric calibration between the two fields allows the observer to point the IFU by putting a guide star at specific physical coordinates on the guider's detector. Adams et al. (2011b) found systematic offsets of the order of $1''$ between pointings made during different observing runs. In order to accurately recover the astrometry of the VENGA science observations, we use a cross-correlation between reconstructed broad-band images of the galaxies made from the IFU data, and archival broad-band images. These comparisons are also used to calibrate the spectra in terms of absolute flux. In this section we present the results for the NGC0628 red setup data, which we compare to the SDSS DR8 r-band mosaic[4] of the same galaxy.

For every science exposure at each dither position, we integrate the spectrum of each fiber over the SDSS r-band transmission curve to measure the monocromatic flux at the effective wavelength of the broad-band filter. Simultaneously we convolve the SDSS image of the galaxy with a gaussian kernel, to match the image PSF to the seeing under which the VIRUS-P data

[4]http://data.sdss3.org/mosaics

was taken, and we perform aperture photometry at the fiducial position of each fiber. We use circular apertures that match the size of the fibers. The VIRUS-P and SDSS fluxes are fitted using the following expresion:

$$f_{SDSS} = A \times f_{VIRUS-P} + B \tag{4.1}$$

where A is a normalization factor recovering the absolute flux scale, and B recovers any residual background left from the sky subtraction process. A perfect background subtraction in both the SDSS image and the VIRUS-P spectra should translate in $B = 0$.

We perturb the fiducial astrometry of the VIRUS-P pointing by applying offsets in both right ascension and declination, in order to minimize the χ^2 of the fit. This registering process provides a corrected astrometry for each science frame. Given the wealth of spatial information encoded in the relative brightness of hundreds of VIRUS-P fibers, the registering is very accurate, and has a typical uncertainty of $\sim 0.1''$. The value of A at the registered position provides the absolute scale for the flux calibration and the science frame is multiplied by this value. This ties our flux calibration to that of SDSS, which has a zero-point uncertainty in the r-band of 2%. For the 102 individual frames used to construct the NG0628 red-setup dataset, we measure a mean $\langle B \rangle = -2 \times 10^{-18}$ erg s^{-1} cm $^{-2}$ Å, with a standard deviation of $\sigma_B = 5 \times 10^{-18}$ erg s^{-1} cm $^{-2}$ Å. This level of sky subtraction residuals correspond to less than 2% of the median continuum flux level in the data, and it is only an upper

limit since the residuals have some contribution from the error in the SDSS backgorund subtraction.

Figure 4.6 shows the astrometric offsets we measure for the three pointings on NGC0628, with respect to the fiducial dithering pattern. For each pointing, the fiducial positions of a fiber on dithers 1, 2, and 3 are marked by the stars and solid red, green, and blue circles respectively. Color crosses mark the actual positions at which independent science exposures were obtained. These positions are measured using the registration method described above. The squares, and color dashed circles show the average position for all exposures in each dither. After different exposures are combined (§4.4.7), these average positions are adopted as the final fiber coordinates on sky.

Overall, the astrometric accuracy of the observations is good. We observe systematic offsets from the fiducial dithering pattern in the range 0.07″-0.82″, with a mean of 0.39″. It is important to note that while these deviations will translate in a slightly irregular sampling of the field-of-view (effect which is attenuated by the large 4.2" diameter fibers), the average *corrected* positions are adopted as the fiber centers in all the following analysis, so these offsets are taken into account. We also observe random deviations for individual exposures around the average corrected coordinates which show a mean value of 0.33″, or less than a tenth of the fiber size.

4.4.7 Spectral Extraction, Combination of Frames, and Formatting of RSS Files

At this stage in the data reduction process, we have a reduced, sky subtracted, wavelength and flux calibrated 2D flux spectrum of each fiber (and its associated 2D error spectrum) for every individual science exposure. In this section we describe the methods used to combine data from different exposures at the same dither position, and to extract a 1D flux and error spectrum for each fiber. We also describe the format of the VENGA data-cube files.

Data from different nights and observing runs have independent wavelength solutions, therefore, before combining, we need to re-sample all the spectra to a common wavelength grid. In VENGA, we produce two independent data products for each of the three dithers obtained at each pointing in the survey. These products correspond to two versions of the same data-cube, one with a regularly spaced linear sampling of wavelength, and another with a regular logarithmic sampling (i.e. spaced regularly in velocity space). The *linear* data-cubes have pixels spaced by 1.1Å (similar to the average dispersion in the original data), while the *logarithmic* data-cubes have pixels that are spaced by $(\Delta\lambda/\lambda)c = 60$ km s^{-1}.

The reason behind producing two versions of the same data-cube, is that while most users will be interested in using the *linear* version for many applications, the spectral fitting software used in the following section to extract stellar, and gas kinematics, as well as emission line fluxes, requires input spectra that is regularly sampled in velocity space. Instead of interpolat-

ing the spectra to a linear grid for the effects of combining, and then later re-interpolating the combined spectra to a logarithmic scale, we do both re-samplings directly from the original data. In this way, we avoid the effects of S/N degradation associated with extra re-samplings.

After re-sampling in both cases, for each fiber, at any given wavelength, we have $N_{pix} = 5 \times N_{frames}$ pixels, which provide N_{pix} measurements (with errors) of the flux density. After applying a 3σ clipping rejection to remove any cosmic rays that were not identified in §4.4.1, we combine the data by calculating the inverse variance weighted mean of the remaining pixels.

As mentioned in §4.4.2, the instrumental spectral resolution at different wavelengths, for each fiber, can be extracted from the arc lamps. To create a proper resolution map for each data-cube, we combine the master arc lamp frames associated with each individual science frame in the same way as the science data is combined (i.e. using the same weighting). We then use the method described in §4.4.2 to create a map of the instrumental spectral resolution from this combined arc.

The final processed VENGA data is stored in multi-extension FITS[5] files which contain the following information in their different extensions:

1. Flux density spectrum of each fiber (RSS) in units of erg s^{-1} cm^{-2} $Å^{-1}$.

2. Error spectrum of each fiber (RSS) in units of erg s^{-1} cm^{-2} $Å^{-1}$.

[5]Flexible Image Transport System

3. Wavelength array for each fiber (RSS) in units of Å.

4. Right ascension and declination of each fiber in units of decimal degrees.

5. Instrumental spectral resolution (FWHM) array for each fiber (RSS) in units of Å.

Given the non-regular spatial sampling of our dither pattern, we decide to use the row-stacked spectrum (RSS) format to store our IFU data. Producing data-cubes sampled on a regular grid in right ascension and declination would require further re-sampling of the data, which we consider unnecessary. These combined, background subtracted, wavelength, and flux calibrated, multi-extension RSS fits files are the final data products of VENGA.

The final data-cube for NGC0628 includes spectra for 2190 independent fibers over the three pointings obtained on this galaxy. Figure 4.7 shows an r-band image of NCG0628, reconstructed from the final VENGA data-cube. All the maps presented in this paper have north pointing up and east pointing left. The final combined spectra was integrated over the SDSS r-band transmission curve to create this map. For comparison, Figure 4.8 shows the SDSS r-band mosaic of NGC0628. The image is convolved to match the average seeing under which all the VENGA data was taken ($2.24''$), and we have performed aperture photometry (matching the fiber size) at the right ascension and declination of fibers in the data-cube. The similarity between the two maps shows that the flux calibration and astrometric correction of independent dithers has been done properly.

As stated in §4.2.2, the goal of VENGA is to achieve a median $S/N = 40$ per resolution element (FWHM) in continuum, per fiber. In Figure 4.9 we present a map of S/N across the data-cube. For reference, the VENGA r-band flux contours are overlaid. In order to transform S/N per pixel to S/N per resolution element we multiplied by $\sqrt{4.5}$, which roughly assumes $FWHM = 5.0$Å at our 1.1Å pixel^{-1} scale. Our NGC0628 data achieves a median $S/N = 68$. In the central parts of the galaxy we typically have $S/N > 100$ per fiber. More than 80% (1762/2190) of the fibers are above our goal of $S/N = 40$, and less than 2% (39/2190) of the fibers have $S/N < 15$, limit under which it becomes hard to extract the line of sight velocity from the spectrum. As shown in the next section, even at these low S/N we can still sometimes extract Hα emission line fluxes.

4.5 Spectral Analysis Pipeline

In order to extract emission line fluxes, gas and stellar kinematics, and information about the stellar populations present in different parts of the galaxies, we fit the VENGA spectra using a linear combination of empirical stellar templates, convolved with a LOSVD, plus a set of Gaussian emission line profiles. To do the fitting, we use the pPXF (Cappellari & Emsellem, 2004) and GANDALF (Sarzi et al., 2006) IDL routines developed for this purpose by the SAURON team. In this section we describe the fitting process, and present some example fits to fibers in the NGC0628 data-cube.

4.5.1 Stellar Kinematics

We first mask the spectrum of each fiber around regions affected by sky subtraction residuals due to bright sky lines, and regions potentially affected by the nebular emission lines listed in Table 4.6. Then, we fit for the stellar line-of-sight velocity (v_*) and velocity dispersion (σ_*) with the pPXF software, which uses the "penalized pixel" technique (Cappellari & Emsellem, 2004) to fit the spectrum with a linear combination of templates convolved with a LOSVD. The software uses a Gauss-Hermite polynomial LOSVD, and allows for the fitting of high order terms (h_3,h_4). In the case of the VENGA data, the instrumental resolution is too low to allow for the measurement of these higher order terms, so we restrict the LOSVD to have a simple Gaussian form.

The logarithmically sampled data-cubes are used as input for pPXF, which requires the input data to be regularly sampled in velocity space. We use the MILES stellar library (Sánchez-Blázquez et al., 2006), as a source of empirical templates. A subset of 72 stars spanning a wide range in spectral types (O through M), luminosity classes (I to V), and metallicities ($-2 <$[Fe/H]< 1.5) is used. We also include a few horizontal branch and asymptotic giant branch (AGB) stars in the template subset. Before fitting, the templates are resampled to the wavelength scale of the data, and we degrade the instrumental resolution of both the data and the templates to a $\sigma_{ins} = 148.7$ km s^{-1}, by convolving with a Gaussian kernel. This corresponds to the worst resolution in the VENGA data-cube of NGC0628. We assume the corrected MILES library intrinsic resolution of 2.54Å (Beifiori et al., 2010).

In order to account for the effect of dust extinction on the shape of the spectral continuum, and for potential systematic differences in the flux calibration of the data and the templates, during the minimization we fit a 5th order Legendre polynomial, by which the templates are multiplied. The low order of the polynomial prevents it from introducing features on small scales, of the order of the instrumental resolution. The polynomial only matches the large-scale ($\sim 100\mathring{A}$) shape of the continuum in the linear combination of stellar templates and the data, so it does not affect the fitting of individual spectral features.

In this way, we fit each fiber individually, and store the kinematic parameters (v_*, σ_*). We keep these parameters fixed over the next fitting iteration, in which we also fit for the emission lines in the spectrum.

4.5.2 Emission Line Fluxes and Ionized Gas Kinematics

After measuring the LOSVD of each fiber by masking the regions of the spectra affected by sky residuals and nebular emission lines, we use the GANDALF software to fit the full spectrum, including the emission lines. GANDALF re-fits the spectrum by recomputing the weights given to the different stellar templates, at the same time of adding Gaussian profiles to model the contribution to the spectrum of the emission lines. We attempt to fit all the transitions presented in Table 4.6.

This second fit is done while keeping constant the stellar LOSVD obtained in the previous section, but independently fitting for the emission lines

velocity, velocity dispersion, and amplitude, as well as the relative weights given to the stellar templates. While in principle we could obtain independent kinematic measurements from different lines, this becomes very hard for faint transitions detected at low S/N. Therefore, we tie the kinematics of all emission lines to a common set of parameters (v_{gas}, $sigma_{gas}$) during the fit. This ensures that the kinematic parameters obtained are mostly constrained by the brightest emission lines in the spectrum (typically Hα, and [OIII]λ5007). In this second step we also run GANDALF using a 5th order multiplicative Legendre polynomial to match the continuum shape.

In Figures 4.10, 4.11, 4.12, and 4.13, we present the observed and best-fit spectra of four randomly selected fibers in different S/N ranges, having $S/N = 128$, 77, 25, and 15, respectively. The spectra is presented from highest to lowest S/N, and provides a good representation of the quality of our fits. The observed spectrum is shown in blue, with errors marked by the cyan envelope. The solid red line shows the best-fit stellar plus emission line spectrum, while the dotted line shows the best-fit stellar spectrum only. The four vertical cyan bands represent regions masked around sky line residuals. We also show zoomed in spectra around Hβ, Mgb, and Hα. Analyzing the S/N map presented in Figure 4.9, we can see that the typical fiber in the VENGA NGC0628 data-cube is best represented by a fit like the one shown in Figure 4.11.

Fits are usually of excellent quality, except at very low $S/N \lesssim 15$ (less than 2% of the NGC0628 data), where we can still make good emission

line measurements for the brightest lines, but parameters derived from the continuum, like the line-of-sight velocity, becomes noisy. This can be clearly appreciated in Figures 4.14 and 4.15 which present the velocity field of stars and ionized gas in NGC0628. While the maps are noisy because the galaxy is close to face-on, it is evident that in the lowest S/N regions, the emission lines provides a less noisy measurement than the stellar features. The point sources at extremely low velocities in the stellar velocity field correspond to fibers contaminated by foreground stars.

Figure 4.16 shows a map of the Hα flux across NGC0628. The Hα flux clearly traces the two main spiral arms, where ongoing star formation gives rise to prominent HII regions. In the inter-arm regions we still detect significant amounts of Hα emission, although with a surface brightness that is one to two orders of magnitude fainter than on the arms. A large fraction of this emission arises from the diffuse ionized gas component of the galaxy's ISM (Mathis, 2000; Haffner et al., 2009; Blanc et al., 2009).

For each transition in Table 4.6, we report the median S/N over all fibers with which the flux is measured, and the number of fibers detected at 5σ and 3σ. Also, in Figure 4.17 we present the S/N as a function line flux for all the emission lines we attempted to fit. Our observations reach a 3σ line flux limit per fiber of 5×10^{-17} erg s^{-1} cm^{-2} (8×10^{-17} erg s^{-1} cm^{-2} at 5σ). This corresponds to 3σ and 5σ intensity limits of 4×10^{-18} and 6×10^{-18} erg s^{-1} cm^{-2} arcsec^{-2}. We detect Hα at 5σ in 98% (2143/2190) of the fibers in the data-cube, and only in 7/2190 fibers we do not obtain a 3σ detection. The

median S/N in the flux measurement of the line is 30.

Other transitions are usually detected at lower significance than Hα. All members of the [NII]$\lambda\lambda$6548,6583 and [SII]$\lambda\lambda$6717,6731 doublets, as well as Hβ and [OIII]λ5007 are detected at 3σ in more than 89% (1953/2190) of all fibers in the data-cube. The [OIII]λ4959 line is detected at 3σ in 47% (1031/2190) of the fibers, while the fainter HeIIλ4685 and [NII]$\lambda\lambda$5198,5200 transitions are rarely detected.

4.6 Results

4.6.1 A previously undetected low-luminosity AGN in NGC0628

Using the emission line fluxes measured in the last section, we search for the presence of AGN activity in the central part of NGC0628. The nucleus of this galaxy has been previously classified as a purely star-forming region by Moustakas et al. (2010), based on a circum-nuclear ($20'' \times 20''$) optical drift-scan spectrum. Furthermore, Ho et al. (1997), who performed a systematic search for nuclear activity in a sample of 486 nearby galaxies in the Palomar optical spectroscopic survey (Filippenko & Sargent, 1985), did not detect an AGN in the center of this galaxy. This last non-detection was caused by the inability to classify the spectrum due to its low level of nebular emission, and not because the measured emission line fluxes were not consistent with the presence of an AGN. Observations done with the *Chandra* space observatory show a low luminosity ($\sim 10^{38}$ erg s^{-1}) X-ray emitting nucleus (Terashima et al., 2004), which is thought to be associated with an ultra-low luminosity

AGN previously undetected in the optical spectroscopy. The probability of a chance superposition of an unrelated X-ray binary with the central part of the galaxy is not negligible, therefore, the AGN nature of the nucleus is not fully certain.

Thanks to the depth, and good spatial resolution of the VENGA data, we are able to clearly identify a low-luminosity AGN in NGC0628, by studying the diagnostic nebular emission line ratios of [OIII]λ5007/Hβ (hereafter [OIII]/Hβ), and [NII]λ6583/Hα (hereafter [NII]/Hα). Figure 4.18 shows the diagnostic BPT-diagram (Baldwin et al., 1981; Veilleux & Osterbrock, 1987) for all fibers in the NGC0628 VENGA data-cube. This diagram is a standard tool used to distinguish the nebular spectrum of star-forming and active galaxies. Shown as dashed and dotted curves are the AGN/star-formation classification criteria of Kewley et al. (2001) and Kauffmann et al. (2003). All emission line ratios have been corrected for dust extinction using the Balmer decrement method.

The red filled circle in Figure 4.18 shows the line ratios integrated over the whole data-cube. The nebular spectrum of NGC0628 is clearly dominated by star-formation. Many regions that are not associated with the nucleus of the galaxy seem to lie above the AGN classification criteria. Most of these fibers showing enhanced emission line ratios are physically associated with the inter-arm regions of the galaxy, where the spectrum is dominated by the diffuse ionized gas component of the ISM. This can be clearly appreciated in Figure 4.19, which presents a map of the [NII]/Hα ratio across the galaxy. We will

discuss the contribution from the DIG in more detail during the next section.

In the BPT diagram shown in Figure 4.18 we have highlighted 7 regions which are above both the Kauffmann et al. (2003) and Kewley et al. (2001) selection criteria for AGN, and also lie at a galactocentric radius of less than 500 pc (marked as a thick oval contour in Figure 4.19). While four of these regions seem to follow the sequence traced by DIG dominated regions in the BPT diagram, at least the other three show extremely enhanced emission line ratios (particularly [NII]/Hα), and populate the region of the diagram usually occupied by LINERs. The seven fibers are marked by the small circles in Figure 4.19. Therefore, we have found direct evidence from the nebular emission line ratios, that the gas in the central part of NGC0628 is being ionized by a low-luminosity active galactic nuclei. This confirms the AGN nature of the X-ray nucleus detected by Terashima et al. (2004), and exemplifies the power that integral field spectroscopic observations have at identifying the nature of the sources of ionizing radiation in different regions within galaxies.

4.6.2 Diffuse Ionized Gas

Estimating the local SFR in different regions of a galaxy from the Hα emission, requires that we separate and remove the contribution from the DIG in front of the galaxy. The DIG is thought to be photo-ionized by Lyman continuum radiation from young stars leaking above the disk (see reviews by Mathis, 2000; Haffner et al., 2009). Thanks to the presence of giant ionized super-bubbles in the ISM, these UV photons can travel large distances, of up

to ~ 1 kpc, before ionizing extra-planar neutral hydrogen, and producing Hα emission (e.g. Dove et al., 2000). Therefore, although the ultimate origin of the DIG is related to the presence of young stars in the galaxy, its spatial distribution is smoothed, and does not trace the local ongoing star-formation in the disk, along a given line of sight.

Following the method developed in Blanc et al. (2009), we use the [SII]λ6716/Hα ratio (hereafter [SII]/Hα) to separate the contribution of the DIG to the observed Hα flux across the galaxy. This method takes advantage of the bimodal behavior observed in the [SII]/Hα ratio, when measured in HII regions and the DIG. This bimodality has been measured in the Milky Way (Madsen et al., 2006), and in Blanc et al. (2009) we scaled the fiducial Galactic values of the [SII]/Hα ratio for HII regions and the DIG, to model the spectra of different regions in the disk of NCG5194 as a linear combination of both. In this work, we go one step further, and measure the fiducial DIG and HII region [SII]/Hα ratios directly from the VENGA data. We then use these values to model the spectra across NGC0628, without the need of re-scaling the Galactic values, which, as discussed in Blanc et al. (2009), requires knowledge of the relative ion abundances between the two galaxies, and is subject to differences in the interstellar ionizing radiation field and ISM structure which cannot be easily taken into account.

In Figure 4.20 we present the same Hα map of NGC0628, previously presented in Figure 4.16, but now we have overlaid two sets of isophotal contours. These red and blue contours have been set at Hα flux levels of 3×10^{-16}

and 7×10^{-15} erg s^{-1} cm^{-2} respectively, and encompass regions in which the spectra is fully dominated by DIG (red contours), and HII regions (blue contours). Figure 4.21 shows a histogram of the [SII]/Hα ratio for all fibers in the data-cube, as well as for all fibers within the red and blue contours tracing pure DIG and pure HII region emission. In NGC0628 we see the same behavior observed in the Milky Way by Madsen et al. (2006) and in NGC5194 by Blanc et al. (2009), in the sense that the DIG shows strongly enhanced [SII]/Hα emission line ratios. This is thought to arise as a consequence of the lower ionization parameter and higher electron temperature typical of this phase of the ISM (Haffner et al., 1999). In NG0628, the DIG shows a median [SII]/Hα=0.49, while HII regions have [SII]/Hα=0.12. Following Blanc et al. (2009) we model the Hα flux at each position as a linear combination of a flat surface brightness distribution from the DIG, plus HII regions in the disk, so for each fiber we have

$$\begin{aligned} f(H\alpha) &= f(H\alpha)_{HII} + f(H\alpha)_{DIG} \\ &= C_{HII} f(H\alpha) + C_{DIG} f(H\alpha) \end{aligned} \tag{4.2}$$

where C_{HII}, and C_{DIG} correspond to the fraction of the Hα flux coming from each component, so

$$\begin{aligned} C_{HII} &= 1.0 - \tfrac{f_{0,DIG}}{f(H\alpha)} \quad ; \quad (\text{for } f(H\alpha) > f_{0,DIG}) \\ C_{HII} &= 0 \qquad\qquad\quad ; \quad (\text{for } f(H\alpha) \leq f_{0,DIG}) \end{aligned} \tag{4.3}$$

where $f_{0,DIG}$ is the constant flux level being contributed by the DIG for all

fibers. This is only a first-order modelling, which is useful to remove the DIG contribution from the local SFR measurements. In reality, the DIG does not present a perfectly flat Hα surface brightness distribution, but rather has structure which is dependent on the density, temperature, and ionization structure of the ISM and the distance to the ionizing sources. In any case, the structure in the DIG is much smoother than that of the Hα surface brightness coming from HII regions (Greenawalt et al., 1998). Furthermore, the DIG shows a broad distribution in [SII]/Hα ratios, which is thought to arise from temperature inhomogeneities in the gas (Haffner et al., 2009), therefore assuming a constant line ratio for this component only provides an average correction.

In order to measure $f_{0,DIG}$, we fit the observed [SII]/Hα ratio as a function of Hα flux using the following expression

$$\frac{[SII]}{H\alpha} = \left[C_{HII} \left(\frac{[SII]}{H\alpha} \right)_{HII} + C_{DIG} \left(\frac{[SII]}{H\alpha} \right)_{DIG} \right] \tag{4.4}$$

where [SII]/Hα is the observed dust corrected ratio for each fiber, and the intrinsic values for HII regions and the DIG are taken to be the median of the red and blue histograms in Figure 4.21. This fit is shown in Figure 4.22, along with the observed values. We measure a DIG flux level of $f_{0,DIG} = 3.3 \times 10^{-16}$ erg s^{-1} cm^2. This translates in the DIG contributing to 20% of the total Hα luminosity over the region sampled by the data-cube.

4.6.3 The Nebular Oxygen Abundance Gradient in NGC0628

One of the goals of VENGA is to use the IFU spectra of spirals galaxies to study the chemical structure of their disks, with the ultimate intention of constraining the formation history of these objects. The metallicity of stars and gas, at different positions within the galaxies, can be measured from the VENGA spectra by means of stellar aborption features and nebular emission lines. The level of chemical enrichment of a region within a galaxy is determined by both the local star formtion history, the accretion of external gas, and by secular and externally induced processes (mergers, interactions) which can transfer angular momentum across the disk, and therefore induce radial migrations of both gas and stars. Therefore, while the physical interpretation of the observed chemical structure of galaxies is non-trivial, all these dependences imply that much can be learned about the formation and evolution of galaxies from studying their chemical structure.

Ever since the seminal work of Aller (1942) and Searle (1971), it has become evident that disk galaxies in the local universe (including the Milky Way) present radial metallicity gradients, with heavy element abundances decreasing towards large galactocentric radii (e.g., Vila-Costas & Edmunds, 1992; Zaritsky et al., 1994; Kennicutt & Garnett, 1996; van Zee et al., 1998; Rosolowsky & Simon, 2008; Magrini et al., 2009; Moustakas et al., 2010). Observationally, these studies have been typically done using single or multi-slit spectroscopy of individual HII regions, or stars in nearby galaxies. This somewhat limits the number of measurements available for individual galaxies. The full 2D

coverage that can be achieved with wide-field integral field spectroscopy, can increase the number of measurements across the disks of single galaxies considerably, and unveil new radial structures and deviations from axisymetry in the chemical distribution of galaxies, which are beyond the reach of classical methods. For an excellent example of this method see the recent submission by Rosales-Ortega et al. (2011), who presents the radial metallicity gradient of NGC0628 as measured from the PINGS survey data.

In this section, we measure the oxygen nebular abundance across the disk of NGC0628 using the VENGA data, and construct its radial abundance gradient. Since in this work we are only presenting the red-setup data on NGC0628, we lack a measurement of the [OII]λ3727 doublet, and therefore we are somewhat limited in term of the methods we can use to estimate the gas metallicity. In a future publication, we will use the full VENGA spectrum to study the impact of using different abundace determination methods on the measured chemical structure of spiral galaxies. We use the recently published NS method by Pilyugin & Mattsson (2011), which is based on the [OIII]/Hβ, [NII]/Hβ, and [SII]/Hβ strong-line ratios. It has been empirically calibrated against a large sample of HII regions with measured electron temperatures, and shows an typical sacatter in the calibration of 0.08 dex. Empirically calibrated strong-line nebular abundance methods yield, by construction, values that are consistent with the *direct* method (i.e. with direct electron temperature measurements), and about 0.6 dex lower than theroretical strong-line methods based on photoionization models like R23. The aboslute scale of neb-

ular abundance estimators is currently a big subject of debate (**?**Moustakas et al., 2010). Since the NS method has been calibrated against HII regions, we restrict our abundance analysis to fibers in the NGC0628 data-cube that have $f(H\alpha) > 10 \times f_{0,DIG}$, so we ensure that at least 90% of the nebular emission is coming from HII regions. Figure 4.23 shows a map of the oxygen abundance in the widely used units of 12+log(O/H) for these regions. Overlaid are contours of constant galactocentric radii at steps of $0.1R_{25}$. At first sight it would seem as the oxigen abundance follows closely the Hα flux. We warn the reader that this is mostly an artifact of our plotting technique for 2D maps, since non HII region dominated fibers are flagged using a negative value, and the plotting techinque interpolates the fiber values in the space between them, producing a fake gradient at the edge of the regions under consideration. The reader should focus only on the color of the map right under the black dots, which correspond to the actual values measured for the fibers.

Figure 4.24 presents the radial distribution of the nebular oxygen abundance for all HII region dominated fibers. The scatter at any given radii is fully consistent with the 0.08 dex scatter in the NS method calibration, which dominates over mesurement uncertainties given the high S/N of the VENGA spectra in these bright regions. To first order, there is an obvious gradient in the oxygen abundance. A linear fit to the data yields a central abundance $12+\log(O/H)_{r=0}=8.66 \pm 0.01$ and an abundance gradient $\Delta\log(O/H) = -0.25 \pm 0.04$ R_{25}^{-1} (blue line in Figure 4.24). This is shallower than the gradient of -0.38 ± 0.02 R_{25}^{-1} measured by Rosales-Ortega et al. (2011)

using integral field spectroscopic data of similar quality (shown as the dashed line in Figure 4.24), but in excellent agreement with the results of Moustakas et al. (2010), who measured a gradient of -0.27 ± 0.05 R_{25}^{-1} using a large compilation of HII region slit spectra across the galaxy. It is important to note that the values that we are comparing from these two works were calculating using empirically calibrated strong-line methods from the same authors as the one used here, and therefore the comparison is consitent in terms of methodology.

Our observations confirm the flattening in the oxygen abundance gradient reported by Rosales-Ortega et al. (2011) at $r < 0.2R_{25}$. Fitting the radial abundance distribution with a broken power-law, with four free-parameters (the break radius, the abundance at the break radius, and the inner and outer gradients) we find a transition radius of 0.16 ± 0.03 R_{25}, an abundance at the transition radius of $12+\log(\mathrm{O/H})_{r=0.16R_{25}} = 8.65 \pm 0.01$, and an inner and outer gradients of 0.56 ± 0.29 R_{25}^{-1} and -0.44 ± 0.10 R_{25}^{-1} respectively (red solid line in Figure 4.24). It is important to stress that both the single power-law and the broken power-law fits are statistically consistent with the data (i.e. have similar reduced χ^2 values).

4.6.4 The impact of Metallicity in the Star Formation Efficiency

A series of studies (e.g. Kennicutt, 1998b; Kennicutt et al., 2007; Bigiel et al., 2008; Blanc et al., 2009), have established that the availability of molecular gas is the main variable setting the SFR. But these studies also find a very large scatter in the star formation efficiency (SFE), or equivalently

in the gas depletion timescales for regions having similar molecular gas densities. This is indicative of the existence of second order parameters which can influence the SFR beyond the mere presence of molecular gas. Possibilities include metallicity, local gas dynamics, galactic scale dynamics and shear, internal feedback processes in GMCs, etc.

In this section we briefly invistigate the relation between the metallicity and the SFE across the disk of NGC0628. The oxygen abundance gradient found in the previous section, allows us to study the process of star formation in a range of environments showing a range of ~ 0.4 dex in relative metallicity. This is not a very wide range, and this type of study will benefit greatly of the full VENGA sample once it is processed.

We have computed the SFR surface density from the dust corrected Hα emission line flux, and the molecular gas surface density from the BIMA SONG CO J=1-0 map of NGC 0628 (Helfer et al., 2003), following the same procedures presented in Blanc et al. (2009). The SFE is taken to be the ratio between the SFR and H_2 surface densities, or equivalently, the inverse of the molecular gas depletion timescale. Figure 4.25 presents the SFE as a function of oxygen nebular abundance for a subset of the HII-region dominated fibers used in the last section, which also have significant measurements ($> 1\sigma$) of the molecular gas surface density. There seems to be some level of correlation between the SFE and the metallicity, with more enriched regions showing higher efficiencies. The Pearson correlation coefficient between the two variables is $r_P = 0.48$, and there is significant scatter in the correlation, with

regions of similar metallicity showing efficiencies that differ by up to factors of 10.

Rotational line emission from CO, as well as dust thermal emission are thought to be the main coolants in GMCs and cores within GMCs (Spaans & Meijerink, 2005; Tielens, 2005). Therefore, the sense of the observed correlation agrees with an scenario in which a higher oxygen abundance can translate into a higher abundance of molecular coolants and dust grains in GMCs, which at the same time could have a positive effect in the efficiency of star formation. On the other hand, the observed trend goes against the recently proposed theoretical model of Dib et al. (2011). This model is based on the fact that lower metallicity stars have weaker stellar winds than higher metallicty stars. Therefore, lower metallicities translate into a reduced level of stellar feedback, which translates into a higher star formation efficiency. A third phenomenon which could affect the relation between SFE and metallicity, is dust shielding, and its effect on the timescales for ambipolar diffusion. If magnetic fields are important at regulating the rate of gas collapse inside GMCs, then a higher dust optical depth (expected in higher metallicity regions) can translate into a lower abundance of ionized species in the gas, which should decrease the ambipolar diffusion timescale, therefore reducing the level of support provided by magnetic fields, and increasing the star formation efficiency. Furthermore, these same differences in oxygen and carbon abundances, and the dust optical depth in different regions, can have an impact on the CO to H_2 conversion factor (e.g. Leroy et al., 2011), which can introduce an observational bias in

the measurement of the SFE.

It is evident that the issue is non-trivial, and most likely coupled to a series of different physical processes. The observed correlation is a new observation, and further work is required to establish its validity, including looking for its presence in other galaxies in the sample. This will be the focus of a future publication. In the meantime, we stress the power of IFU observations, which allow us to correlate all these important quantities across the different environments present in star forming galaxies in an unprecedented manner.

4.7 Summary and Conclusions

In this work, we have presented the survey design, sample, and observing strategy for VENGA. Wide field integral field spectroscopy proves to be a powerful tool to study a large set of physical phenomena occuring in galaxies, which are associated with the formation and evolution of these objects. We charactherized our sample of disk galaxies in terms of their stellar masses and SFRs, and have shown that VENGA is a representative sample of massive ($> 10^{10}$ $M_{\odot}$) spiral galaxies in the local universe. A large range of morphological parameters (bulge-to-disk ratio, bar presence, bulge sersic index) is represented in the sample, and a typical spatial resolution in physical units of 300 pc is achived with VIRUS-P at the distances of the objects.

The wealth of information produced by integral integral field spectrographs, stresses the need of optimized and pipelined software tools for process-

ing and analysing the data. This becomes essential when this observational techinique is used to conduct large surveys like the one presented here. We have presented the reduction, and calibration pipeline used for the VENGA data. We also have described our spectral analysis pipeline, which we use to extract stellar and gas kinematics, as well as emission line fluxes. When possible, we have adapted existing publicly available software to be used on the VIRUS-P data. We assessed the quality of the data obtained on NGC0628, and we find it to be excellent. VIRUS-P provides high S/N spectra for single fibers out to large galactocentric radii. Thanks to the ability of reconstructing broad-band images from the IFU data, and crosscorrelating them with archival broad-band images of the galaxies, we can achieve good astrometric precision and a reliable flux calibration.

Using the red-setup VENGA data on NGC0628 we have discovered a previously undetected low luminosity AGN in the center of this galaxy. Our results confirm the suspected AGN nature of a very low luminosity X-ray source previously detected with *Chandra* in the center of this galaxy. We have also used the VENGA data, together with the methods presented in Blanc et al. (2008) to measure and separate the contribution to the SFR surface density coming from diffuse ionized extraplanar gas in front of the galaxy. An obvious bimodality in the [SII]/Hα emission line ratio between HII regions and the DIG is detected, and it is similar to the one observed in the Milky Way. We find that over the regions sampled by the VENGA data, the DIG contributes 20% of the total Hα luminosity.

The oxygen abundance of bright star forming regions in NGC0628 was measured using the empirical strong-line method of Pilyugin & Mattsson (2011). We find a clear radial gradient in the gas phase metallicity which is roughly consistent with previous measurements. Integral field spectroscopy allows us to detect details in the structure of the abundance distribution which were not evident in studies based on single or multi-slit HII region spectroscopy. We confirm the flattening of the abundance gradient in the inner part ($< R_{25}$) recently observed with PPAK by Rosales-Ortega et al. (2011). Finally, we have found a correlation between the oxygen aundance of star forming regions and their star formation efficiency. This type of correlation is expected if higher metallicities induce a higher molecular and thermal emission dust cooling rate, or if higher dust column densities reduce the ion abundance inside GMCs, speeding up the ambipolar diffusion process in magnetically suported cores.

The main purpose of this work is to present the VENGA survey, and some preliminary scientific results have been discussed only briefly. We expect to use the VENGA sample to follow-up the subjects presented here, among others, in a series of future publications. Once observations are finished, and all the VENGA data is processed, we expect to make it publicly available to the comunity. The richness of large IFU datasets like the one we are compiling, goes beyond the scientific goals of our team. We expect VENGA to be a useful resource that will complement the wealth of multi-wavelength datasets astronomers have acquired on nearby spiral galaxies over the last few decades.

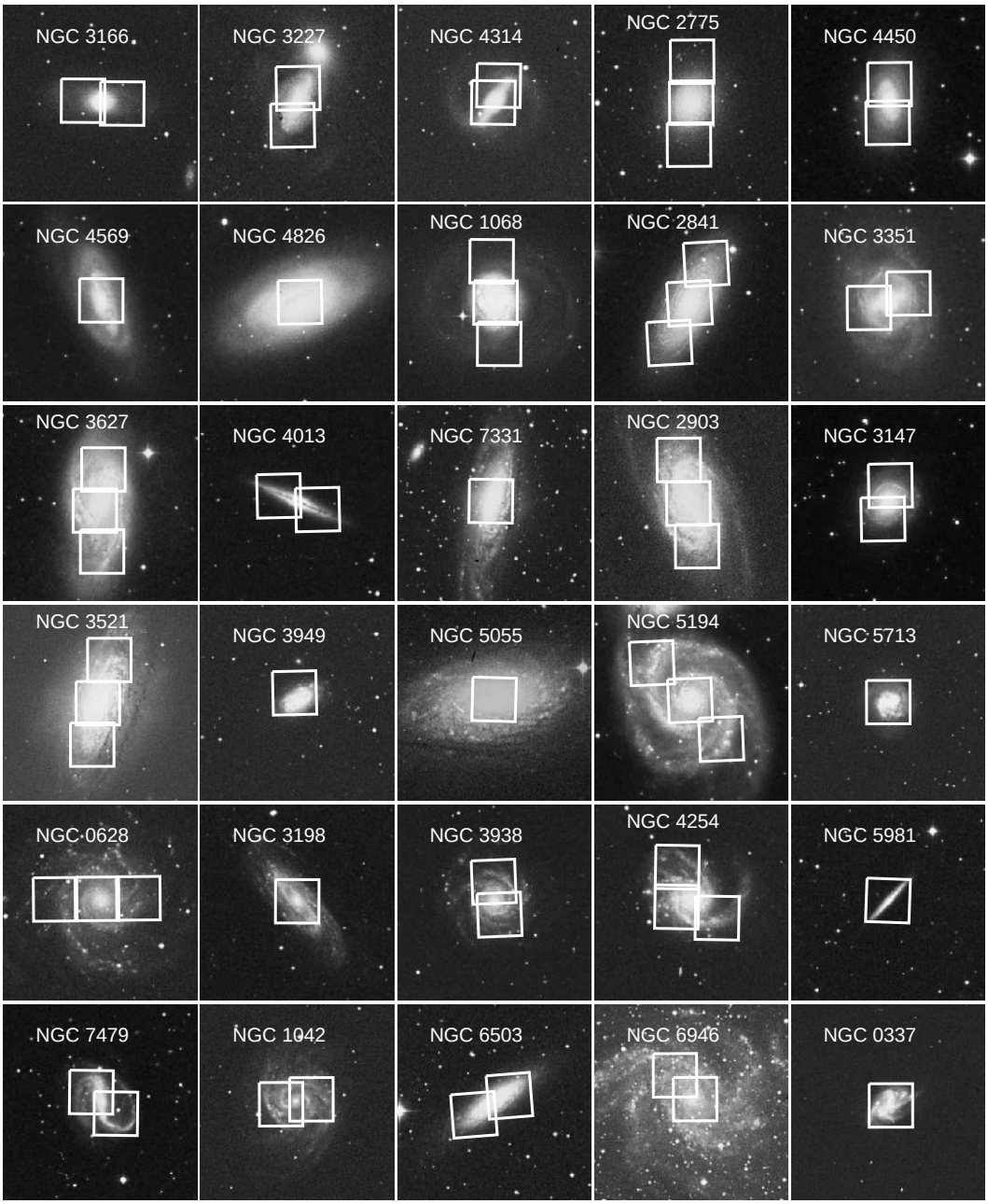

Figure 4.1 Digital Sky Survey cutouts of the 30 galaxies in the VENGA sample. The targets are oredered by Hubble type from earlier to later. White boxes show the VIRUS-P $1.7' \times 1.7'$ pointings obtained on each galaxy.

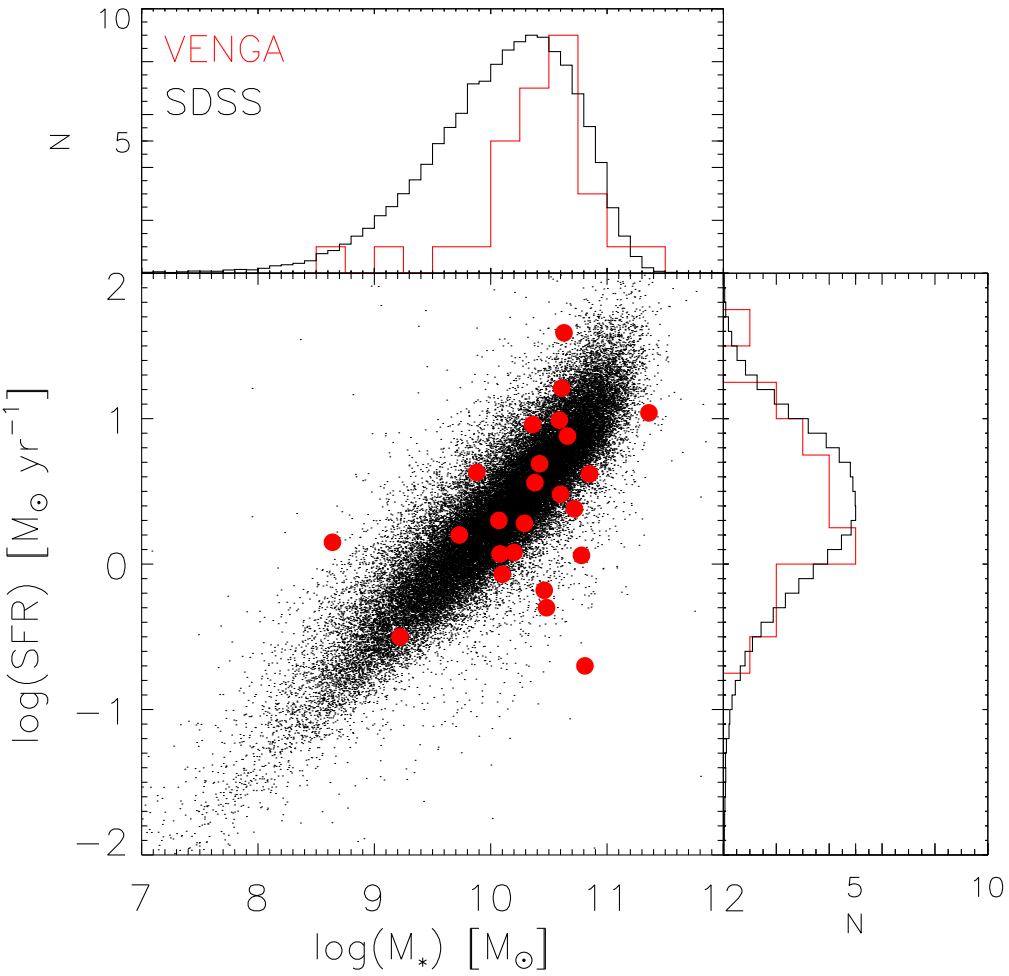

Figure 4.2 Stellar mass versus star formation rate for the VENGA galaxies with SFR measurements in Table 4.3 (red circles), and star forming galaxies in the SDSS MPA/JHU catalog (black dots). The red and black histograms show the distributions for the VENGA and SDSS galaxies respectively. The stellar mass histogram includes the VENGA targets without SFR measurements.

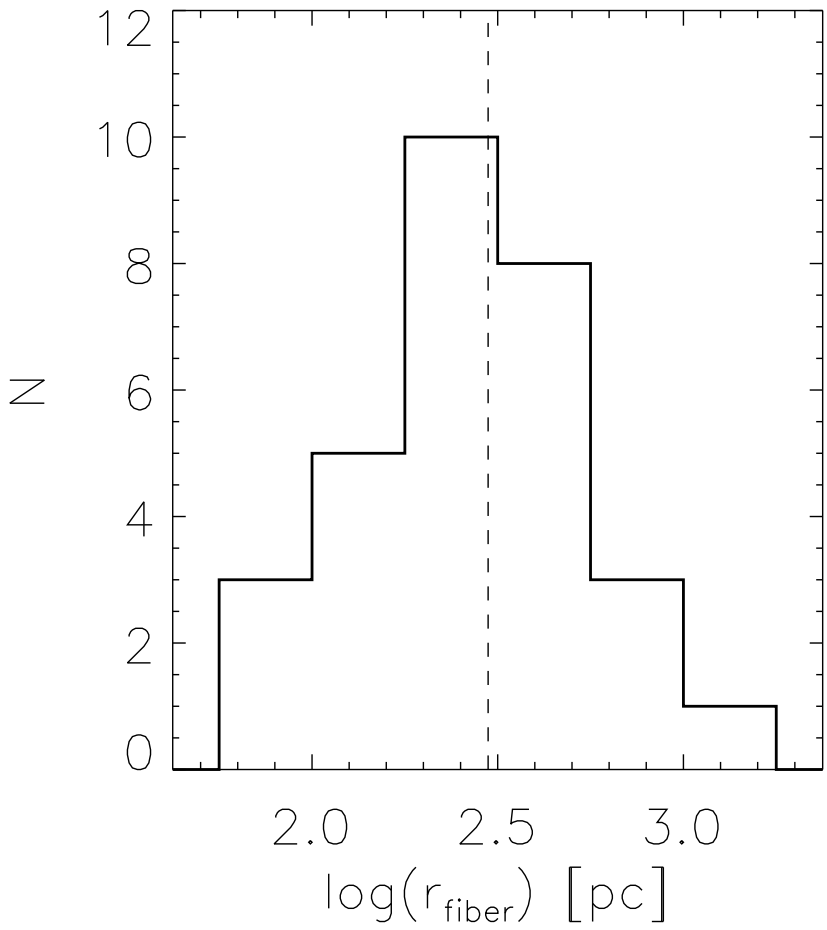

Figure 4.3 Histogram of the logarithm of the VIRUS-P 4.235″ fiber size in physical units (parsecs) for each galaxy in the VENGA sample, given the distances adopted in Table 4.1. The vertical dashed line marks the median spatial resolution of 300 pc.

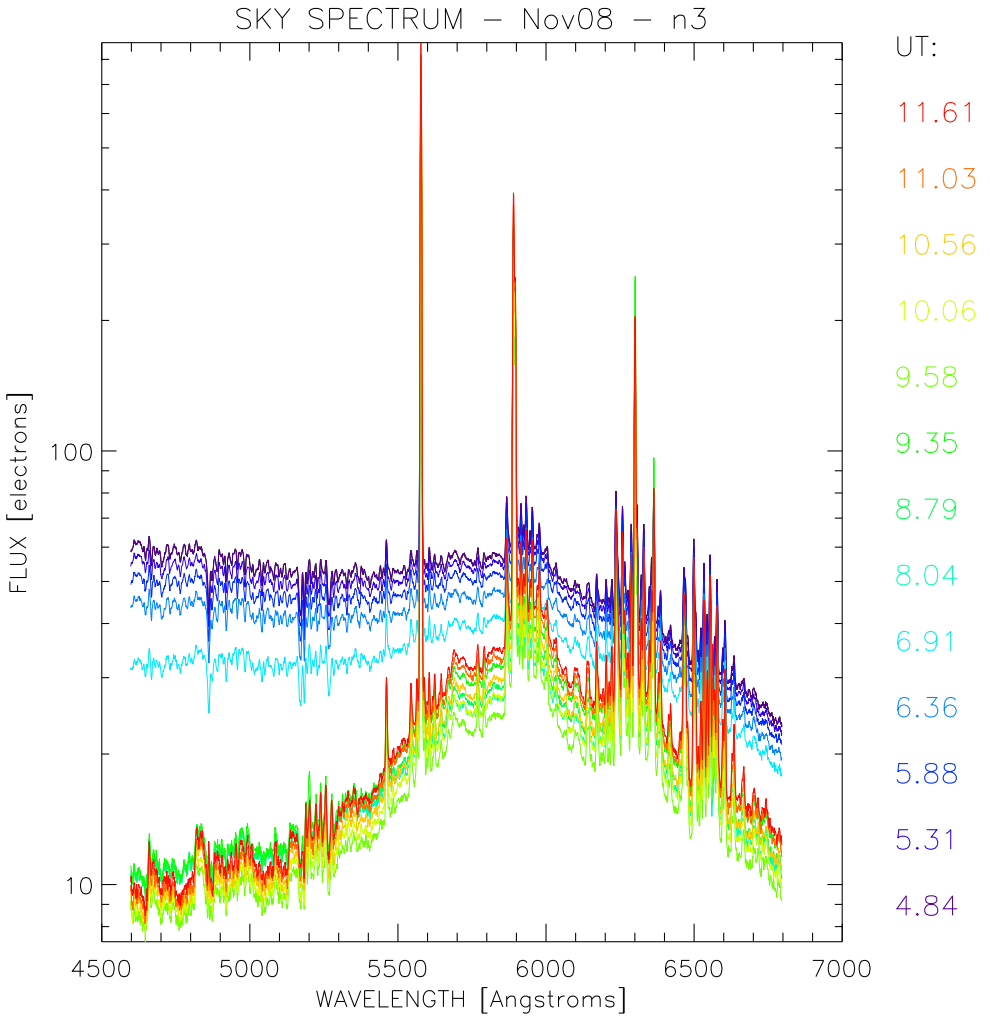

Figure 4.4 Sky spectrum in raw units (before flux calibration) at different UT times (color coded) during the night of November 7th 2008.

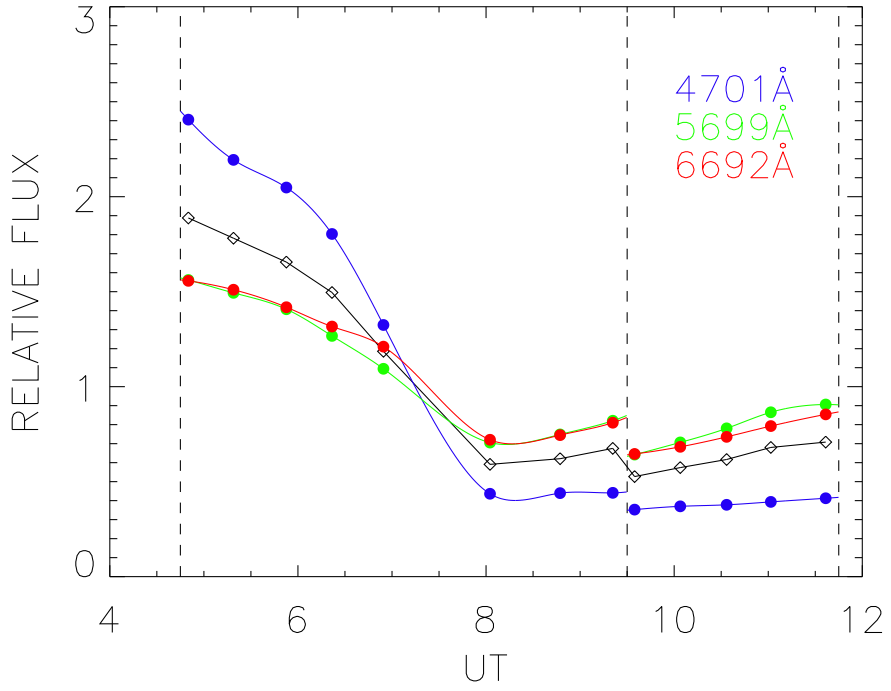

Figure 4.5 Relative sky brightness as a function of UT time for the same night shown in Figure 4.4, at three different wavelength (blue, green, and red). Filled circles correspond to measurements of the sky brightness from the off-source background frames. The beginning and end of observations of the same target are shown as vertical dashed lines. Solid color curves show cubic spline fits to the sky brightness. The black open diamonds and black solid curve show the relative sky brightness averaged over the full spectrum.

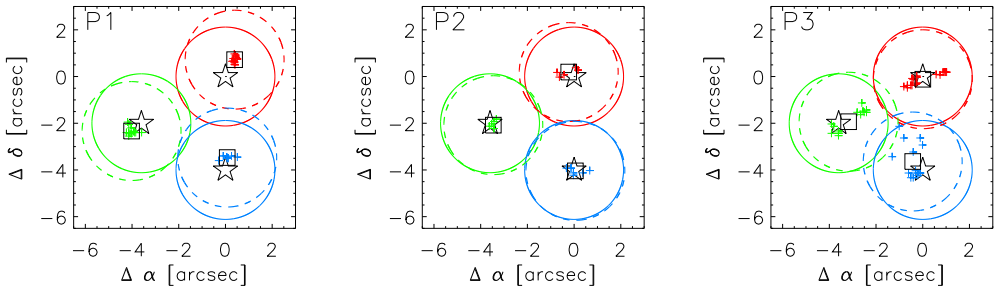

Figure 4.6 Attempted and actual relative positions of the three sets of dithered exposures for the three pointings obtained on NGC0628. Stars and solid circles mark the attempted fiducial positions for dithers 1, 2, and 3 (red, green, and blue respectively). Crosses mark the actual position at which each exposure was obtained. The open squares and dashed color circles show the average fiber position of the actual observations.

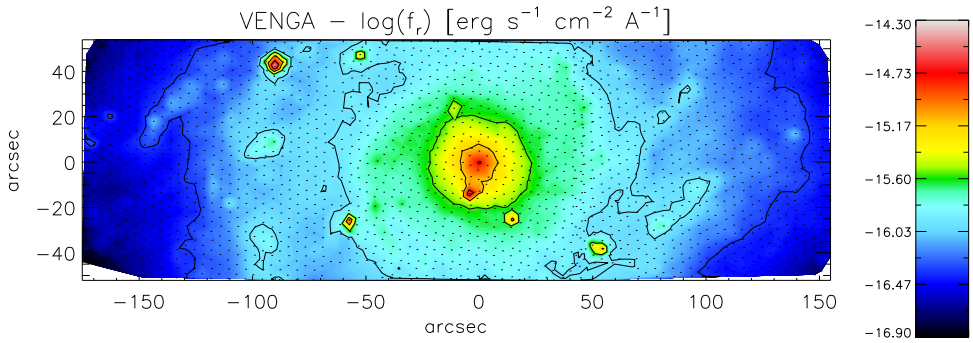

Figure 4.7 Map of the r-band flux reconstructed from the VENGA spectral data-cube of NGC0628. Black contours mark steps in surface brightness of 1 magnitude. Black dots mark the position of each fiber. This and all maps presented in this work where constructed using the PLOT_VELFIELD IDL routine written by Michele Cappellari (http://www-astro.physics.ox.ac.uk/ mxc/idl/), and correspond to linearly interpolated maps based on the discrete values at the position of each fiber.

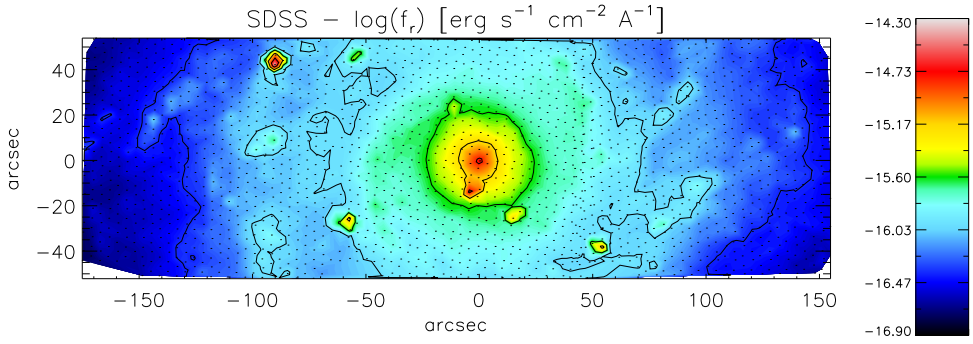

Figure 4.8 Map of the r-band flux after doing aperture photometry matching the VIRUS-P fiber size in the SDSS mosaic image of NGC0628. Black contours mark steps in surface brightness of 1 magnitude.

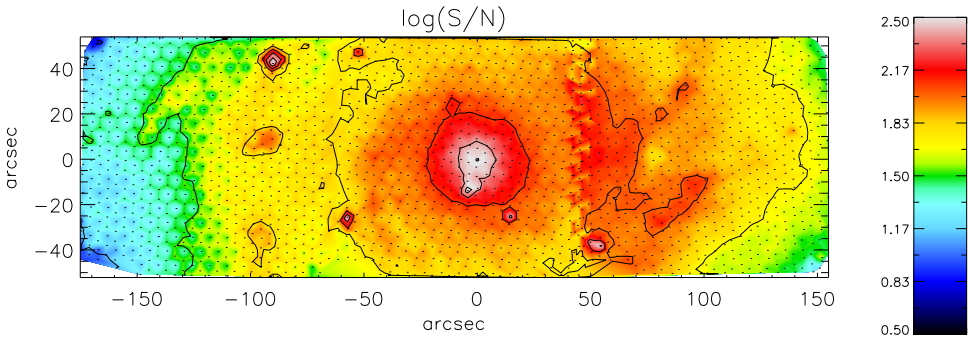

Figure 4.9 Map of the signal-to-noise ratio per spectral resolution element in continuum of the VENGA NGC0628 data-cube. Contours are the same as in Figure 4.7.

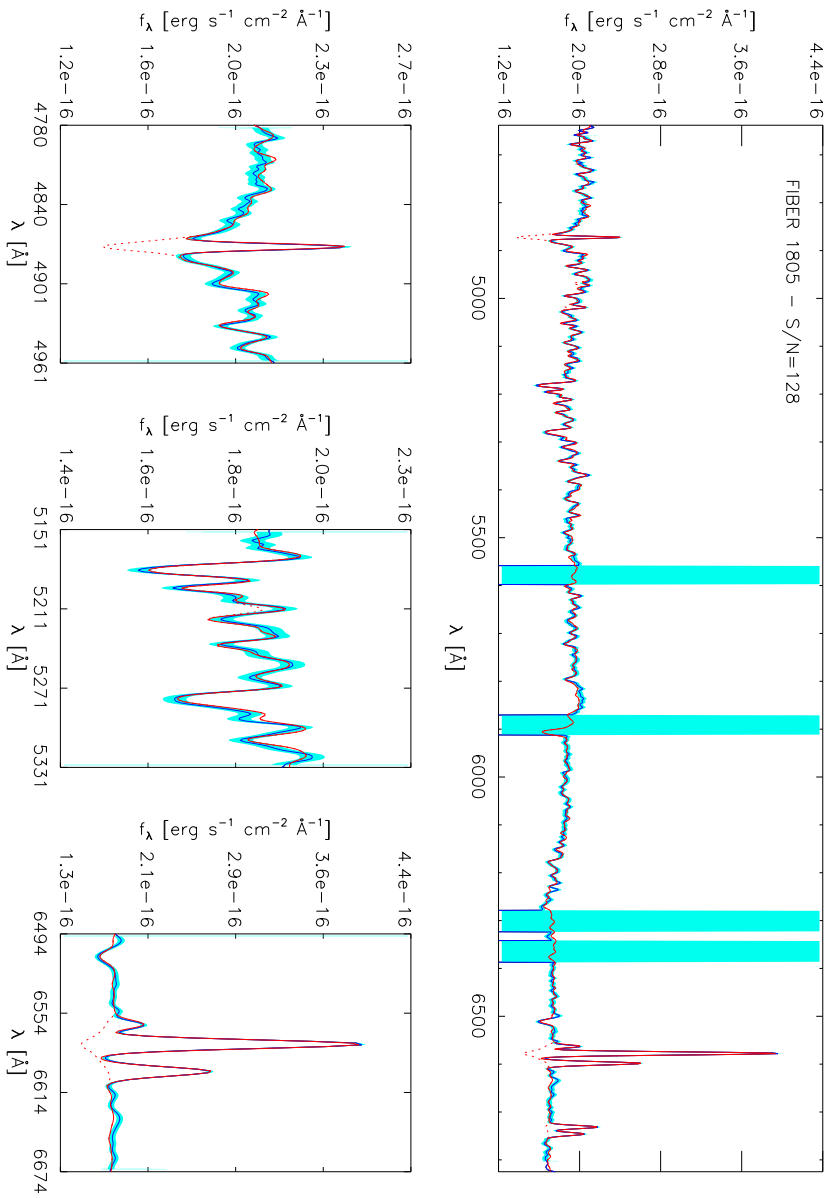

Figure 4.10 *Top panel:* Spectrum of fiber 1805 (S/N=128) in the VENGA data-cube of NGC0628. The observed spectrum is shown in blue with 1σ uncertainties marked by the cyan envelope. The solid red line shows the best-fit stellar plus emission line spectrum, while the dotted red line shows the stellar component of the fit without the emission lines. The four vertical cyan bands represent regions masked around sky line residuals. *Bottom Panels:* Zoomed in regions around Hβ, Mgb, and Hα (left to right).

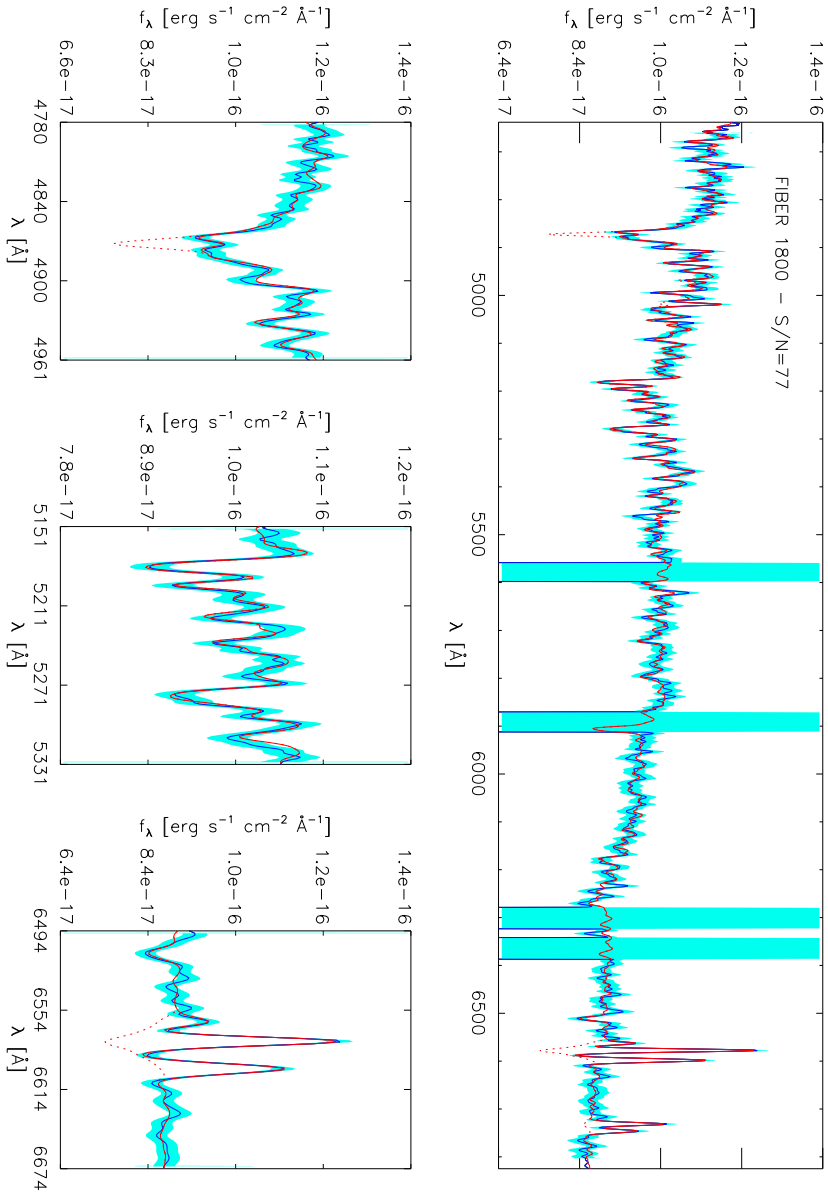

Figure 4.11 Same as Figure 4.10 for fiber 1800 (S/N=77).

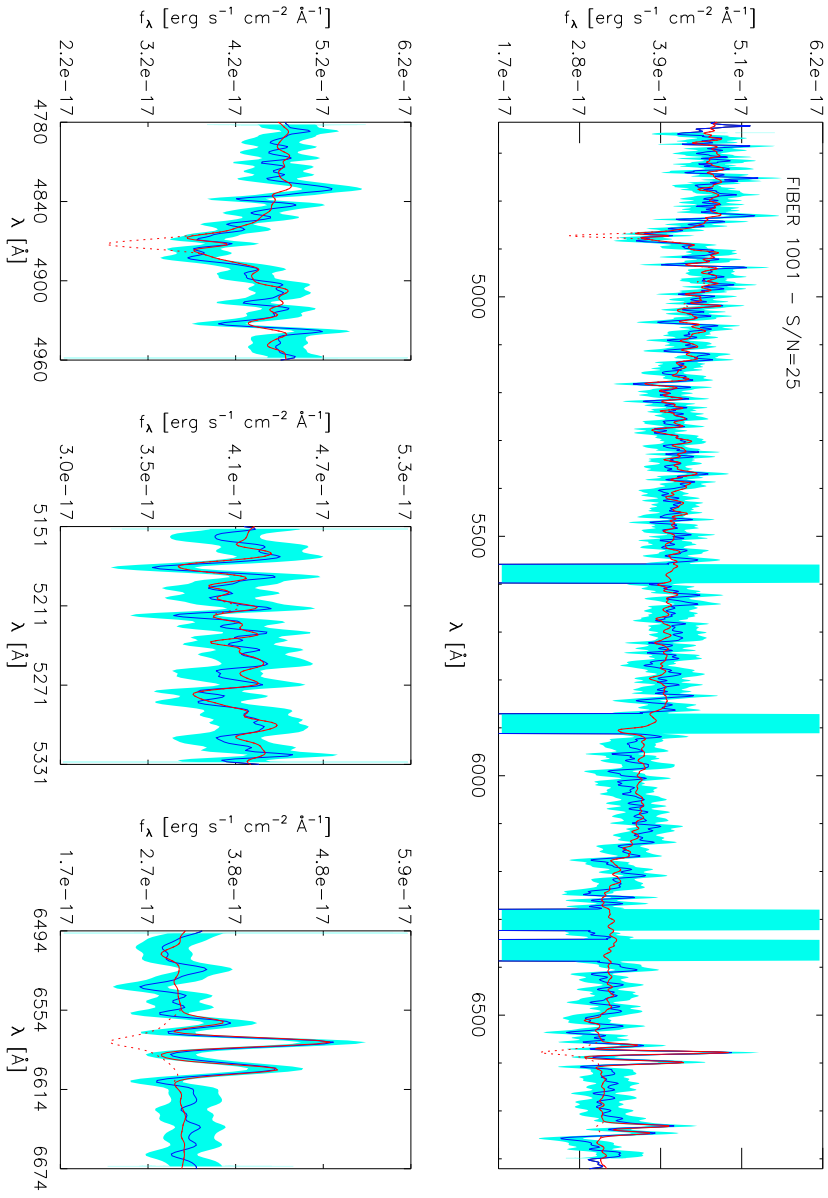

Figure 4.12 Same as Figure 4.10 for fiber 1001 (S/N=25).

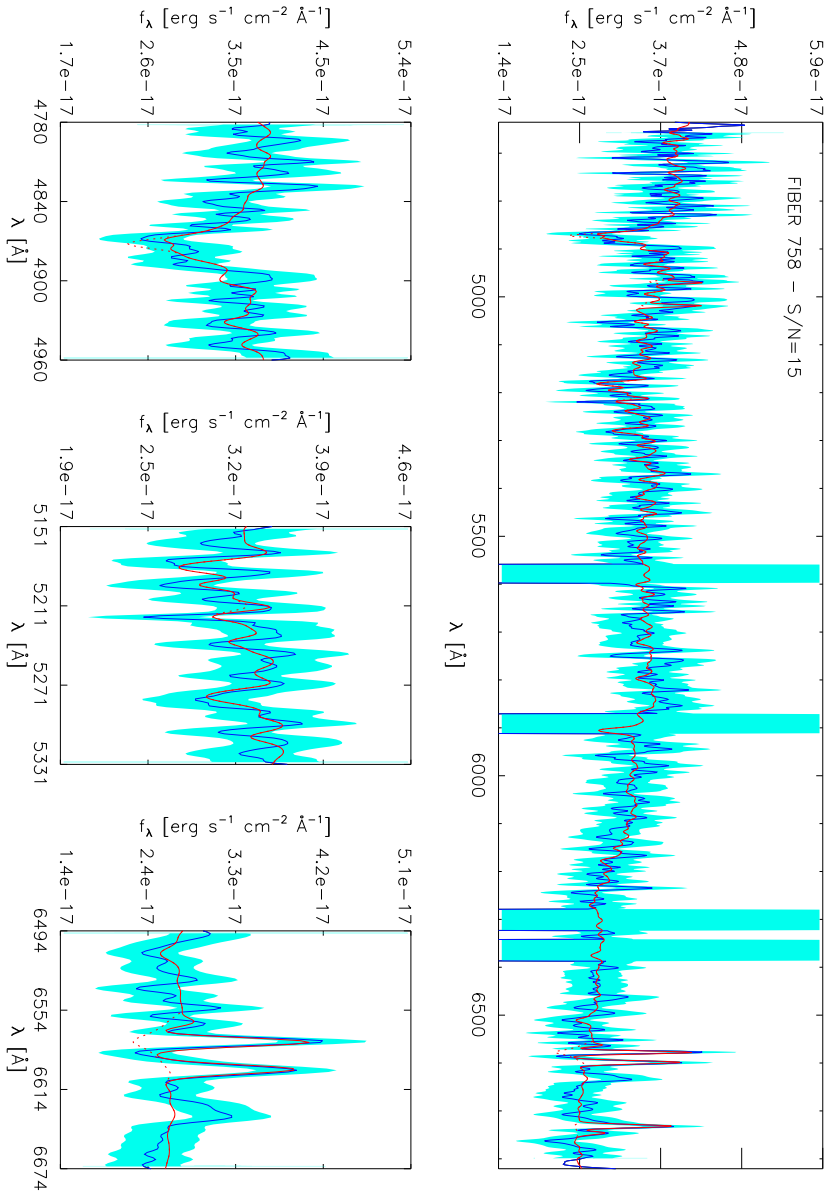

Figure 4.13 Same as Figure 4.10 for fiber 758 (S/N=15).

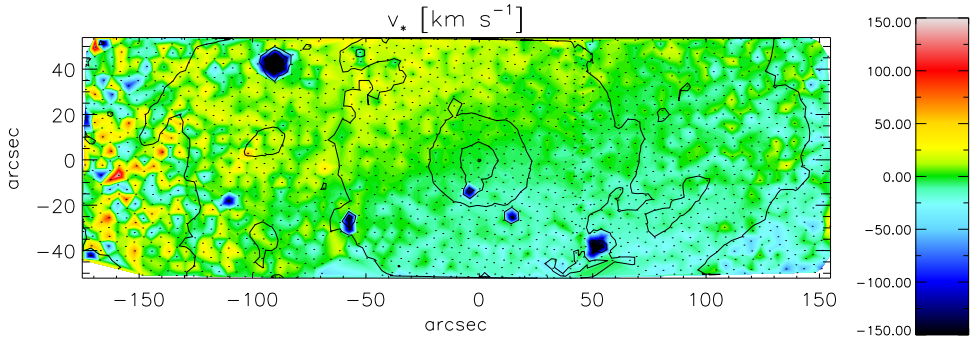

Figure 4.14 Stellar velocity field in NGC0628. Contours are the same as in Figure 4.7.

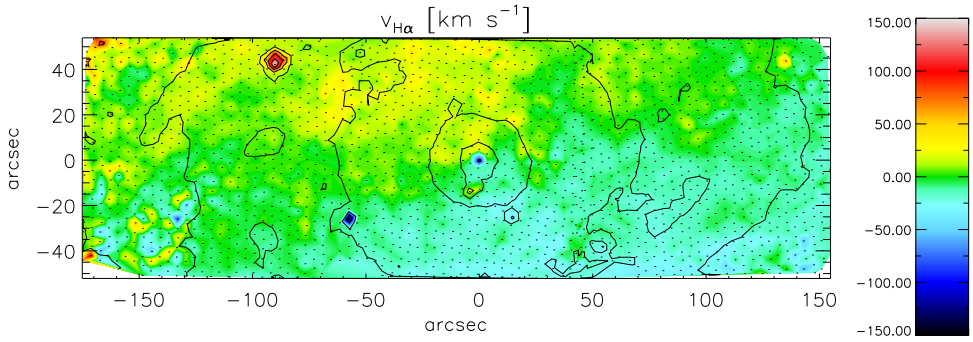

Figure 4.15 Ionized gas velocity field in NGC0628. Contours are the same as in Figure 4.7.

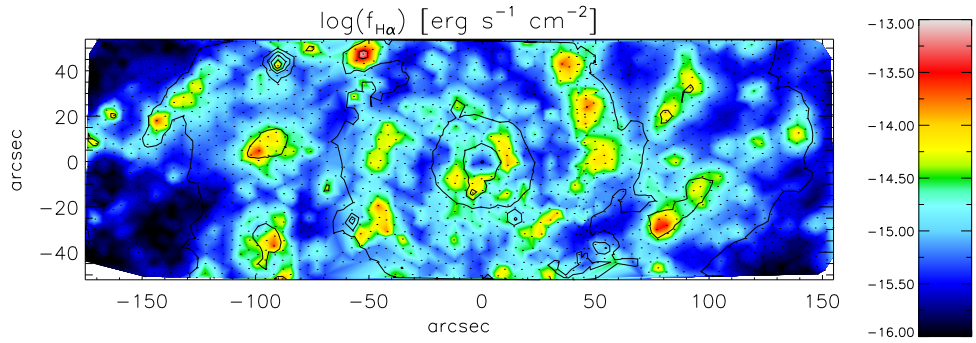

Figure 4.16 Map of the Hα emission line flux in NGC0628. Contours are the same as in Figure 4.7.

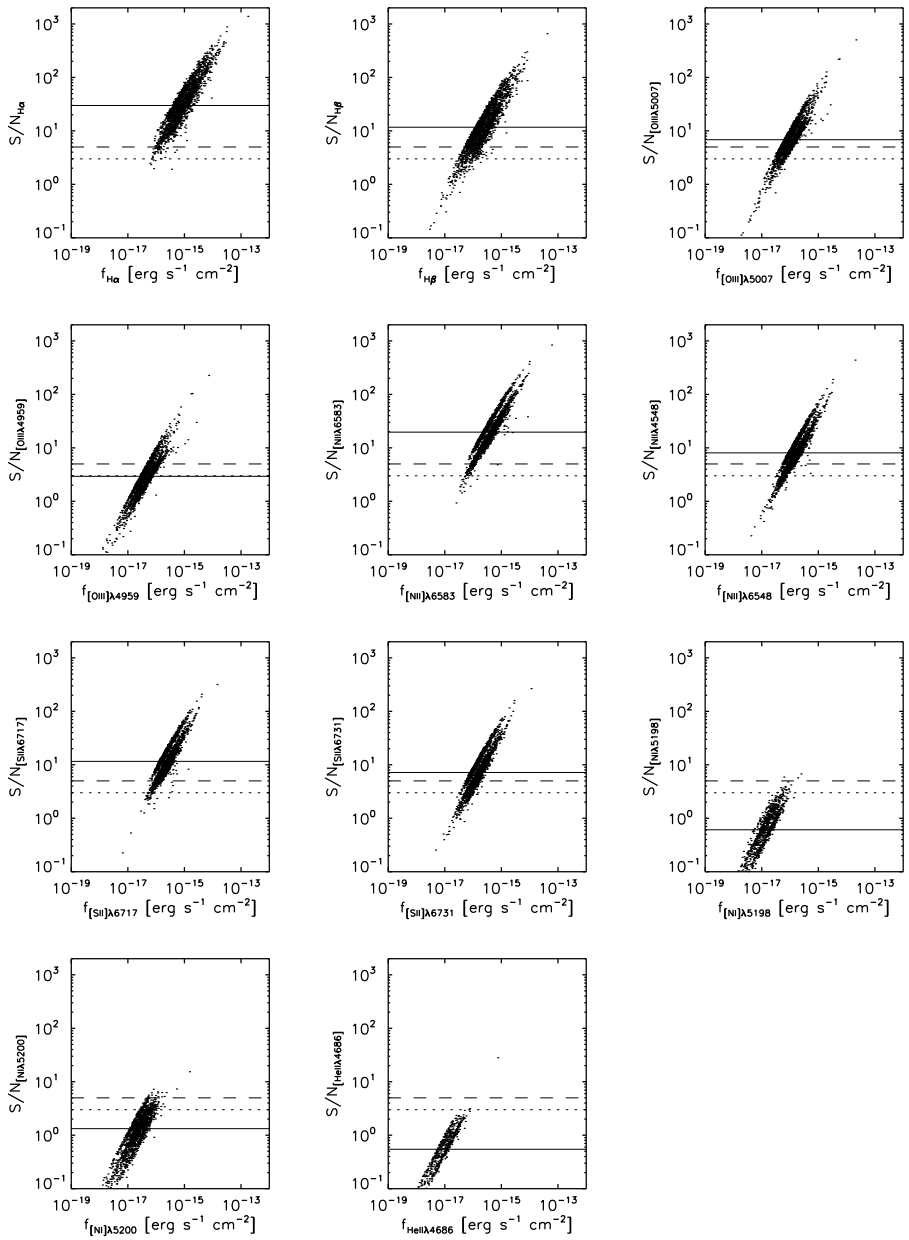

Figure 4.17 Signal-to-noise ratio as a function line flux for all transitions in Table 4.6. Each dot corresponds to an individual fiber in the NGC0628 datacube. The horizontal solid, dashed, and dotted lines mark the median S/N, and the 5σ and 3σ detection limits respectively.

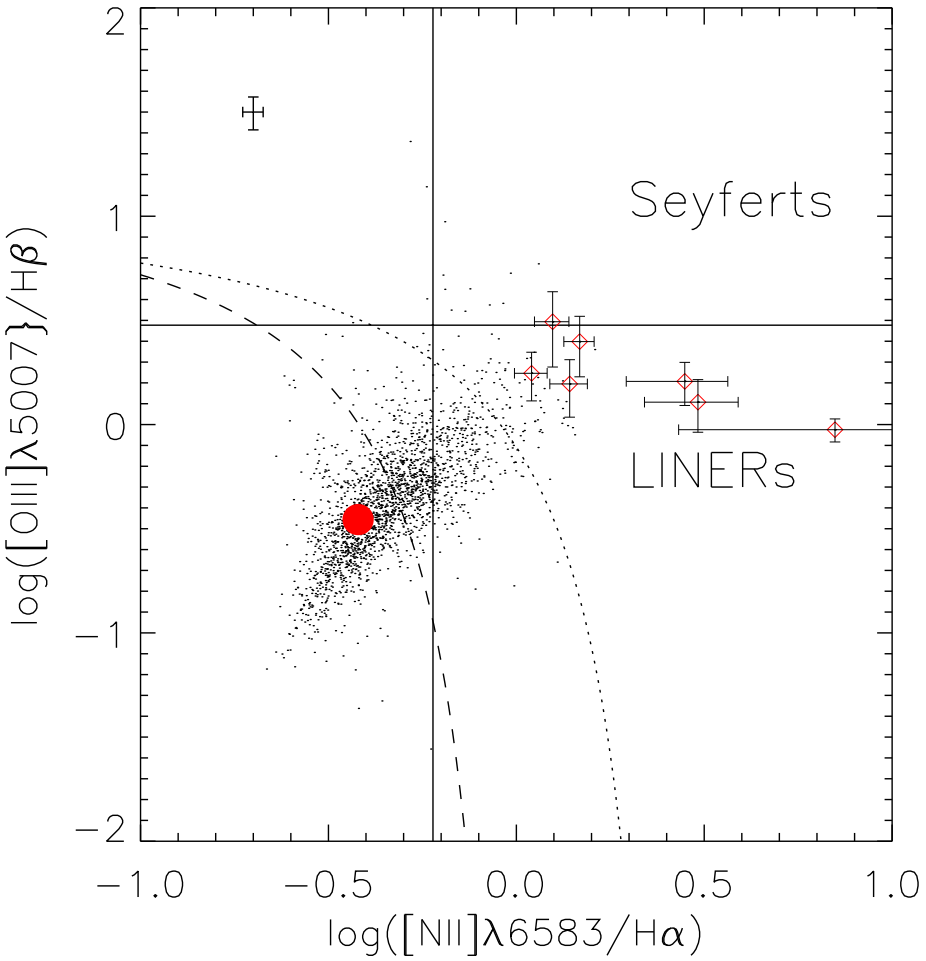

Figure 4.18 Diagnostic [NII]/Hα vs [OIII]/Hα BPT diagram. The dust-corrected line ratios for each fiber are shown as blakc dots. Median errorbars for these line ratios are shown on the upper left corner of the diagram. The filled red circle shows the integrated flux ratio across the whole data-cube. Dashed and dotted curves show the AGN/star-formatioon selection criteria of Kewley et al. (2001) and Kauffmann et al. (2003) respectively. Open red diamonds with The horizontal and vertical lines show divide the right part of the diagram in regions typically populated by Seyfert galaxies (top) and LINERS (bottom). Regions above both AGN selection criteria and laying at less than 500 pc from the center of the galaxy are shown as open red diamonds with error-bars.

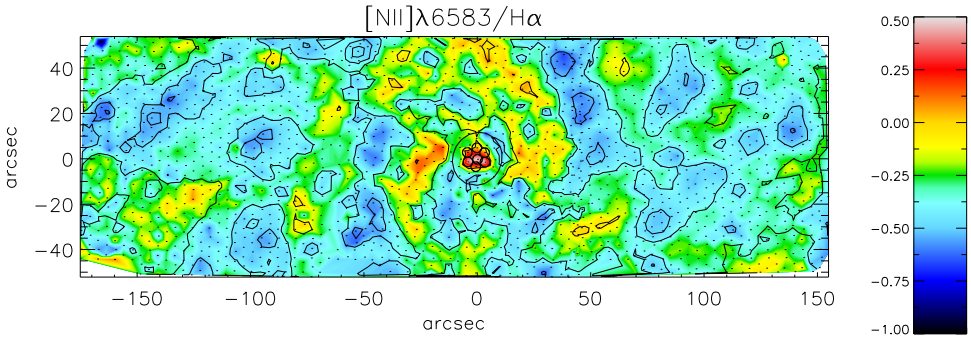

Figure 4.19 Map of the [NII]/Hα ratio across NGC0628. Black contours show Hα flux. Fibers classified as AGN dominated are marked in the central part of teh galaxy. The thick oval contour marks a galactocentric radius of 500 pc.

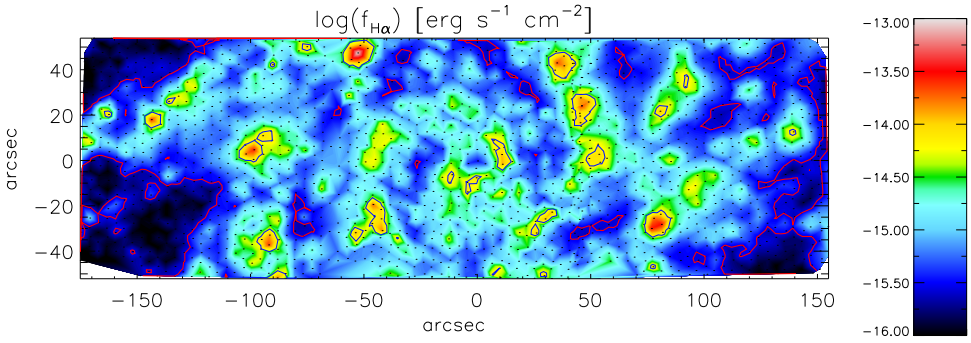

Figure 4.20 NGC0628 map of the Hα emission line flux, overlaid with contours surrounding pure DIG regions (red) and pure HII regions (blue).

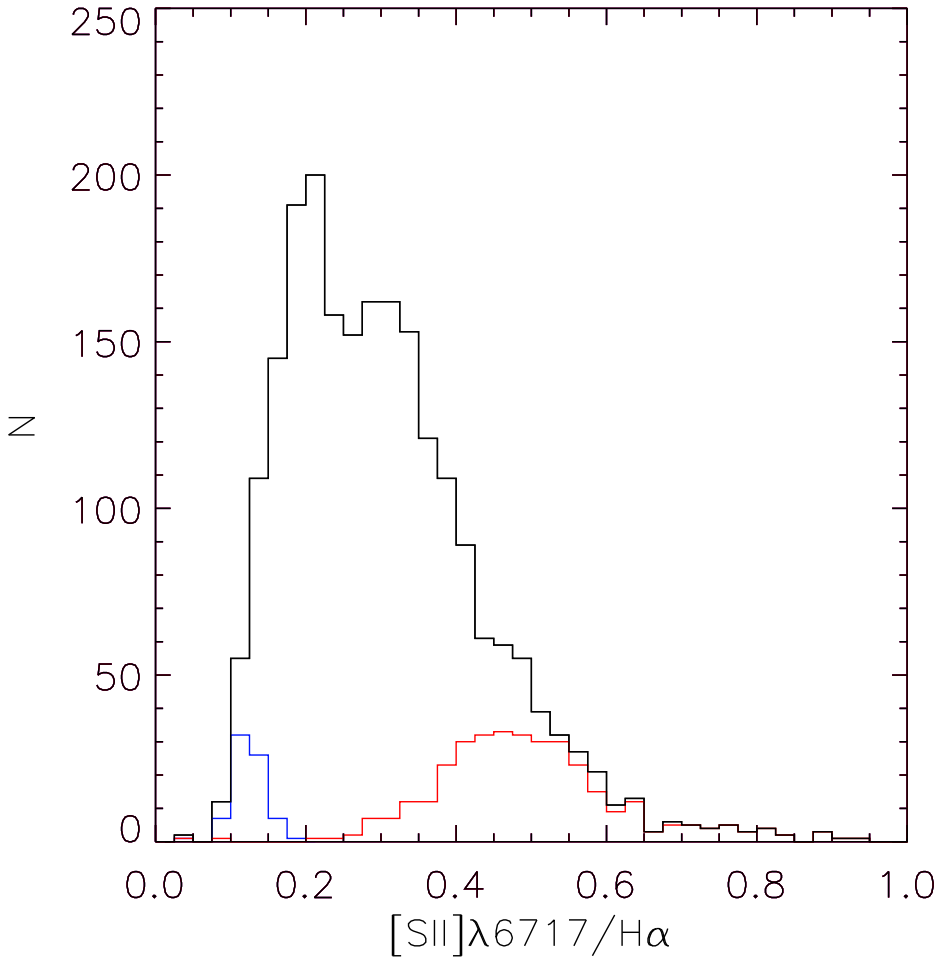

Figure 4.21 Histogram of the [SII]/Hα emission line ratio for all fibers (black), HII region dominated fibers (blue), and DIG dominated fibers (red).

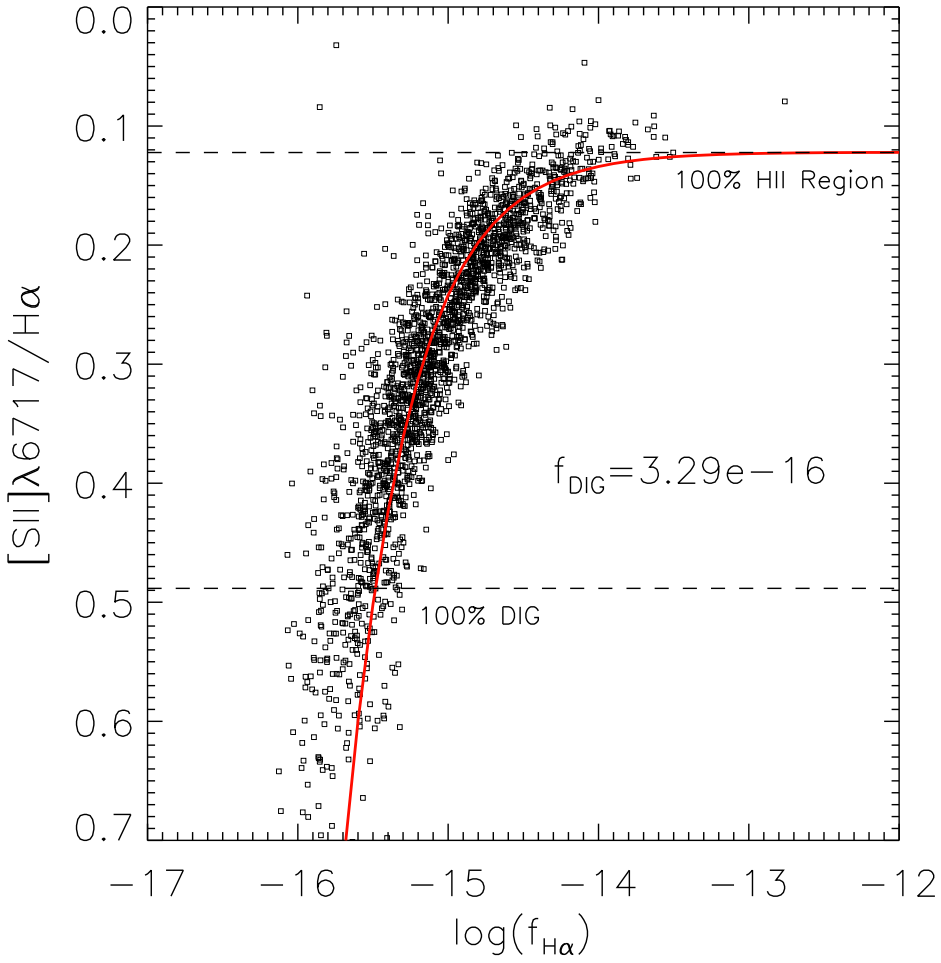

Figure 4.22 [SII]/Hα emission line ratio as a function of Hα flux. Horizontal dashed lines show the fiducial values adopted for HII regions and the DIG. The best fit given by Equation 4.4 is shown as the solid red line.

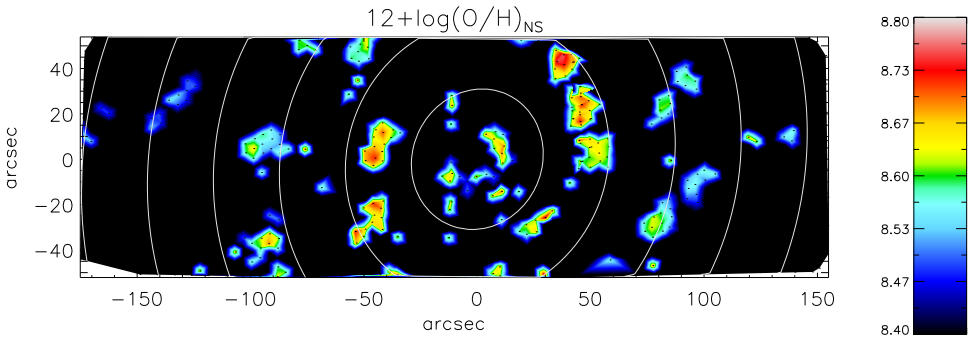

Figure 4.23 Map of the nebular oxygen abundance computed using the NS method, for HII region dominated fibers. White contours mark constant galactocentric radii in steps of 0.1 R_{25}.

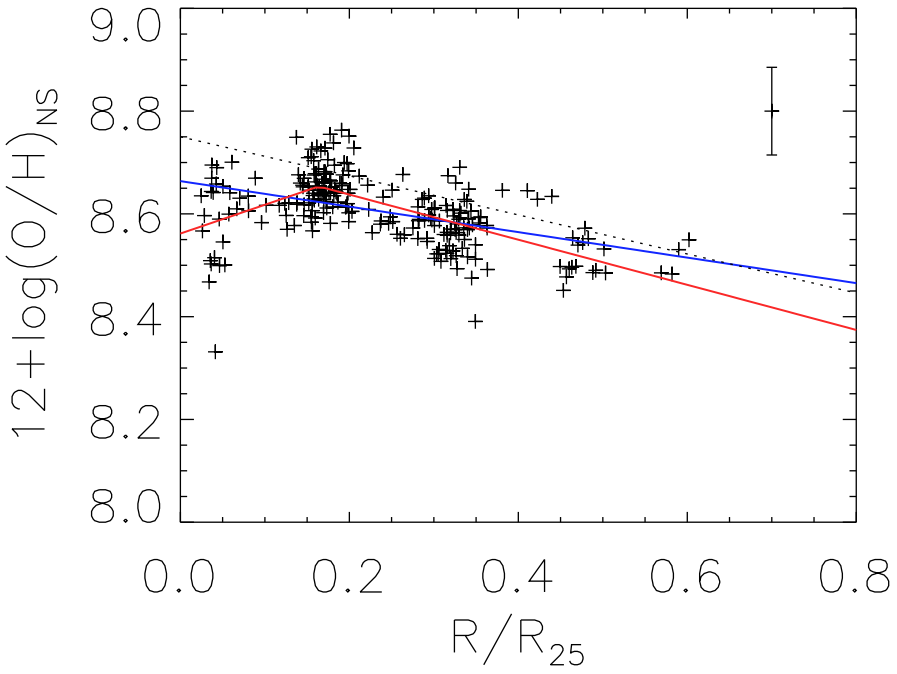

Figure 4.24 Oxygen nebular abundance as a function of isophotal radius for HII region dominated fibers in NGC0628. Best single and broken power-law fits are shown in blue and red respectively. The measurement of Rosales-Ortega et al. (2011) is shown as the black dashed line.

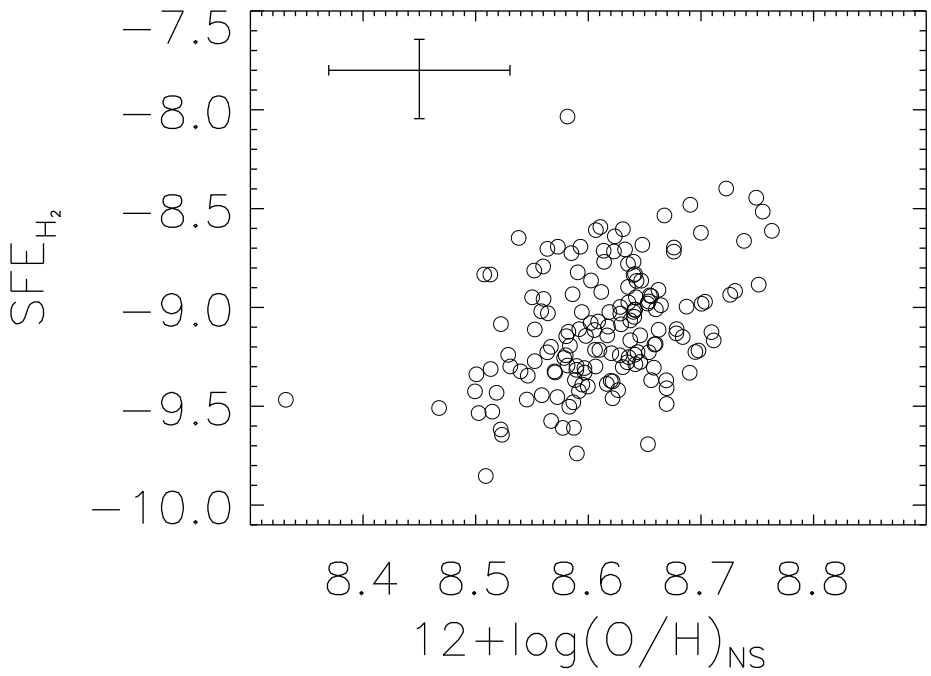

Figure 4.25 Star formation efficiency as a function of oxygen nebular abundance for HII region dominated fibers having significant measurements of Σ_{H_2}.

Table 4.1. The VENGA Sample

Object	Equatorial Coord.		Type	i	θ	d_{25}	D	Method[c]	pc/"	M_K	μ_B	N_P
	α	δ		deg	deg	arcmin	Mpc			mag	mag arcsec^{-2}	
NGC0337	00:59:50.0	-07:34:41	SB(s)d	52	130	2.9×1.8	19.5 ± 1.5	TF	95	-22.35 ± 0.18	21.54	1
NGC0628	01:36:41.7	15:47:00	SA(s)c	25	25	10.5×9.5	8.6 ± 0.3	PNLF	42	-22.83 ± 0.09	22.56	3
NGC1042	02:40:24.0	-08:26:02	SAB(rs)cd	40	6[b]	4.7×3.6	4.2 ± 0.7	TF	20	-19.27 ± 0.36	23.27	2
NGC1068	02:42:40.2	-00:00:48	SA(rs)b	32	70	7.1×6.0	10.1 ± 1.7	TF	49	-24.23 ± 0.36	19.54	3
NGC2775	09:10:20.1	07:02:17	SA(r)ab	40	155	4.3×3.3	21.5 ± 1.5	Flow	104	-24.60 ± 0.15	20.94	3
NGC2841	09:22:01.8	50:58:31	SA(r)b	67	147	8.1×3.5	14.1 ± 1.5	Ceph	68	-24.69 ± 0.23	21.43	3
NGC2903	09:32:09.7	21:30:02	SB(s)d	64	17	12.6×6.0	8.6 ± 1.4	TF	41	-23.62 ± 0.35	21.31	3
NGC3147	10:16:53.2	73:24:04	SA(rs)bc	28	155	3.9×3.5	43.1 ± 3.0	Flow	209	-25.76 ± 0.15	21.16	2
NGC3166	10:13:45.0	03:25:31	SAB(rs)0	63	87	4.8×2.3	22.0 ± 1.5	Flow	107	-24.50 ± 0.15	20.38	2
NGC3198	10:19:54.9	45:33:09	SB(rs)c	70	35	8.5×3.3	13.7 ± 0.5	Ceph	66	-22.90 ± 0.09	22.70	1
NGC3227	10:23:31.5	19:51:48	SAB(s)pec	49	155	5.4×3.6	20.3 ± 1.4	Flow	99	-23.90 ± 0.15	22.60	2
NGC3351	10:43:58.1	11:42:15	SB(r)b	49	13	7.4×5.0	5.3 ± 0.1	TRGB	26	-21.97 ± 0.05	21.57	2
NGC3521	11:05:49.0	-00:02:15	SAB(rs)bc	64	163	11.0×5.1	11.2 ± 1.8	TF	54	-24.47 ± 0.35	20.69	3
NGC3627	11:20:15.0	12:59:29	SAB(s)b	65	173	9.1×4.2	8.3 ± 0.3	TRGB	40	-23.71 ± 0.09	20.84	3
NGC3938	11:52:49.8	44:07:26	SA(s)c	25	52[b]	5.4×4.9	15.6 ± 1.1	Flow	75	-23.15 ± 0.16	22.11	2
NGC3949	11:53:41.5	47:51:35	SA(s)bc	57	120	2.9×1.7	19.1 ± 3.1	TF	92	-22.80 ± 0.35	-	1
NGC4013	11:58:31.7	43:56:48	SAb	90	66	5.2×1.0	18.9 ± 3.1	TF	92	-23.75 ± 0.35	22.95	2
NGC4254	12:18:49.4	14:25:07	SA(s)c	30	60[b]	5.4×4.7	14.6 ± 2.0	Flow	71	-26.07 ± 0.15	21.16	3
NCG4314	12:22:32.2	29:53:47	SB(rs)a	28	145[b]	4.2×3.7	17.9 ± 1.2	Flow	87	-23.81 ± 0.15	21.11	2
NGC4450	12:28:29.4	17:05:05	SA(s)ab	43	175	5.2×3.9	15.3 ± 2.5	TF	74	-23.87 ± 0.35	21.79	2
NGC4569	12:36:50.1	13:09:48	SAB(rs)ab	65	23	9.5×4.4	9.9 ± 0.2	STF	48	-23.39 ± 0.06	22.10	1
NGC4826	12:56:44.3	21:41:05	SA(rs)ab	59	115	10.0×5.4	4.4 ± 0.1	TRGB	21	-22.87 ± 0.03	20.69	1
NGC5055	13:15:49.3	42:02:06	SA(rs)bc	57	105	12.6×7.2	9.0 ± 0.1	TRGB	44	-24.16 ± 0.03	21.39	1
NGC5194	13:29:53.4	47:11:48	SA(s)bc	20[a]	163	11.2×6.9	9.1 ± 0.6	Flow	44	-24.30 ± 0.15	21.40	3
NGC5713	14:40:11.6	-00:17:26	SAB(rs)bc	28	10	2.8×2.5	31.3 ± 2.2	Flow	152	-24.15 ± 0.15	21.36	1
NGC5981	15:37:53.4	59:23:34	Sc	90	140	2.8×0.5	49.7 ± 9.2	TF	241	-24.19 ± 0.40	-	1
NGC6503	17:49:27.7	70:08:41	SA(s)cd	74	123	7.1×2.4	4.0 ± 0.1	TRGB	19	-20.71 ± 0.04	21.08	2
NGC6946	20:34:52.3	60:09:14	SAB(rs)cd	32	60[b]	11.5×9.8	6.1 ± 0.6	PNLF	29	-23.55 ± 0.21	22.93	2
NGC7479	23:04:57.1	12:19:18	SB(s)c	42	25	4.1×3.1	30.2 ± 5.6	TF	146	-24.20 ± 0.40	22.42	2
NGC7331	22:37:04.0	34:24:56	SA(s)b	72	171	10.5×3.7	14.5 ± 0.6	Ceph	70	-24.78 ± 0.09	21.51	1

[a] For NGC5194 we use kinematic inclination angle derived by Tully (1974)

[b] Position angles from Paturel et al. 2000 (NGC1042, NGC3938), Springob et al. 2007 (NGC4254, NGC6946), and Jarret et al. 2003 (NGC4314)

[c] Distance methods and references; TRGB: Tip of the red giant branch (Jacobs et al. 2009, Tully et al. 2009); Ceph: Cepheid variables (Freedman et al. 2001, except for NGC2841 taken from Macri et al. 2001); TF: HI 21cm Tully-Fisher (Tully et al. 2008, for NGC0337 we used the group Tully-Fisher distance); STF: Stellar kinematics Tully-Fisher (Cortes et al. 2008); PNLF: Planetary nebulae luminosity function (Herrman et al. 2008); Flow: Derived from redshift, and corrected for peculiar velocities (Mould et al. 2000, taken from NED)

Table 4.2. Bulge Structural Parameters

Object	B/T	n_{Bulge}
NGC0337	-	-
NGC0628	0.10[a]	1.35
NGC1042	-	-
NGC1068	-	-
NGC2775	0.61[b]	4.85
NGC2841	0.17[c]	2.97
NGC2903	0.09[c]	0.42
NGC3147	0.25[a]	3.66
NGC3166	0.25[b]	0.56
NGC3198	0.11[a]	5.12
NGC3227	-	-
NGC3351	0.17[c]	1.51
NGC3521	0.10[a]	3.20
NGC3627	0.08[a]	2.90
NGC3938	0.07[b]	1.18
NGC3949	-	-
NGC4013	-	-
NGC4254	0.39[b]	2.68
NCG4314	-	-
NGC4450	0.17[b]	2.26
NGC4569	0.06[c]	1.90
NGC4826	0.13[c]	3.94
NGC5055	0.26[a]	1.84
NGC5194	-	-
NGC5713	0.33[b]	1.84
NGC5981	-	-
NGC6503	-	-
NGC6946	-	-
NGC7479	0.09[b]	1.09
NGC7331	-	-

[a]K-band Decomposition, Dong & De Robertis 2006

[b]H-band Decomposition, Weinzirl et al. 2008

[c]V-band Decomposition, Fisher & Drory 2008

Table 4.3. Stellar Masses and Star Formation Rates

Object	$\log(M_*)$	$\log(SFR)$	Ref.
	$M_\odot$	$M_\odot$ yr^{-1}	
NGC0337	9.9	0.63	K03[a]
NGC0628	10.0	0.30	L09[c]
NGC1042	8.6	0.15	T07[b]
NGC1068	10.6	1.59	T07
NGC2775	10.8	0.06	T07
NGC2841	10.8	-0.70	K03
NGC2903	10.4	0.56	L09
NGC3147	11.2	-	-
NGC3166	10.7	-	-
NGC3198	10.1	-0.07	K03
NGC3227	10.5	-	-
NGC3351	9.7	0.20	L09
NGC3521	10.7	0.38	L09
NGC3627	10.4	0.69	L09
NGC3938	10.2	0.08	K03
NGC3949	10.1	-	-
NGC4013	10.4	-	-
NGC4254	11.4	1.04	K03
NCG4314	10.5	-0.18	T07
NGC4450	10.5	-0.30	K03
NGC4569	10.3	0.28	K03
NGC4826	10.1	0.07	L09
NGC5055	10.6	0.48	L09
NGC5194	10.7	0.88	L09
NGC5713	10.6	0.99	T07
NGC5981	10.6	-	-
NGC6503	9.2	-0.50	L09
NGC6946	10.4	0.96	L09
NGC7479	10.6	1.21	T07
NGC7331	10.9	0.62	K03

[a]K03: Kennicutt et al. 2003

[b]T07: Thilker et al. 2007

[c]L09: Lee et al. 2009

Table 4.4. VENGA Observing Runs

Dates	Observed Nights	Instrumental Setup	Observed Galaxies
08/04/2008	1	red	NGC5194
11/04/2008 - 11/09/2008	6	red	NGC0628, NGC1068
01/28/2009 - 01/31/2009	4	red	NGC2903, NGC3521
02/01/2009 - 02/03/2009	3	red	NGC1042, NGC2775, NGC3227, NGC3949, NGC4314
03/30/2009 - 04/02/2009	3	red	NGC3351, NGC4254
04/17/2009 - 04/19/2009	4	red	NGC4254, NGC5194
07/15/2009 - 07/16/2009	2	red	NGC5713, NGC6503
07/21/2009 - 07/23/2009	1	red	NGC6503
09/11/2009 - 09/15/2009	3	red	NGC0337, NGC1068, NGC5981, NGC6503, NGC7479
11/09/2009 - 11/15/2009	4	red	NGC0628, NGC1042, NGC1068, NGC2775
12/09/2009 - 12/21/2009	12	red	NGC0628, NGC1042, NGC2775, NGC2841, NGC3166, NGC3227, NGC3521, NGC3627
01/11/2010 - 01/16/2010	4	red	NGC1042, NGC2841, NGC3147, NGC3627, NGC4013
02/14/2010 - 02/18/2010	4	red	NGC1068, NGC2775, NGC3147, NGC3198, NGC4013, NGC4254
05/18/2010 - 05/20/2010	3	red	NGC3998, NGC5055
06/04/2010 - 06/06/2010	2	red	NGC3198, NGC4450, NGC6964
07/05/2010 - 07/09/2010	3	red	NGC4450, NGC6946
09/01/2010 - 09/07/2010	6	blue	NGC1068, NGC5981, NGC6503, NGC6946, NGC7479, NGC7731
10/01/2010 - 10/06/2010	5	blue	NGC0337, NGC0628, NGC1068, NGC6946, NGC7731
11/10/2010 - 11/14/2010	2	blue	NGC0628
12/07/2010 - 12/12/2010	5	blue	NGC0628, NGC1042, NGC2775, NGC2903
12/27/2010 - 01/02/2011	5	blue	NGC0628, NGC2775, NGC2841, NGC3147, NGC3227
01/27/2011 - 02/02/2011	4	blue	NGC0628, NGC2775, NGC2841, NGC3147, NGC3166, NGC3198, NGC3227
02/07/2011 - 02/10/2011	3	blue	NGC2841, NGC3147, NGC3166, NGC3198, NGC3227, NGC3521

Table 4.4 (cont'd)

Dates	Observed Nights	Instrumental Setup	Observed Galaxies
03/28/2011 - 03/31/2011	4	blue	NGC2775, NGC3147, NGC3351, NGC3627, NGC5713
04/08/2011 - 04/10/2011	1	blue	NGC3351, NGC3949

Table 4.5. Summary of Red-setup Observations of NGC0628

Pointing	Equatorial Coord.		Dither	Exposure Time	N	⟨Seeing⟩	⟨Transparency⟩
	α	δ		hours		$''$	
P1	01:36:42.45	15:47:04.6	D1	4.00	12	2.06	0.87
			D2	4.33	13	2.22	0.85
			D3	3.33	10	2.20	0.89
P2	01:36:49.45	15:47:04.2	D1	3.00	6	1.92	0.65
			D2	3.50	7	2.00	0.67
			D3	3.50	7	1.87	0.68
P3	01:36:35.51	15:47:05.0	D1	8.50	17	2.62	0.63
			D2	7.50	15	2.72	0.61
			D3	7.50	15	2.57	0.68

Table 4.6. Fitted Emission Lines

Transition	Wavelength	Median S/N	$N_{5\sigma}$	$N_{3\sigma}$
	Å			
HeII	4685.74	0.5	1	2
Hβ	4861.32	11.7	1813	2035
[OIII]	4958.83	2.9	432	1032
[OIII]	5006.77	6.9	1560	1975
[NI]	5197.90	0.6	3	20
[NI]	5200.39	1.3	17	174
[NII]	6547.96	8.1	1709	1979
Hα	6562.80	29.9	2143	2183
[NII]	6583.34	19.7	2083	2169
[SII]	6716.31	11.6	2007	2151
[SII]	6730.68	7.2	1546	1953

Chapter 5

Summary

The collection of results presented in this thesis, is only a limited example of the potential that integral field spectroscopy has for studying galaxy evolution across cosmic time, from the earliest times in the history of the universe to the present day. In Chapter 2, I presented results from the HETDEX Pilot Survey. The VIRUS-P data allowed me to measure the Lyα luminosity function and its evolution with redshift, and also constrain the cosmic history of the Lyα photon escape fraction from galaxies.

By combining Lyα measurements from the Pilot Survey, with deep publicly available broad-band imaging of the targets, I measured the Lyα escape fraction and dust reddening $E(B-V)$ of individual LAEs in the sample. The Lyα escape fraction in LAEs correlates with $E(B-V)$ in a way that is expected if Lyα photons suffer from similar amounts of dust extinction as UV continuum photons. This result implies that a strong enhancement of the Lyα EW with dust, due to a clumpy multi-phase ISM, is not a common process in LAEs at these redshifts. It also suggests that while in other galaxies Lyα can be preferentially quenched by dust due to its scattering nature, this is not the case in LAEs. The mean Lyα escape fraction of the overall galaxy population

decreases significantly from $z \sim 6$ to $z \sim 2$. Our results point towards a scenario in which star-forming galaxies build up significant amounts of dust in their ISM between $z \sim 6$ and 2, reducing their Lyα escape fraction, with LAE selection preferentially detecting galaxies which have the highest escape fractions given their dust content. The fact that a large escape of Lyα photons is reached by $z \sim 6$ implies that better constraints on this quantity at higher redshifts might detect re-ionization in a way that is uncoupled from the effects of dust.

The Pilot Survey is nothing more than a modest sample of what the actual HETDEX Survey on the 9.2m HET will do. The first three science exposures with VIRUS, covering three dithers on a single VIRUS field-of-view, will detect more LAEs than we did over three years of observations with VIRUS-P on the 2.7m telescope. While the reader might thing that this would fill us with a sense of futility, the reality is that HETDEX will provide one of the most powerful samples to study galaxy evolution ever constructed. Not only we expect to detect $\sim 700,000$ LAEs, but also about $1,000,000$ [OII] emitters at $z < 0.48$, and thousands of nearby galaxies which will be spatially resolved with VIRUS. This enormous and unprecedented sample, will help further our understanding of the different physical processes involved in the formation and evolution of galaxies, and will fuel a large number of publications in the next few years.

While originally designed as a test-bench for VIRUS, and a proof of concept for HETDEX, the VIRUS-P spectrograph has proven to be highly

competitive in the world of today's large field-of-view IFUs. This has permitted the conduction of VENGA, a large survey dedicated to spectroscopically map the disks of 30 nearby massive spiral galaxies. In Chapters 3 and 4, I have presented the first results published with VENGA data, and I provided a detailed description of the survey design, observing strategy, data reduction and analysis pipelines, and final data products.

In particular, in Chapter 3, I presented a study of the spatially resolved star-formation law (i.e. the correlation between the SFR and gas surface densities) for both the atomic, and molecular components of the ISM in the central region of the Sbc galaxy NGC5194. My results show that the SFR in a given region within the galaxy is mostly set by the availability of molecular gas. The atomic gas surface density is mostly uncorrelated with the SFR surface density, at least in the central regions of this galaxy, where the ISM is mostly dominated by H_2. On the experimental side, I discussed a series of systematic uncertainties affecting the measurement of Hα fluxes in nearby galaxies, which can be easily controlled when using integral field spectroscopy, but can strongly impact narrow-band imaging measurements. I expect this discussion to be useful for researchers attempting to use this latter technique.

The VENGA Survey is still in the phase of data acquisition. The team expects to complete the VENGA observations during 2011. As discussed in the introduction of Chapter 4, the VENGA data will be used to conduct a large number of studies on star-formation, structure assembly, stellar populations, gas and stellar dynamics, chemical evolution, ISM structure, and galactic feed-

back. Besides describing the techniques used to acquire and analyze the data, I presented preliminary results on the Sc face-on galaxy NGC0628, including the discovery of a previously undetected low-luminosity AGN in the nucleus of the galaxy, and measurement of the nebular oxygen abundance radial gradient in this system. I also measured the star formation efficiency of bright star forming regions in NGC0628, and found a correlation between the gas phase oxygen abundance and SFE. The physical origin of this correlation is currently unknown, but it might be related to impact that the abundance of molecular coolants and dust have on the process of core collapse and subsequent star formation. The metallicity-SFE correlation found here provides a natural explanation for the decrease of the SFE towards the outer parts of the disks of spiral galaxies.

Bibliography

Adams, J. J., Gebhardt, K., Hill, G. J., Blanc, G. A., & van den Bosch, R. 2010, in Astronomical Society of the Pacific Conference Series, Vol. 432, New Horizons in Astronomy: Frank N. Bash Symposium 2009, ed. L. M. Stanford, J. D. Green, L. Hao, & Y. Mao, 175–+

Adams, J. J., Hill, G. J., & MacQueen, P. J. 2009, ApJ, 694, 314

Adams, J. J., Uson, J. M., Hill, G. J., & MacQueen, P. J. 2011a, ApJ, 728, 107

Adams, J. J., et al. 2011b, ApJS, 192, 5

Ajiki, M., Mobasher, B., Taniguchi, Y., Shioya, Y., Nagao, T., Murayama, T., & Sasaki, S. S. 2006, ApJ, 638, 596

Allende Prieto, C., Lambert, D. L., & Asplund, M. 2001, ApJ, 556, L63

Aller, L. H. 1942, ApJ, 95, 52

Atek, H., Kunth, D., Hayes, M., Östlin, G., & Mas-Hesse, J. M. 2008, A&A, 488, 491

Atek, H., Kunth, D., Schaerer, D., Hayes, M., Deharveng, J. M., Östlin, G., & Mas-Hesse, J. M. 2009, A&A, 506, L1

Bacon, R., et al. 2001, MNRAS, 326, 23

Baldwin, J. A., Phillips, M. M., & Terlevich, R. 1981, PASP, 93, 5

Beers, T. C., Flynn, K., & Gebhardt, K. 1990, AJ, 100, 32

Beifiori, A., Maraston, C., Thomas, D., & Johansson, J. 2010, ArXiv e-prints

Bershady, M. A., Andersen, D. R., Harker, J., Ramsey, L. W., & Verheijen, M. A. W. 2004, PASP, 116, 565

Bershady, M. A., Verheijen, M. A. W., Swaters, R. A., Andersen, D. R., Westfall, K. B., & Martinsson, T. 2010, ApJ, 716, 198

Bertin, E., & Arnouts, S. 1996, A&AS, 117, 393

Bigiel, F., Leroy, A., Walter, F., Brinks, E., de Blok, W. J. G., Madore, B., & Thornley, M. D. 2008, AJ, 136, 2846

Blanc, G. A., Heiderman, A., Gebhardt, K., Evans, N. J., & Adams, J. 2009, ApJ, 704, 842

Blanc, G. A., et al. 2008, ApJ, 681, 1099

Blanc, G. A., et al. 2010, in Astronomical Society of the Pacific Conference Series, Vol. 432, New Horizons in Astronomy: Frank N. Bash Symposium 2009, ed. L. M. Stanford, J. D. Green, L. Hao, & Y. Mao, 180–+

—. 2011, ArXiv e-prints

Blitz, L., Fukui, Y., Kawamura, A., Leroy, A., Mizuno, N., & Rosolowsky, E. 2007, Protostars and Planets V, 81

Bloemen, J. B. G. M., et al. 1986, A&A, 154, 25

Blumenthal, G. R., Faber, S. M., Primack, J. R., & Rees, M. J. 1984, Nature, 311, 517

Boissier, S., et al. 2007, ApJS, 173, 524

Bolatto, A. D., Leroy, A. K., Rosolowsky, E., Walter, F., & Blitz, L. 2008, ApJ, 686, 948

Bouwens, R. J., et al. 2009, ApJ, 705, 936

—. 2010a, ApJ, 709, L133

—. 2010b, ApJ, 708, L69

Bradley, L. D., Kaiser, M. E., & Baan, W. A. 2004, ApJ, 603, 463

Bresolin, F., Garnett, D. R., & Kennicutt, Jr., R. C. 2004, ApJ, 615, 228

Brinchmann, J., Charlot, S., White, S. D. M., Tremonti, C., Kauffmann, G., Heckman, T., & Brinkmann, J. 2004, MNRAS, 351, 1151

Brocklehurst, M. 1971, MNRAS, 153, 471

Bruzual, G., & Charlot, S. 2003, MNRAS, 344, 1000

Calzetti, D. 1997, AJ, 113, 162

Calzetti, D., Armus, L., Bohlin, R. C., Kinney, A. L., Koornneef, J., & Storchi-Bergmann, T. 2000, ApJ, 533, 682

Calzetti, D., Kinney, A. L., & Storchi-Bergmann, T. 1994, ApJ, 429, 582

Calzetti, D., et al. 2005, ApJ, 633, 871

Capak, P., et al. 2004, AJ, 127, 180

—. 2007, ApJS, 172, 99

Cappellari, M., & Emsellem, E. 2004, PASP, 116, 138

Cappellari, M., et al. 2011, MNRAS, 269

Cassata, P., et al. 2011, A&A, 525, A143+

Castanheira, B. G., Winget, D. E., Williams, K., Montgomery, M. H., Falcon, R. E., & Hermes, J. J. 2010, in American Institute of Physics Conference Series, Vol. 1273, American Institute of Physics Conference Series, ed. K. Werner & T. Rauch, 160–163

Charlot, S., & Fall, S. M. 1993, ApJ, 415, 580

Charlot, S., & Longhetti, M. 2001, MNRAS, 323, 887

Cowie, L. L., Barger, A. J., & Hu, E. M. 2010, ApJ, 711, 928

Cowie, L. L., & Hu, E. M. 1998, AJ, 115, 1319

Crane, P. C., & van der Hulst, J. M. 1992, AJ, 103, 1146

Croton, D. J., et al. 2006, MNRAS, 365, 11

Daddi, E., Cimatti, A., Renzini, A., Fontana, A., Mignoli, M., Pozzetti, L., Tozzi, P., & Zamorani, G. 2004, ApJ, 617, 746

Dawson, S., Rhoads, J. E., Malhotra, S., Stern, D., Wang, J., Dey, A., Spinrad, H., & Jannuzi, B. T. 2007, ApJ, 671, 1227

de Vaucouleurs, G., de Vaucouleurs, A., Corwin, Jr., H. G., Buta, R. J., Paturel, G., & Fouqué, P. 1991, Third Reference Catalogue of Bright Galaxies. Volume I: Explanations and references. Volume II: Data for galaxies between 0^h and 12^h. Volume III: Data for galaxies between 12^h and 24^h., ed. de Vaucouleurs, G., de Vaucouleurs, A., Corwin, H. G., Jr., Buta, R. J., Paturel, G., & Fouqué, P.

de Zeeuw, P. T., et al. 2002, MNRAS, 329, 513

Deharveng, J., et al. 2008, ApJ, 680, 1072

Deharveng, L., Peña, M., Caplan, J., & Costero, R. 2000, MNRAS, 311, 329

Dekel, A., et al. 2009, Nature, 457, 451

Dib, S., Piau, L., Mohanty, S., & Braine, J. 2011, ArXiv e-prints

Dickinson, M., Giavalisco, M., & GOODS Team. 2003, in The Mass of Galaxies at Low and High Redshift, ed. R. Bender & A. Renzini, 324–+

Dijkstra, M., Haiman, Z., & Spaans, M. 2006, ApJ, 649, 14

Dijkstra, M., Lidz, A., & Wyithe, J. S. B. 2007, MNRAS, 377, 1175

Dijkstra, M., & Westra, E. 2010, MNRAS, 401, 2343

Dolphin, A. E., et al. 2001, MNRAS, 324, 249

Dong, X. Y., & De Robertis, M. M. 2006, AJ, 131, 1236

Dove, J. B., Shull, J. M., & Ferrara, A. 2000, ApJ, 531, 846

Drory, N., Feulner, G., Bender, R., Botzler, C. S., Hopp, U., Maraston, C., Mendes de Oliveira, C., & Snigula, J. 2001, MNRAS, 325, 550

Dunkley, J., et al. 2009, ApJS, 180, 306

Erb, D. K., Steidel, C. C., Shapley, A. E., Pettini, M., Reddy, N. A., & Adelberger, K. L. 2006, ApJ, 646, 107

Evans, N. J., et al. 2009, ApJS, 181, 321

Fabricius, M. H., Barnes, S., Bender, R., Drory, N., Grupp, F., Hill, G. J., Hopp, U., & MacQueen, P. J. 2008, in Society of Photo-Optical Instrumentation Engineers (SPIE) Conference Series, Vol. 7014, Society of Photo-Optical Instrumentation Engineers (SPIE) Conference Series

Ferguson, A. M. N., Wyse, R. F. G., Gallagher, III, J. S., & Hunter, D. A. 1996, AJ, 111, 2265

Filippenko, A. V., & Sargent, W. L. W. 1985, ApJS, 57, 503

Finkelstein, S. L., Papovich, C., Giavalisco, M., Reddy, N. A., Ferguson, H. C., Koekemoer, A. M., & Dickinson, M. 2010, ApJ, 719, 1250

Finkelstein, S. L., Rhoads, J. E., Malhotra, S., & Grogin, N. 2009, ApJ, 691, 465

Finkelstein, S. L., Rhoads, J. E., Malhotra, S., Grogin, N., & Wang, J. 2008, ApJ, 678, 655

Finkelstein, S. L., et al. 2011, ApJ, 729, 140

Fisher, D. B., & Drory, N. 2008, AJ, 136, 773

Förster Schreiber, N. M., et al. 2006, ApJ, 645, 1062

Ganda, K., Falcón-Barroso, J., Peletier, R. F., Cappellari, M., Emsellem, E., McDermid, R. M., de Zeeuw, P. T., & Carollo, C. M. 2006, MNRAS, 367, 46

Gawiser, E., et al. 2006a, ApJS, 162, 1

—. 2006b, ApJ, 642, L13

—. 2007, ApJ, 671, 278

Genzel, R., et al. 2006, Nature, 442, 786

Gil de Paz, A., et al. 2005, ApJ, 627, L29

González, V., Labbé, I., Bouwens, R. J., Illingworth, G., Franx, M., Kriek, M., & Brammer, G. B. 2010, ApJ, 713, 115

Greenawalt, B., Walterbos, R. A. M., Thilker, D., & Hoopes, C. G. 1998, ApJ, 506, 135

Grevesse, N., Noels, A., & Sauval, A. J. 1996, in Astronomical Society of the Pacific Conference Series, Vol. 99, Cosmic Abundances, ed. S. S. Holt & G. Sonneborn, 117–+

Gronwall, C., et al. 2007, ApJ, 667, 79

Guaita, L., et al. 2010, ApJ, 714, 255

Haffner, L. M., Reynolds, R. J., & Tufte, S. L. 1999, ApJ, 523, 223

Haffner, L. M., et al. 2009, Reviews of Modern Physics, 81, 969

Haiman, Z., & Spaans, M. 1999, ApJ, 518, 138

Hansen, M., & Oh, S. P. 2006, MNRAS, 367, 979

Hayes, M., Östlin, G., Atek, H., Kunth, D., Mas-Hesse, J. M., Leitherer, C., Jiménez-Bailón, E., & Adamo, A. 2007, MNRAS, 382, 1465

Hayes, M., Östlin, G., Mas-Hesse, J. M., Kunth, D., Leitherer, C., & Petrosian, A. 2005, A&A, 438, 71

Hayes, M., Schaerer, D., Östlin, G., Mas-Hesse, J. M., Atek, H., & Kunth, D. 2011, ApJ, 730, 8

Hayes, M., et al. 2010, Nature, 464, 562

Helfer, T. T., Thornley, M. D., Regan, M. W., Wong, T., Sheth, K., Vogel, S. N., Blitz, L., & Bock, D. 2003, ApJS, 145, 259

Hibon, P., et al. 2010, A&A, 515, A97+

Hill, G. J., et al. 2008a, in Society of Photo-Optical Instrumentation Engineers (SPIE) Conference Series, Vol. 7014, Society of Photo-Optical Instrumentation Engineers (SPIE) Conference Series

Hill, G. J., et al. 2008b, in Astronomical Society of the Pacific Conference Series, Vol. 399, Panoramic Views of Galaxy Formation and Evolution, ed. T. Kodama, T. Yamada, & K. Aoki, 115–+

Hill, G. J., et al. 2010, in Society of Photo-Optical Instrumentation Engineers (SPIE) Conference Series, Vol. 7735, Society of Photo-Optical Instrumentation Engineers (SPIE) Conference Series

Ho, L. C., Filippenko, A. V., & Sargent, W. L. W. 1997, ApJ, 487, 568

Hoopes, C. G., & Walterbos, R. A. M. 2003, ApJ, 586, 902

Hoopes, C. G., Walterbos, R. A. M., & Greenwalt, B. E. 1996, AJ, 112, 1429

Hu, E. M., Cowie, L. L., & McMahon, R. G. 1998, ApJ, 502, L99+

Hummer, D. G., & Kunasz, P. B. 1980, ApJ, 236, 609

Isobe, T., Feigelson, E. D., Akritas, M. G., & Babu, G. J. 1990, ApJ, 364, 104

Jarrett, T. H., Chester, T., Cutri, R., Schneider, S., Skrutskie, M., & Huchra, J. P. 2000, AJ, 119, 2498

Jarrett, T. H., Chester, T., Cutri, R., Schneider, S. E., & Huchra, J. P. 2003, AJ, 125, 525

Jeong, D., & Komatsu, E. 2006, ApJ, 651, 619

—. 2009, ApJ, 691, 569

Kashikawa, N., et al. 2006, ApJ, 648, 7

Kauffmann, G., Colberg, J. M., Diaferio, A., & White, S. D. M. 1999, MNRAS, 303, 188

Kauffmann, G., et al. 2003, MNRAS, 346, 1055

Kelz, A., et al. 2006, PASP, 118, 129

Kennicutt, Jr., R. C. 1998a, ARA&A, 36, 189

—. 1998b, ApJ, 498, 541

Kennicutt, Jr., R. C., & Garnett, D. R. 1996, ApJ, 456, 504

Kennicutt, Jr., R. C., et al. 2003, PASP, 115, 928

—. 2007, ApJ, 671, 333

Kewley, L. J., Dopita, M. A., Sutherland, R. S., Heisler, C. A., & Trevena, J. 2001, ApJ, 556, 121

Koehler, R. S., Schuecker, P., & Gebhardt, K. 2007, A&A, 462, 7

Kormendy, J., & Kennicutt, Jr., R. C. 2004, ARA&A, 42, 603

Kornei, K. A., Shapley, A. E., Erb, D. K., Steidel, C. C., Reddy, N. A., Pettini, M., & Bogosavljević, M. 2010, ApJ, 711, 693

Krumholz, M. R., & McKee, C. F. 2005, ApJ, 630, 250

Krumholz, M. R., McKee, C. F., & Tumlinson, J. 2008, ApJ, 689, 865

—. 2009a, ApJ, 693, 216

—. 2009b, ApJ, 699, 850

Krumholz, M. R., & Tan, J. C. 2007, ApJ, 654, 304

Kudritzki, R., et al. 2000, ApJ, 536, 19

Kunth, D., Leitherer, C., Mas-Hesse, J. M., Östlin, G., & Petrosian, A. 2003, ApJ, 597, 263

Kunth, D., Mas-Hesse, J. M., Terlevich, E., Terlevich, R., Lequeux, J., & Fall, S. M. 1998, A&A, 334, 11

Kurk, J. D., Cimatti, A., di Serego Alighieri, S., Vernet, J., Daddi, E., Ferrara, A., & Ciardi, B. 2004, A&A, 422, L13

Lai, K., et al. 2008, ApJ, 674, 70

Laursen, P., Sommer-Larsen, J., & Razoumov, A. O. 2011, ApJ, 728, 52

Law, D. R., Steidel, C. C., Erb, D. K., Larkin, J. E., Pettini, M., Shapley, A. E., & Wright, S. A. 2007, ApJ, 669, 929

Le Delliou, M., Lacey, C., Baugh, C. M., Guiderdoni, B., Bacon, R., Courtois, H., Sousbie, T., & Morris, S. L. 2005, MNRAS, 357, L11

Lee, J. C., et al. 2009, ApJ, 706, 599

Leitherer, C., & Heckman, T. M. 1995, ApJS, 96, 9

Lemoine-Busserolle, M., Bunker, A., Lamareille, F., & Kissler-Patig, M. 2010, MNRAS, 401, 1657

Lemoine-Busserolle, M., & Lamareille, F. 2010, MNRAS, 402, 2291

Leroy, A. K., Walter, F., Brinks, E., Bigiel, F., de Blok, W. J. G., Madore, B., & Thornley, M. D. 2008, AJ, 136, 2782

Leroy, A. K., et al. 2011, ArXiv e-prints

Machalek, P., Waghorn, B., & Allen, R. 2005, in Bulletin of the American Astronomical Society, Vol. 37, Bulletin of the American Astronomical Society, 452–+

Madau, P. 1995, ApJ, 441, 18

Madsen, G. J., Reynolds, R. J., & Haffner, L. M. 2006, ApJ, 652, 401

Magrini, L., Sestito, P., Randich, S., & Galli, D. 2009, A&A, 494, 95

Malhotra, S., & Rhoads, J. E. 2002, ApJ, 565, L71

Martin, C. L., & Sawicki, M. 2004, ApJ, 603, 414

Massey, P., Strobel, K., Barnes, J. V., & Anderson, E. 1988, ApJ, 328, 315

Mathis, J. S. 2000, ApJ, 544, 347

McKee, C. F. 1999, in NATO ASIC Proc. 540: The Origin of Stars and Planetary Systems, ed. C. J. Lada & N. D. Kylafis, 29–+

McKee, C. F., & Ostriker, E. C. 2007, ARA&A, 45, 565

Mellier, Y., Bertin, E., Hudelot, P., Magnard, F., McCracken, H., Monnerville, M., Schultheis, M., & G., S. 2008, in http://terapix.iap.fr/cplt/oldSite/Descart/CFHTLS-T0005-Release.pdf, Vol. 1

Meurer, G. R., Heckman, T. M., & Calzetti, D. 1999, ApJ, 521, 64

Meurer, G. R., Heckman, T. M., Leitherer, C., Kinney, A., Robert, C., & Garnett, D. R. 1995, AJ, 110, 2665

Moustakas, J., Kennicutt, Jr., R. C., Tremonti, C. A., Dale, D. A., Smith, J., & Calzetti, D. 2010, ApJS, 190, 233

Murphy, J. D., Gebhardt, K., & Adams, J. J. 2011, ApJ, 729, 129

Mutchler, M., et al. 2005, in Bulletin of the American Astronomical Society, Vol. 37, American Astronomical Society Meeting Abstracts #206, 452–+

Neufeld, D. A. 1991, ApJ, 370, L85

Nilsson, K. K., & Møller, P. 2009, A&A, 508, L21

Nilsson, K. K., Tapken, C., Møller, P., Freudling, W., Fynbo, J. P. U., Meisenheimer, K., Laursen, P., & Östlin, G. 2009, A&A, 498, 13

Nilsson, K. K., et al. 2007, A&A, 471, 71

Oesch, P. A., et al. 2009, ApJ, 690, 1350

Oey, M. S., et al. 2007, ApJ, 661, 801

Oke, J. B. 1990, AJ, 99, 1621

Ono, Y., Ouchi, M., Shimasaku, K., Dunlop, J., Farrah, D., McLure, R., & Okamura, S. 2010, ApJ, 724, 1524

Osterbrock, D. E., & Ferland, G. J. 2006, Astrophysics of gaseous nebulae and active galactic nuclei, ed. Osterbrock, D. E. & Ferland, G. J.

Ouchi, M., et al. 2003, ApJ, 582, 60

—. 2008, ApJS, 176, 301

—. 2010, ApJ, 723, 869

Partridge, R. B., & Peebles, P. J. E. 1967, ApJ, 147, 868

Pei, Y. C. 1992, ApJ, 395, 130

Pettini, M., Kellogg, M., Steidel, C. C., Dickinson, M., Adelberger, K. L., & Giavalisco, M. 1998, ApJ, 508, 539

Pflamm-Altenburg, J., & Kroupa, P. 2008, Nature, 455, 641

Pflamm-Altenburg, J., Weidner, C., & Kroupa, P. 2007, ApJ, 671, 1550

Pierre, M., et al. 2004, Journal of Cosmology and Astroparticle Physics, 9, 11

Pilyugin, L. S., & Mattsson, L. 2011, MNRAS, 412, 1145

Press, W. H., Flannery, B. P., Teukolsky, S. A., & Vetterling, W. T. 1989, Numerical recipes in Pascal. The art of scientific computing, ed. Press, W. H., Flannery, B. P., Teukolsky, S. A., & Vetterling, W. T.

Rauch, M., et al. 2008, ApJ, 681, 856

Reddy, N. A., Erb, D. K., Pettini, M., Steidel, C. C., & Shapley, A. E. 2010, ApJ, 712, 1070

Reddy, N. A., Steidel, C. C., Pettini, M., Adelberger, K. L., Shapley, A. E., Erb, D. K., & Dickinson, M. 2008, ApJS, 175, 48

Reynolds, R. J. 1985, ApJ, 294, 256

Rhoads, J. E., Malhotra, S., Dey, A., Stern, D., Spinrad, H., & Jannuzi, B. T. 2000, ApJ, 545, L85

Rosales-Ortega, F. F., Díaz, A. I., Kennicutt, R. C., & Sánchez, S. F. 2011, ArXiv e-prints

Rosales-Ortega, F. F., Kennicutt, R. C., Sánchez, S. F., Díaz, A. I., Pasquali, A., Johnson, B. D., & Hao, C. N. 2010, MNRAS, 405, 735

Rosolowsky, E., & Simon, J. D. 2008, ApJ, 675, 1213

Sánchez, S. F., et al. 2010, ArXiv e-prints

Sánchez-Blázquez, P., et al. 2006, MNRAS, 371, 703

Sarzi, M., et al. 2006, MNRAS, 366, 1151

Sawicki, M., et al. 2008, ApJ, 687, 884

Schaerer, D. 2003, A&A, 397, 527

Schaerer, D., & Pelló, R. 2005, MNRAS, 362, 1054

Schechter, P. 1976, ApJ, 203, 297

Schlegel, D. J., Finkbeiner, D. P., & Davis, M. 1998, ApJ, 500, 525

Schmidt, M. 1959, ApJ, 129, 243

Schuster, K. F., Kramer, C., Hitschfeld, M., Garcia-Burillo, S., & Mookerjea, B. 2007, A&A, 461, 143

Scoville, N., et al. 2007, ApJS, 172, 1

Scoville, N. Z., Polletta, M., Ewald, S., Stolovy, S. R., Thompson, R., & Rieke, M. 2001, AJ, 122, 3017

Searle, L. 1971, ApJ, 168, 327

Shapley, A. E., Steidel, C. C., Adelberger, K. L., Dickinson, M., Giavalisco, M., & Pettini, M. 2001, ApJ, 562, 95

Shaver, P. A., McGee, R. X., Newton, L. M., Danks, A. C., & Pottasch, S. R. 1983, MNRAS, 204, 53

Shetrone, M., Martell, S. L., Wilkerson, R., Adams, J., Siegel, M. H., Smith, G. H., & Bond, H. E. 2010, AJ, 140, 1119

Shimasaku, K., et al. 2006, PASJ, 58, 313

Shu, F. H., Adams, F. C., & Lizano, S. 1987, ARA&A, 25, 23

Spaans, M., & Meijerink, R. 2005, Ap&SS, 295, 239

Stark, D. P., Ellis, R. S., Chiu, K., Ouchi, M., & Bunker, A. 2010, MNRAS, 408, 1628

Steidel, C. C., Adelberger, K. L., Shapley, A. E., Pettini, M., Dickinson, M., & Giavalisco, M. 2003, ApJ, 592, 728

Tan, J. C. 2010, ApJ, 710, L88

Tapken, C., Appenzeller, I., Noll, S., Richling, S., Heidt, J., Meinköhn, E., & Mehlert, D. 2007, A&A, 467, 63

Tapken, C., et al. 2006, A&A, 455, 145

Terashima, Y., Ho, L. C., & Ulvestad, J. S. 2004, in IAU Symposium, Vol. 222, The Interplay Among Black Holes, Stars and ISM in Galactic Nuclei, ed. T. Storchi-Bergmann, L. C. Ho, & H. R. Schmitt, 61–64

Terashima, Y., & Wilson, A. S. 2001, ApJ, 560, 139

Thilker, D. A., Walterbos, R. A. M., Braun, R., & Hoopes, C. G. 2002, AJ, 124, 3118

Thilker, D. A., et al. 2005, ApJ, 619, L79

—. 2007, ApJS, 173, 538

Thompson, T. A. 2008, ApJ, 684, 212

Tielens, A. G. G. M. 2005, The Physics and Chemistry of the Interstellar Medium, ed. Tielens, A. G. G. M.

Toomre, A., & Toomre, J. 1972, ApJ, 178, 623

Tran, K., Lilly, S. J., Crampton, D., & Brodwin, M. 2004, ApJ, 612, L89

Tully, R. B. 1974, ApJS, 27, 437

Valdes, F., Gupta, R., Rose, J. A., Singh, H. P., & Bell, D. J. 2004, ApJS, 152, 251

Vallejo, O., Braine, J., & Baudry, A. 2002, A&A, 387, 429

van Breukelen, C., Jarvis, M. J., & Venemans, B. P. 2005, MNRAS, 359, 895

van Dokkum, P. G. 2001, PASP, 113, 1420

van Zee, L., Salzer, J. J., Haynes, M. P., O'Donoghue, A. A., & Balonek, T. J. 1998, AJ, 116, 2805

Veilleux, S., & Osterbrock, D. E. 1987, ApJS, 63, 295

Verhamme, A., Schaerer, D., Atek, H., & Tapken, C. 2008, A&A, 491, 89

Verhamme, A., Schaerer, D., & Maselli, A. 2006, A&A, 460, 397

Vila-Costas, M. B., & Edmunds, M. G. 1992, MNRAS, 259, 121

Walter, F., Brinks, E., de Blok, W. J. G., Bigiel, F., Kennicutt, R. C., Thornley, M. D., & Leroy, A. 2008, AJ, 136, 2563

Weinzirl, T., Jogee, S., Khochfar, S., Burkert, A., & Kormendy, J. 2009, ApJ, 696, 411

Wong, T., & Blitz, L. 2002, ApJ, 569, 157

Wright, S. A., et al. 2007, ApJ, 658, 78

Yoachim, P., Roškar, R., & Debattista, V. P. 2010, ApJ, 716, L4

York, D. G., et al. 2000, AJ, 120, 1579

Zaritsky, D., Kennicutt, Jr., R. C., & Huchra, J. P. 1994, ApJ, 420, 87

Zheng, Z., Cen, R., Trac, H., & Miralda-Escudé, J. 2010, ApJ, 716, 574

Vita

Guillermo Blanc was born in Santiago, Chile, where he attended Tabancura school. He received his degree of Bachelor in Science from Universidad de Chile in 2004, and of Master in Science with mention in Astronomy, from the same institution, in 2006. In August 2006 he entered the Graduate School at the University of Texas at Austin. Upon graduation he will be a Postdoctoral Fellow at the Observatories of the Carnegie Institution for Science in Pasadena, CA.

Permanent address: gblancm.astro@gmail.com

This dissertation was typeset with LaTeX[†] by the author.

[†]LaTeX is a document preparation system developed by Leslie Lamport as a special version of Donald Knuth's TeX Program.